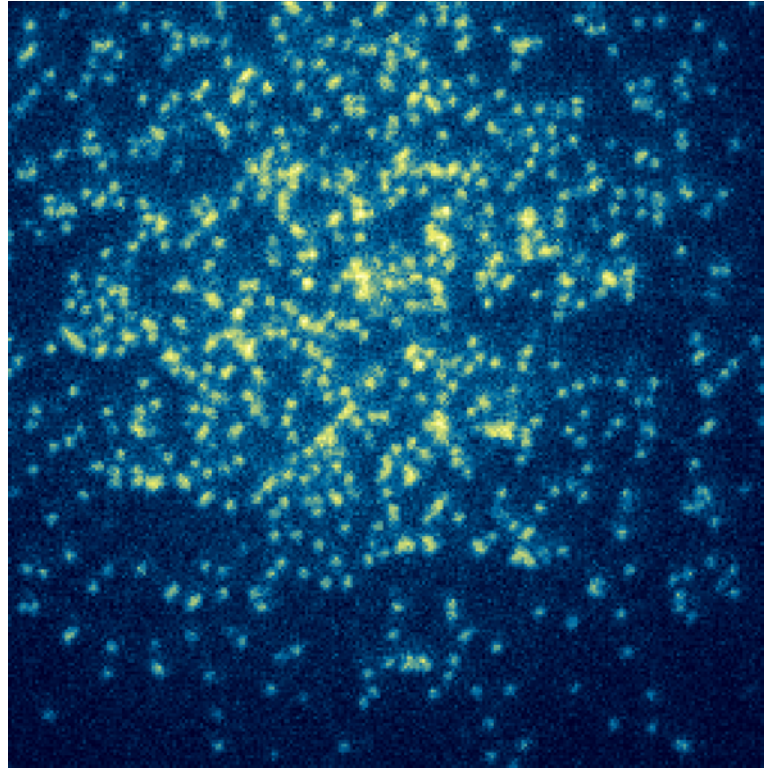
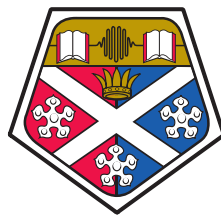


A single-site resolution fermionic quantum-gas microscope



Ph.D. Student:
Dylan A. COTTA

Principal Investigator:
Prof. Stefan KUHR



UNIVERSITY OF STRATHCLYDE

DOCTORAL DISSERTATION

submitted to the Physics Department of the University of Strathclyde
in the partial fulfillment of the requirements for the degree of Doctor of Philosophy

June 12, 2018

Des flots où nous nous trouvions, nous lançons des
ponts et fondions des îles dont nous ne serions ni l'invité ni l'habitant.
Tel est le destin des poètes exaspérés, ouvriers qualifiés en prévisions
et en préparatifs.

René Char

إهداء إلى الرائعه حد الكمال جدتي، ماما عائشه. فكمآ تمنيتي، لم تذهب جيناتك إلى الاشياء، بل ساعدت علي تطور
بعض من الاختراعات الاكثر تطورا في تاريخ الانسانيه الحديث.

Acknowledgements

My journey in atomic physics started during my second year at ENS when Laurent Sanchez-Palencia explained to the audience of his tutorial class how cold atoms and BEC were experimentally achieved. Shortly after I began looking for a research group which would host me for a year. I could hardly have found a better one than Markus Greiner's Lithium lab at Harvard University which two years later lead me into Stefan Kuhr's laboratory at the University of Strathclyde where I performed my doctoral research.

Professor Stefan Kuhr granted me the chance of being part of his team which was back then composed of post doctoral fellows Elmar Haller and Graham Bruce and PhD students James Hudson and Andrew Kelly. I immediately took over Andreas Shindewolf, a master student from Germany, who had been in charge of building the premises of the 3D lattice. I could never thank Stefan enough for allowing me to be part of the fermionic quantum-gas microscope race again, especially being supervised by such driven, dedicated, skilled and knowledgeable trio.

The first general impression that I got when I joined the group was one of out most competency and kindness. Even though the group composed of eight members was reasonably large, we never experienced any form of internal competitive behaviour, there was simply too many stimulating tasks to perform, goals to reach in a kindred surrounding atmosphere typical of the Scottish spirit to go down that futile route. Graham's and Elmar's experimental skills and massive experience, the curiosity and thirst to learn of the lower life forms that graduate students are and the most decisive and driven leadership of Stefan fused into an astonishingly well oiled machinery of which being a cog was far more than simply pleasant.

Mainly because of the synchronicity of our natural clocks, I had the chance to work a little more (and to annoy him quite a lot in the process) with Elmar than the other PhD students. Those late nights optimizing our respective setups were the occasion of some discussions which made the lab life far closer to what a bound team would ideally be. Thanks again for being so genuinely kind, giving and altruistic during all those years and for letting me store my sentimental belongings in your personal space when I had to. Graham's departure was sublimated by Bruno Peaudecerf's arrival which on top of enhancing the french life spirit of the lab also brought with him an appreciated different way of performing experimental physics from what we already had. All his organisational and musical/singing skills have so far be fully recognized and employed by the whole EQOP group which would not have been the same without him. The most recent additions to the lab were post doctoral fellow Manuel Andia,

master student Jan-Philipp Schröder and PhD student Andrés Ulibarrena who have brought some fresh air and boost to our group activities in and outside the lab. The stays of Nicolas Sangouard and Jakob Hinney were all memorable and enjoyable and I am glad to have met those physicists and selfishly wish they had stayed a little longer.

Besides immediate co-workers, it seems impossible not to also thank the people of the EQOP group with whom I have been interacting on a regular basis over the last 4 years beginning with PhD students Pedro Gomes, Jesus Garcia for bringing with him his Día de los Muertos national customs, Andrea Di Carli, Craig Colquhoun, Billy Roberston, Ivor Kresic simply for 'being Ivor', atypical physicist Calum MacRae, James McGilligan for the binding time we had in Glasgow and in Columbus and the routine hot beverages and pool games at the Todd's bar I enjoyed with Remy Legaie amongst many other things. Ending with the higher staff Stuart Ingleby, Jonathan Pritchard, Aidan Arnold, Thorsten Ackemann, refreshing Andrew Daley and mostly Paul Griffin for being so supportive in any situation, as available as he could be and for quite logically becoming the adamantium pillar of the whole EQOP group and Erling Riis for still managing to find time to teach me some Ti:Sapph practical tweaks while superbly heading the whole Physics department.

All our work was magnificently seconded by the electronics and mechanical workshops technicians and would like to deeply thank all of them who so often took the time to pass their experienced knowledge onto us, give some necessary design corrections and of course skip the queue mainly Ewan MacLagan and Robert Wylie in the machine shop and Ken Gibson, John Broadfoot and Mark Hutcheon in the electronics workshop.

Only a year earlier the Rubidium lab had achieved single site resolution of bosons in a lattice and Markus simultaneously initiated the construction of the Lithium experiment which goal was to accomplish the same with fermions. As part of this team composed of Widagdo Setiawan, Florian Huber and Kate Wooley-Brown, I was given the opportunity to learn a massive amount of technical and engineering skills ranging from the use of heavy machinery, welding (many thanks to Stanley Cotreau), plumery, PCB micro-electronics and of evidently optics in particular high power ones when the task of setting up the 300 W transport trap on the experiment ended up quite surprisingly in my hands.

On top of that much practical knowledge required to build a state of the art cold atoms experiments, I was also given the opportunity to learn about the physics underlying the bosonic quantum gas microscope as all the members of the Greiner group were tightly sitting in a U-shaped room. It would be improper to mention the nick-

names we gave to this packed arrangement but they were never used on a complaining tone as we knew that it was such a density of bright, passionate and motivated people that gave birth to the tremendously stimulating and tension-free spirit it possessed. So my ignorance coupled with curiosity made me, maybe quite annoyingly for them, ask Jonathan Simon and Waseem Bakr (back then post doctoral fellow and PhD student and now Professors) about pretty much anything.

I could not end this paragraph within mentioning Alex Ruichao Ma, Eric Tai and Philipp Preiss and thanking again all the previously cited people for the great eye-opening year mostly spent in the south east basement of the John Anderson building with a daily intake of the renown lemon-grass chicken and some unforgettable moments such as: some discovering that yes, outside of the Harvard campus, Piña coladas do contain alcohol; the same can also, genuinely without the intent, end up in one of the best and probably most expensive stone crabs restaurant of a conference area, or succeeding in the unsafe manipulation of alkalis in quite awkward conditions.

That year made me absolutely adamant about pursuing my studies in the same field and I managed to come up to an arrangement with Professor Agnes Maître that would let me attend her master in Paris and go back for a full semester to the Center for Ultracold Atoms but this time at MIT to work for and follow the AMO class of Professor Wolfgang Ketterle. Thanks to him I acquired the essential basic knowledge to start a good PhD in the field while we were able to make some new discoveries in the lab, mainly a long awaited ultracold molecule, NaLi.

The lab consisted of post doctoral fellow Myoung-Sun Heo and PhD students Tout Wang and Timur Ravchov. We got to share our office space with Colin Kennedy, without whom our collective experience would not have been the same. Thanks to all of them for those thrilling months which began with Colin, Timur and I working intensely on the weekly class homework, striking Wolfgang's joy when being shown the undeniable proof of the existence of the NaLi molecules and the entertaining weekend road trips surrounding DAMOP 2012 especially our visit to a fine Californian dancing establishment, some Timur's side stories from the EDC in Las Vegas and making me hike part of the Grand Canyon path with, what would be revealed shortly afterwards, a mild form of pneumonia.

Finally I shall renew my deepest gratitude toward all the Professors who hosted and supervised me particularly Stefan and Elmar before concluding by expressing my love to my friends, significant other and family who have permitted, tolerated, supported and advised me along this fantastic adventure.

Abstract

Quantum-gas microscopes have become an important tool in quantum simulation as they enable direct probing of local quantities by single-atom-resolved detection in optical lattices. Recent years have seen many fascinating results from the bosonic quantum-gas microscopes using ^{87}Rb . However, no such device existed for fermionic species.

The goal of this thesis work was to develop and build a quantum-gas microscope setup for fermionic potassium-40. Single-atom-resolved imaging of ^{40}K has proven very challenging due to its smaller mass and smaller excited-state hyperfine splitting compared to ^{87}Rb . In addition, the inverted excited state trapping potential required us to employ electromagnetically induced transparency (EIT) cooling instead of sub-Doppler molasses cooling. EIT cooling occurs when a coherent driving of a three-level system generates a spectrally narrow Fano-like resonance which can be set to favour red-sideband transitions over blue ones of the quantised vibrational levels in the optical lattice potential. During the cooling process, the fluorescence light is collected by a high-NA objective to image the atomic distribution in a two-dimensional square lattice potential.

Due to the physical constraints of our apparatus, EIT cooling had to be combined with coupling between different motional axes via Raman transitions to achieve cooling of all degrees of freedom. Our imaging method allowed us to collect about 1,000 fluorescence photons per atom within a 1.5 s exposure time. From the analysis of two distinct subsequent fluorescence images, we found that less than 5% of the atoms hopped or were lost during 1s of EIT cooling. Such fidelity will allow fermionic quantum-gas microscopes to investigate fermionic quantum phases, spin-spin correlations, and out-of-equilibrium dynamics of correlated fermionic many-body quantum systems.

Contents

Introduction	ix
1 Theoretical toolbox	1
1.1 Atomic physics	1
1.1.1 Potassium level structure	1
1.1.1.1 Spectroscopic notation	1
1.1.1.2 External static magnetic field	3
1.1.2 Atom-light interaction	6
1.1.2.1 Two-level atom - Near resonant interaction	7
1.1.2.2 Dressed state picture	8
1.1.2.3 A.C. Stark shift of a "real" atom	11
1.1.2.4 Spontaneous emission	16
1.2 Atoms in traps	17
1.2.1 Quantum harmonic oscillator	17
1.2.2 Optical dipole trapping	18
1.2.2.1 Gaussian beam propagation	18
1.2.2.2 Trap depth and trap frequencies	20
1.2.2.3 Optical lattices	22
1.3 Lattice physics	25
1.3.1 Basic crystal formalism	25
1.3.2 Band structure	26
1.3.3 Band mapping	28
1.3.4 Tight-binding model	30
1.3.5 Fermi-Hubbard model	33
2 Experimental setup	37
2.1 Vacuum chamber	37
2.1.1 Overview	37
2.2 Resonant lasers	39
2.2.1 D_2 setup	39
2.2.2 D_1 laser	40
2.2.2.1 Master laser	40
2.2.2.2 Slaves and distribution	41

2.2.3	Titanium-Sapphire laser	44
2.2.3.1	Setup	44
2.3	Trapping lasers	46
2.3.1	MOT CODT	46
2.3.2	Transport	46
2.3.2.1	Mephisto Multipass Optical Parametric Amplifier (MOPA)	46
2.3.2.2	High-power fibre coupling	48
2.3.2.3	Transport	50
2.3.3	Vertical lattice	51
2.3.3.1	Modulation spectroscopy of trap frequencies	53
2.3.4	Horizontal lattices	53
2.3.4.1	Seeding of the fibre amplifiers	53
2.3.4.2	Regulation setups	54
2.3.4.3	Optical lattice breadboards/setup	57
2.3.4.4	Alignment of lattice beams	59
2.3.5	Squeezing beam	61
2.3.6	Horizontal dimple trap	62
2.3.6.1	Amplification	62
2.3.6.2	Polarisation spectroscopy	64
2.4	Lattice chamber	65
2.4.1	Overview	65
2.4.2	Microwave	66
2.4.3	Feshbach coils	68
2.4.3.1	Bias fields - Helmholtz configuration	68
2.4.3.2	Magnetic field gradient - Anti-Helmholtz configuration	69
2.4.3.3	Current supply stability	69
2.5	Microscope	71
2.5.1	Overview	71
2.5.2	Optical setup	71
2.5.2.1	Fluorescence	74
2.5.2.2	Addressing beam	74
2.5.2.3	Dimple trap	75
2.5.3	Objective Mounting	76
2.5.4	Installation and Alignment	76
2.5.5	Initial Lateral and Angular Positioning	77
2.5.6	^{87}Rb Fluorescence Summary	78
2.5.7	Fine angular tilt Correction	78

3	Detection of single fermions	81
3.1	From a MOT to the microscope	81
3.2	Microwave spectroscopy	83
3.3	EIT cooling	85
3.3.1	Tensorial D_2 AC Stark shifts	85
3.3.2	Nulling vectorial light shifts	86
3.3.3	Theory of EIT cooling	87
3.3.4	3D EIT Cooling	89
3.3.5	Fluorescence with 2D EIT Cooling	91
3.4	Motion coupling via Raman transitions	92
3.4.1	Far-detuned Raman transitions	93
3.4.2	2D EIT Cooling + Raman exchange	96
3.4.2.1	Implementation of Raman exchange	96
3.4.2.2	Final configuration	96
3.4.2.3	Rabi frequencies	99
3.4.3	Raman spectroscopy	101
3.5	Layer selection	103
3.5.1	Optical pumping	103
3.5.2	Blowout process	105
3.5.3	Layer selection optimisation	106
3.5.3.1	Minimising horizontal bias field	107
3.5.3.2	Compensating residual gradient	108
3.5.3.3	Single layer resolution	109
3.6	Imaging performances	113
3.6.1	Single-site resolution	113
3.7	Image fidelity	115
3.7.1	Inhomogeneity of EIT cooling - Lifetimes	115
3.7.2	Hopping and losses	116
3.7.3	Stochastic heating	118
4	Outlook	121
4.1	Optical dimple traps	121
4.1.1	Squeezing beam	121
4.1.2	Horizontal dimple - 850 nm	121
4.2	Evaporation tools	123
4.2.1	Spin mixture	123
4.2.2	Feshbach resonances	124
4.2.3	High Field Imaging	126

Conclusion	129
Appendix A : Publications	131
A.1 Single-atom imaging of fermions in a quantum-gas microscope	131
A.2 Sub-Doppler laser cooling of ^{40}K with Raman gray molasses on the D_2 line	131
Appendix B : m_F dependent A.C. Stark shift "experimentalist" form	147
Appendix C : Squeezing beam	149
Appendix D : Atomic physics derivations	151
Appendix E : Optical components legend	155
Appendix F : ^{39}K hyperfine level structure	157
Appendix G : Waist measurements	159

Introduction

Superconductivity

In 1908, after a decade long effort, a team lead by Kamerlingh Onnes successfully liquified ^4He [1] by reaching temperatures of only a couple of Kelvins and doing so opened the gates of low temperature physics which was rewarded with the Nobel Prize in 1913. Astonishing results quickly followed as it took the same team only three years to discover superconductivity in Hg [2] then in Pb and Sn [3] shortly after. Hg exhibited an almost null electrical resistivity below 4.2 K which increased 400 times only 0.1 K hotter, see Figure 0.1. Two decades later, the Meissner effect, the property of superconductors to cancel all internal magnetic fields was discovered [4]. Contrary to the infinite electrical conductance property, it couldn't be explained by classical physics only and became the necessary proof of a superconducting state.

Null electrical resistance with levitation capability provided by the Meissner effect made two justified incentives to explore this domain further in the hope of one day providing superconductors which could be employed on an industrial scale, thus economically viable. And so the race to higher critical temperature superconductors began. In 1957, Barden, Cooper and Schrieffer provided the eponymous BCS theory [5, 6] which explained superconductivity by phonons mediated pairing of electrons called Cooper pairs which would "flow" into their hosting crystalline structure unperturbed by Coulomb interaction. This theory supported all the previous discoveries and its predictions led to advances in the search for superconductor materials with an higher critical temperature up to 23 K with Nb_3Ge films in 1974 [7, 8].

The theoretical side of the field was left in shock while its experimental one started jubilating after the discoveries of two superconductor materials LaBaCuO and YBaCuO exhibiting critical temperatures of 35 and 92 K respectively [10, 11] in the late eighties. $\text{LaBa}_2\text{Cu}_3\text{O}_7$ was the first compound to have a critical temperature above 30 K which could not and still can not be explained by the BCS theory [12, 13] and $\text{YBa}_2\text{Cu}_3\text{O}_7$ was the first one to acquire a superconducting behaviour at a temperature high enough to be reached with liquid nitrogen rendering the applications of the superconductors available in laboratories or in bulky apparatus such as MRI machines significantly more convenient and less dangerous than what it would have been with liquid helium.

Those two materials inaugurated the first family of High- T_c superconductors known as the cuprates (oxide copper ceramics) with a compound detaining the record of

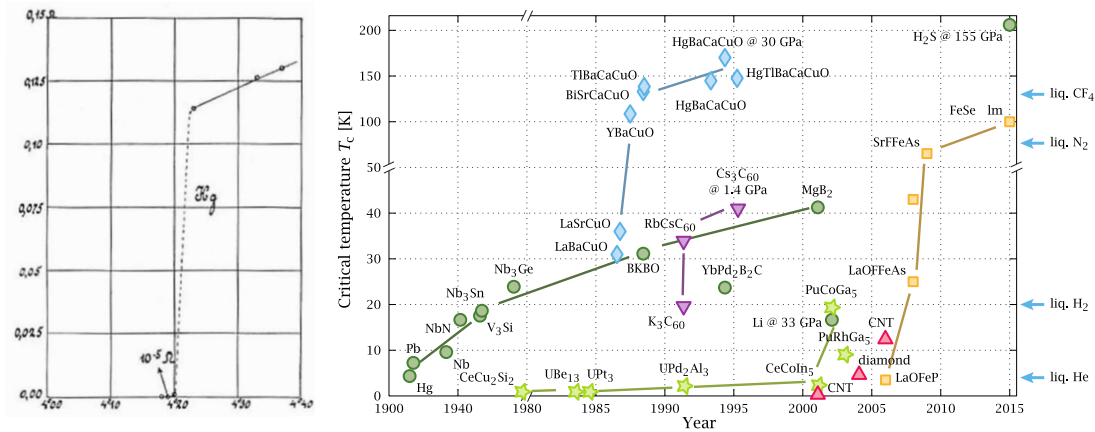


Figure 0.1: Left: Historical plot of the discovery of superconductivity in Hg from the laboratory notes of Prof. Onnes [2] display the jump in resistivity (Ohms) as a function of temperature (Kelvin) across the $T_c = 4.2$ K phase transition. Right: Timeline of superconductor materials. Courtesy of [9].

highest T_c of 138 K and 166 K [14, 15] under normal conditions and at high pressure respectively. The recent discovery of the pnictides family (Fe Ar/P oxydes) [16, 17, 18] gave hope to help understanding the cuprates and to establish a working theoretical framework for non-BCS superconductivity which now may be the most elusive and puzzling goal [19] of condensed matter physics amongst others such as spin and non-Fermi liquids [20, 21] mainly so from the difficulty if not impossibility of computation of many strongly correlated fermionic quantum systems.

Computational issues

This impossibility stems from two main sources, the first one being the storage of the necessary variables arising from "the characteristic treat of quantum mechanics" [22] : *entanglement*; which in general is directly linked to the dimension of the Hilbert space describing the quantum mechanical wavefunction. The simplest illustration can be given by taking a system of N spin- $\frac{1}{2}$ particles. Only considering the spin observable, classically, the number of possible configurations of N spins is 2^N and each one of those set of spins requires N variables for a total of 2^{N+1} parameters for a full description of the system. With entanglement, the mathematical description of a quantum system of N spin- $\frac{1}{2}$ is expressed as the superposition of all possible configurations and now requires $2^N - 1$ complex variables to be fully characterised. At the end of the third chapter, binary occupation maps of a 20×20 lattice sites square are displayed on Figure 3.27 for illustration purposes. A classical simulation of the quantum dynamics

of such an area uniformly filled with spin- $\frac{1}{2}$ particles would require the insane amount of $2^{400} - 1 \simeq 2 \times 10^{120}$ variables.

The second source of difficulty is known as the *sign problem* when applying Monte Carlo integration [23] to quantum systems of numerous fermions [24, 25]. The introduction of Ref. [26] provides a concise explanation of the numerical problem. In statistical mechanics, Monte Carlo computation of a classical observable involves integrating over all accessible states weighted by their respective occurring probability which are always positive. When transposed to quantum mechanics the same approach can formally be taken but only applied numerically to systems in which the probabilities remain positive as for most bosonic systems but not for generic fermionic ones. Indeed, due to the Pauli exclusion principle, the wavefunction of a system changes sign when two fermions are interchanged and so does the probabilistic weight in the Monte Carlo integrand. Integrating such fast oscillatory quantities causes the required time to obtain a result with a chosen satisfactory precision to grow exponentially with the number of particles, N , involved [26].

An answer to the impossibility of versatily using classical computers to compute quantum systems came at the beginning of the eighties when Richard Feynman suggested that the only way quantum mechanics outcomes could be predicted were to use a machine itself running on quantum mechanical principles [27].

Quantum computation

Following Feynman's proposal, Deutsch proved that quantum theory and the 'universal quantum computer' are compatible [28] with the assertion that 'every finite realizable physical system can be perfectly simulated by a universal model computing machine operating by finite means', a principle which underlies the Church-Turing hypothesis [29, 30]. But it is only once that Peter Shor formulated a quantum algorithm [31] which could factorise any number in a polynomial time, faster than any classical methods, that the field of quantum computation really took off.

During the past thirty years, the field of experimental quantum computation has seen tremendous progress toward the realisation of a universal quantum computer. It started with laying the theoretical framework of the core components for reversible computation [32], namely quantum gates and the property of a reduced set of them to be universal, i.e. that any unitary transformation could be reduced to the use of gates from said set [33], e.g. a set constituted of Hadamard and Toffoli gates [34].

After Shor's algorithm being experimentally implemented [35] using Nuclear Magnetic Resonance; the field of trapped ions [36] which promised better coherence time, easiness of manipulation and some hopes for scalability rapidly took over with the ex-

perimental realisation of the CNOT gate [37] in 2003 following the Cirac and Zoller's proposal [38] of 1995. At this time, trapped ions are leading the field with complex gates [39] with high efficiencies [40], already within range of self-correcting algorithms [41].

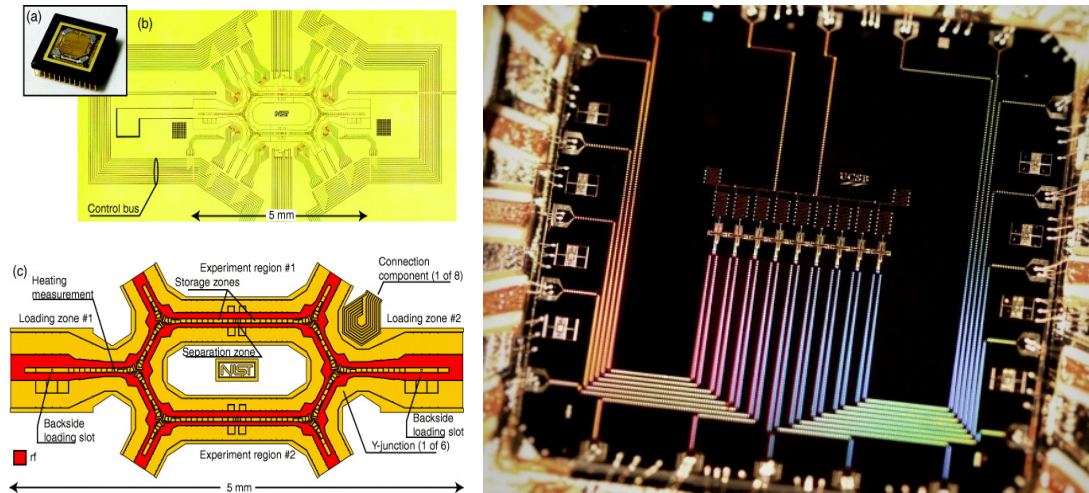


Figure 0.2: Left: Photographs of a. the overall ions chip and b. its active region made of 150 elements which can store, transport and make interact trapped ions with c. a schematic of the core interacting region. Such chips could one day be the basic components of trapped ions quantum computers, cf. [42]. Right: Close photograph of a superconducting quantum circuit composed of 9 q-bits linearly arranged where state preservation from natural errors has been successfully implemented. The picture has a width of about 10 mm. For more details see [43]. Photo credit: Julian Kelly.

Besides the need for self-correction, universal quantum computers would require a decent amount of qubits. The quest for architectures which would scale up the number of ions qubits into the tens and hundreds has experienced interesting advances [44, 45, 46] but has simultaneously triggered competitive efforts from other supports such as superconducting q-bits [47, 48] or neutral atoms using Rydberg blockade [49, 50] or in optical lattices [51, 52], both of them currently exhibiting less q-bits coherence relative to trapped ions but in favour of more promising prospects for convenience of scalability as illustrated on Figure 0.2.

Quantum simulation

The work presented in this thesis aims at building a less universal machine than a quantum computer for investigating quantum behaviours: an analogue *quantum simulator*. A device built to simulate a specific system would require the set of critical parameters to be varied across a wide range to be able to confirm past results and go

beyond into the unknown. The last four decades of advances in atomic physics and quantum optics have led to an unprecedented level of manipulation and control of quantum systems in the field of atomic dilute gases that such tools are now considered to constitute quantum engineering, with the prospect of an analogue quantum simulator of strongly correlated fermions in periodic potentials finally within reach.

Laser cooling of atomic gases to the Doppler limit [53, 54, 55] and beyond [56, 57] started a new era in the investigation of the quantum properties and capabilities of atomic gases. The field experienced a boost of interest when a long predicted new state of matter [58] was discovered by the teams of Cornell [59], Wieman [60] and Ketterle [61] in 1995: the *Bose-Einstein Condensate* (BEC). When reaching temperatures low enough that the thermal De Broglie wavelength [62] becomes larger than the inter-particle distance, bosons start to condense into the lowest energy wavefunction and form a macroscopic quantum dilute atomic gas.

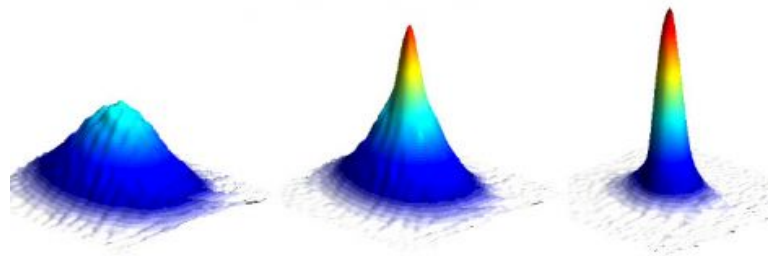


Figure 0.3: Series of 2D velocity distributions obtained after time-of-flight ballistic expansion of, from left to right, a thermal cloud, a partially condensed cloud and an almost pure BEC. Credit: Foot group, Oxford, [63].

Even if the atomic physicists immediately saw quantum many-body physics within reach, it took several years to convince condensed matter physicists that this realm of study had been reached after the proposal [64] and experimental realisation [65] of the Superfluid to Mott-insulator transition in optical lattices. The initial motivation behind the proposal was to provide a controlled way to prepare large samples of uniformly singly populated optical lattice sites as the basis for a universal quantum computer. With the use of Feshbach resonances [66, 67] to tune the sign and amplitude of the interactions between the particles, it can now be considered as the starting point of ultracold atoms in optical lattice serving as quantum simulators of strongly correlated quantum systems.

Indeed, the electrons evolving into the periodic potentials created by the Coulomb interaction with the solid nuclei can be simulated with neutral atoms placed into the sinusoidal potential created by optical lattices. A plethora of optical lattices geometries have nowadays been engineered and tested with ultracold atoms [68, 69, 70] in

which almost all the common parameters such as tunnelling, filling factor, interaction strength, overall confinement and defects can be tuned sometimes across several orders of magnitude. For a more exhaustive list of the analogies between solid state systems and ultracold atoms in optical lattices, the reader could consult Table 1.1 of Widagdo Setiawan's thesis [71].

The achievement of *Degenerate Fermi Gases* (DFG) [72, 73, 74] and the study of their quantum phase transitions [75, 76] confirmed that fermions in an optical lattice are a promising path toward simulating highly correlated fermions in periodic potentials: a quantum simulator for High- T_c superconductivity. The reader can consult Section 1.3 of [77] listing the various many-body systems simulated with ultracold atoms in optical lattices.

Quantum gas microscopy

The motivation behind single-site resolution quantum gas microscopy was to acquire the capability of probing local properties of ultracold atoms in optical lattices. When this thesis' work began, only two bosonic quantum gas microscopes running with ^{87}Rb existed [78, 79, 80] and have already been used to study quantum phenomena which would not have been accessible with bulk-only observables such as non-local string ordering [81] and strongly correlated dynamical processes [82, 83, 84]. Quantum simulation of pseudo antiferromagnetic spin chains [85] and the obtention of large uniformly singly populated optical lattice areas [86] with the ability to address single-sites [87], a promising basis for scalable quantum computing in optical lattices [64], proved how valuable quantum gas microscope could be.

Quite logically those results sparked the construction of many quantum gas microscopes: another bosonic one with ^{174}Yb [88, 89] which could recently operate with non-fluorescence optical detection [89] and many fermionic ones either using ^{40}K or ^6Li to finally being able to simulate the Fermi-Hubbard model, especially the topics of antiferromagnetic ordering [90] and d-wave superfluidity [91] which are believed to hold some clues toward the key principles at play in High- T_c superconductivity.

Our machine, using EIT cooling, was one of the first three fermionic quantum gas microscopes to achieve single-site resolution [92], the two others using Raman sideband cooling also on ^{40}K [93] and on ^6Li [94], respectively within the Zwierlein (MIT) and Greiner (Harvard) groups. Other groups across the world quickly caught up and brought their fermionic microscope into operational stages [95, 96] to very recently observe the fermionic Mott insulator [97] and spin-correlation functions of the Fermi-Hubbard model [98].

Thesis outlook

This thesis is constructed as follow:

- The first chapter will introduce the key theoretical concepts behind the manipulation of cold atoms in optical lattices.
- The second chapter constitutes an almost exhaustive list of all the lasers, optical setups and other components such as magnetic coils and the microscope objective used to create the 3D optical lattice, perform to the layer selection and microscopically imaging the atoms being EIT cooled.
- The third chapter shall display all the characteristics of the EIT cooling and of the layer selection process with some of the crucial quantities linked to imaging fidelity.
- The thesis will end with a fourth and final chapter focused on the efforts toward obtaining a dense degenerate Fermi gas under our microscope.

Chapter 1

Theoretical toolbox

1.1 Atomic physics

1.1.1 Potassium level structure

1.1.1.1 Spectroscopic notation

Potassium 40, ${}^{40}_{19}\text{K}$, is one of the three stable and naturally abundant isotopes of potassium; ${}^{39}\text{K}$, ${}^{41}\text{K}$ and ${}^{40}\text{K}$ with respective relative natural abundance of 93.3%, 6.7% and 0.012%. It is also the only fermionic isotope out of those three which makes it a good candidate for building a fermionic quantum-gas microscope.

The level structure of atoms can be described using the Russell-Saunders notation

$$n^{2S+1}L_J \quad (1.1.1)$$

where n is the principal quantum number and S , L and J are the quantum numbers corresponding to the spin, \vec{S} , orbital and total angular momenta, \vec{L} and \vec{J} , of the outer shell electron.

According to the commonly used angular momentum framework in quantum mechanics; if \vec{X} is set to be an angular momentum and \hat{X} its associated operator, the quantum numbers X and m_X respectively are the quantum numbers associated with $X(X+1)\hbar^2$ and $m_X\hbar$ the eigenvalues of \hat{X}^2 and \hat{X}_z , the projection of \vec{X} on the quantisation axis z .

In the case of potassium, $n = 4$ and $S = \frac{1}{2}$, because there is only one electron in the valence shell. This is true for all alkalis and the spin multiplicity $2S+1$ will always be equal to 2 and is therefore usually omitted in the term notation.

L can take all integer values up to $n - 1$,

$$L \in \mathbb{N}, \quad 0 \leq L < n, \quad (1.1.2)$$

and its projection on the quantisation axis, m_L , can take all the relative integer values from $-L$ to L ,

$$m_L \in \mathbb{Z} , \quad -L \leq m_L \leq L , \quad (1.1.3)$$

a bounding property shared by all couples of quantum numbers (X, m_X) .

The letter L takes the following notation depending on its value; $S, P, D, F...$ for $L = 0, 1, 2, 3...$. The letters after F go in alphabetical order with J being omitted to avoid confusion with the total angular momentum quantum number.

The state of lowest energy has $n = 4$, $L = 0$ and $2S + 1 = 2$ as quantum numbers and the spectroscopic notation 4^2S . The first excited state corresponds to the excitation of the electron to (the first angular momentum accessible) of $L = 1$, denoted 4^2P .

The fine structure arises from the coupling between the spin angular momentum \vec{S} and the effective magnetic field \vec{B} that is generated by the electron orbiting around the nucleus. This effective magnetic field is proportional to \vec{L} and the magnetic dipole Hamiltonian H_{fs} takes the form

$$H_{\text{fs}} = -\vec{\mu}_S \cdot \vec{B} \propto \vec{L} \cdot \vec{S} , \quad (1.1.4)$$

where $\vec{\mu}_S$ is the operator of the spin magnetic moment related to the spin, \vec{S} , by

$$\vec{\mu}_S = g \frac{q}{2m} \vec{S} , \quad (1.1.5)$$

with g the *Landé factor*, q the electric charge and m the mass of the particle.

The addition of angular momenta will not be treated extensively here but we recapitulate the basic formulae. The presence of the scalar product $\vec{L} \cdot \vec{S}$ justifies the addition of \vec{L} and \vec{S} to create the total electronic angular momentum,

$$\vec{J} = \vec{L} + \vec{S} . \quad (1.1.6)$$

Its associated quantum number, J , can take all the integer or half-integer values in unit step bound by the condition

$$|L - S| \leq J \leq |L + S| . \quad (1.1.7)$$

$$H_{\text{fs}} \propto \vec{L} \cdot \vec{S} \propto \frac{1}{2}(\hat{J}^2 - \hat{L}^2 - \hat{S}^2) \propto \frac{1}{2}[J(J+1) - L(L+1) - S(S+1)] \quad (1.1.8)$$

It follows that the Hamiltonian is proportional to a simple expression of J , L and S and therefore lifts the degeneracy of states having different J values within a ^{2S+1}L term.

For ^{40}K , the ground state $4S$ does not contain any fine structure because $L = 0$, so $J = 1/2$. The first excited state, $4P$, has an orbital angular momentum number $L = 1$, and J can take either the value of $1/2$ or $3/2$ such that the level splits into two states, $4P_{1/2}$ and $4P_{3/2}$, separated in wavelength by about 3 nm (about 1.73 THz).

The hyperfine structure is revealed when the coupling between the nuclear spin angular momentum \vec{I} and the total electronic angular momentum \vec{J} is taken into account. If we set \vec{F} to be the total angular momentum of the atom,

$$\vec{F} = \vec{J} + \vec{I}, \quad (1.1.9)$$

its associated quantum numbers are bounded by,

$$|J - I| \leq F \leq |J + I|. \quad (1.1.10)$$

The degeneracy is lifted for all states because none of them has a null total electronic angular momentum J . The nuclear spin of ^{40}K value is $I = 4$ which allows $F = 9/2$ and $F = 7/2$ for the $4S_{1/2}$ and $4P_{1/2}$ states and $F = 11/2$ to $F = 5/2$ in unit steps for $4P_{3/2}$ as sketched in Fig.1.1.

1.1.1.2 External static magnetic field

One can lift the degeneracy of a hyperfine state by applying a static magnetic field. The external static magnetic field interacts with each individual angular momentum and the Hamiltonian can be expressed as

$$H_B = \frac{\mu_B}{\hbar} (g_L \vec{L} + g_S \vec{S} + g_I \vec{I}) \cdot \vec{B} \quad (1.1.11)$$

with μ_B being the *Bohr magneton* and $g_{L,S,I}$ the Landé g-factors.

If the energetic shift is small compared to the hyperfine splitting, then F and m_F are good quantum numbers. This regime is called the *Zeeman regime* [101, 102], schematised and plotted respectively in Figures 1.2 and 1.3, and the energy shift of each hyperfine state $|F, m_F\rangle$ is

$$\Delta E_{F, m_F} = \mu_B g_F m_F B_z. \quad (1.1.12)$$

In the presence of a strong magnetic field, the induced coupling to each angular momentum can be greater than the hyperfine splitting. The quantum numbers

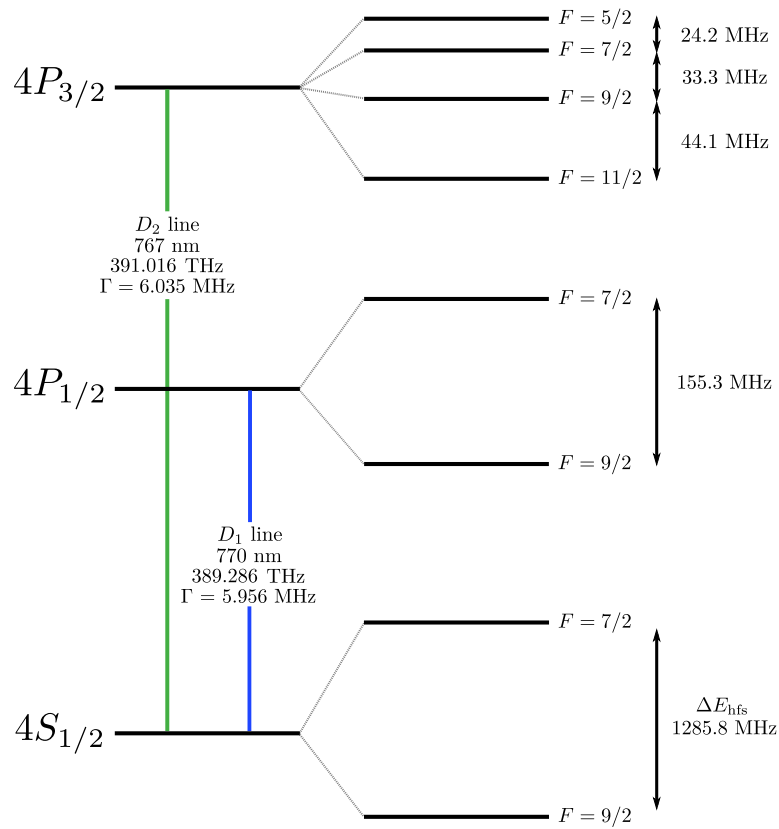


Figure 1.1: Hyperfine level structure of ^{40}K . The values for the energy splitting not to scale and are taken from [99] and [100]. Their measured uncertainties are much smaller than the last significant number displayed and have been removed for clarity.

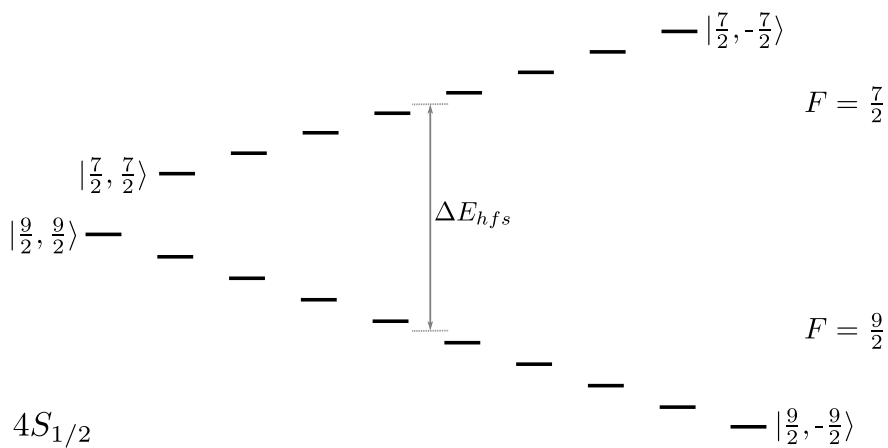


Figure 1.2: Hyperfine structure of the ground states, $|F, m_F\rangle$, of ^{40}K in a small static magnetic field: the *Zeeman effect*.

F, m_F are no longer good quantum numbers and one has to consider the eigenstates $|J, m_J, I, m_I\rangle$, this is the *Paschen-Back regime* [103] as plotted in Figure 1.3.

The expression of this energetic shift is quite cumbersome but a convenient exact analytical solution exists for the ground state of alkali: the *Breit-Rabi formula* [104]

$$\Delta E_{J=1/2, m_J, I, m_I} = -\frac{\Delta E_{\text{hfs}}}{2(2I+1)} + g_I \mu_B m B \pm \frac{\Delta E_{\text{hfs}}}{2} \left(1 + \frac{4m x}{2I+1} + x^2 \right)^{\frac{1}{2}} \quad (1.1.13)$$

where ΔE_{hfs} is the hyperfine splitting, $m = m_I \pm m_J = m_I \pm 1/2$ and

$$x = \frac{(g_J - g_I) \mu_B B}{\Delta E_{\text{hfs}}} . \quad (1.1.14)$$

An oddity of ^{40}K is the inverted hyperfine structure for the ground state. Indeed the energy of a hyperfine state will be higher for a lower value of F . This is due to the high value of $I = 4$ and ^{40}K is the only isotope of alkalis to present such property.

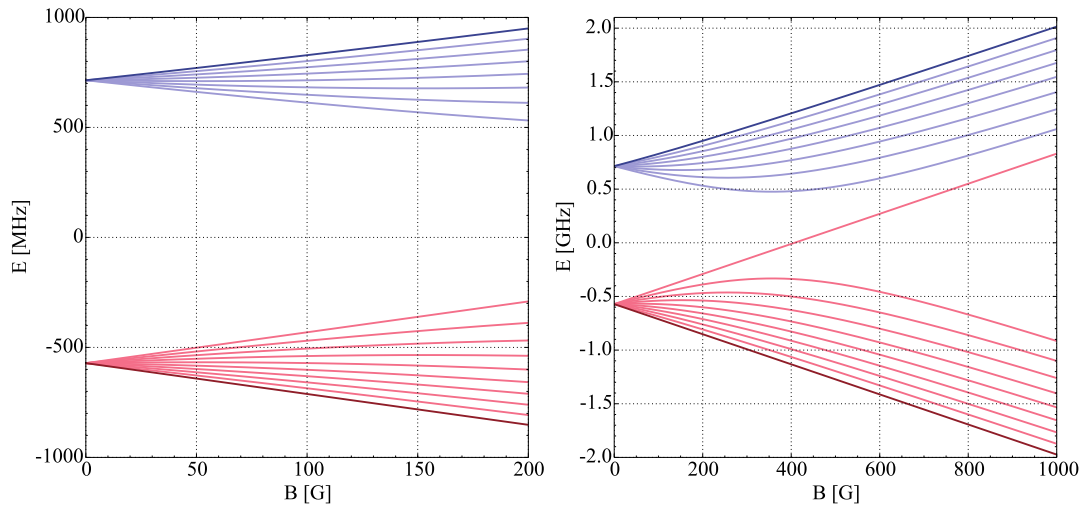


Figure 1.3: Left/right: Zeeman/Paschen-Back regimes of the ground state of ^{40}K . The $F = -9/2$ and $F = -7/2$ states are respectively represented in red and blue with the "stretched" $|-9/2, -9/2\rangle$ and $|-7/2, -7/2\rangle$ hyperfine states being darkened.

The hyperfine splitting of the first two excited fine structure states, $^4P_{1/2}$ and $^4P_{3/2}$, are large compared to the atomic linewidth and to the one of the near-resonant lasers which are commonly used in cold atoms labs. We use External Cavity Diode Lasers (ECDL) which are locked on atomic transitions with a frequency accuracy of < 6 MHz. The natural linewidth of the D_1 and D_2 transitions (the transitions from the $^4S_{1/2}$ ground state to the $^4P_{1/2}$ and $^4P_{3/2}$ excited ones) are of the same magnitude

which enable us to access sub-Doppler cooling regimes, see our publication [105] placed in Appendix A.2 .

1.1.2 Atom-light interaction

Here we will treat the interaction between an atom and an oscillatory electric field. The basic near-resonant atom-light interaction results will be presented and the dressed state picture will be recapitulated for the ease it brings in the understanding of electromagnetic-induced-transparency (EIT) cooling. A longer study of the less simple case of far off-resonant atom-light interaction with a multi-level system, which is of great importance when using high intensity light to trap ^{40}K , shall ultimately be presented.

The general equation at the root of the interaction between an atom and time dependent electromagnetic radiation is the Schrödinger equation [106]

$$i\hbar \frac{\partial \varphi}{\partial t} = \hat{H} \varphi . \quad (1.1.15)$$

The full Hamiltonian of the system,

$$\hat{H} = \hat{H}_0 + \hat{H}_L + \hat{H}_I , \quad (1.1.16)$$

is composed of the intrinsic atomic Hamiltonian \hat{H}_0 , the Hamiltonian of the light field \hat{H}_L , and the time dependent interaction Hamiltonian, \hat{H}_I .

In the so-called *semi-classical* picture, we assume high photon numbers which can be approximated as constant during the interaction. The light Hamiltonian \hat{H}_L can then be neglected and our lasers are considered as monochromatic coherent electromagnetic radiation sources whose light field can be simplified classically as

$$\vec{E}(\vec{r}, t) = \frac{1}{2} E_0 \vec{\varepsilon} e^{-i(\omega t - \vec{k} \cdot \vec{r})} + \text{c.c.} \quad (1.1.17)$$

where E_0 , $\vec{\varepsilon}$, ω and \vec{k} correspond respectively to the electric field amplitude, the electric field polarization vector, the field angular frequency and wavevector.

The main interaction between an atom and light is via the induced dipole moment. The interaction Hamiltonian can then be written as

$$\hat{H}_I(t) = -\vec{d} \cdot \vec{E}(\vec{r}, t) . \quad (1.1.18)$$

The electric dipole operator \vec{d} expressed in terms of the atomic eigenstates $|n\rangle$ and dipole matrix elements $\mu_{n,n'} = \langle n | \vec{d} | n' \rangle$ is

$$\vec{d} = \sum_{n,n'} |n'\rangle \langle n | \mu_{n',n} . \quad (1.1.19)$$

Here the higher order electric and magnetic multipole interactions, which usually contribute orders of magnitude less than the induced electric dipole, have been neglected.

1.1.2.1 Two-level atom - Near resonant interaction

We can simplify equation (1.1.17) to

$$\vec{E}(\vec{r}, t) = \frac{1}{2} E_0 \frac{\vec{r}}{|\vec{r}|} e^{-i\omega t} + \text{c.c.} \quad (1.1.20)$$

by assuming that the characteristic length of the electric dipole (the atom has a size on the order of 10^{-10} m = Å) is much smaller than the characteristic length of the variation of the electric field amplitude ($\lambda/4 = 10^{-7}$ m for a UV/blue radiation). This is called the *dipole approximation* ($e^{\pm i\vec{k}\cdot\vec{r}} \approx 1$) which is almost always justified when using visible to near visible radiations with alkalis. Also the dipole moment of the atom is collinear with the electric field polarisation, $\vec{\epsilon} = \frac{\vec{r}}{|\vec{r}|}$, at any given time. This is in general not true for multi-level atoms, as discussed in Section 1.1.2.3.

For a two-level atom, the Hamiltonian can be simplified further. The states of lower and higher energy are respectively called *ground* and *excited states* designated by the wavefunctions $|g\rangle$ and $|e\rangle$. If we set the zero energy reference to be the ground state and $\hbar\omega_0$ is the energy difference between the ground and excited states, the atomic Hamiltonian and Eq. (1.1.19) then become

$$\hat{H}_0 = \hbar\omega_0 |e\rangle \langle e| , \quad (1.1.21)$$

$$\vec{d} = |e\rangle \langle g | \mu_{e,g} + |g\rangle \langle e | \mu_{g,e} . \quad (1.1.22)$$

Inserting Eq. (1.1.21), (1.1.22) and (1.1.20) in (1.1.16) leads to

$$\hat{H} = \hbar\omega_0 |e\rangle \langle e| - \frac{1}{2} (|e\rangle \langle g | \mu_{e,g} + |g\rangle \langle e | \mu_{g,e}) \cdot (E_0 e^{-i\omega t} + E_0^* e^{i\omega t}) . \quad (1.1.23)$$

The wavefunction of the two-level atom can be written as the superposition of the ground and excited states as follow

$$|\varphi\rangle = c_g(t) |g\rangle + c_e(t) |e\rangle . \quad (1.1.24)$$

For experimentalists the population is the easiest observable. Using the normalization condition $|c_g|^2 + |c_e|^2 = 1$, the two eigenstates dynamics are given by

$$|c_g(t)|^2 = 1 - \left(\frac{\Omega}{\Omega'}\right)^2 \sin^2\left(\frac{\Omega't}{2}\right) \quad ; \quad |c_e(t)|^2 = \left(\frac{\Omega}{\Omega'}\right)^2 \sin^2\left(\frac{\Omega't}{2}\right) \quad (1.1.25)$$

where Ω , Δ and Ω' are the commonly called Rabi frequency, detuning and generalized Rabi frequency and are introduced in the derivation given in Appendix D.

On resonance ($\Delta = 0$ and $\Omega' = \Omega$), the excited state population undergo what is called *Rabi oscillations* at the Rabi frequency with unitary amplitude. As soon as the system is driven off resonantly ($\Delta \neq 0$ and $\Omega' > \Omega$), the excited state oscillates faster than on resonance and with a lower amplitude ($\left(\frac{\Omega}{\Omega'}\right)^2 < 1$).

For a coherent excitation of constant coupling, one can perform a so-called π pulse by applying such coupling for a duration of $t = \pi/\Omega'$. If the particle was initially in the ground state, it will be in the excited state after such interaction, $|\varphi\rangle = -i|e\rangle$. Similarly a $\pi/2$ pulse would leave the quantum state in a superposition of the ground and excited state of the form $|\varphi\rangle = 1/\sqrt{2}(|g\rangle + -i|e\rangle)$.

1.1.2.2 Dressed state picture

In the rotation frame transformation (with $|g\rangle$ and $|\tilde{e}\rangle$ as eigenvectors) and after the rotating wave approximation has been done, the complete Hamiltonian of the system can be written in matrix form as

$$\hat{H} = -\hbar \begin{bmatrix} \Delta & \Omega/2 \\ \Omega^*/2 & 0 \end{bmatrix} \quad (1.1.26)$$

The energy eigenvalues of the system, plotted in Figure 1.4, are easily derived to be

$$\epsilon_{\pm} = \hbar \frac{-\Delta \mp \sqrt{\Delta^2 + |\Omega|^2}}{2} = \hbar \frac{-\Delta \mp \Omega'}{2} \quad (1.1.27)$$

and correspond to the energies of the eigenvectors

$$\begin{aligned} |+\rangle &= \sin \theta |g\rangle + \cos \theta |\tilde{e}\rangle \\ |-\rangle &= \cos \theta |g\rangle - \sin \theta |\tilde{e}\rangle \end{aligned} \quad (1.1.28)$$

with θ defined as

$$\tan 2\theta = \frac{\Omega}{\Delta} \quad \left(0 \leq \theta < \frac{\pi}{2}\right) \quad (1.1.29)$$

Without any interaction field ($\Omega = 0$), we obtain the following expressions for the dressed states and respective energies

$$\theta = 0, \Omega' = \Delta \Rightarrow \begin{aligned} |+\rangle &= |\tilde{e}\rangle & \epsilon_+ &= -\hbar\Delta \\ |-\rangle &= |g\rangle & \epsilon_- &= 0 \end{aligned} \quad (1.1.30)$$

which exactly corresponds to what we would expect for the rotating frame scheme.

An interesting result is when considering a large detuning relative to the Rabi frequency ($\Delta \gg \Omega$) which is realised for sufficiently small light intensities. The generalised Rabi frequency can be approximated to $\Omega' = \Delta\sqrt{1 + (|\Omega|/\Delta)^2} \approx \Delta + |\Omega|^2/2\Delta$ and at the first order $\tan 2\theta \approx 2\theta \approx \Omega/\Delta$, $\cos \theta \approx 1$ and $\sin \theta \approx \Omega/2\Delta$ which gives

$$\begin{aligned} |+\rangle &= |\tilde{e}\rangle + \frac{\Omega^*}{2\Delta} |g\rangle & \epsilon_+ &= -\hbar\Delta - \hbar\frac{|\Omega|^2}{4\Delta} \\ |-\rangle &= |g\rangle - \frac{\Omega}{2\Delta} |\tilde{e}\rangle & \epsilon_- &= \hbar\frac{|\Omega|^2}{4\Delta}. \end{aligned} \quad (1.1.31)$$

In this situation, both ground and excited state contain a small admixture of the other and their energies are respectively shifted by $\pm\hbar\frac{|\Omega|^2}{4\Delta}$. This quantity is called the *A.C. Stark shift* or *light shift* and can generate a trapping force when the radiation field strength is spatially dependent. Such traps are commonly called *optical dipole traps*.

For large negative detunings, $\Delta/\Omega \leq -5$, $|-\rangle$ becomes equivalent to $|g\rangle$. Similarly for large positive detunings, $5 \leq \Delta/\Omega$, $|-\rangle$ would behave as $|\tilde{e}\rangle$. According to the adiabatic theorem [107], sweeping Δ slowly enough to remain adiabatic through the resonance therefore "following" state $|-\rangle$, would lead to an inversion of population from $|g\rangle$ to $|e\rangle$. This reasoning is identical if the wave function were to "start in" state $|\tilde{e}\rangle$, "follow" state $|+\rangle$ and "end up" in state $|g\rangle$. Such a sweep through resonance is called a *rapid adiabatic passage* and inverts the population of the bare states $|g\rangle$ and $|e\rangle$. The condition that sweep has to fulfil to be adiabatic is the *Landau-Zener criterion*

$$\frac{|\Omega|^2}{\frac{d}{dt}\Delta} \ll 1, \quad (1.1.32)$$

named after its demonstrators [108, 109]. An alternative name to *rapid adiabatic passage* is *Landau-Zener sweep*. Such sweep is much more robust than a π -pulse against external field fluctuations and frequency uncertainties in order to transfer population between states and is used quite often during our experimental sequence.

In our experiments, an atom is far from being a two-level system and the derivation of the light shifts created by an high intensity, far detuned laser beam turns out to be much more complicated. For large values of detuning, the rotating wave approximation

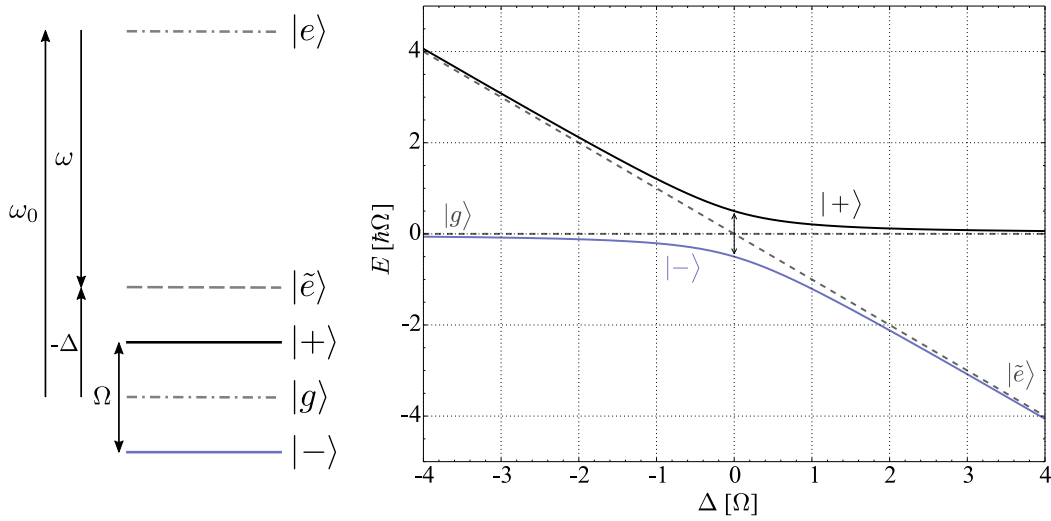


Figure 1.4: Left: Effective energy level structure of a two-level system composed of the bare states $|g\rangle$ and $|e\rangle$ energetically separated by $\hbar\omega_0$. $|\tilde{e}\rangle$ is down shifted by $\hbar\omega$ after a transformation in a frame rotating at angular frequency ω and is only $-\hbar\Delta$ away from the ground state $|g\rangle$. The two dressed states $|+\rangle$ and $|-\rangle$ are represented as if $\Delta = 0$ and their respective energy are $\pm\hbar\Omega/2$ away from $|g\rangle$. Right: Normalized energy in units of $\hbar\Omega$ of the bare states $|g\rangle$ and $|e\rangle$ (pointed-dashed and dashed lines) and of the dressed states $|+\rangle$ and $|-\rangle$ (solid black and solid blue curves). The energy splitting of the dressed states for a null detuning $\Delta = 0$ is represented by the two-headed arrow and equals $\hbar\Omega$.

(RWA) can lead to error in the experienced light shift by tens of percent and neglecting the hyperfine structure and the electric field polarisation would also result in missing important properties of how a real atom behave in optical dipole traps.

1.1.2.3 A.C. Stark shift of a "real" atom

In the treatment of a two-level system, the light couples ground and excited states via the electric dipole operator. So far we have assumed that the electric field polarization was collinear with the dipole moment and we have neglected any angular momentum aspect of the states' wavefunctions.

The strength of the light-induced interaction between two levels will greatly depend on their characteristic quantum numbers, $|F, m_F\rangle$.

All the light interaction strength between two hyperfine states $|F, m_F\rangle$ and $|F', m'_F\rangle$ lies in the expression of the dipole matrix element μ_{F, m_F, F', m'_F} which can be decomposed into a reduced matrix element and a Wigner 3j symbol (denoted by round brackets) [110] using the Wigner-Eckart theorem [111, 112] :

$$\langle F, m_F | e r_q | F', m'_F \rangle = \langle F || e \vec{r} || F' \rangle (-1)^{F'-1+m_F} \sqrt{2F+1} \begin{pmatrix} F' & 1 & F \\ m'_F & q & -m_F \end{pmatrix}. \quad (1.1.33)$$

Here q labels the decomposition of \vec{r} in the spherical basis [113],

$$\vec{u}_{-1} = (\vec{x} - i\vec{y})/\sqrt{2}, \quad \vec{u}_0 = \vec{z}, \quad \vec{u}_{+1} = -(\vec{x} + i\vec{y})/\sqrt{2}, \quad (1.1.34)$$

with \vec{x} , \vec{y} and \vec{z} being the basis unit vectors of the Cartesian coordinate system.

The parameter q characterises the handedness of the light polarization with respect to the quantization axis. Taking the light propagation vector \vec{k} to be collinear and share the same direction as the quantization axis \vec{z} , if the light is left-circularly polarized (LCP) then $q = +1$ reversely for right-circularly polarized light (RCP) we get $q = -1$. The light polarization has to be linearly polarized along the quantization axis to obtain $q = 0$ which cannot occur when \vec{k} and \vec{z} are collinear because the polarization vector evolves into a plane orthogonal to \vec{k} . The $q = 0$ condition can easily be obtained by propagating the light beam orthogonally to the quantization axis \vec{z} and aligning the linearly polarization onto it.

Selection rules

From this first decomposition arise the selection rules between dipole induced hyperfine transitions. The 3j-symbol is non-zero if the sum of its last row is zero,

$m'_F = m_F - q$. Dipolar transitions only allow the total angular momentum of the atom to remain identical ($q = 0$) or change by ± 1 ($q \mp 1$). Other conditions need to be met for the 3j-symbol not to vanish which combined with the previous one give the hyperfine selection rules [114] :

$$\begin{aligned} F' &= F - 1, F \quad \text{or} \quad F + 1 \\ m'_F &= m_F - 1, m_F \quad \text{or} \quad m_F + 1 \\ F &\neq F' \quad \text{if} \quad m_F = m'_F \end{aligned} \quad (1.1.35)$$

The experimentalist can find it more convenient to describe a laser beam by the kind of hyperfine transition it can drive. A laser beam that would drive only $m'_F = m_F \pm 1$ transitions is denoted σ^\pm . Because this property of a beam isn't intrinsic but also depends on the beam propagation relative to the quantization axis, it might be useful to condense those conventions into the following array

$$\begin{array}{ll} \text{co-propagating} \left(\frac{\vec{k}}{\|\vec{k}\|} \cdot \vec{z} = 1 \right) & \text{counter-propagating} \left(\frac{\vec{k}}{\|\vec{k}\|} \cdot \vec{z} = -1 \right) \\ \text{LCP} \quad \sigma^- \quad (q = +1) & \sigma^+ \quad (q = -1) \\ \text{RCP} \quad \sigma^+ \quad (q = -1) & \sigma^- \quad (q = +1) \end{array} \quad (1.1.36)$$

The hyperfine dipole matrix element, Eq. (1.1.33), can be further simplified by extracting the dependence of the total angular and nuclear spin momentum quantum numbers F, I from the reduced matrix element using a 6j-symbol (curly bracket)

$$\langle F \parallel e\vec{r} \parallel F' \rangle = \langle J \parallel e\vec{r} \parallel J' \rangle (-1)^{F'+J+1+I} \sqrt{(2F'+1)(2J+1)} \left\{ \begin{array}{ccc} J & J' & 1 \\ F' & F & I \end{array} \right\}. \quad (1.1.37)$$

The values of the reduced matrix elements $\langle J \parallel e\vec{r} \parallel J' \rangle$ can be inferred from the natural linewidth, $\Gamma_{JJ'}$, using the formula [115]

$$\Gamma_{JJ'} = \frac{\omega_0^3}{3\pi\epsilon_0\hbar c^3} \frac{2J+1}{2J'+1} |\langle J \parallel e\vec{r} \parallel J' \rangle|^2, \quad (1.1.38)$$

Considering the coupling with a classical field of the form Eq. (1.1.17), second-order time-independent perturbation theory gives the following expression [116] for the energy shift $\Delta E_{F,m_F}$ of the state $|F, m_F\rangle$ induced by the interaction through the dipolar operator \hat{d} with all the other existing hyperfine states $|F', m'_F\rangle$

$$\Delta E_{F,m_F} = \frac{1}{4} \sum_{F', m'_F} \frac{1}{\hbar} \left(\frac{1}{\omega - \omega_{FF'}} + \frac{1}{-\omega - \omega_{FF'}} \right) |\langle F, m_F | \hat{d} \cdot \vec{E} | F', m'_F \rangle|^2 \quad (1.1.39)$$

where $\omega_{FF'}$ correspond to the angular frequency of the transitions between states $|F, m_F\rangle$ and $|F', m'_F\rangle$, i.e. $\omega_{FF'} = (E_{F', m'_F} - E_{F, m_F})/\hbar$.

Performing the dipole but not the rotating wave approximation, the dipole matrix element can be expressed in terms of measured quantities ($\Gamma_{JJ'}$) and explicit functions of the quantum numbers J, J', I, F, F', m_F and m'_F as seen earlier. It can be easier to compute by expressing some quantities in the form in which they are tabulated in spectroscopic databases or used in the lab to characterize the radiation fields [117]. Equation (1.1.39) becomes

$$\Delta E_{F, m_F} = \frac{3\pi I c^2}{2} \sum_{F', m'_F} \frac{A_{FF'}}{\Delta_{FF'} \omega_{FF'}^3} (2F+1)(2F'+1)(2J'+1) \left\{ \begin{matrix} J & J' & 1 \\ F' & F & I \end{matrix} \right\}^2 \left(\begin{matrix} F' & 1 & F \\ m'_F & q & -m_F \end{matrix} \right)^2 \quad (1.1.40)$$

with the first I in the formula is the intensity of the laser beam and

$$\frac{1}{\Delta_{FF'}} = \left(\frac{1}{\omega - \omega_{FF'}} + \frac{1}{-\omega - \omega_{FF'}} \right) \quad A_{FF'} = \frac{2.02613 \times 10^{18}}{\lambda_{FF'}^3} \frac{2J+1}{2J'+1} d^2 \quad (1.1.41)$$

where the quantities in $\Delta E_{F, m_F}$ and $\Delta_{FF'}$ are in SI units but not in $A_{FF'}$ in which the radiation wavelength $\lambda_{FF'} = 2\pi c/\omega_{FF'}$ and the transition matrix element d have to be respectively expressed in angstroms and atomic units of ea_0 . Derivation of the expression of $A_{FF'}$ is given in Appendix B.

Scalar, vectorial and tensorial Stark shifts

As we saw in the case of the two-level system using the dressed state picture, the Stark shift experienced by both states is equal in amplitude but not in sign. For red-detuned radiation, the lower state energy is lowered and the upper state lifted. The exact formula of Eq. 1.1.40 derived earlier will allow to sum all the two-level energy shifts depending on their state quantum numbers and polarization.

In the case of ^{40}K , we shall only study the Stark shifts of the $4S_{1/2}$, $4P_{1/2}$ and $4P_{3/2}$ manifolds of states, the ones we manipulate with resonant light.

For hyperfine manifolds with $J = 1/2$, e.g $4S_{1/2}$, $4P_{1/2}$, and a π -polarised beam ($q = 0$), the A.C. Stark shift has no m_F dependency. The Stark shifts are called *scalar*. This changes when $J \neq 1/2$, where the light shifts also experience a quadratic m_F dependence ($\propto m_F^2$), independent of the light polarization, those are called *tensorial* light shifts, shown in Figure 1.5.

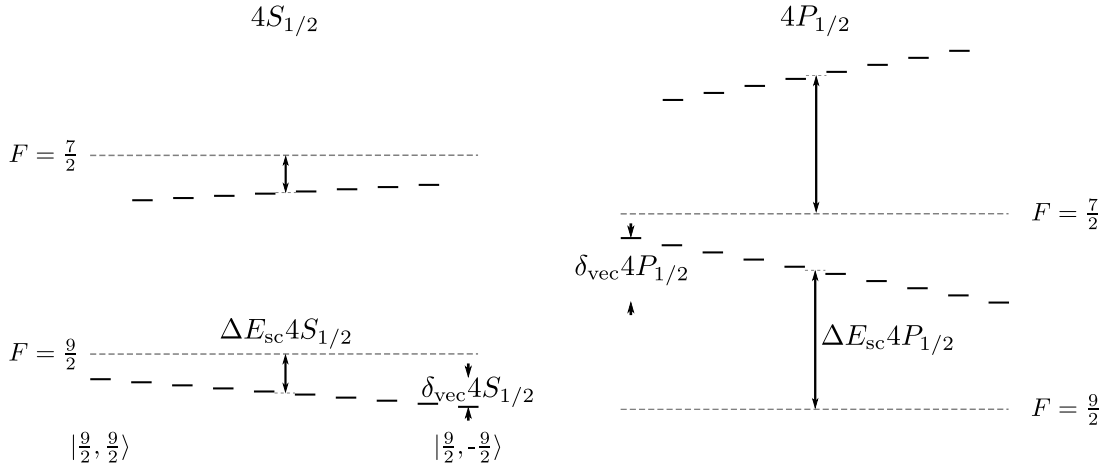


Figure 1.6: *Scalar* and *vectorial* A.C. Stark shifts on the $4S_{1/2}$ and $4P_{1/2}$ states induced by a σ^+ -polarised 1064 nm laser beam. The energy shifts are not up to scale with the hyperfine splitting. For pure σ^+ -radiation, the degeneracy between the m_F sublevels is broken as it would be by the presence a weak magnetic field. The vectorial effect shifts the m_F sublevels with an amplitude proportional to m_F from the scalar value got in the case of the pure π radiation.

The values of the light shifts denoted in Figure 1.5 and Figure 1.6 are given in the following table in MHz respectively for a 1 Watt σ^+ -polarised and π -polarised 1064 nm Gaussian laser beam of 100 μm waist :

$$\begin{array}{cccccc}
 \Delta E_{\text{sc}}4S_{1/2} & \delta_{\text{vec}}4S_{1/2} & \Delta E_{\text{sc}}4P_{1/2} & \delta_{\text{vec}}4P_{1/2} & \Delta E_{\text{sc}}^{F=11/2}4P_{3/2} & \delta_{\text{tens}}^{F=11/2} \\
 -0.372 & 3.44 \times 10^{-3} & 2.000 & 0.937 & 2.123 & 1.018
 \end{array} \quad (1.1.42)$$

For a purely circularly polarized light beam, the ratio of the vectorial splitting to the scalar shift of the $4S_{1/2}$ ground state is about 1%. This might seem small but the beams used in the experiment can be considerably more intense than the one considered for these calculations and the vectorial splitting can go up to several hundreds of kHz which would prevent any kind of process requiring degeneracy between the m_F sublevels. The ratio of vectorial to scalar shifts of the $4P_{1/2}$ state is about 50% for the assumed laser power which is tremendous even at low beam intensities. The polarization is far less convenient to adjust than applying a weak magnetic field. Good care is taken to null those vectorial shifts by setting the light to drive purely π transitions or an equal admixture of σ^+ and σ^- when the latest configuration is not achievable. Associated experimental results will be presented in Section 3.3.2.

The tensorial contribution to the light shifts of the hyperfine manifold of the $4P_{3/2}$ state cannot be neglected. It reduces the light shift experienced by the still-degenerate

lowest levels $\left| \frac{11}{2}, \pm \frac{11}{2} \right\rangle$ by almost 50%. We shall later see how this tensorial contribution will prevent us from using standard cooling techniques.

1.1.2.4 Spontaneous emission

So far we have only considered stimulated emission and eluded a crucial property of a two-level system: *spontaneous emission*. Even if Einstein found in 1917 [118] the exact expression of this quantity in his seminal article, it was only years afterwards that the true origin of spontaneous emission, which resides in the coupling between the two-level system and the quantized vacuum field, was demonstrated. It would be superfluous here to elaborate on a fully quantized model of atom-light interaction and we shall refer to the development of the Wigner-Weisskopf theory [119] which finds the expression of the spontaneous emission rate Γ to be

$$\Gamma = \frac{\omega_0^3 \mu^2}{3\pi\epsilon_0 \hbar c^3} \quad (1.1.43)$$

where ϵ_0 and c are the dielectric permittivity and speed of light in vacuum and μ and ω_0 are the dipole matrix element and angular frequency corresponding to the energy splitting of the two-level system.

The derivation of the phenomena of saturation and power broadening using the optical Bloch equations obtained with the density matrix formalism can be found in Appendix D and gives a scattering rate of

$$\Gamma_{\text{tot}} = \frac{s_0}{1+s_0} \frac{\Gamma/2}{1+(2\Delta/\Gamma')^2} \quad \Gamma' = \Gamma\sqrt{1+s_0} \quad (1.1.44)$$

where s_0 is called the *saturation parameter*, see Appendix D and Γ' , the *power-broadened linewidth*.

For weak driving field, $s_0 \ll 1$, the total scattering rate has a Lorentzian shape with a Full Width at Half Maximum (FWHM) of Γ . When the driving field power increases, the maximum scattering rate will eventually saturate at $\Gamma/2$ on resonance ($\Delta = 0$) and its unbound FWHM Γ' will continue to widen.

1.2 Atoms in traps

1.2.1 Quantum harmonic oscillator

To the first non-vanishing lowest order, any conservative trapping potential can be approximated by a harmonic one. The quantum mechanics of such traps are governed by the quantum harmonic oscillator Hamiltonian using the Schrödinger equation 1.1.15. Said Hamiltonian is

$$\hat{H}_{\text{QHO}} = \frac{\hat{p}^2}{2m} + \frac{1}{2}m\omega^2\hat{x}^2, \quad (1.2.1)$$

with ω being the harmonic oscillator angular frequency and where \hat{x} , $\hat{p} = -i\hbar\frac{\partial}{\partial x}$ are respectively the position and momentum operators.

The system has the following wavefunctions φ_n as solutions,

$$\varphi_n(x) = \frac{1}{\sqrt{2^n n!}} \left(\frac{m\omega}{\pi\hbar} \right)^{1/4} \exp\left(-\frac{m\omega x^2}{2\hbar}\right) H_n\left(\sqrt{\frac{m\omega}{\hbar}}x\right), \quad (1.2.2)$$

where H_n denotes the n^{th} Hermite polynomial function [120]. Their corresponding eigenenergies E_n are

$$E_n = \hbar\omega \left(n + \frac{1}{2} \right). \quad (1.2.3)$$

It is more convenient to deal with the mathematics of the system by introducing the lowering/annihilation and raising/creation ladder operators \hat{a} and \hat{a}^\dagger and the number operator \hat{N} ,

$$\hat{a} = \sqrt{\frac{m\omega}{2\hbar}} \left(\hat{x} + \frac{i}{m\omega}\hat{p} \right), \quad \hat{a}^\dagger = \sqrt{\frac{m\omega}{2\hbar}} \left(\hat{x} - \frac{i}{m\omega}\hat{p} \right), \quad \hat{N} = \hat{a}^\dagger\hat{a}, \quad (1.2.4)$$

which act the following way on any eigenstate $|n\rangle$:

$$\hat{a}|n\rangle = \sqrt{n}|n-1\rangle, \quad \hat{a}^\dagger|n\rangle = \sqrt{n+1}|n+1\rangle, \quad \hat{N}|n\rangle = n|n\rangle. \quad (1.2.5)$$

In this operator formalism the Hamiltonian simplifies to

$$\hat{H}_{\text{QHO}} = \hbar\omega \left(\hat{N} + \frac{1}{2} \right) \quad (1.2.6)$$

and any eigenfunctions $|n\rangle$, also called a Fock state, can be expressed as a function of the ground state $|0\rangle$:

$$|n\rangle = \frac{(\hat{a}^\dagger)^n}{\sqrt{n!}} |0\rangle. \quad (1.2.7)$$

For a particle evolving in an quantum harmonic oscillator

- the accessible energy levels are quantized and all equally spaced by $\hbar\omega$
- the ground state energy (called *zero point energy*) is non-zero, as we could expect from a classical oscillator, and equals $\hbar\omega/2$
- the Hermite polynomials H_n of degree n and hence also the wavefunction φ_n have the same parity as n . Consequently the wavefunctions alternate parity, a crucial property when driving excitations in harmonic traps as we will explain later in Section 2.3.3.1.

1.2.2 Optical dipole trapping

1.2.2.1 Gaussian beam propagation

The most commonly used form of light radiation is the Gaussian TEM₀₀ laser beam. A particular solution of the Helmholtz propagation equation in the paraxial scalar approximation results in the following solution for the electric field expressed in cylindrical coordinates, where z is the propagation axis and \vec{r} the vector position in the plane orthogonal to the propagation axis:

$$E(\vec{r}, z) = E_0 \left(\frac{w_0}{w(z)} \right) \exp \left(\frac{-r^2}{w(z)^2} \right) \exp \left[-ik \left(z - \frac{r^2}{2R(z)} \right) + i\zeta(z) \right] \quad (1.2.8)$$

with $w(z)$, the *Gaussian beam spot size* (radius), $R(z)$, the radius of curvature and $\zeta(z)$, the *Gouy phase* at z , while the shortened notations $w_0 \equiv w(0)$, designating the beam spot size/radius at the beam waist/focus [121] and $r^2 \equiv \|\vec{r}\|^2$ have been adopted. Those quantities are

$$w(z) = w_0 \sqrt{1 + \left(\frac{z}{z_R} \right)^2}, \quad R(z) = z \left(1 + \left(\frac{z_R}{z} \right)^2 \right), \quad \zeta(z) = \arctan \left(\frac{z}{z_R} \right) \quad (1.2.9)$$

where the *Rayleigh range* z_R has been introduced as

$$z_R = \frac{\pi w_0^2}{\lambda}. \quad (1.2.10)$$

The trapping potential experienced by the atoms is proportional to the intensity of the light (given in W/m²), itself proportional to the square of the norm of the electric field

$$I(r, z) = \frac{n\epsilon_0 c}{2} \| E(\vec{r}, z) \|^2 = I_0 \left(\frac{w_0}{w(z)} \right)^2 \exp \left(\frac{-2r^2}{w(z)^2} \right) \quad (1.2.11)$$

with the maximum intensity given by

$$I_0 = \frac{n\epsilon_0 c E_0^2}{2} \quad (1.2.12)$$

where ϵ_0 is the vacuum electric permittivity and n the refractive index of the medium which, for the relatively low densities assumed here, shall be taken to one for the rest of this dissertation.

The Gaussian beam takes its name from the fact that the transverse intensity profile has a Gaussian shape. The focus of a beam ($z = 0$) is defined as the spatial location at which this Gaussian profile has the smallest surface area. The beam spot size, $w(z)$, is the radius at which the Gaussian transverse intensity profile has dropped to $1/e^2$ of its maximal value in the z transverse plane.

The Rayleigh range z_R denotes the longitudinal position at which the beam radius has increased by a factor of $\sqrt{2}$. For an experimentalist setting up beams, it is convenient to picture the beam as a tube of length $b = 2z_R$ centred at the focus in which the beam will approximately have the same transverse dimensions, for that reason b is called the *confocal parameter* or *depth of focus*.

For absolute axial positions greater than z_R , the beam transverse size will have a linear asymptotic growth. This triggers the introduction of the parameter called the *beam divergence angle* θ (half-total angle) which has the following expression

$$\theta = \lim_{z \gg z_R} \arctan \frac{w(z)}{z} = \frac{w_0}{z_R} = \frac{\pi\lambda}{w_0} \quad (1.2.13)$$

and the *total beam opening angle*, $\Theta = 2\theta$. For a given wavelength, the beam will have a stronger divergence for tighter foci. The radius of curvature $R(z)$ describes the radius of curvature of the phase front of the electric field at the axial position z . It is null only at the focus where the electric field behaves as a plane wave. The Gouy phase is bound to values between $\pm\pi/2$, changing sign at the focus. This is of little importance for trapping atoms but is a crucial property of the phase of the electric field that needs to be considered when building systems where phase matters such as resonators. Figure 1.7 plots a axial cut view using the beam radius in units of its minimal waist as edges.

The total power of the beam P is linked to its peak intensity I_0 by integrating the Gaussian transverse profile at any longitudinal position z

$$P = \int_{r=0}^{\infty} \int_{\theta=0}^{2\pi} I(r,z) r dr d\theta = \frac{\pi w_0^2 I_0}{2} . \quad (1.2.14)$$

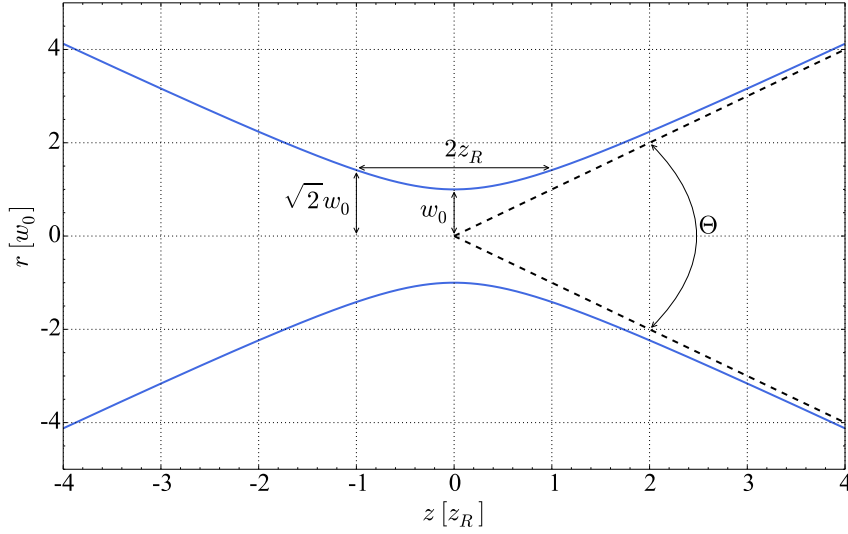


Figure 1.7: Beam spot size/radius in units of waist radius, w_0 , as a function of normalized longitudinal position in units of Rayleigh range, z_R , for a beam of wavelength $\lambda = 1064$ nm and waist spot size $w_0 = 100$ μm .

Beware that θ denotes here the azimuthal angle in the cylindrical coordinate system and has no relation with the *beam divergence angle* introduced in Eq. (1.2.13). Reversing the previous expression yields the peak intensity as a function of the beam power

$$I_0 = \frac{2P}{\pi w_0^2} . \quad (1.2.15)$$

Note that the unintuitive factor of 2 that arises from the definition of the waist.

1.2.2.2 Trap depth and trap frequencies

For a two-level system the expression of the A.C. Stark shift experienced by the ground state, ΔE_g , can be expressed in a more convenient way for the experimentalist by substituting the square of the Rabi frequency, $|\Omega|^2$, by measured quantities and commonly used beam parameters in the lab

$$\begin{aligned} \Delta E_g &= \frac{\hbar |\Omega|^2}{4 \Delta'} = \frac{E_0^2 \mu^2}{4\hbar \Delta'} \\ &= \frac{I_0 \mu^2}{\Delta' 2\hbar\epsilon_0 c} = \frac{3\pi c^2 I_0}{2\omega_0^3} \frac{\omega_0^3 \mu^2}{3\pi\hbar\epsilon_0 c^3} \frac{1}{\Delta'} \\ \Delta E_g &= \frac{3\pi c^2}{2\omega_0^3} \frac{\Gamma}{\Delta'} I_0 \end{aligned} \quad (1.2.16)$$

where we have not performed the rotating wave approximation and the generalized detuning Δ' has the following form:

$$\frac{1}{\Delta'} = \frac{1}{\omega - \omega_0} + \frac{1}{-\omega - \omega_0} . \quad (1.2.17)$$

From now on, U_{ODT} designates the trap depth created by a single laser beam. Using equations (1.2.11) and (1.2.16), the full trapping potential created by a single optical dipole trap is given by

$$U_{\text{ODT}}(r, z) = U_0 \left(\frac{w_0}{w(z)} \right)^2 \exp \left(\frac{-2r^2}{w(z)^2} \right) \quad (1.2.18)$$

where U_0 is the maximum trap depth expressed by

$$U_0 = \frac{3\pi c^2}{2\omega_0^3} \frac{\Gamma}{\Delta'} I_0 = \frac{3c^2}{\omega_0^3 w_0^2} \frac{\Gamma}{\Delta'} P . \quad (1.2.19)$$

The bottom part of such a trap can be approximated by a harmonic oscillator, and by performing a Taylor expansion at the lowest non-vanishing order along both longitudinal (z) and radial (r) axes we can extract their respective oscillator angular frequencies $\omega_{\text{ODT, long}}$ and $\omega_{\text{ODT, rad}}$ given by

$$\omega_{\text{ODT, long}} = \sqrt{\frac{2U_0}{mz_R^2}} , \quad \omega_{\text{ODT, rad}} = \sqrt{\frac{4U_0}{mw_0^2}} . \quad (1.2.20)$$

The ratio of the radial frequency to the longitudinal one is

$$\frac{\omega_{\text{ODT, rad}}}{\omega_{\text{ODT, long}}} = \sqrt{2} \frac{\pi w_0}{\lambda} . \quad (1.2.21)$$

The single-beam traps used in our experiment are all red-detuned in the near infrared with beam waists in the 20 – 300 μm range, which makes them very elongated (frequencies ratio $\approx 80 - 1000$).

Crossing two beams perpendicularly can create an almost perfect spherically symmetric trap geometry (gravity breaking it along one axis). The requirements are that the beams need to be sufficiently incoherent with regard to each other to avoid interferences (achieved by mutually detuning them by a few 10 MHz using AOMs).

A red detuned optical dipole trap causes heating by off-resonant photon scattering. For low saturation intensity and large detunings the scattering rate is

$$\Gamma_{\text{sc}} = \frac{3\pi c^2}{2\hbar\omega_0^3} \left(\frac{\omega}{\omega_0} \right)^3 \left(\frac{\Gamma}{\Delta'} \right)^2 I_0 \quad (1.2.22)$$

which expressed as a function of the maximum trap depth reads

$$\Gamma_{\text{sc}} = \left(\frac{\omega}{\omega_0} \right)^3 \frac{\Gamma}{\Delta'} \frac{U_{\text{ODT}}}{\hbar}. \quad (1.2.23)$$

The equation shows that to minimise heating by off-resonant scattering for a fixed trap depth, one would increase the light detuning but should be aware of the resulting decrease of the trap, as its depth is inversely proportional to the detuning. The commercial NdYAG lasers can easily deliver 1 to 25 Watts at $\lambda = 1064 \mu\text{m}$ which with typical waist sizes of $50 - 300 \mu\text{m}$ provide enough trap depth ($5 - 500 \mu\text{K}$) and sufficiently low scattering rate ($\sim \text{Hz}$) to not heat the atoms on the experimental timescales (100 ms to s).

1.2.2.3 Optical lattices

Interferences

The interference between two counter-propagating laser beams can be treated by adding their respective electric fields. The total real electric field can be written as

$$\vec{E}(z,t) = \vec{E}_{0,1} \cos(k_1 z - \omega_1 t - \phi_1) + \vec{E}_{0,2} \cos(-k_2 z - \omega_2 t - \phi_2). \quad (1.2.24)$$

The resulting intensity is then given by

$$\begin{aligned} \frac{I(z,t)}{\epsilon_0 c} &= |\vec{E}(z,t)|^2 = |\vec{E}_{0,1}|^2 \cos^2(k_1 z - \omega_1 t - \phi_1) + |\vec{E}_{0,2}|^2 \cos^2(-k_2 z - \omega_2 t - \phi_2) + \\ &2\vec{E}_{0,1} \cdot \vec{E}_{0,2} \left(\cos [(k_1 - k_2)z - (\omega_1 + \omega_2)t - (\phi_1 - \phi_2)] + \right. \\ &\quad \left. \cos [(k_1 + k_2)z - (\omega_1 - \omega_2)t - (\phi_1 + \phi_2)] \right). \end{aligned} \quad (1.2.25)$$

Assuming the two beams are derived from the same laser, their respective wavelength can be taken to be quite close and the phase difference to be constant, we introduce the relations $\Delta\omega = \omega_2 - \omega_1$, $k = (k_1 + k_2)/2$, $\Delta k = k_2 - k_1$ and $(\phi_2 + \phi_1) = \phi$. The time scales corresponding to the electric field oscillatory frequencies aren't accessible experimentally ($1/\omega_{1,2} \gg t$) and the time averaging of the cosine functions ($\langle \cos(\omega_{1,2}t) \rangle_t = 0$ and $\langle \cos^2(\omega_{1,2}t) \rangle_t = 1/2$) leads to

$$\frac{2\langle I(z,t) \rangle_t}{\epsilon_0 c} = |\vec{E}_{0,1}|^2 + |\vec{E}_{0,2}|^2 + 2\vec{E}_{0,1} \cdot \vec{E}_{0,2} \cos [(2k + \Delta k)z - \Delta\omega t - \phi] \quad (1.2.26)$$

To avoid interferences, two conditions can suffice:

- the polarization of the beams are orthogonal ($\vec{E}_{0,1} \cdot \vec{E}_{0,2} = 0$)

- the detuning between the two oscillatory angular frequencies is such that on the time scales of the experiment ($1/\Delta\omega \gg t$), the interference term averages to zero.

Equation (1.2.26) can be re-written as

$$\langle I(z,t) \rangle_t = I_{0,\text{tot}} \left(1 + C \cos [(2k + \Delta k)z - \Delta\omega t - \phi] \right) \quad (1.2.27)$$

where $I_{0,\text{tot}} = I_{0,1} + I_{0,2}$ is the incoherent sum of the beam intensities and the interference contrast C is introduced as

$$C \equiv \frac{2\vec{E}_{0,1} \cdot \vec{E}_{0,2}}{|\vec{E}_{0,1}|^2 + |\vec{E}_{0,2}|^2} = \vec{\epsilon}_1 \cdot \vec{\epsilon}_2 \frac{2\sqrt{I_{0,1}I_{0,2}}}{I_{0,1} + I_{0,2}}. \quad (1.2.28)$$

If the beams' electric fields have identical polarisation and magnitude, the contrast is maximised ($C = 1$). Under those conditions, the overall intensity reads

$$\langle I(z,t) \rangle_t = 2I_{0,\text{tot}} \cos^2 [(k + \Delta k/2)z - \Delta\omega t/2 - \phi/2]. \quad (1.2.29)$$

To obtain a standing still lattice, the detuning has to be null ($\Delta\omega = 0$) which simplifies the intensity to

$$\langle I(z,t) \rangle_t = 2I_{0,\text{tot}} \cos^2(kz - \phi/2) \quad (1.2.30)$$

if the global Gaussian beam shape is also taken into account the overall intensity spatial dependence is given by

$$I_{\text{lat}}(r,z) = I_{0,\text{lat}} \left(\frac{w_0}{w(z)} \right)^2 \exp \left(\frac{-2r^2}{w(z)^2} \right) \cos^2(kz - \phi/2) \quad (1.2.31)$$

with the maximum intensity $I_{0,\text{lat}}$ is four times the one of a single beam ($I_{0,\text{lat}} \equiv 4I_0$).

Lattice trapping frequencies

As mentioned earlier in Eq. (1.2.16), the trapping potential is directly proportional to the light intensity

$$U_{\text{lat}}(r,z) = U_{0,\text{lat}} \left(\frac{w_0}{w(z)} \right)^2 \exp \left(\frac{-2r^2}{w(z)^2} \right) \cos^2(kz - \phi/2). \quad (1.2.32)$$

The tightest confinement to consider is the one created by the interference effect and has a spatial period of $a_{\text{lat}} = \lambda/2$. The frequency of the traps ($\omega_{\text{lat},\text{long}}$) created by

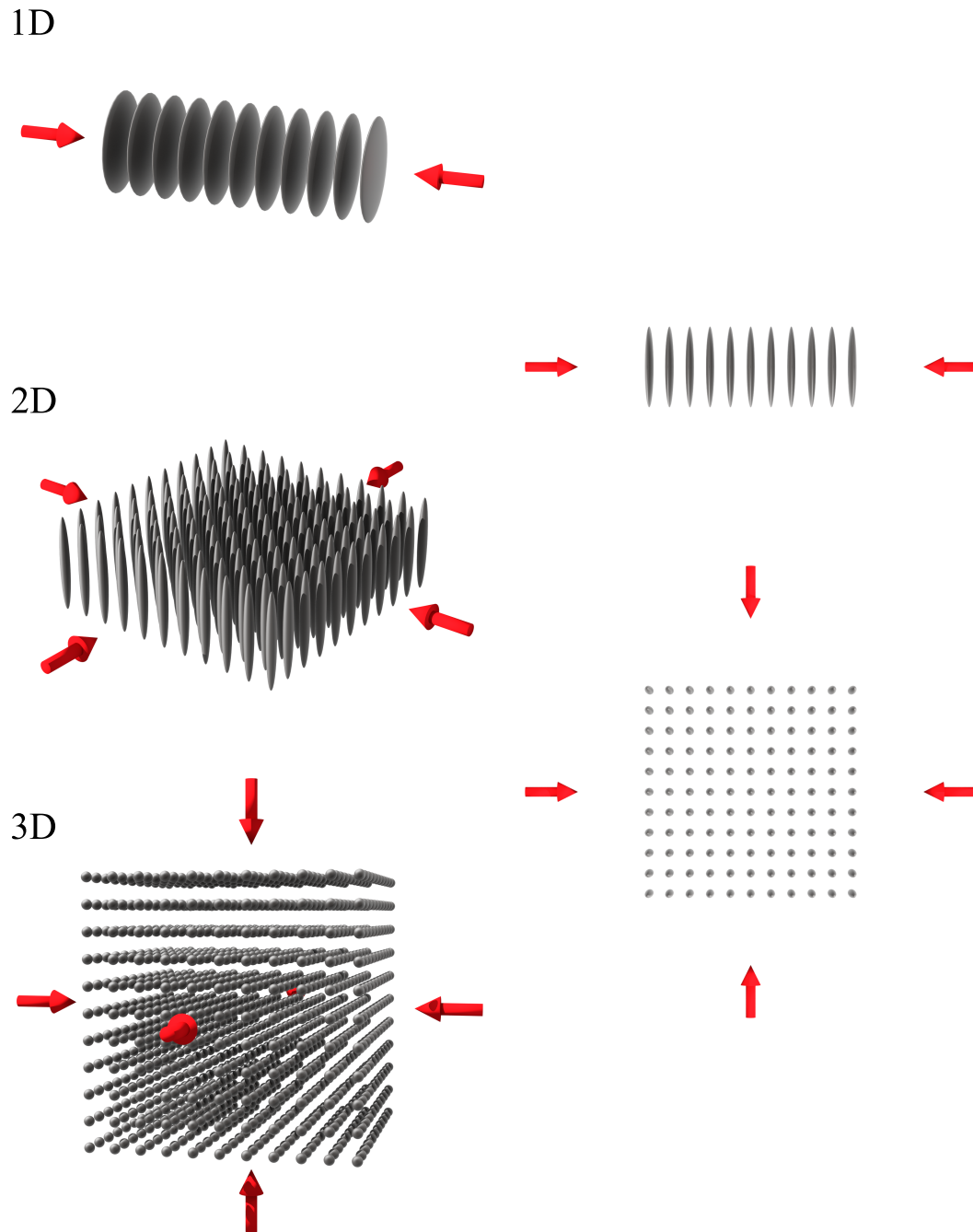


Figure 1.8: Left column: 1D (top), 2D (middle) 3D (bottom) isometric view of equipotential lines lattice configurations. Right column: Top/side view (top) of equipotential lines lattice of 1D/2D lattice configuration. Top view (bottom) of equipotential lines of either 2D or 3D lattice configurations. The pairs of red arrows represent the pair of incoming and retro-reflected beams interfering to create a lattice potential.

the interference effect can be obtained by performing a Taylor expansion of the cosine function to get

$$\omega_{\text{lat,long}} = \sqrt{\frac{2U_{0,\text{lat}}}{m} k^2} = \frac{2\pi}{\lambda} \sqrt{\frac{2U_{0,\text{lat}}}{m}}. \quad (1.2.33)$$

Such a lattice obtained usually by retro-reflecting a beam onto itself is called a "1D"-lattice because the potential is periodic along one axis, the beam axis. However a "1D"-lattice is a succession of traps equally spaced by a_{lat} which have the radial shape of the bare single beam but with a maximum trap depth enhanced by a factor four, see Figure 1.8. Because those traps have a cylindrical symmetry and are quite flat (their diameter to thickness ratio $2w_0/a_{\text{lat}}$ lies within the 150 - 300 range in our experiment), they are usually considered as 2D trap; topological wise, and called "layers". Such a layer has a radial frequency given by

$$\omega_{\text{lat,rad}} = \sqrt{\frac{4U_{0,\text{lat}}}{mw_0^2}} = 2\omega_{\text{ODT,rad}}. \quad (1.2.34)$$

1.3 Lattice physics

1.3.1 Basic crystal formalism

Our experiment aims to create an analogue quantum simulator for electrons in a solid and the physics of cold neutral atoms in periodic potentials can be treated the same way as in solid-state physics.

A lattice can be formally defined as points (or sites) whose positions are given by

$$\vec{R} = n_1\vec{a}_1 + n_2\vec{a}_2 + n_3\vec{a}_3 \quad (1.3.1)$$

where \vec{a}_i are the unit vectors of the lattice and $n_i \in \mathbb{Z}^3$.

The reciprocal lattice can be pictured as a spatial Fourier transform of the "real", also called direct lattice, and the position of sites is described by the ensemble \vec{K} which follow the condition

$$e^{i\vec{K}\cdot\vec{R}} = 1 \iff \vec{K} \cdot \vec{R} = [2\pi] \quad (1.3.2)$$

where $[2\pi]$ reads modulo- 2π and designates the set of relative multiples of 2π , i.e. $[2\pi] = 2\pi n \quad \forall n \in \mathbb{Z}$.

The basis vectors of the reciprocal lattice are expressed in terms of the direct lattice vectors by

$$\vec{b}_1 = \frac{2\pi(\vec{a}_2 \times \vec{a}_3)}{\vec{a}_1 \cdot (\vec{a}_2 \times \vec{a}_3)}, \quad \vec{b}_2 = \frac{2\pi(\vec{a}_3 \times \vec{a}_1)}{\vec{a}_1 \cdot (\vec{a}_2 \times \vec{a}_3)}, \quad \vec{b}_3 = \frac{2\pi(\vec{a}_1 \times \vec{a}_2)}{\vec{a}_1 \cdot (\vec{a}_2 \times \vec{a}_3)} \quad (1.3.3)$$

and satisfy the following condition with respect to the direct lattice vectors \vec{a}_i

$$\vec{a}_i \cdot \vec{b}_j = 2\pi\delta_{i,j} \quad (i,j) \in (1,2,3)^2 . \quad (1.3.4)$$

For a simple cubic lattice of spacing a , the direct and reciprocal lattice vectors are aligned with the orthonormal basis $(\vec{e}_x, \vec{e}_y, \vec{e}_z)$ and are equal to

$$\vec{a}_i = a \vec{e}_i \quad \vec{b}_i = \frac{2\pi}{a} \vec{e}_i \quad i \in (x,y,z) . \quad (1.3.5)$$

For a complete description of all the formalism that surrounds lattices, in particular the definitions of unit cells (especially the Wigner-Seitz cell), lattice planes and Miller indices, the reader can consult chapters 4 to 7 of the book by Ashcroft and Mermin [122].

1.3.2 Band structure

In a three dimensional periodic potential, $V(\vec{r})$, of characteristic spacing a_i , i.e. $\forall \vec{R} \quad V(\vec{r}) = V(\vec{r} + \vec{R})$, the wave function of a single particle of mass m is governed by the following Schrödinger equation

$$\left[\frac{\hat{p}^2}{2m} + \hat{V}(\vec{r}) \right] \psi_{\vec{q}}^{(n)}(\vec{r}) = E_{\vec{q}}^{(n)} \psi_{\vec{q}}^{(n)}(\vec{r}) . \quad (1.3.6)$$

The set of solutions that satisfies this equation are the so-called Bloch functions. Bloch's theorem stipulates [122] that a wave function solution can be expressed as the product of a plane wave and of a function having the same periodicity as the potential

$$\psi_{\vec{q}}^{(n)}(\vec{r}) = e^{i\vec{q}\cdot\vec{r}} u_{\vec{q}}^{(n)}(\vec{r}) \quad (1.3.7)$$

with

$$u_{\vec{q}}^{(n)}(\vec{r} + \vec{R}) = u_{\vec{q}}^{(n)}(\vec{r}) \quad (1.3.8)$$

and where $n \in \mathbb{N}$ is the band index and \vec{q} , the wave vector or quasimomentum.

Simplifying to one dimension, $\vec{r} \equiv x \vec{e}_x$ and $\vec{q} \equiv q \vec{e}_x$, the periodic function $u_{\vec{q}}^{(n)}$ obeys the following 1D Schrödinger equation

$$\left[\frac{(p + \hbar q)^2}{2m} + V(x) \right] u_q^{(n)}(x) = E_q^{(n)} u_q^{(n)}(x) . \quad (1.3.9)$$

Bloch's theorem introduces q as a quantum number characteristic of the potential periodicity $a \equiv a_{lat}$. Because of such periodicity, the study of u_q^n can be restricted to the first Brillouin zone defined as $q \in [-\pi/a, \pi/a]$, $k_B = \pi/a$ being defined as the

Bragg vector. The band index n arises from the existence of an infinite number of solutions to Eq. (1.3.9) for a fixed quasimomentum q .

In the case of a perfect optical lattice potential which can be written as

$$V(x) = V_0 \sin^2(k_B x) \quad (1.3.10)$$

where

$$k_B = \pi/a . \quad (1.3.11)$$

the band structure can be obtained by solving the 1D Mathieu equation:

$$\left(-\frac{d^2}{dx^2} + \frac{V_0}{4E_r}(2 - 2\cos(2x)) \right) \psi_q^{(n)}(x) = \frac{E_q^n}{E_r} \psi_q^{(n)}(x) \quad (1.3.12)$$

with $E_r = \hbar^2 k^2 / 2m$ defined as the lattice energy recoil. The first five levels dispersion relation of said band structure are plotted for various trap depths given in units of recoil energy on Figure 1.9.

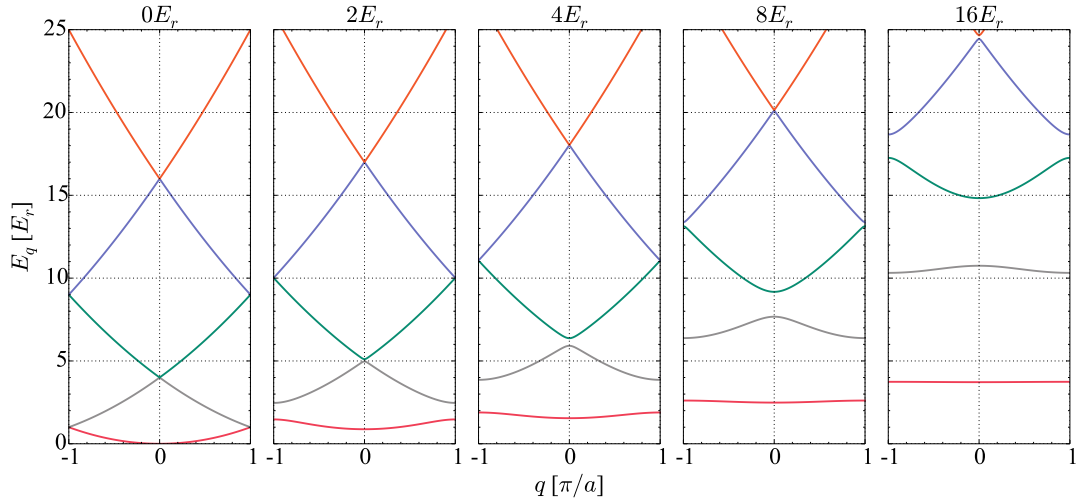


Figure 1.9: Dispersion relation for the five first bands in the first Brillouin zone for increasing lattice depths (left to right): 0, 2, 4, 8 and 16 recoil energies. In the limit of a very weak lattice, the energy spectrum is continuous, the degeneracy is quickly broken when the lattice depth increases which triggers the creation of energy gaps between the different bands. Also the deeper the lattice, the flatter the band becomes behaving like its corresponding quantum harmonic oscillator energy level.

1.3.3 Band mapping

Band mapping [123, 124] is a technique that allows the observation of the population of the bands by switching off the lattice potential adiabatically with respect to the interactions between the bands and diabatically with respect to processes that changes the quasimomentum q , i.e. the vibrational frequency of the trap. The condition reads [125]

$$h\nu_{lat} \ll h/\tau_{BM} \ll E_{BG} \quad (1.3.13)$$

where E_{BG} is the smallest band gap in the system, τ_{BM} is the characteristic time of the lattice switch off curve and ν_{lat} is the lattice vibrational frequency.

In 1D it is relatively easy to make the transformation from quasimomentum to real momentum. Indeed, the quasimomentum q in the band n will be "mapped" onto its real free-space momentum p which lies in the interval $[-(n+1)k_B, -nk_B] \cup [nk_B, (n+1)k_B]$. The mapping of quasimomentum onto real momentum via time of flight (TOF) imaging leads to the ballistic expansion of the atoms in the shape of the lattice Brillouin zones.

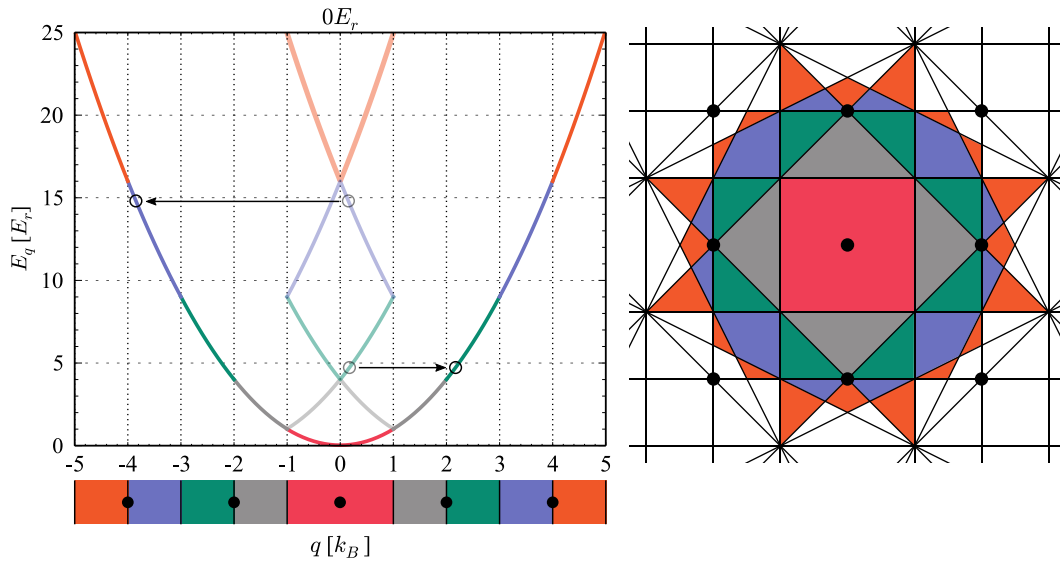


Figure 1.10: Left: 1D Band mapping where, after ramping down the lattice, the quasimomentum q reduced to the first Brillouin zone of a particle in the n th band is projected onto its real momentum in the $(n+1)$ th Brillouin zone. Right: Brillouin zones inferred from the construction of the Bragg planes of a reciprocal 2D simple square lattice. The plain black dots represent the atoms locations in the reciprocal lattice which, for a 2D simple square lattice, are spaced by $2k_B = 2\pi/a$ in both directions.

The topology of the Brillouin zones is not straightforwardly generalised in higher dimensions. As well explained in the Diploma thesis of T. Müller [126], in 2D, the second and third bands are partially degenerate and together fill, on each axis, the

space which would have corresponded to the second band (and Brillouin zone) in 1D i.e. $\forall q \in [-2k_B, -k_B] \cup [k_B, 2k_B]$, this band degeneracy increases with the band index as the fourth, fifth, sixth and seventh bands in 2D fill the equivalent of the 1D third Brillouin zone as shown in Figure 1.10.

In 3D the bands are no longer uniquely identifiable and we introduce a new notation of the observed quantised arrays of real momentum into quantised vibrational bands equivalent to the 1D Brillouin zones. A vibrational band is defined as the spatial equivalent to one of the 1D Brillouin zones on each axis. Referring to Figure 1.11 which presents on the left the ballistic expansion of atoms held in a simple cubic lattice after adiabatic ramp off of the lattice potential on all three axis, the vibrational band shall be noted $[XYZ]$ with $X, Y, Z \in \mathbb{Z}$. For instance, the second vibrational band on the vertical axis $[001]$ matches all the characteristic of the second 1D Brillouin zone along that axis even if it does correspond to the particles lying in the second, third or fourth bands of the 3D cubic lattice. Conveniently, independently on the number of dimensions, the atoms mapped onto the first Brillouin zone are always uniquely from the lowest band.

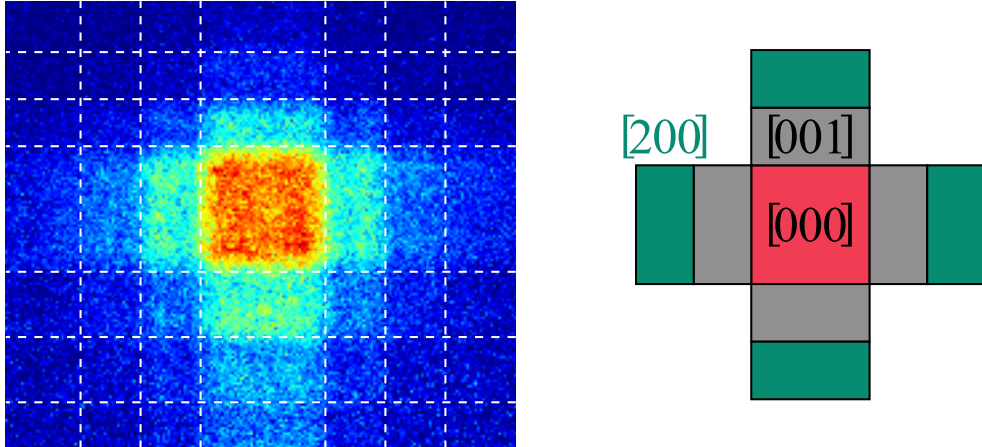


Figure 1.11: Left: Ballistic expansion of our simple cubic (3D) lattice after exponential adiabatic ramp off with a 1 ms decay constant. The white dotted line represented the inferred vibrational excitations quanta spaced by k_B from the edge of the first Brillouin zone. The expansion is asymmetric along the z-axis due to the acceleration of gravity. Note that the population in the first Brillouin zone is enhanced by the projection of the excited vibrational zones corresponding the third axis along the imaging axis i.e. $[0Y0] \forall Y \in \mathbb{Z}^*$. Right: Schematic representation of the introduced 3D vibrational zones equivalent to the 1D Brillouin zones.

1.3.4 Tight-binding model

Wannier functions

The Bloch functions form an orthogonal solutions basis of the lattice Hamiltonian. Inconveniently, each Bloch wavefunction corresponds to a representation of a particle that is fully delocalised in space and fully localised in momentum space. Taking the Fourier transform of the Bloch functions across the first Brillouin zone, we obtain another orthogonal set of solutions which are now fully localised in space: the Wannier functions.

$$w_n(x - x_j) = \frac{1}{v_{BZ}} \sum_q \psi_q^{(n)}(x) e^{-iqx} dq \quad (1.3.14)$$

where $w_n(x - x_j)$ denotes the Wannier function in the band n localised at lattice site x_j , v_{BZ} is the volume of the Brillouin zone and equals $(2\pi/a)^N$ for a N -dimensional simple orthogonal lattice and where the summation runs over the first Brillouin zone, i.e. $-k_B \leq q \leq k_B$.

They satisfy the following orthonormality condition:

$$\int_x w_{n'}^*(x - x_j) w_n(x - x_i) dx = \frac{1}{v_{BZ}} \delta_{n,n'} \delta_{x_i, x_j} . \quad (1.3.15)$$

Two Wannier functions localised at different lattice sites are therefore orthogonal to each other within a band as well as across the bands without regards to the lattice sites. Moreover the local aspect of the Wannier function increases with the lattice depth, see Figure 1.12. Those two properties make these functions particularly well suited to describe sets of interacting particles in lattices.

U, J parameters

Using the Wannier functions, it becomes much easier to calculate the tunneling term, denoted J (or t for condensed matter physicists), which is the matrix element corresponding to the process of a particle tunneling from a site to another. Not immediately restricting ourselves to the nearest neighbour sites nor to a single band, $J_{i,j}^{n,n'}$ resulting from the tunneling from site i to another site j from band n to n' is given by

$$J_{i,j}^{n,n'} = - \int_V w_{n'}^*(\vec{r} - \vec{R}_j) \left(\frac{\hat{p}^2}{2m} + \hat{V}(\vec{r}) \right) w_n(\vec{r} - \vec{R}_i) d\vec{r} \quad (1.3.16)$$

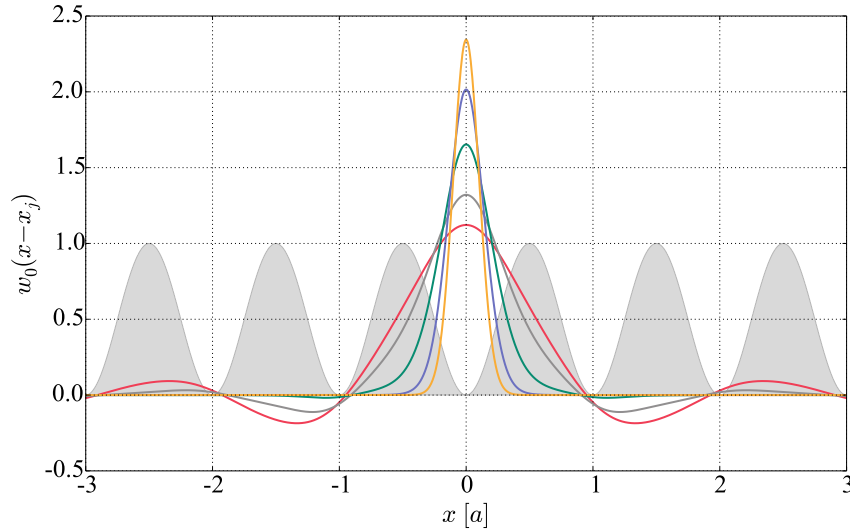


Figure 1.12: Real part of Wannier function in the ground band for the following lattice depths: 0.5 , 2 , 8 , 32 and $100 E_r$ respectively in red, gray, green, blue and orange for $x_j = 0$. The lattice potential is represented in filled light gray. For low lattice depths, e.g. 0.5 and $2 E_r$, the Wannier wave functions exhibit non-negligible amplitude in their side lobes and therefore a probability of finding the particle on a neighbouring site. As the lattice depth increases, those side lobes vanishes and the wave function/particle become entirely localised on an unique lattice site.

The interaction term, commonly denoted $U_{i,j}^{n,n'}$, represents the extra energy that it would cost the system to place a particle in band n at site i in the presence of a particle in band n' at site j and reads

$$U_{i,j}^{n,n'} = \frac{4\pi\hbar^2 a_s}{m} \int_V w_{n'}^*(\vec{r} - \vec{R}_j) w_n^*(\vec{r} - \vec{R}_i) w_{n'}(\vec{r} - \vec{R}_j) w_n(\vec{r} - \vec{R}_i) d\vec{r}. \quad (1.3.17)$$

with m being the mass of the particle and where a_s is the s-wave scattering length [127].

Particles in a periodic potential are said to evolve in the *tight-binding regime* when the overlap of Wannier functions to nearest lattice sites needs to be taken into account while the locality of the wavefunction remains valid. In simpler terms, only the processes involving nearest neighbouring sites in the same band shall be retained. The tunneling terms reduces to $J_{i,j}^{n,n'} \equiv J^n$ and only the on-site interaction term $U^n \equiv U_{i,i}^{n,n}$ remains, the integral over Wannier function being on the fourth order, the neighbouring interaction are neglected as the next-nearest neighbouring sites tunneling is.

A known result of the tight-binding regime can be obtained by calculating the energy of a particle of quasimomentum q using the Wannier functions [128]

$$\begin{aligned}
E_{\vec{q}}^{(n)} &= \int_V \psi_{\vec{q}}^{(n)*}(\vec{r}) \left(\frac{\hat{p}^2}{2m} + \hat{V}(\vec{r}) \right) \psi_{\vec{q}}^{(n)}(\vec{r}) d^3r \\
&= \sum_{i,j} e^{-i\vec{q} \cdot (\vec{R}_j - \vec{R}_i)} \int_V w_n^*(\vec{r} - \vec{R}_j) \left(\frac{\hat{p}^2}{2m} + \hat{V}(\vec{r}) \right) w_n(\vec{r} - \vec{R}_i) d^3r \\
&= E_0^{(n)} + \sum_{\langle i,j \rangle} J_{i,j}^n e^{-i\vec{q} \cdot (\vec{R}_j - \vec{R}_i)} \\
&= E_0^{(n)} + \sum_j J_j^n e^{-i\vec{q} \cdot \vec{R}_j}
\end{aligned} \tag{1.3.18}$$

where $\langle i,j \rangle$ signifies that i and j are neighbouring sites. Only considering nearest neighbour tunneling in a simple cubic lattice corresponds to $\vec{r}_j = \pm a \vec{e}_{x,y,z}$ resulting in

$$E_{\vec{q}}^{(n)} = E_0^{(n)} + 2J^n \sum_{d \in \{x,y,z\}} \cos(q_d a) \tag{1.3.19}$$

running over the whole first Brillouin zone we obtain

$$J^n = \frac{1}{4d} \Delta E^{(n)} \tag{1.3.20}$$

where $\Delta E^{(n)} = \max E_{\vec{q}}^{(n)} - \min E_{\vec{q}}^{(n)}$ correspond to the energetic band width of band n and the d is the number of dimensions considered.

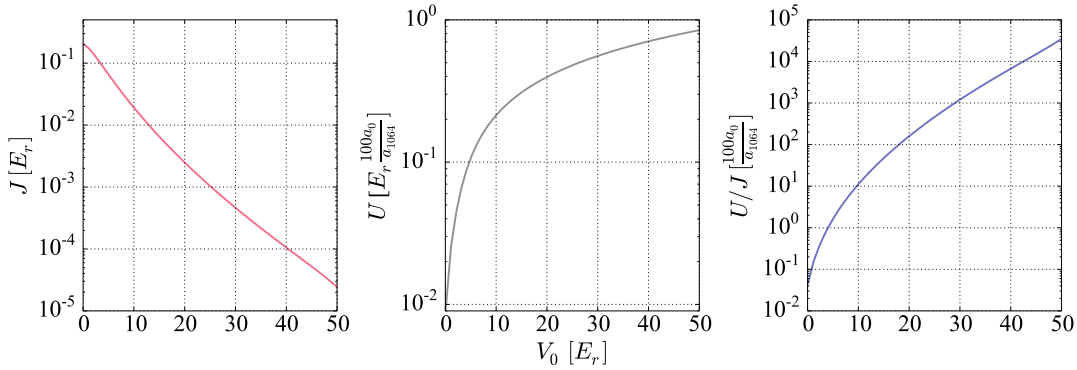


Figure 1.13: Left to right: Tunneling matrix element, on-site interaction and ratio of on-site interaction to tunneling in a 3D simple cubic lattice. Here, the s-wave scattering length a_s was chosen to be 100 a_0 , with a_0 being a Bohr radius and the lattice spacing a_{lat} to be $a_{1064} = 532$ nm.

As presented in Figure 1.13, the ratio of the on-site interaction over the tunneling matrix element can easily be varied over orders of magnitude when varying the lattice depths through the lattice beams power making the exploration of the phase diagram experimental convenient.

1.3.5 Fermi-Hubbard model

The assumption that all the particles are fermions with spin- $\frac{1}{2}$ and shall evolve in the lowest band, i.e. $J \equiv J^0$ and $U \equiv U^n$, allows to condense all the physics into a second quantised Hamiltonian which governs the famous Fermi-Hubbard model:

$$\hat{H}_{FH} = -J \sum_{\langle i,j \rangle, \sigma} (\hat{c}_{i,\sigma}^\dagger \hat{c}_{j,\sigma} + h.c.) + U \sum_i \hat{n}_{i,\uparrow} \hat{n}_{i,\downarrow} + \sum_{i,\sigma} \varepsilon_i \hat{n}_{i,\sigma} \quad (1.3.21)$$

where $\sigma \in \{\uparrow, \downarrow\}$ designates the spin- $\frac{1}{2}$ basis, $\langle i,j \rangle$ signifies that i and j are neighbouring sites, $\hat{c}_{i,\sigma}^\dagger, \hat{c}_{i,\sigma}$ are respectively the creation and annihilation operators at site i and obey the fermionic anti-commutation rule $\{\hat{c}_{i,\sigma}^\dagger, \hat{c}_{j,\sigma'}\} = \delta_{i,j} \delta_{\sigma,\sigma'}$, $\hat{n}_{i,\sigma} = \hat{c}_{i,\sigma}^\dagger \hat{c}_{i,\sigma}$ correspond to the usual number operator for a particle of spin σ at site i and ε_i represents the energy offset at site i usually the slowly (relative to the lattice spacing) varying harmonic envelope created by the Gaussian shaped trapping beams, schematised in Figure 1.14.

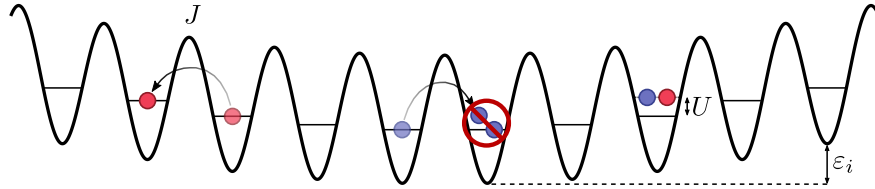


Figure 1.14: Schematic of the four main parameters/principles of the Fermi-Hubbard model in 1D. From left to right: tunneling rate J from one site to a neighbouring adjacent site, due to the Pauli exclusion principle, the occupation of the same site by two particles with identical spin is forbidden, interaction energy U lifts the bare energy occupation of a site when occupied by two particles (necessarily with opposite spin) and ε_i denotes the energy offset from an ideal periodic potential (here showed as a weak harmonic confinement).

The phase diagram of the Fermi-Hubbard model is still very much open for debate but the one at half filling, i.e. $\langle \hat{n}_{i,\uparrow} + \hat{n}_{i,\downarrow} \rangle = 1$, is less subject to controversy. We shall proceed to the qualitative analysis of this phase diagram presented on Figure 1.15 by considering the two main regimes: the attractive part $U < 0$ and the repulsive one $U > 0$. The crucial energies to consider are the ones associated with the temperature T , the on-site interaction energy U and the kinetic energy J , the first two are normalized with respect to the latter in the presented phase diagram.

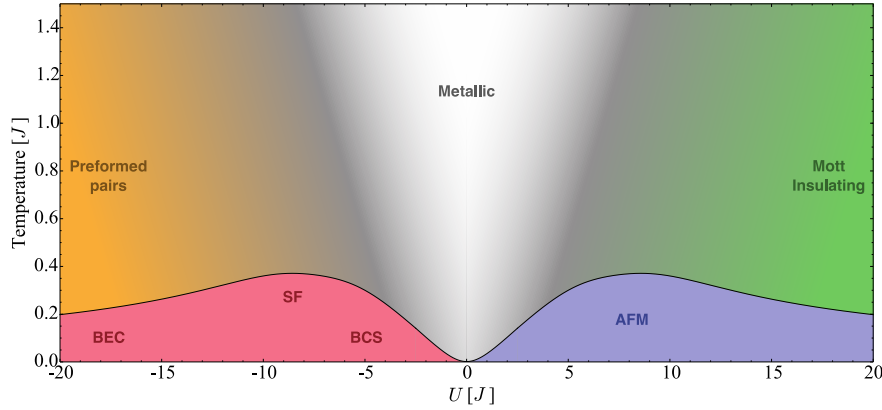


Figure 1.15: Schematic phase diagram of the Fermi-Hubbard model at half filling. BEC, SF, BCS and AFM respectively stand for Bose-Einstein condensation, superfluid, Bardeen-Cooper-Schrieffer and anti-ferromagnetic phase. Inspired from [129, 130]. Boundary of the AFM phase transition composed of the modified Hartree-Fock theory[131, 132] for small U/J and of the Heisenberg limit for high temperature expansion[133] for large U/J according to [134].

There is also an obvious phase at unit filling, $\langle \hat{n}_{i,\uparrow} + \hat{n}_{i,\downarrow} \rangle = 2$, which correspond to two particles per site, naturally with opposite spin called a *band insulator*, 3D modelled on Fig. 1.16, simply because the band is fully occupied. Therefore no degree of movement is allowed, and it would be an insulator if the particles were electrons in a metallic crystal.

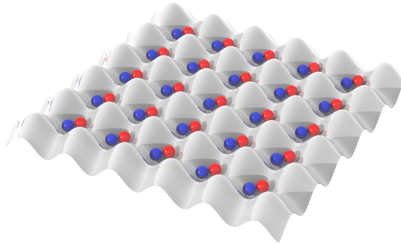


Figure 1.16: 2D band insulator of the Fermi-Hubbard model without external confinement.

Attractive regime at half-filling

The reader should consult Ulrich Schneider's thesis [135] for an extended and in-depth description of interacting fermions in optical lattices. What follows is a concise summary of the main phases at half-filling. What drives the attractive regime physics is the tendency of pairs of fermions with opposite spin to form pairs which can then be considered as bosons. For small attractive on-site interactions, this regime exhibits a transition from a metallic to a BCS phase whose boundary evolves as $|U|/J$. The BCS phase will evolve into a BEC (left of Figure 1.17), through a superfluid state if the interactions are increased. The critical temperature at which the transition from a metal (right of Figure 1.17) or a preformed pairs phase into a BEC occurs decreases as $J^2/|U|$. All the fermions pair and tend to occupy every other lattice site. Indeed the tunneling of pairs operates at a rate proportional to J^2/U characteristic of a second-order process while the repulsion between pairs has the same dependency and is repulsive.

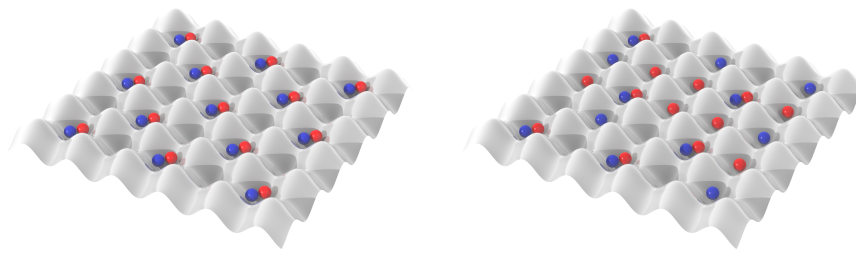


Figure 1.17: BEC of fermionic pairs (left) and metallic (right) phases of the attractive Fermi-Hubbard model at half-filling.

Repulsive regime at half-filling

The repulsive regime is subject to much interest because it might be where, at very low temperature and with some doping from half-filling, d-wave superfluidity could occur. In the metallic phase, the on-site interaction between the particles is low and they tend to be mostly delocalised across the lattice with freedom of movement. Increasing the interaction will localise the particles on every lattice site in a *Mott insulator* phase not exhibiting any particular spin ordering, internal degree of freedom which now contains all the entropy of the system. In the temperature is decrease below the Néel temperature, the particles start to interact via super-exchange interaction; second order process in which a particle virtually hops on a neighbouring site, interacts and hops back to its site at a rate $4J^2/U$ to achieve alternative spin ordering driving by Heisenberg spin Hamiltonian $H = \frac{4J^2}{U} \sum_{\langle i,j \rangle} S_i S_j$ characteristic of an *anti-ferromagnetic* phase. Both phases are schematised and rendered on Figure 1.18.

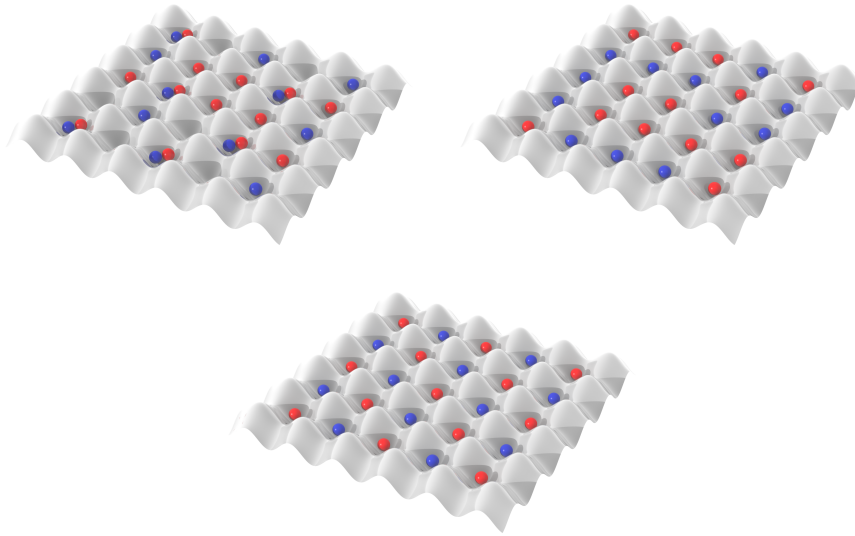


Figure 1.18: Metallic (top left), Mott insulating (top right) and anti-ferromagnetic (bottom) phases of the repulsive Fermi-Hubbard model at half-filling.

Chapter 2

Experimental setup

2.1 Vacuum chamber

2.1.1 Overview

Our vacuum chamber consists of two main sections, as shown in Figures 2.1 and 2.2. The 2D-MOT section includes the rubidium and potassium ovens, the titanium vacuum chamber and a differential pumping tube. This section is connected to the other vacuum chamber, the Science section, through a manual valve which can be closed in order to fully seal one section from the other.

The rubidium and potassium ovens respectively contain ^{87}Rb and a 200 mg ampoule of 5% enriched ^{40}K and are heated to temperatures of 50°C and 120°C . The temperature of the potassium oven exceeds the melting point of potassium so opening the oven to the 2D-MOT section lets atoms effuse such that they coat its walls. This guarantees a high pressure of roughly 6×10^{-7} mbar for a duration of a couple of months while it is constantly being pumped by a $8 \text{ L}\cdot\text{s}^{-1}$ ion pump¹.

This pressure would be too high to perform most of atomic physics experiments so the 2D-MOT section is separated from the Science section by a differential pumping tube ($\varnothing 1\text{mm} \times 55 \text{ mm}$). The Science section is maintained at a pressure lower than 10^{-11} mbar by a $55 \text{ L}\cdot\text{s}^{-1}$ ion pump², a titanium sublimator³ and a Zr-V-Fe getter⁴.

The Science section is divided into the 3D-MOT chamber and the Lattice (Science) chamber which are separated by 15 cm. The atoms are captured in a 3D-MOT from a 2D-MOT after being pushed by a push beam through the differential pumping tube and later on transported by moving the focus of an optical dipole trap from the 3D-MOT to the lattice chamber.

¹8l/s Vaclon, *Agilent Technologies*

²Vaclon Plus 55, *Agilent Technologies*

³SBST22, *VG Scienta*

⁴Capacitor[®]-D 400-2, *SAES[®] Getters*

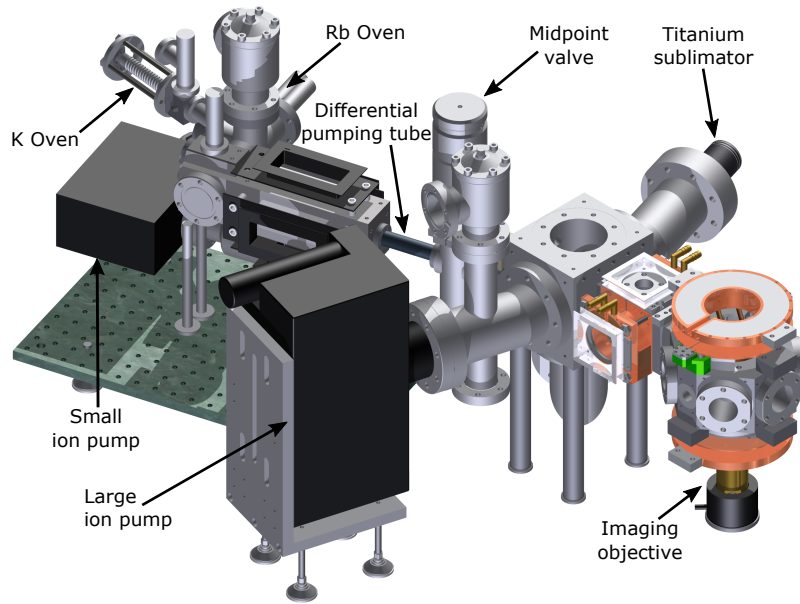


Figure 2.1: Vacuum chamber isometric view.

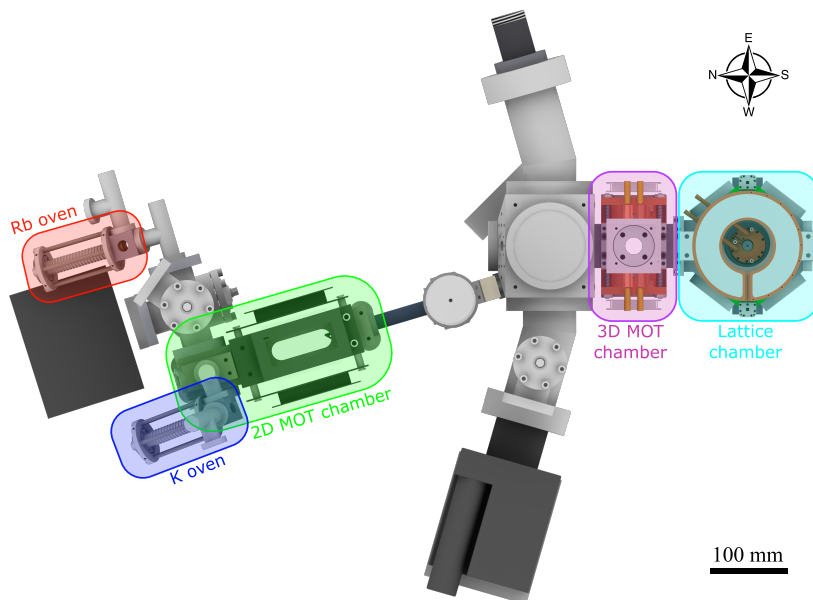


Figure 2.2: Vacuum chamber top-down view.

2.2 Resonant lasers

2.2.1 D_2 setup

Our MOTs use near-resonant light on the D_2 line ($4S_{1/2} \rightarrow 4P_{3/2}$ transition at 767 nm). Each MOT requires cooling and repumper radiations which are all generated by three TOPTICA TA PROs offset locked to a reference generated by a TOPTICA DL PRO locked using saturated absorption spectroscopy of ^{39}K . Figure 2.3 is a schematic overview of how the D_2 laser beams are generated, intensity controlled and frequency shifted using acousto-optic modulators⁵ (AOMs).

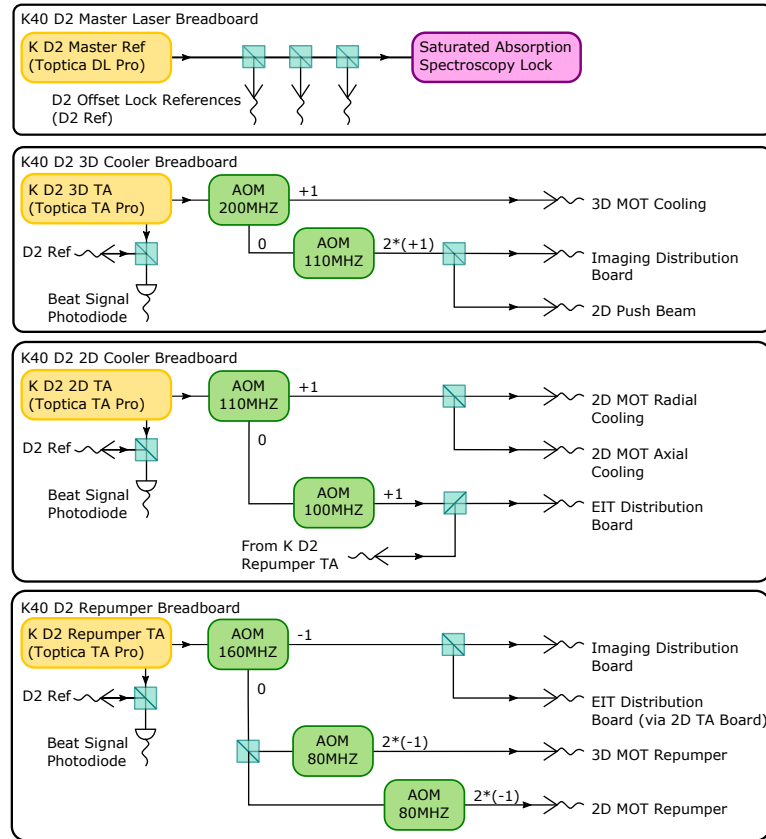


Figure 2.3: Overview of the ^{40}K D_2 beam generation.

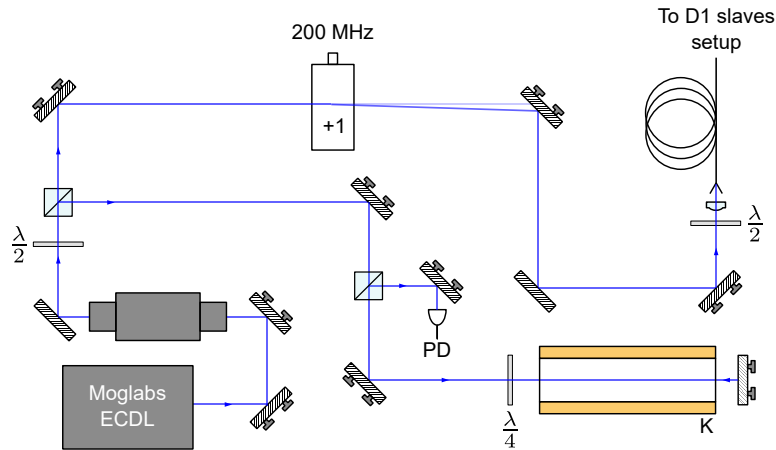


Figure 2.4: D_1 master laser setup. The optical components legend is located in Appendix E.0.1.

2.2.2 D_1 laser

2.2.2.1 Master laser

The light near resonant to the D_1 transition @ 770 nm is also obtained by offset locking two homebuilt ECDLs (External Cavity Diode Lasers) [136] to a master laser locked on a saturated absorption reference. The D_1 reference light is generated by a GaAs semiconductor laser diode⁶ placed in a MOGLabs ECDL module⁷. Some of the laser beam power ($< 1\text{mW}$) is used for the spectroscopy while the rest passes through an AOM, permanently shifting its frequency by 200 MHz, and then is sent through a fibre to the D_1 cooler and repumper slave lasers where it is superimposed with each lasers to obtain a beat signal used to generate the offset lock error signals.

A 720 kHz bandwidth photodiode⁸ receives the saturated absorption light and relays the signal to the MOGLabs laser driver⁹ which on top of driving the laser diode also performs its temperature stabilisation, current dithering and subsequent locking. The lock provided by the MOGLabs laser driver has a jitter of about 6 MHz which is roughly equal to Γ . Schematics of the optical setup and obtained signals respectively displayed as Figures 2.4 and 2.5.

⁵3080-xxx and 3110-xxx series, *Gooch&Housego* formerly *Crystal Technology Inc.*

⁶EYP-RWE-0780-02000-1300-SOT12-0000, *Eagleyard Photonics*

⁷ECD004, *MOGLabs*

⁸PDD0001, *MOGLabs*

⁹DLC202, *MOGLabs*

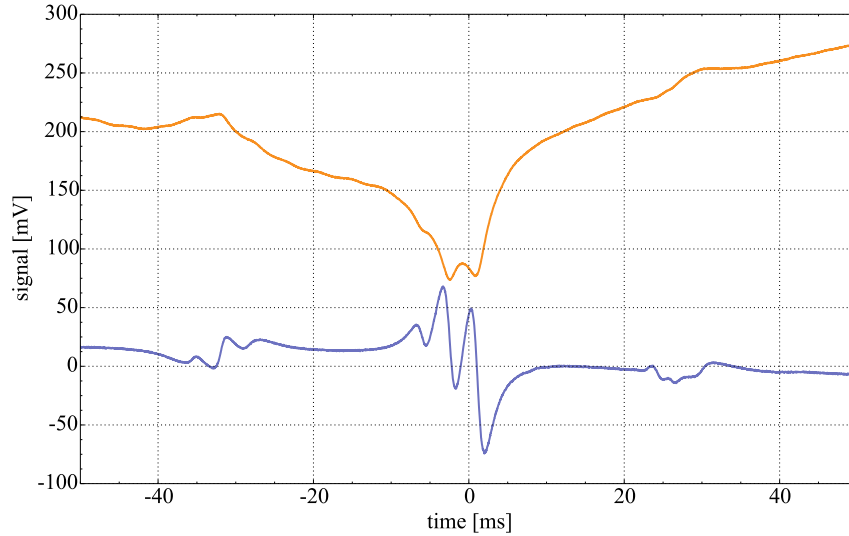


Figure 2.5: Doppler free spectrum (orange) of the D_1 transition of ^{39}K and the derived error signal (blue). The left (right) series of three transitions correspond to the $F=2(1) \rightarrow F'$ transitions with their inner crossover, separated by 462 MHz. The middle feature contains the $2,1 \rightarrow 1$ and 2 crossovers with their crossover $2,1 \rightarrow 1,2$ in between. Our lock is set onto the $2,1 \rightarrow 2$ feature which is only located 46 MHz below the D_1 line of ^{40}K .

2.2.2.2 Slaves and distribution

Light from the master laser is sent through an optical fibre to each of the cooler and repumper lasers and a beat signal is created on a fast photodiode silicon amplified photodetector¹⁰ as schematised in Figures 2.6. The beat signal is then amplified and sent to a frequency-to-voltage (F-V) converter with voltage controlled offset. In this homemade device built by the electronics workshop, the photodiode signal is set to a F-V converter that generates a signal with a slope of 50 MHz/V onto which an analog controlled offset voltage is added to shift the zero-crossing used as the input error signal for the slaves laser drivers. The phase can also be tuned (side of the error signal on which to lock) to obtain slave lasers locking capabilities in the $\pm[100..900]$ MHz ranges away from the reference radiation. For more details on the ^{39}K reference light frequency and offset frequencies to address the ^{40}K D_1 cooler and repumper transitions, the reader should consult Nicolas Sangouard's master thesis [137].

The EIT cooling, which theory is dealt with in Section 3.3.3, is required in all three spatial directions. The purpose of the EIT/Molasses board, Figure 2.7, is to split the light into three distinct paths, each one controlled independently by its own AOM and mechanical shutter. Each one of those paths is sent to the experimental apparatus where it is superimposed with each of the optical lattices.

¹⁰ET-2030A, *Electro-optics Technologies Inc.*

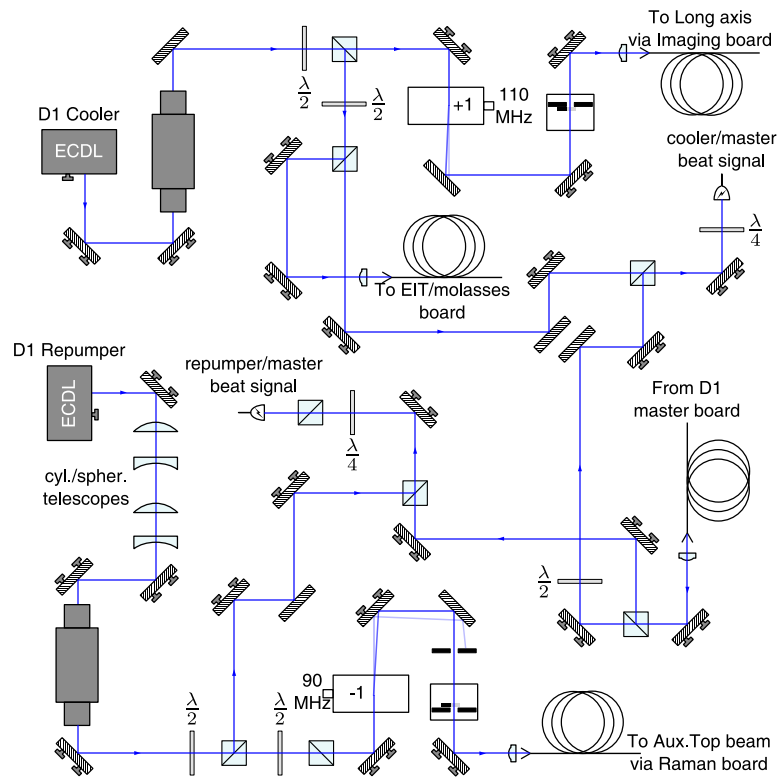
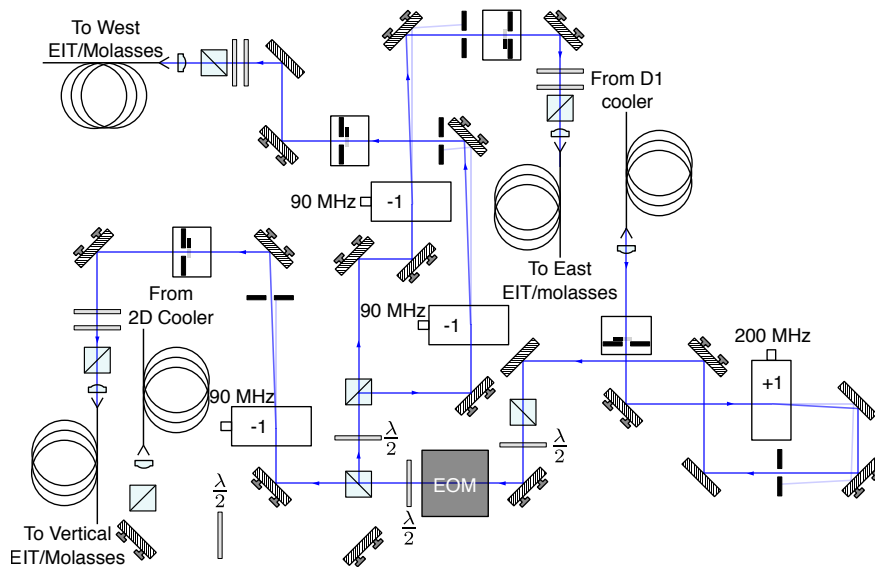
Figure 2.6: D_1 cooler and repumper (slaves) lasers setup.

Figure 2.7: EIT/Molasses distribution board setup.

An EOM¹¹, driven at the frequency of the hyperfine splitting ΔE_{hfs} , creates sidebands of the radiation in order to have identical phase and frequency fluctuations between the cooler light and said sideband ($\pm\Delta E_{\text{hfs}}$ away), one of them acting as a weak repumper necessary for EIT cooling.

Figure 2.8 serves as overview of all D_1 radiations used on the apparatus.

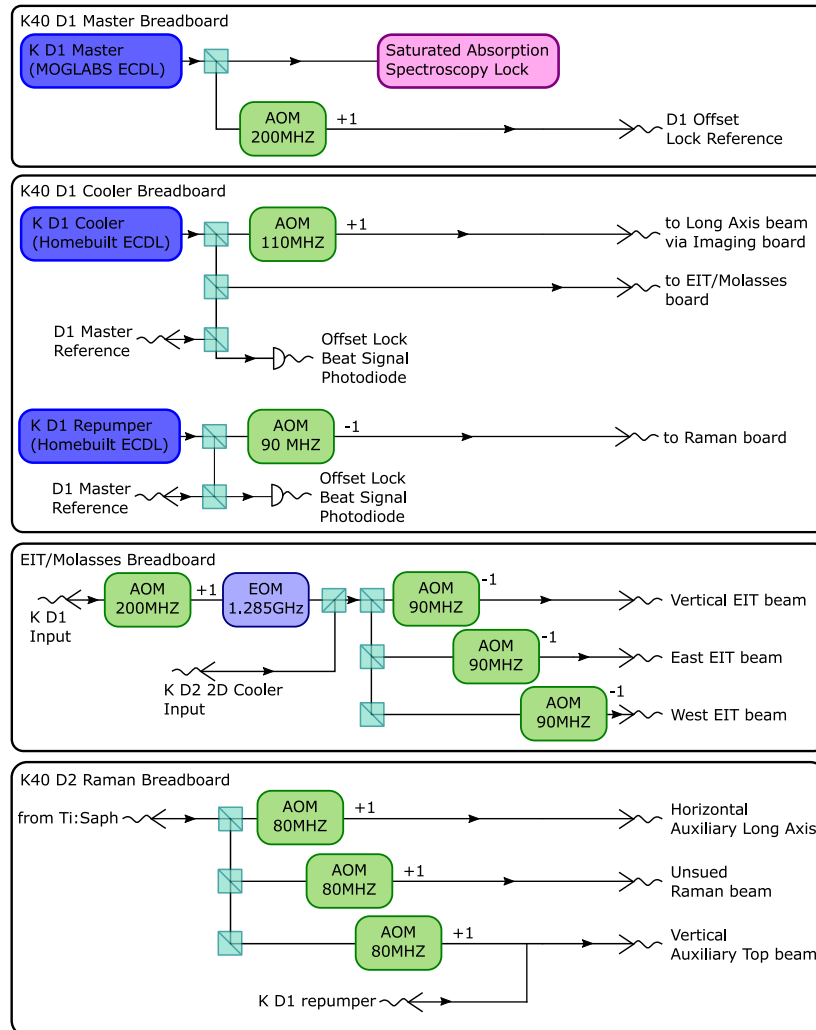


Figure 2.8: D_1 lasers overview.

¹¹EO-K40-3M, Qubig GmbH

2.2.3 Titanium-Sapphire laser

2.2.3.1 Setup

The light driving the Raman transitions at 767 nm is generated in a CW Titanium-Sapphire bow-tie cavity laser¹² pumped by 6.5 W of 532 nm light produced by a diode-pumped solid state laser¹³.

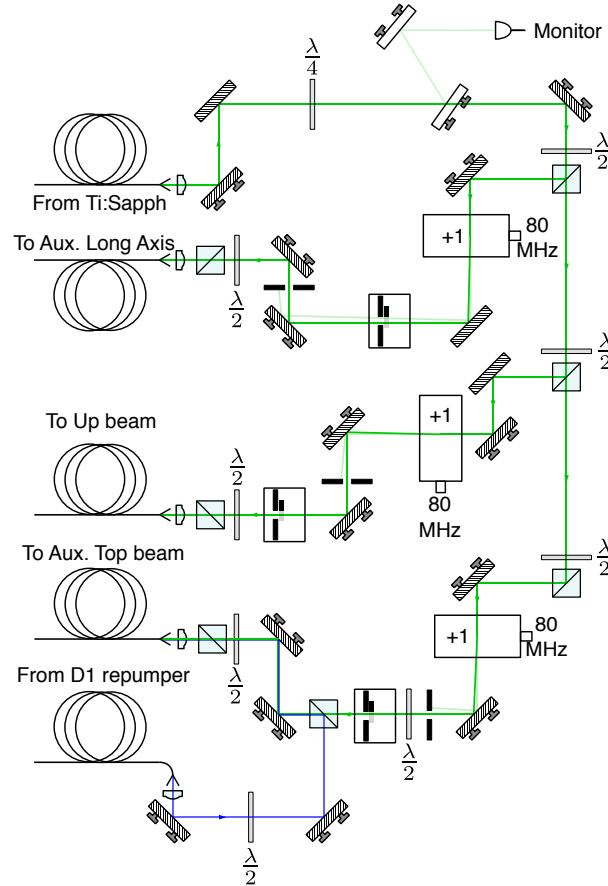


Figure 2.9: Raman distribution setup.

This laser is located in a room distant from our experimental apparatus and the light needs to be sent there through a 50 m long fibre that feeds our Raman distribution setup as depicted in Figure 2.9. Upon arrival, the light is then split into three paths, two of those being the Auxiliary Long Axis, an horizontal beam hitting the lattice chamber centre at a slight angle from the Long axis and the Auxiliary Top beam which combines with the Vertical EIT/Molasses beam on the Lattice Chamber Vertical axis, see Figure 2.10.

¹²MBR-110, *Coherent Inc.*

¹³Verdi V8 (8 Watts), *Coherent Inc.*

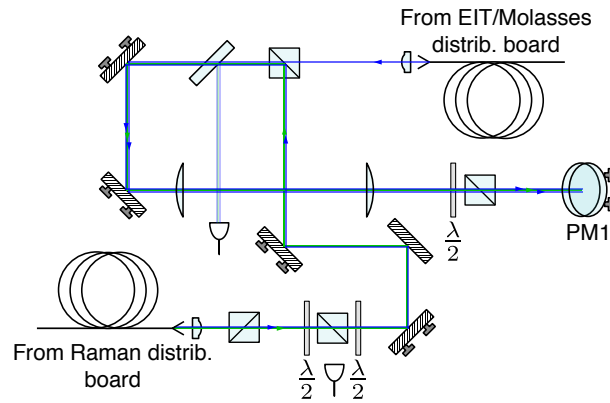


Figure 2.10: Optical setup for the vertical resonant beams. The EIT/Molasses beam is combined with the Auxiliary Top beam carrying Raman and D_1 Repumper radiations prior to being itself combined with the Vertical lattice beam on a dichroic mirror to reach the lattice chamber centre. See Figure 2.16. where the beam path is continued and where the first periscope mirror (PM1) is represented too.

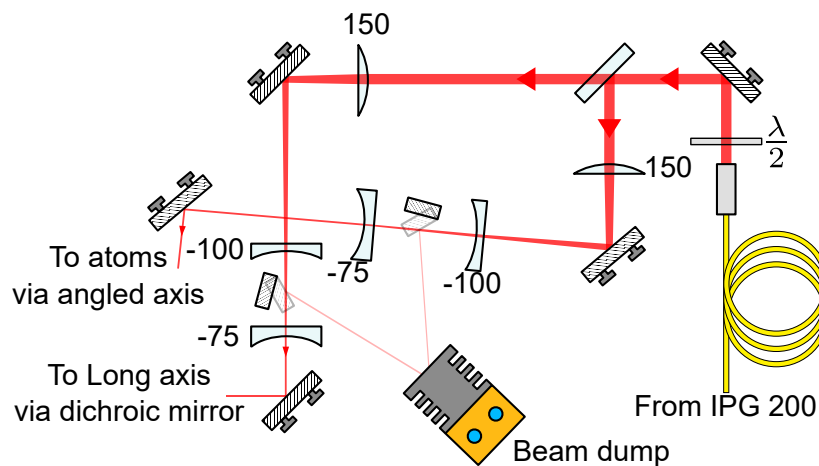


Figure 2.11: IPG 200 setup for MOT CODT.

2.3 Trapping lasers

2.3.1 MOT CODT

To increase the phase-space density after the 3D MOT phase, a crossed optical dipole trap (CODT) is employed. A diode pumped spatially single-mode Ytterbium fibre laser¹⁴ called the "IPG200", capable of delivering up to 200 Watts of linearly polarised 1064nm light with almost purely gaussian profile, has its output split into two beams of equal power (100 W) as depicted on Figure 2.11.

Those two beams, focused down to 300 μm , cross at the centre of the 3D MOT chamber at an angle of 16.3° . The last lens (-75 mm effective focal length (EFL)) on the path is placed at the focal image location on the first one (150 mm EFL), a mobile lens (100 mm EFL) placed [50..56] mm away from the last allows for the output beam waist radius to take its values in the [119..466] μm range while the focus moves longitudinally by about 250 mm. The exact theoretical lenses locations to obtain a 300 μm waist are

lens EFL (mm)	150	-100	-75	300 μm focus
axial location (mm)	0	95.4	150	500

After placing a beam profiler on a diverted path outside the vacuum chamber at a distance roughly equal to the 3D MOT chamber center location, the -100 mm lens was carefully translated along its cage system to obtain a 300 μm waist. Because the Rayleigh range at this wavelength and for this waist equals 260 mm, fine adjustment of the focus axial position on the atoms is unnecessary. The beam aligned with the Long axis is combined with one of the 3D MOT beam using a dichroic mirror while the other is sent directly to the atoms.

2.3.2 Transport

In this section is introduced for the first time the usage of the single-mode, polarisation maintaining (PM) photonic crystal fibres¹⁵. The description of the optical setup feeding the transport and vertical lattice beam will be accompanied by the particular protocols needed to aligned and operate such fibres.

2.3.2.1 Mephisto Multipass Optical Parametric Amplifier (MOPA)

Our transport and vertical lattice beams are both derived from an ultra-narrow linewidth high power laser at 1064 nm wavelength¹⁶ with an output power of 55 Watts. This laser

¹⁴YLR-200-LP-WC-Y11, *IPG Photonics Corp.*

¹⁵LMA-PM-15, *NKT Photonics Inc.*

¹⁶Mephisto MOPA, *Coherent Inc.* previously *Innolight GmbH*

consists of an oscillator amplified by four Nd:Yag crystals pumped by fibre-coupled laser diodes pump modules. Beside its narrow linewidth, tunable over 30 GHz, it exhibits a very low relative intensity noise of less than -130 dBc per Hz.

The MOPA output is isolated by a -39 dB optical isolator¹⁷ before being sent by a periscope to an upper board. The beam profile is dependent on the output power so two high power optically contacted polarising beam splitter (PBS) cubes are placed to allow the user to reduce the power in the beam to workable condition for alignments while having the same beam profile as for high powers, see Figure 2.12.

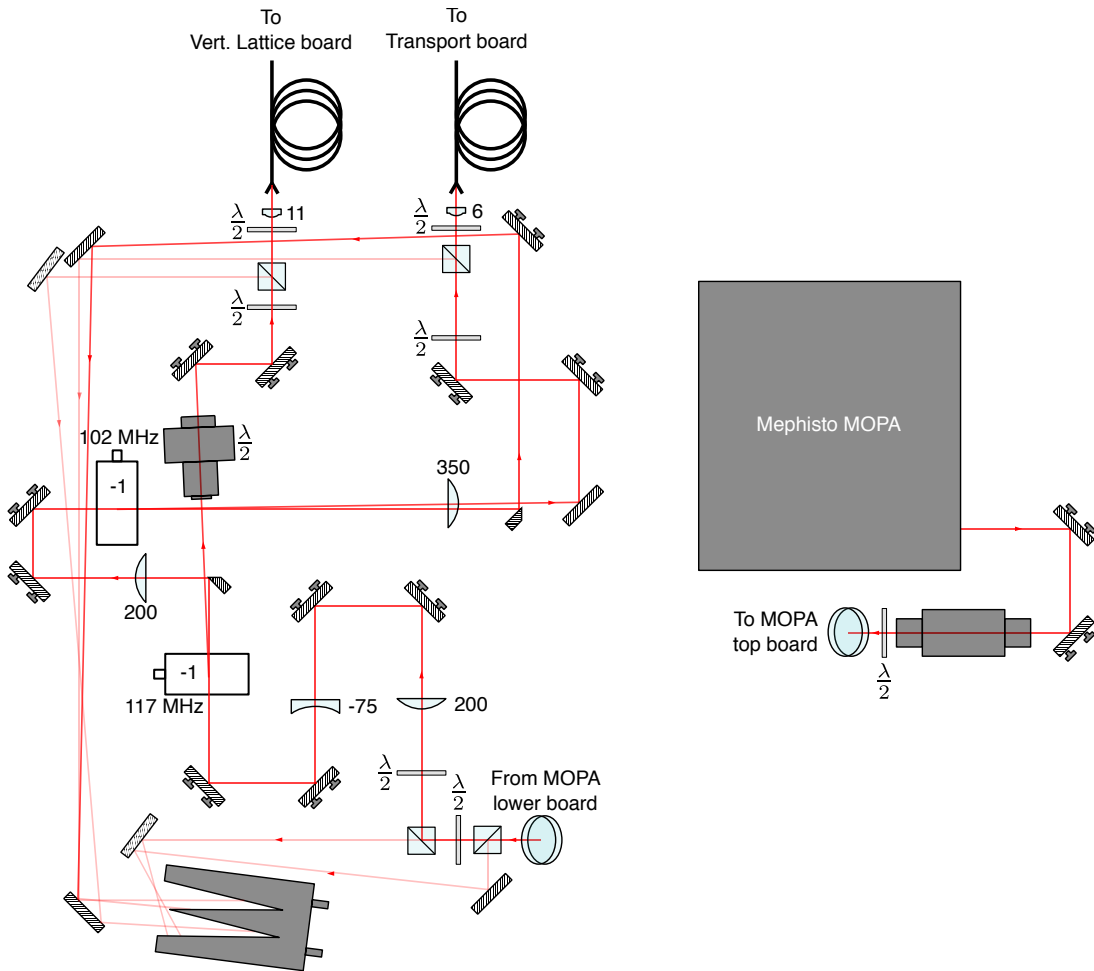


Figure 2.12: Mephisto MOPA two stages setup.

After the PBS, the beam is reduced by a 8:3 telescope¹⁸ to be small enough (300 μm) to pass through an AOM¹⁹. The -1st order of this AOM, driven at 117 MHz,

¹⁷IO-5-1064-VHP, Thorlabs, Inc.

¹⁸200 mm and -75 mm V-coated lenses

¹⁹3110-197, Gooch&Housego

goes through a motorised mounted²⁰ half-wave plate and a PBS cube to adjust power and then through another half-wave plate before being coupled by a 11mm V-coated aspheric lens into a high power fibre feeding the vertical lattice beam.

The 0th order of the AOM is diverted to another AOM driven at 102 MHz of the same type. Before entering the AOM, a 200mm EFL lens refocuses the beam to obtain a similar size as when it went through the first AOM. The fibre leading to the Transport board is more than two Rayleigh ranges away from the focus so a 350 mm EFL lens collimates the beam to a waist of about 500 μm .

10% of the light power is being lost through the optical isolator and with the AOMs and fibre coupling efficiencies being respectively about 80% and 75%, the power transmitted through the fibres to each of the transport and vertical lattice boards is 25 W.

2.3.2.2 High-power fibre coupling

When fibre coupling powers above 20 W, one has to meet a series of condition to obtain a stable transmitted power. Those are:

- Achieve high AOM diffraction efficiency ($> 80\%$) at high powers and have a beam waist small enough to avoid clipping on the AOM aperture entrance. Clipping will degrade the Gaussian beam profile necessary to obtain high fibre coupling efficiency. This is even valid at low powers but the extra optical heating of the crystal amplifies the Gaussian profile degradation at high powers.
- Achieve high fibre coupling efficiency ($> 70\%$) at low and high powers. The uncoupled power only heats the surroundings of the fibre tip and thermal effects will further degrade the efficiency, though without necessarily causing permanent damages.
- The polarisation of the light going through an AOM has to match the one recommended by the manufacturer. The effect of a mismatch can be negligible at low powers but is really not at high ones. (Notice the half-wave plate before the 8:3 telescope to optimise the linear polarisation of the light to keep a good AOM diffraction efficiency for durations superior to 0.5 s)
- Aligning the input light linear polarisation to the axis of the high-power polarisation maintaining fibre.

²⁰8MRU-1, *Standa*

Polarisation "walking" of the high power fibres

The polarisation maintaining low power fibres from Thorlabs used for resonant light have their axis aligned with the notch of the fibre connector. The high power fibres were terminated without any special orientation so extra half-wave plates (HWP1&2 on Fig. 2.13) are used on both ends of those fibres to "walk" the polarisation of the beam and match it with the polarisation maintaining (PM) axis. The walking procedure consists in placing a photodiode (PD in Fig. 2.13) in reflection of the PBS cube placed at the end of the fibre. The two half-wave plates are then "walked" to find the global minimum of the light power deflected by the receiving PBS cube. Not finding such axis will result in a fast rotation of the polarisation of the light at the output of the fibre translated into power fluctuations of the beam after it passes through the first PBS cube.

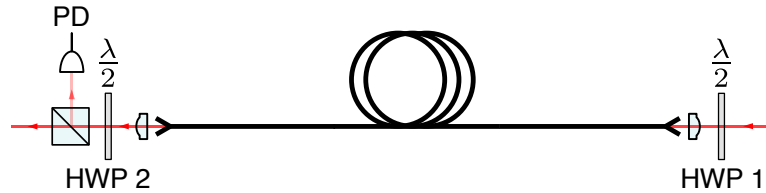


Figure 2.13: Schematic for finding the PM axis of a high power fibre.

High power fibre coupling optimisation

To couple our high power fibres, the AOM drivers are switched to pulse mode with 1:1000 on-off ratio. This way high optical powers can go through the AOM crystal, optically heating it as it would in continuous RF operation, whereas the pulse mode allows the fibre to safely remain cold. Using a triggered oscilloscope, the transmitted light pulse powers are measured and compared to a photodiode calibrated at low continuous optical power. If the fibre coupling reaches acceptable efficiencies ($> 70\%$), continuous AOM driving could be switched on. Exposing the fibre to powers exceeding 10 Watts over more than 5 seconds should be avoided as it may still cause small permanent damages to the fibre tip and reduce significantly the lifetime of a fibre.

When those conditions are met, unfluctuated power up to 25 Watts can be transported through the fibres for over 3 seconds. Because the fibre are aligned cold, an initial fast (< 100 ms) drop of about 5-8% can not be prevented and correspond to a loss in fibre coupling efficiency due to heating.

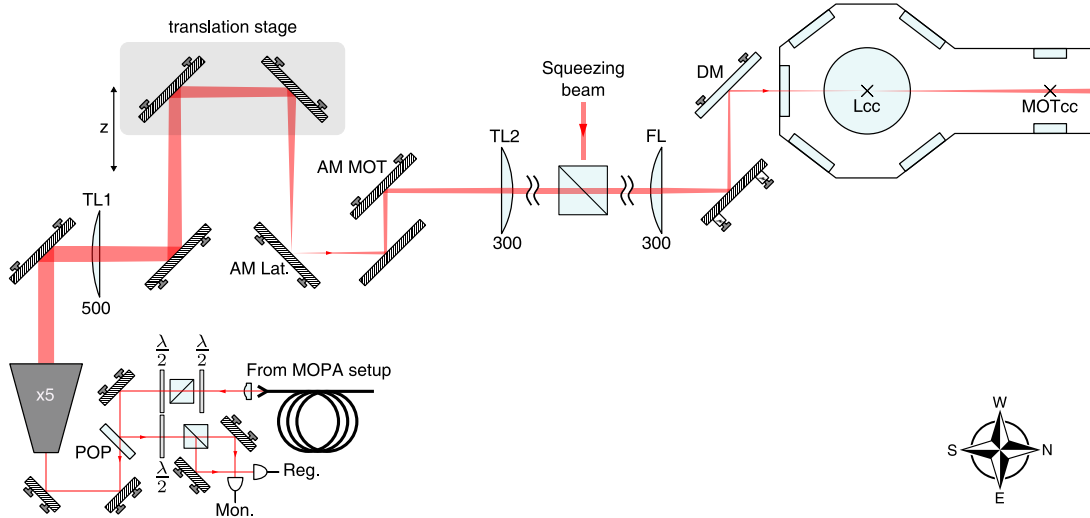


Figure 2.14: Optical transport setup.

2.3.2.3 Transport

The output of the high power fibre coming from the Mephisto board gets collimated by a 6.24mm aspheric lens before a small fraction of the beam is picked-off by a AR plate which serves for monitoring and intensity regulation. The beam is expanded by a factor of 5 by a beam expander²¹ and subsequently goes through a set of three lenses (500 , 300, 300 mm EFL respectively "TL1", "TL2" and "FL" on Fig. 2.14). The first two are spaced by 800 mm making it a 5:3 telescope while the last 300 mm EFL lens is located 300 mm away from the Lattice chamber center and focuses the collimated beam coming out the 5:3 telescope to a waist of 50 μm .

Between the two lenses of the 5:3 telescope the beam travels to a board mounted on a linear servo-motorized translation stage²². When the translation stage is set so that the focus of the beam in the vacuum chamber is located at the Lattice chamber center, the focus inside the 5:3 telescope created by the 500 mm lens resides on the first("AM Lat." in Fig. 2.14) of the two 2 inches alignment kinematic mirrors (the other mirror being "AM MOT" in Fig. 2.14) placed inside the telescope. The "AM Lat." mirror is 300 mm away from the 300 mm lens so the beam gets out of the telescope collimated and the last 300 mm lens reproduces the in-telescope focus at the Lattice chamber center. By shortening the in-telescope optical path by 150 mm using the translation stage, the in-telescope focus is moved onto "AM MOT". The beam goes out of the telescope diverging and the focusing 300 mm lens focuses it further away in the vacuum chamber at the MOT chamber centre.

²¹G038675911, *Qioptiq* formerly *LINOS*

²²DDS200/M, *Thorlabs Inc.*

2.3.3 Vertical lattice

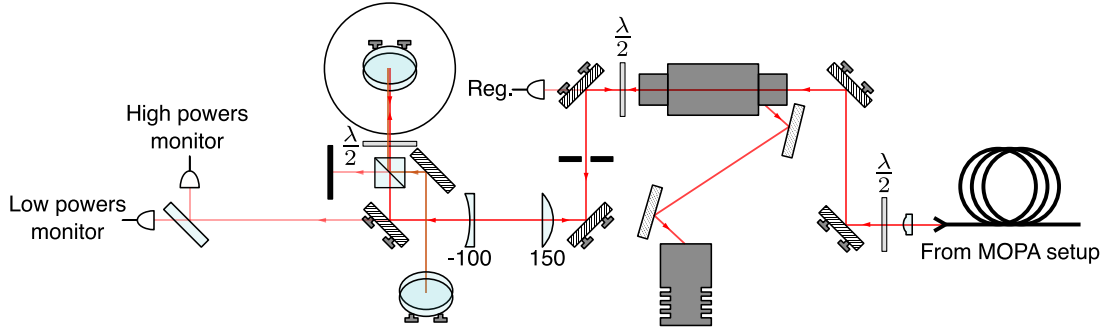


Figure 2.15: Vertical lattice setup.

The vertical lattice beam starts on a breadboard which sits about 30 cm on top of the lattice chamber centre and is schematised on Figure 2.15. The output of the high power fibre coming from the Mephisto MOPA breadboard is collimated by a 11 mm aspheric lens into a 1 mm waist beam. It goes through an optical isolator and an adjustable iris which is fully opened in normal operation. The beam waist is reduced by a 3:2 telescope before going through a polarisation cleaning cube and a half-wave plate. This plate sets the final polarisation of the beam as it will be experienced by the atoms. A dichroic mirror inclined at an angle of 45° with respect to the horizontal plane directs the beam directly toward a 10 mm EFL lens sitting in a long cage plate system hanging from the vertical lattice board by two fine precision micrometer screws as sketched in Figure 2.16. The lens height is carefully adjusted so that its imaging plane merges with the bottom vacuum window coated to be fully reflective at 1064 nm. The waist of the focus created on the bottom window is about $105 \mu\text{m}$. The retro-reflected beam follows its incoming path, creating a lattice, until it reaches the optical isolator which deflects it to a beam dump.

If the optical isolator is adjusted to deflect more than 80% of the incoming light, the iris can be used at low optical power to align the retro-reflected beam more precisely. First the iris is set to clip the incoming beam symmetrically, afterwards the camera is moved to the other side of the iris to monitor how the retro-reflected beam hits it. By progressively reducing the iris and correcting the alignment, one can almost reach interferometric precision.

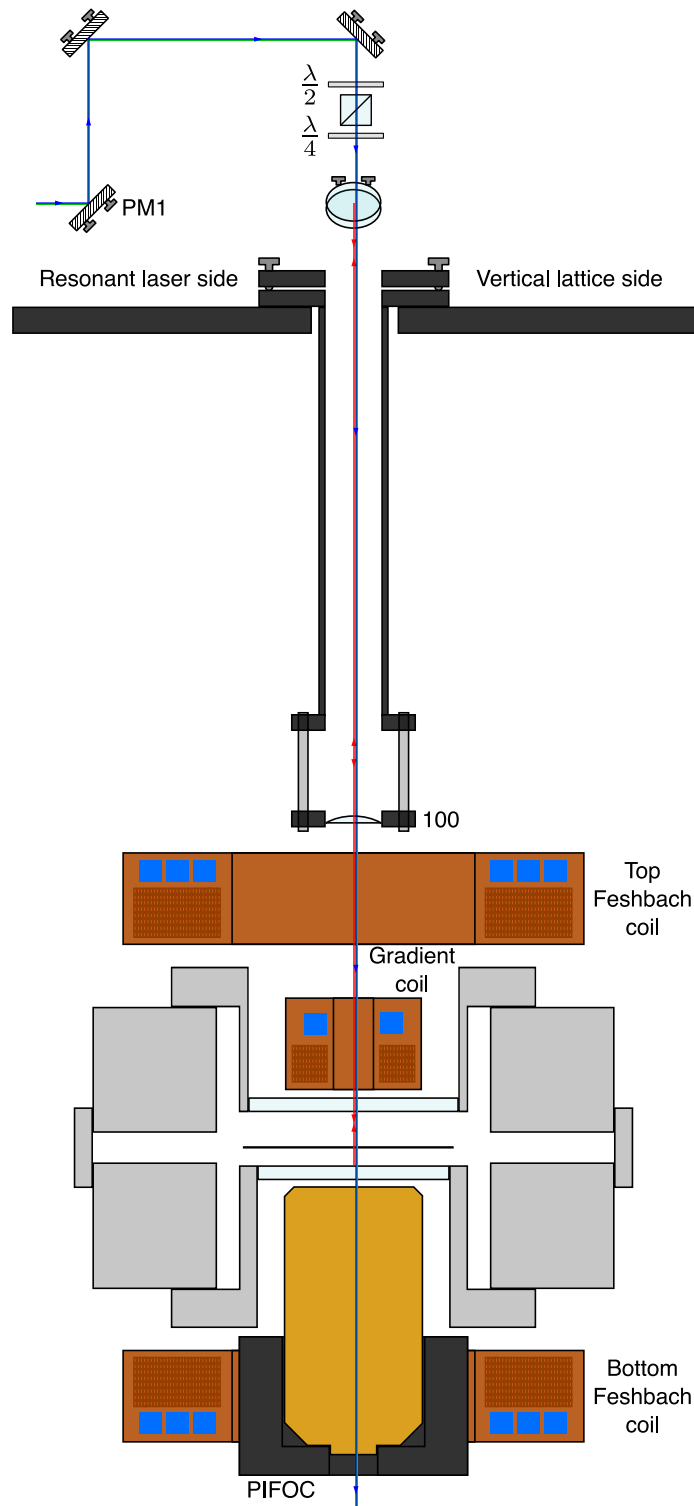


Figure 2.16: Vertical cutaway of the vertical lattice and vertical resonant beams to the lattice chamber.

2.3.3.1 Modulation spectroscopy of trap frequencies

Once the mechanical alignment has been performed, the waist of lattice beam experienced by the atoms needs to be measured which can be done using modulation spectroscopy. A signal generator²³ connected to our regulation circuit via a bias-tee²⁴ is employed to add a relatively small fraction of sinusoidal oscillation to a constant optical power in the beam. As mentioned in Section 1.2.1, the parity of this parametric excitation determines what kind of transitions is driven in a quantum harmonic trap. Because amplitude modulation is symmetric, only the $|n\rangle \rightarrow |n+2\rangle$ transitions are triggered where n denotes the vibrational level in the trap.

The spectroscopy signal is detected by monitoring the width of the atomic cloud after a fixed time-of-flight (TOF) expansion duration. The higher the average vibrational level occupation, the wider the atomic cloud expands. A non-ideal lattice (as they all are) will experienced excitations at the lattice frequency ($|n\rangle \rightarrow |n+1\rangle$) and also at the allowed first harmonics of a symmetric parametric excitation ($|n\rangle \rightarrow |n+2k\rangle$), $k \in \mathbb{N}^* \cap k > 1$) leading to heating of the cloud at frequencies of $\nu_{lat,long}$ and $2k.\nu_{lat,long}$ ($k \in \mathbb{N}^* \cap k > 1$). Even if those signals are significantly weaker (1/4) than the one at $2.\nu_{lat,long}$, the careful experimentalist shall check at half and twice the frequency of a detected excitation to make sure that it is indeed the predominant one occurring at $2.\nu_{lat,long}$.

The results of the vertical lattice waist measurement are given in Figure 2.17. It relies on our knowledge of the lattice contrast which in the case of the vertical lattice must be close to one. Indeed the atoms lie about 4 mm above the retro-mirror (bottom window of the Lattice chamber) so at waists of about 100 μm , the Rayleigh range being on the order of 30 mm, the retro-beam geometric shape must be quite similar. There is also no optical components between the incoming beam and its retro-reflection and the specifications of the coating reads 99.7% reflected power for an AOI of 0° . When a lattice contrast is less trivial to guess, sloshing or breathing spectroscopy measurements should be performed on an optical dipole trap (ODT) beam instead of using a lattice configuration which was done for the horizontal ODT/lattice beams.

2.3.4 Horizontal lattices

2.3.4.1 Seeding of the fibre amplifiers

Each of our two horizontal ODT/lattice beams is generated by a Nufern[®] polarisation maintaining fibre amplifier²⁵ specially designed to deliver up to 50 Watts when provided

²³Marconi 2025, *Aeroflex Inc.*

²⁴ZX85-12G+, *Mini-Circuits*[®]

²⁵NUA-1064-PD-0050-D0, *Nufern Inc.*

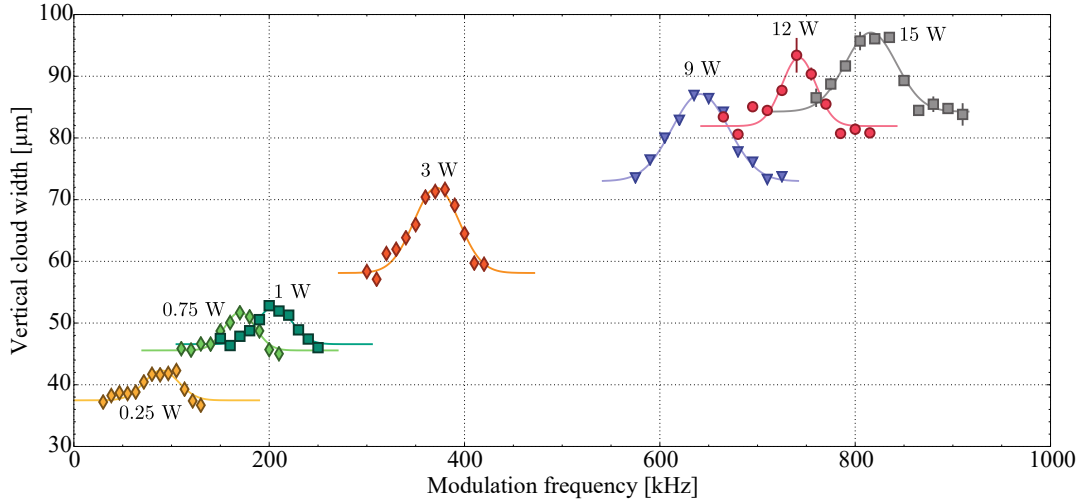


Figure 2.17: Atomic cloud vertical size after TOF expansion versus modulation frequency for the following powers: 0.25 W (yellow diamonds), 0.75 W (green diamonds), 1 W (green squares), 3 W (orange diamonds), 9 W (blue triangles), 12 W (red circles), 15 W (gray squares). From a Gaussian fit we determine the corresponding lattice axial frequencies to be (in increasing power order): 45(1), 85.1(7), 102.6(7), 185.7(7), 320.8(7), 371(1) and 408(1) kHz. Note that those are halved of the fitted Gaussian centres because the measured excitation occurs at twice the lattice frequency for an amplitude (symmetric) modulation. The fit of the frequencies versus power relation yields a vertical lattice waist of 104.9(7) μm .

with 50 - 200 mW of ultra-narrow linewidth 1064 nm seed radiation carried over PM fibres from a 0.5 Watt ultra-narrow Mephisto²⁶ laser identical to the one amplified in the Mephisto MOPA.

As depicted in Figure 2.18 the output of the Mephisto is passed through an optical isolator and is split into two paths which are coupled into fibre carrying the light to the Nufern amplifiers. An extra fibre has recently been inserted to make good use of the outstanding spectral properties of the Mephisto light to also seed fibre amplifiers on another experimental apparatus.

2.3.4.2 Regulation setups

In order to increase the lifespan of Nufern amplifiers, we run their pump current at 38 Amps which reduce their optical power output to 45 Watts. For historical reasons the West and East lattice regulation boards are slightly different in terms of their optical components but yield the same results. On both boards, the beam is collimated by a 20 mm EFL aspheric condenser lens²⁷, isolated and passed through an AOM before

²⁶Mephisto, *Coherent Inc.*

²⁷ACL2520U-B, *Thorlabs Inc.*

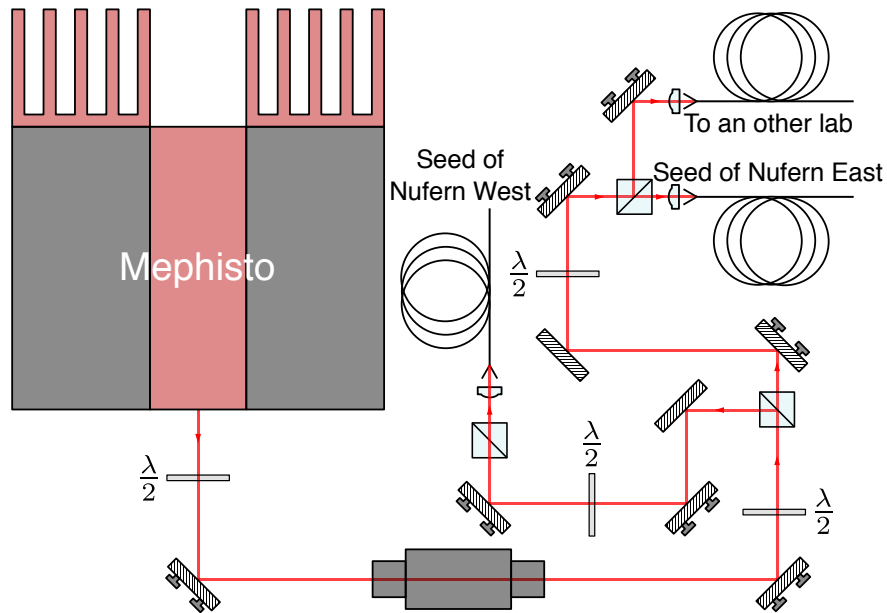


Figure 2.18: Mephisto setup for seeding the Nufern amplifiers.

being coupled to a high power optical fibre similarly to the other high power regulation setups as seen on Figure 2.19.

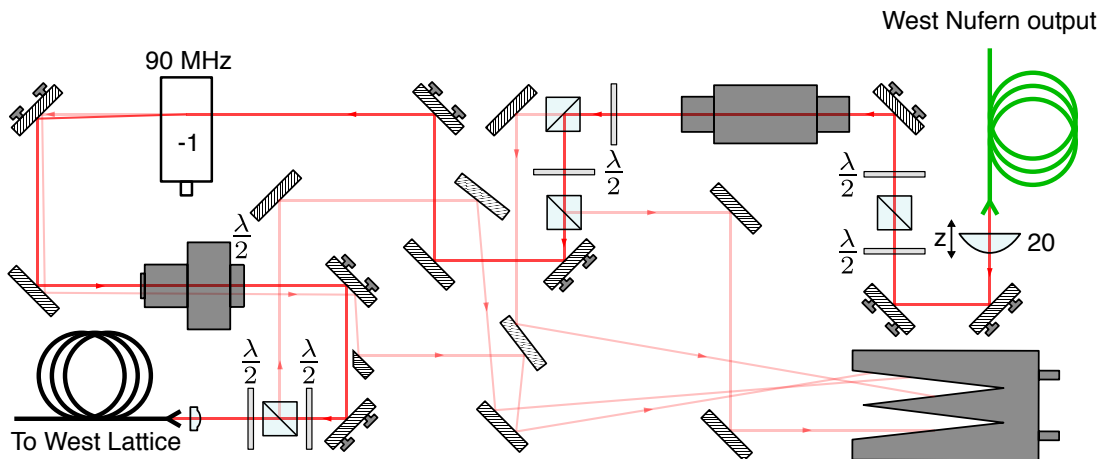


Figure 2.19: West lattice beam regulation setup.

Fibre coupling efficiencies were good or acceptable at low to medium optical powers (1 - 20 Watts) but decreased quickly to 40-50% for high powers (28 - 35 Watts). The beam was diverted and dumped before it could reach the fibre and pictures of its transverse profile at different beam powers (diode pump current) were acquired using a beam profiler²⁸ on a lower power mirror leakage. This method guarantees that the

²⁸CinCam CMOS-1201, CINOGY Technologies GmbH

observed profile is the closest (in term of fidelity) to one of the high power beams under investigation. The non-normalized beam profile pictures are shown in Figure 2.20 and reveal a clear deviation from Gaussian shape at high pump currents, inevitably leading to a reduction in fibre efficiency in those regime. This issue was fixed by placing the collimation lens on an axial rotation-free high-precision translation mount²⁹.

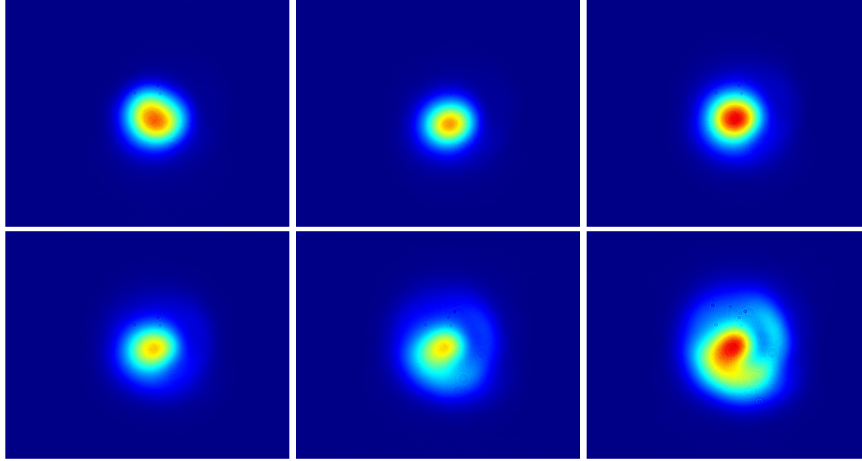


Figure 2.20: Beam profiles prior to fibre coupling for increasing Nufern output optical powers (2, 8, 18, 28, 34, 41 W) from left to right, top to bottom corresponding to pump diodes seed currents (5, 15, 25, 30, 35, 38 A). At low optical powers (top row - 5,15,25 A) the beam profile is close to be Gaussian but thermal effects, mainly in the optical isolator and the AOM, induce aberrations visible for higher optical power (bottom row).

Following the high power fibre coupling procedure, this translation mount was "walked" with the coupling mirrors and fibre z-translator progressively from low to high power to achieve efficiencies above 70%. The translation mount deviation from ideal collimation causes the beam to focus close to the AOM to prevent clipping and thermal effects. The East lattice regulation setup, see Figure 2.21, does not contain such a zooming translation mount for the input beam but a 8:3 telescope to reduce the beam to match the AOM aperture which was replicated on the Mephisto MOPA setup as explained before.

The efficiencies of the optical isolator transmission, AOM and fibre coupling are respectively 88%, 85% and 70% at high powers, the regulation setup efficiency is therefore of about 52%. With the Nufern amplifier set to output 41 Watts, we have at our disposal around 23 W for each of the horizontal lattice beam to hit the atoms in the lattice chamber.

²⁹SM1ZM, Thorlabs Inc.

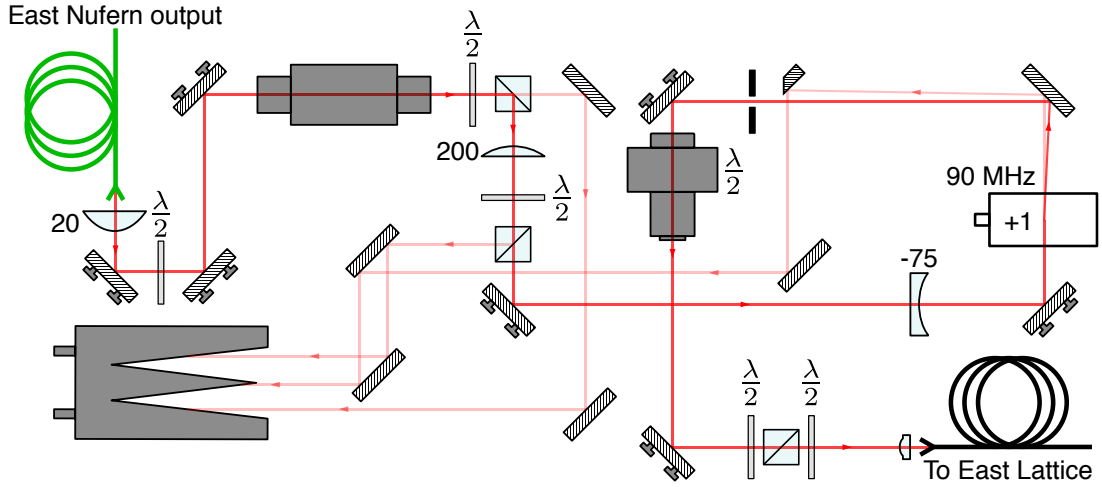


Figure 2.21: East lattice beam regulation setup.

2.3.4.3 Optical lattice breadboards/setup

On each of our two "wing" breadboards are combined, a lattice beam, a EIT/Molasses beam and an imaging beam (High/Low resolution on the East/West board). Only the lattice beam optical setup will be described in this section, the near-resonant paths being rather straightforward.

Upon exiting the high power fibre coming from the East lattice regulation board the beam passes through a polarisation "cleaning" cube and a small fraction of it gets diverted into two beams by a anti-reflective coated plate ("POP" in Fig. 2.22). One of the "pick-off" beams goes to a photodiode used for regulation while the other one is simply for monitoring the beam power in the low power regime. Prior to entering the optical isolator, a photodiode is also placed on transmission leakage of a reflective mirror to monitor the beam in the high power regime. Because this beam is fully retro-reflected on itself when used as a lattice, the optical isolator deflection ports must be very carefully dealt with especially the one corresponding to the back coming beam which gets dumped into a water cooled beam dump.

Similarly to the Vertical lattice beam setup an iris is placed for lattice alignment, the beam is then enlarged by a 1:2 telescope made of a -100 and a 200 mm EFL lens before being focused by a 300 mm EFL lens at the centre of the lattice chamber. Two kinematic mirrors, one of them on a piezoelectric actuated mount follow the telescope and are the one used for the alignment of the incoming beam. The polarisation is filtered as close as possible to the atoms by a polarising plate beamsplitter ("PPB" in Fig. 2.22) and half-wave plate. The beam is then sent into the vacuum chamber through a viewport by a dichroic mirror which combines the lattice beam and the other two resonant beam (EIT/molasses and imaging) on the East axis.

After the vacuum chamber, the lattice beam is separated from the other two by a 2 inches dichroic mirror on the West wing board. A 175 mm EFL lens collimates it prior to being focused again on a 1/2 inch high-reflective mirror ("LM" on Fig. 2.22) at 90° AOI (Angle Of Incidence) by a 50mm EFL lens in a "cat-eye" configuration. A servo-motor can be actuated to flip a mirror in between the focusing lens and the retro-mirror to divert the light in a beam dump in order to only have an optical dipole trap instead of a lattice. The lens creating the cat-eye configuration is mounted in a precision zooming translation stage to place the focus well on the retro-mirror.

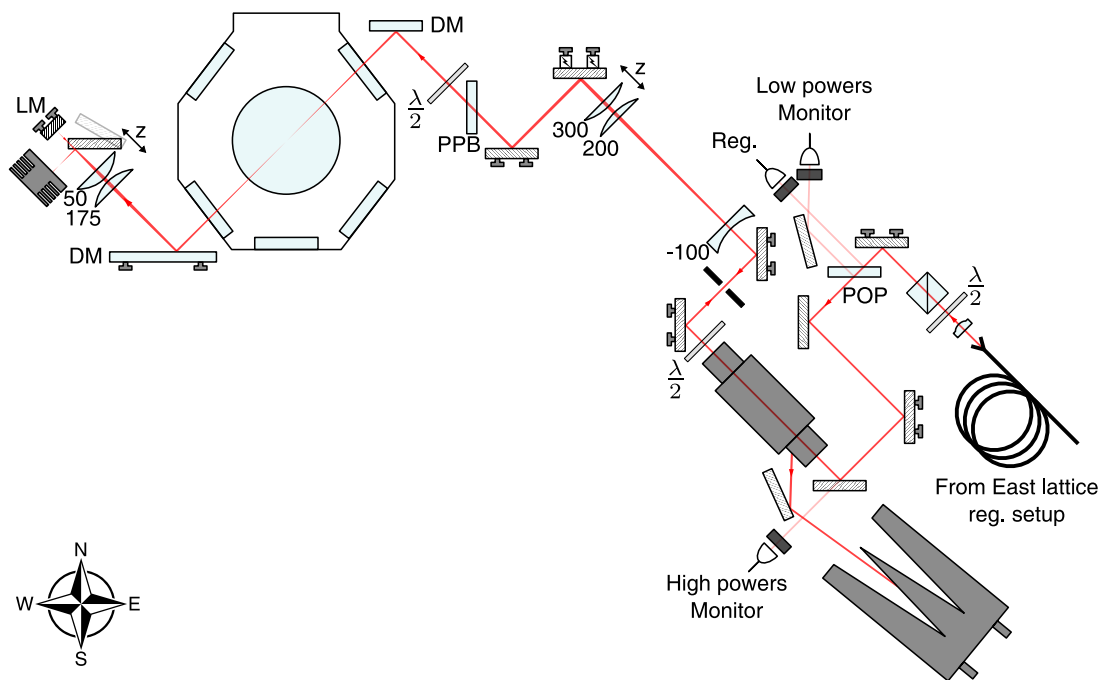


Figure 2.22: East lattice optical setup on the East and West wing boards.

To measure the power experienced by the atoms, the geometric mean between the one measured before the chamber and the one after (between the two dichroic mirrors and their respective facing view ports) is performed. This value was measured for several powers up to 0.5 W and was consistently 90% of the one measured just before the optical isolator where it is much more convenient and far less dangerous to measure it. With a maximum 23 W of achievable power before the optical isolator, one can infer if the magnitude of the losses behave linearly with power that 20 W can be shone for multiple seconds on the atoms on both horizontal lattice beams.

2.3.4.4 Alignment of lattice beams

The retro-reflection of each of the horizontal lattice beams can be blocked using mirrors and the lattices are turned into optical dipole traps. A sloshing motion consists in the oscillations of the atoms' centre of mass around its rest position while a breathing motion is a symmetric collective oscillations of the atoms around their immobile centre of mass. Sloshing/breathing oscillations can be measured by fitting the atomic cloud after ballistic expansion in TOF imaging with a Gaussian profile and extracting its central position displacement/width. Displayed on Figure 2.23, the acquired signals oscillate at one/twice the trap frequency of the monitored axis.

After the waists were determined using sloshing spectroscopy, the servo-mirror are set back to let the retro-reflection pass so that modulation spectroscopy in the lattice can be performed. The longitudinal position of the cat-eye lens was adjusted alongside with the lattice retro-mirror angles to maximise the modulation frequency. This process guarantees that our lattice has the best achievable interference contrast.

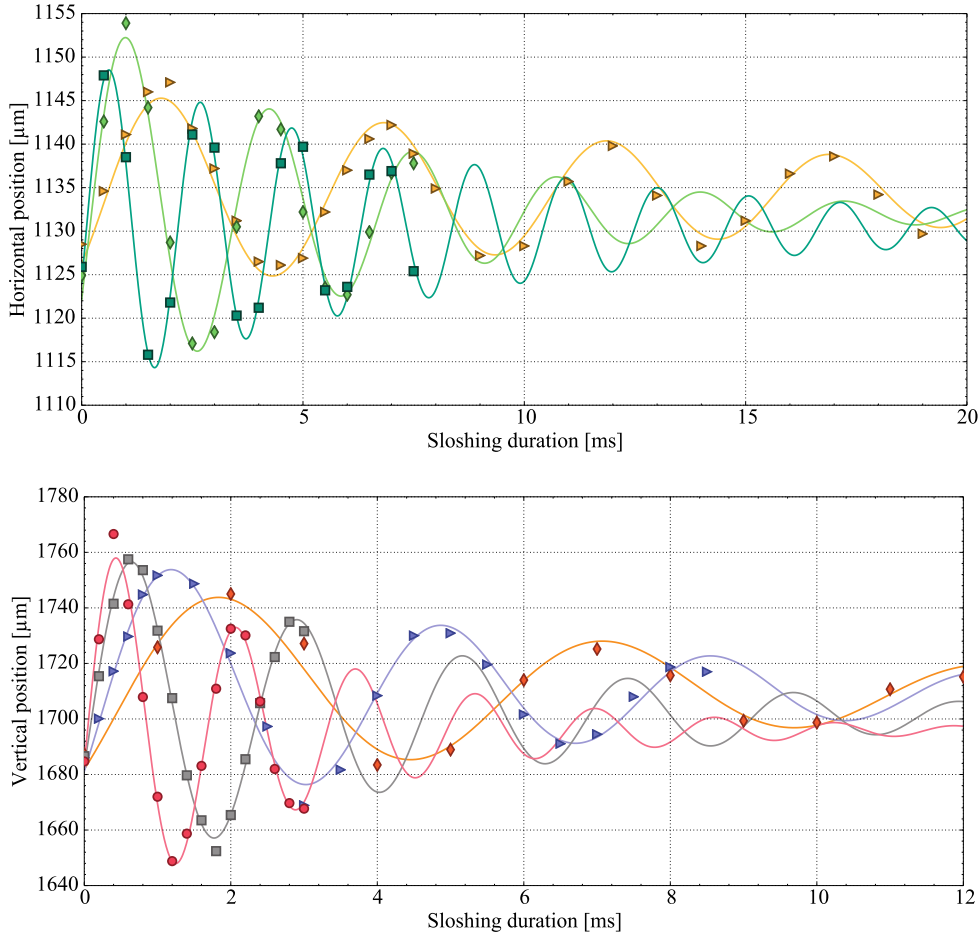


Figure 2.23: Top: Oscillation of the atom cloud in East ODT for three different beam powers: 1W (orange triangles), 2.5W (green diamonds) and 5.3 W (green squares) with their damped sine fits giving respective sloshing frequencies of 199(2), 308(3) and 484(2) Hz. Bottom: Vertical sloshing in West ODT for four different beam powers: 0.5W (dark orange diamonds), 1W (blue triangles), 2.5W (gray squares) and 4.65 W (red circles) with respective sloshing frequencies of 191(4), 272(3), 443(3) and 611(6) Hz. Fits of the radial trap frequency as a function of the squareroot of power yields East/West waists of 80.6(7)/69.9(4) μm . See Appendix G.

2.3.5 Squeezing beam

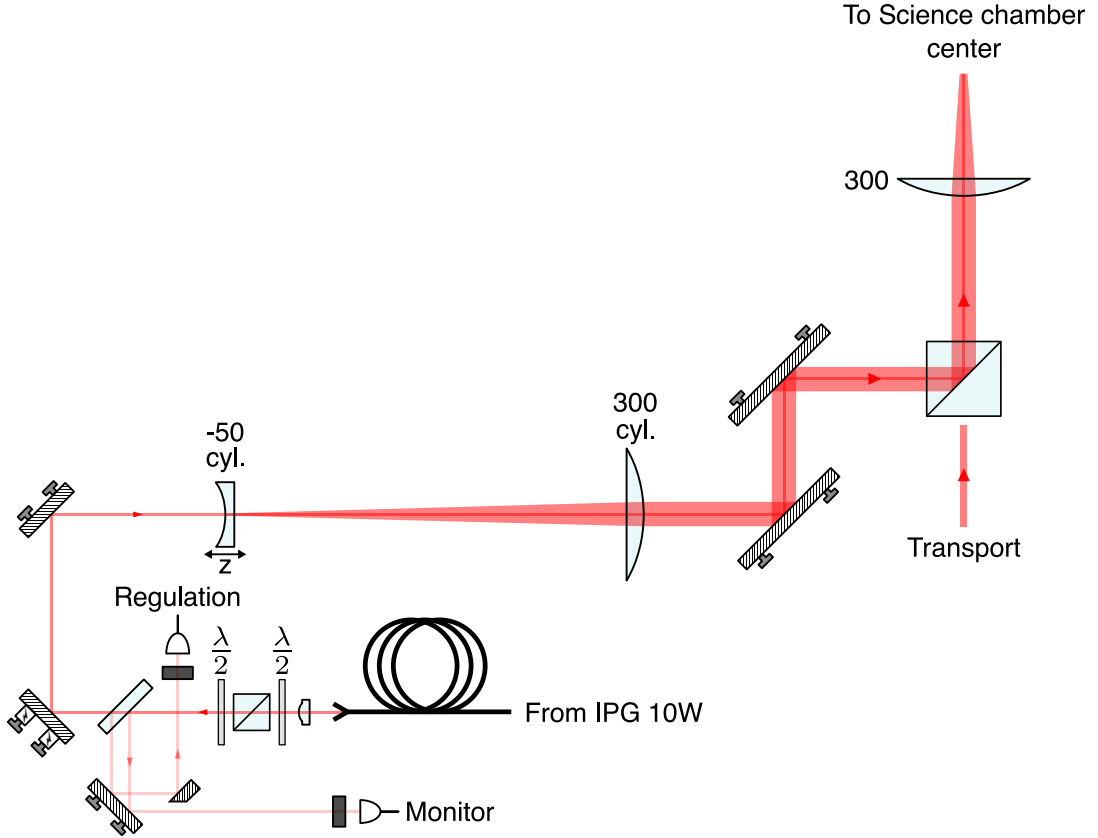


Figure 2.24: Squeezing beam optical setup.

We introduced a beam with a 6:1 aspect ratio which squeezes the atomic cloud vertically in order to increase the density of atoms in the imaged layer of our vertical lattice.

The output of a 10W Ytterbium fibre laser³⁰ is optically isolated, passed into an AOM for intensity regulation and fibre coupled into a high-power fibre.

As shown on Figure 2.24 The cylindrical telescope needed to achieve an aspect ratio of 6:1 is composed of two square shaped cylindrical lenses of -50 and 300 mm EFL. It forms a 1:6 magnification telescope that enlarges the beam vertically to a waist of about 6.3 mm. The focus created by a 300 mm EFL lens should then be six times smaller than the unmagnified axis, around 17 μm . The usual pick-off plate and photodiodes for monitoring and regulation were included prior to the telescope.

The horizontal and vertical waists of the squeezing beam were measured outside the vacuum chamber with a beam profiler mounted on a fine precision translation stage,

³⁰YLM-10-LP-SC, IPG Photonics Inc.

the results and their fits are presented in Figure C.0.1. The horizontal and vertical waists inferred from the fits are respectively $106.24(8)$ and $15.23(3)$ μm which is what is theoretically predicted. Note that if the fits to vertical waist curve gives a waist at focus of $15.23(3)$, clear deviations from this value is measured close to focus (see Figure C.0.2).

Alignment

The longitudinal position of the first lens can be adjusted manually using a linear translation stage³¹. There is a 1:1 magnification between the change in longitudinal position of the lens and the position of the vertical focus in the vacuum chamber. The position of the horizontal waist is tuned using the z-translator of the collimation aspheric lens. The fine alignments are performed by the piezo mirror shared with the transport trap.

Attempt to measure the vertical waist by sloshing oscillations revealed that the atoms quickly expand horizontally in the trap. Because of the very short Rayleigh range of about 1.2 mm for a 20 μm waist at focus, 1070 nm wavelength beam; the atoms can not be still considered at the beam focus location during more than a couple sloshing periods. The alignment was simply done by maximizing the vertical oscillation frequency for the first periods.

2.3.6 Horizontal dimple trap

Similarly to our need of compressing the atomic cloud vertically, a horizontal dimple was designed to implement the same evaporative process as in Markus Greiner's Lithium microscope [94].

2.3.6.1 Amplification

To create such a trap, a home-made 850 nm tapered amplifier module was built with at its core a butterfly packaged TA chip³². This chip can provide up to 1 W of power when seeded with input powers ranging from 2 to 20 mW. The TA module was initially being seeded with unlocked light from a laser diode³³ placed in one of our homebuilt ECDL cavity. The output power monitor of the TA showed fast mode-hopping and the lifetime of the atoms in any trap while this radiation was being shown was extremely short ($\simeq ms$). Our investigations led to four improvements, all necessary to prevent mode-hopping of the TA chip:

³¹M-UMR5.16, *Newport Corp.* formerly *Micro-controlle*

³²TA850P010, *Thorlabs Inc.*

³³L850P030, *Thorlabs Inc.*

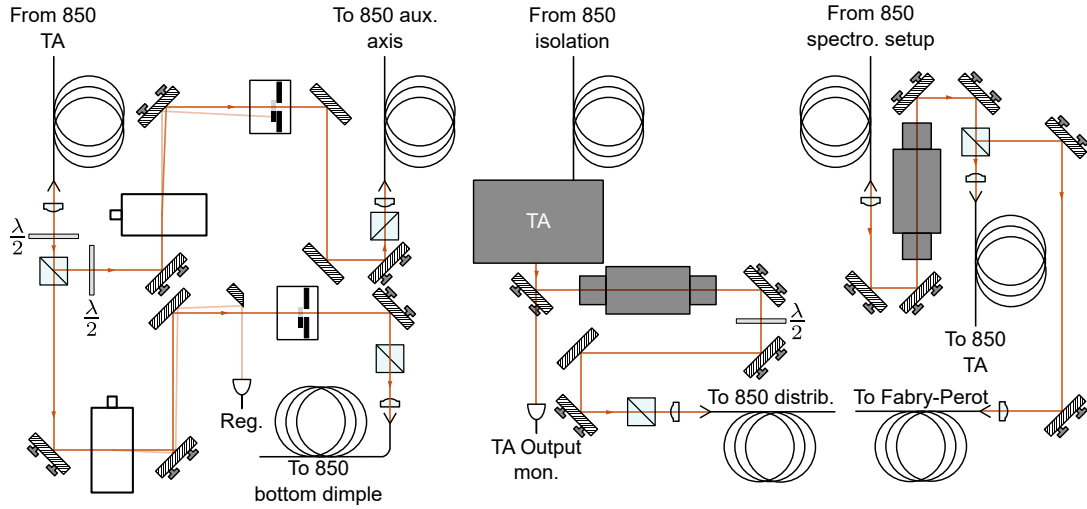


Figure 2.25: Isolation, amplification and distribution boards schematics of the 850 nm radiation.

- optically isolate the seed light before being sent to the TA (right part of Fig. 2.25).
- improve the temperature stabilisation of the first prototype to prevent overheating of the tapered amplifier chip and temperature regulation electronics.
- monitor of the temporal mode quality of the seed light using a fibred Fabry-Perot cavity³⁴ (bottom-right on Fig. 2.25).
- lock the frequency of the seed light.

The last step required a more delicate approach than the common Pound-Drever-Hall technique [138] with laser diode current dithering. Indeed our goal is here to create a small dimple in the horizontal plane of a vertical lattice layer to perform evaporative cooling and reach quantum degeneracy. During usual evaporation, the dimple trap depth is lowered by reducing the laser beam power which simultaneously decreases the trap frequency. Calculations showed that the decrease of trap frequency should cross the laser diode current dithering frequency which has a small but not negligible contribution in the laser frequency when this method is used. Polarization spectroscopy, which enables the generation of an error signal without any current dithering, was therefore opted for.

³⁴SA200-5B, *Thorlabs Inc.*

2.3.6.2 Polarisation spectroscopy

Following a paper on polarization spectroscopy of Cesium [139], a setup was built to obtain an error signal on which one could lock an ECDL cavity without any current dithering, cf. Figure 2.26 and 2.27 for schematics and measured error signal. The qualitative principle is rather straightforward to understand. Instead of using a linearly polarised probe and pump beams as in standard Doppler-free spectroscopy, the pump beam goes through a quarter-wave plate to acquire a circular polarisation. In the absence of external magnetic fields, the beam propagation axis sets the quantization axis and the atoms are preferably pumped to one side of their hyperfine sub-levels depending on the circularity of the polarisation.

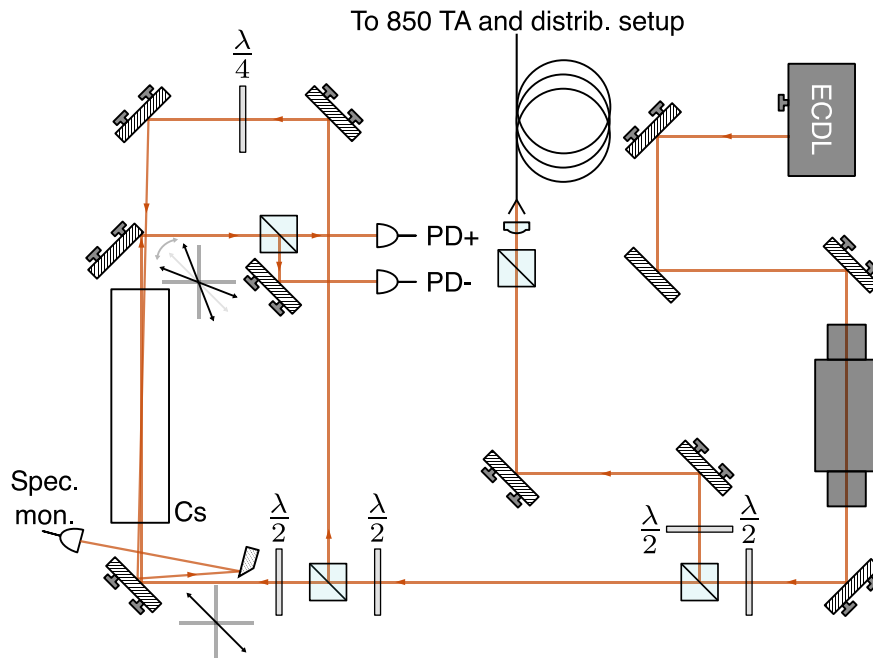


Figure 2.26: Cesium polarisation spectroscopy setup.

The weak probe beam is linearly polarised which can be mathematically decomposed into half left and right circularly polarised radiation. Because the hyperfine sub-levels population symmetry is broken by the polarising strong pump beam, one of the circular polarised component of the probe beam will get more absorbed by the medium than its counter-rotative part.

In the absence of the pump beam, the half-wave plate on the probe beam prior to the Cesium cell is set to obtain the same amount of light on both photo-diodes. With the strong pump beam's polarising radiation, the anisotropy in refractive index between the two circular polarisation causes the linear polarisation of the probe beam to change into a rotated ellipsis. This is directly translated into changes in the output

powers of the cube, exactly like in a polarimeter. The difference of the photo-diode signals then shows sharp features at the locations of the hyperfine transitions which is enough to lock on and obtain a stable laser.

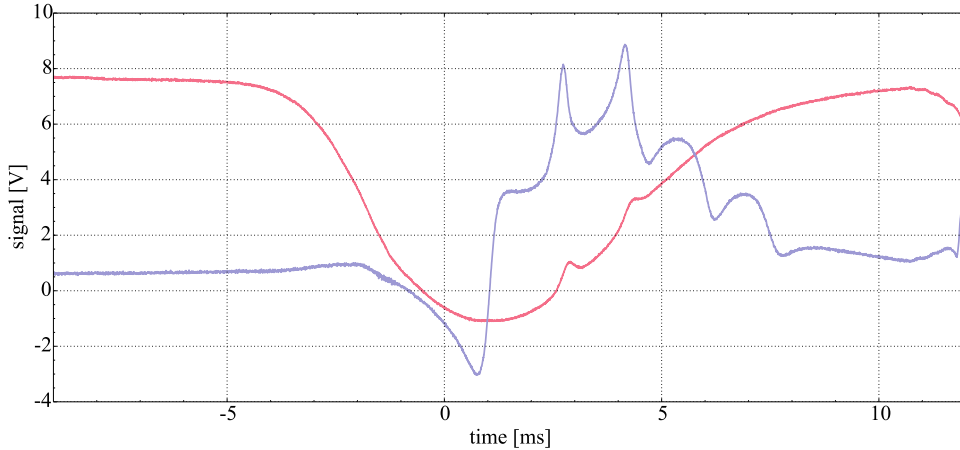


Figure 2.27: Doppler (red) and polarisation (blue) spectra of the $F=4 \rightarrow F'$ manifold of the D_2 line of Cesium 133. On the polarisation spectrum we recognize, from left to right, the features associated with the $F'=5, 4/5, 3/5$ & 4 (only 25 MHz apart), $3/4$ and 3 transitions where X/Y signifies the crossover between the $F'=X$ and $F'=Y$ transitions. The energetic splitting between the two visible features on the Doppler spectrum is 110(10) MHz.

2.4 Lattice chamber

2.4.1 Overview

The lattice chamber or science chamber has four main optical axes: the East and West lattice axes, the Long axis which are all in the horizontal plane and the vertical axis which goes successively, from top to bottom, through the centres of the vertical lattice focusing lens cage system, Top Feshbach coil, Gradient coil, the lattice chamber top window, atoms located about 4 mm above the bottom window, the microscope objective and PIFOC[®] mount, cf. Figure 2.28 for a vertical cut view.

The lattice chamber is equipped with three pairs of small coils in Helmholtz configuration (called "shim" coils) to negate the residual permanent fields or applying small bias fields on the Long, Horizontal (WE axis) and vertical axes. An unpaired water-cooled coil lies in the top window recessed space and had the initial purpose of generating a strong vertical gradient for our layer selection process. It is no longer in use as it was simultaneously adding too much of a bias field which prevented the use of our microwave amplifiers. Instead a set of two large coils, also water-cooled, called

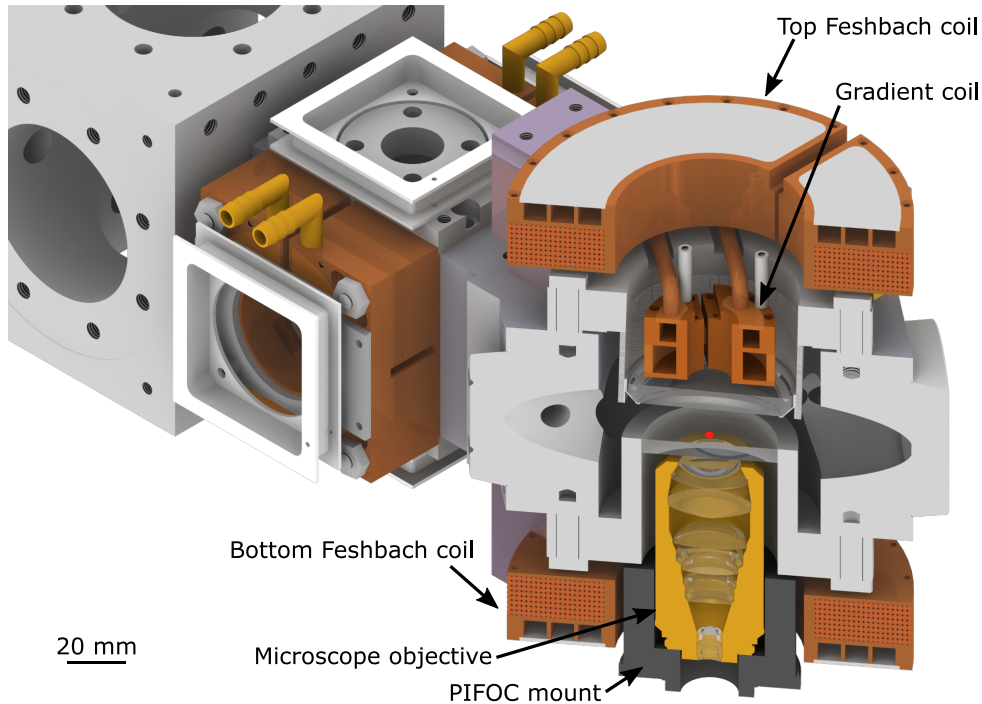


Figure 2.28: Lattice chamber vertical cutaway along the West axis. The atoms cloud location is represented by a bright red sphere lying approximately 4 mm above the lattice chamber bottom window.

the Feshbach coils, can be switched from Helmholtz to anti-Helmholtz configuration to replace our Gradient coil and to generate bias fields up to 300 Gauss.

Each of the small bias pairs of coils are connected to a laser diode current controller. The Gradient coil and Feshbach coils are respectively driven by a 40 V/30 A high precision unipolar current source³⁵ and a 120 V/50 A general purpose high power supply³⁶. Finally a high precision 4A current supply³⁷ drives an independent coil placed on the South-West window of the chamber for magnetic gradient compensation involved in the layer selection process.

2.4.2 Microwave

Our microwave antenna is a single end wire looped once to create a 2 cm diameter coil which was slid between the Gradient coil and the top window cylinder case to vertically lie between them resting on the edge of the top window. It is the best configuration found to provide some microwave radiation at the frequency of the ground state hyperfine splitting at the atoms location in the lattice chamber.

³⁵UCS40/30*HighFinesse GmbH*.

³⁶SM6000-120-50, *Delta Elektronika*

³⁷PS 8160-04, *EA Elektro-Automatik GmbH&Co. KG*

Driving the coil with 40 Watts of microwave power led to a 5 kHz Rabi frequency of microwave interaction strength as measured and fitted on Figure 2.29. With those levels of power, a switch coupled to a duty cycle fail-safe circuit is connected in between the 4 GHz signal generator³⁸ and the first amplifier³⁹ to only allow pulses of 450 ms duration every 10 seconds. If the full power were sent to the antenna for more than a second, it would overheat, melt the wire and its plastic housing which may irretrievably coat/damage the top window. The complete setup consists of the frequency generator which seeds a 5 W amplifier, in turn seeding a 40 W, 1.3-1.4 GHz wide LD-MOSFET amplifier⁴⁰ connected to the antenna through a circulator⁴¹ and a resonant triple-stub tuner⁴² for impedance matching.

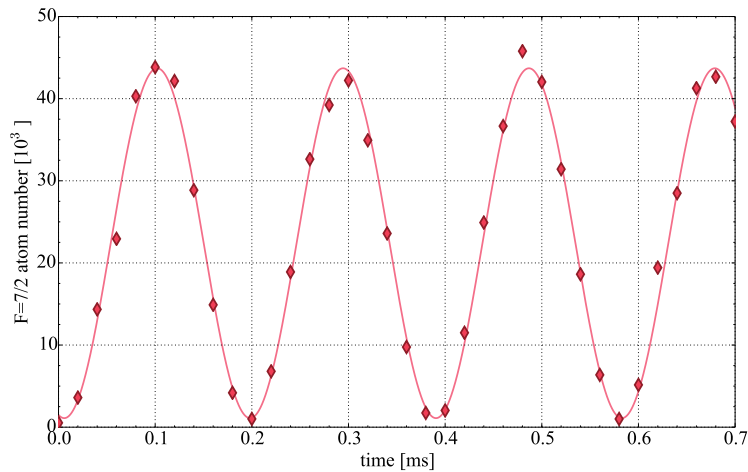


Figure 2.29: Rabi oscillations of the atomic population between the $|9/2, -9/2\rangle$ and $|7/2, -7/2\rangle$ ground states. A 0.378 G vertical magnetic field lifts the degeneracy of the ground states hyperfine transitions to bring the $|9/2, -9/2\rangle \rightarrow |7/2, -7/2\rangle$ transition (stretched states transition) 941 kHz away from its bare value. The atoms are imaged using repumper light only on the $F=7/2 \rightarrow F'=5/2$ transition along the low resolution imaging path which enables an excellent SNR when the $F=7/2$ manifold is initially vacant even if the total measured atom number is lower than expected because of the non-cycling nature of the repumper transition. The measurement of the Rabi frequency yields 5.23(1) kHz.

³⁸E4433B, *Keysight Technologies* formerly *Hewlett-Packard*

³⁹ZHL-5W-1, *Mini-Circuits*[®]

⁴⁰KU PA 1430 A., *Kuhne electronic GmbH*.

⁴¹D3C0102S, *DiTom*

⁴²1819B, *Maury Microwave Corp.*

2.4.3 Feshbach coils

The Feshbach coils consist of a copper block housing for wires and a cavity in which water circulates to prevent overheating. This cavity is sealed by a copper plate soldered onto the copper block. Unfortunately the bottom coil lid unsealed during braising and was sealed with glue which aged and leaked water when directly connected to the processing water system. Since then, water is being circulated through the Feshbach coils by a 12V DC pump which runs a low pressure close circuit system composed of the Feshbach coils and heat exchangers connected to the high pressure processing water circuit. The water flow proved to be sufficient to prevent overheating but not temperature fluctuations which, as we shall see in Section 3.5.3.3, hinders the reproducibility of the layer selection process.

2.4.3.1 Bias fields - Helmholtz configuration

Working at high magnetic fields can generate transition frequency shifts several orders of magnitude stronger than the Rabi frequency. Because the speed and width of sweeps are limited by our Rabi frequency, it becomes necessary to precisely calibrate the high current coils. Starting at low fields, the stretched transition is found and bootstrapped to high current values until a satisfactory number of points is reached for a fit.

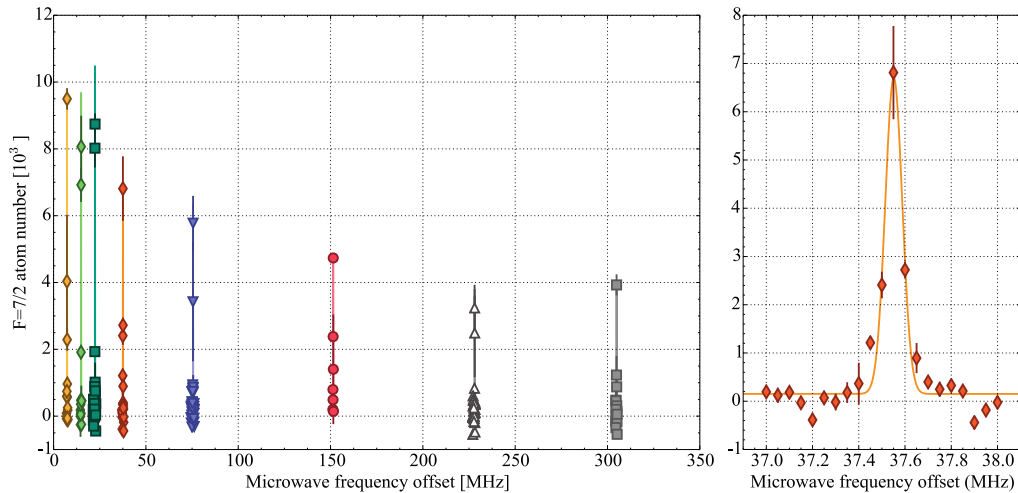


Figure 2.30: Left: Atom numbers transferred from the $|9/2, -9/2\rangle$ to $|7/2, -7/2\rangle$ by microwave linear sweeps versus microwave offset frequency from the bare hyperfine splitting for the following values of current in the Feshbach coils in Helmholtz configuration [left (yellow diamonds) to right (grey squares)]: 0.2, 0.4, 0.6, 1, 2, 4, 6 and 8 A. Right: Stretched state microwave transfer for 1 A in the Feshbach coils.

The offset frequencies corresponding to 0.2, 0.4, 0.6, 1, 2, 4, 6 and 8 A run in the Feshbach coils are respectively 7.296(2), 14.927(2), 22.426(1), 37.551(3), 75.535(3), 151.442(3), 228.017(4) and 304.897(4) MHz, measurements and fits on Figure 2.30. Fitting those results with a linear function gives a current to magnetic field factor of 14.97(2) G/A with an almost null offset current of 1 μ A.

2.4.3.2 Magnetic field gradient - Anti-Helmholtz configuration

The Gradient coil which generates a strong enough gradient for layer selection is also accompanied by a bias field. This bias field is strong enough to offset the stretched states transition frequency well beyond the bandwidth of our 40 W microwave amplifier. One of the Feshbach coil was therefore equipped with a computer controlled homebuilt inverter switch to allow the use of the pair of coils in anti-Helmholtz configuration to generate our gradient without a bias field.

To measure such vertical gradient, the atoms are loaded into the 3D lattice, deep enough to prevent any tunnelling between the lattice sites. The atoms are optically pumped to the $|9/2, -9/2\rangle$ state before applying a microwave sweep with a width that doesn't cause an overall cloud transfer to the $|7/2, -7/2\rangle$ stretched state. The microwave sweep central frequency is then scanned to transfer horizontal layers of the lattice whose transition frequency depends on their vertical location due to the presence of the magnetic field gradient.

After the microwave sweep is completed, some radiation on resonance with the $|9/2, -9/2\rangle \rightarrow |11/2, -11/2\rangle$ cycling transition of the D_2 line is shone at the cloud to excite the atoms untransferred by the microwave sweep and expel them out. The remaining atoms in the $F=7/2$ hyperfine manifold of the ground state are imaged using normal absorption imaging. By counting the remaining atom number, this measurement, performed for two values of coil currents in Figure 2.31, yields the centre location of the lattice with respect to the microwave transition frequency offset (bottom) as well as the magnetic field gradient magnitude (top) for those two currents. The magnetic field gradients at 12 and 20 A are respectively 15.53(2) and 20.45(5) kHz/ μ m.

2.4.3.3 Current supply stability

While the HighFinesse power supply is designed to have good stability and reproducibility, the measurement had to be done to ensure that the 120V/50A Delta Elektronika supply could have the same properties.

A coil wired to the Delta power supply was placed in a water-cooled bucket of water and an ultra stable, low temperature drift current transducer⁴³ was used to monitor

⁴³IT 60-S ULTRASTAB, LEM

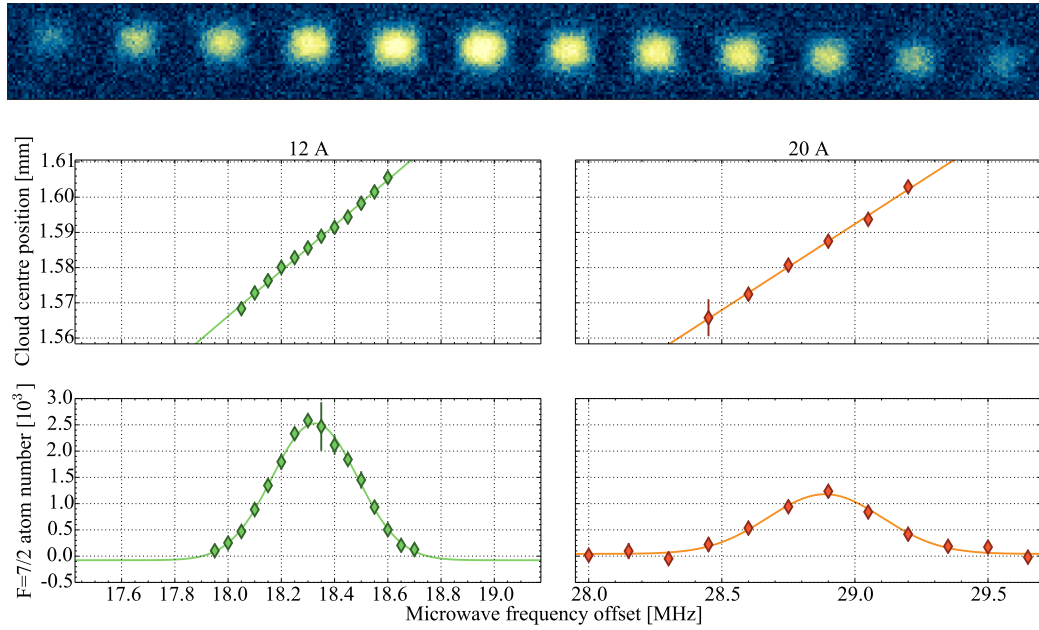


Figure 2.31: Top: Series of pictures corresponding to the cloud centre position points on the upper left graph of cloud centre positions for the 12 A set. The height is about $140 \mu\text{m}$. Bottom: Cloud centre position (top) and atom numbers (bottom) as a function of stretched transition frequency offset for currents of 12 and 20 A (left and right) in the Feshbach coils in anti-Helmholtz configuration.

the coil current. The output current of the current transducer, which linearly depends on the measured current, was measured by taking the voltage across a couple of very low temperature drift ($1 \text{ ppm}/^\circ\text{C}$) 20 Ohms shunt resistors placed in series on the current transducer output with a high precision 8 digits multimeter⁴⁴.

A function generator was set up to enable the power supply output for 2.5 seconds every 5 seconds and the multimeter was programmed to acquire a measurement for the last 0.5 s of the power supply active period. A computer was set to retrieve said measurement from the multimeter through GPIB every cycle. At last the power supply was interlocked with a temperature sensor placed on the coil.

The results are presented in Figure 2.32 and display the following properties:

- A quite slow increase with exponential decay of the driven current. The fit reveals a characteristic time of 1.5 hours. This growth only presents itself when the PSU is powered on. The Delta power supply connected to the Feshbach coils is therefore never powered down.

⁴⁴3458A, Agilent Technologies

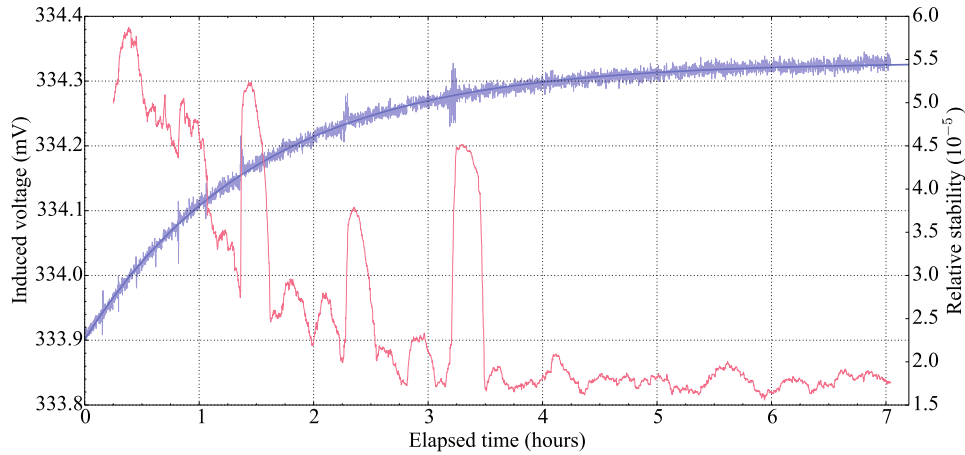


Figure 2.32: Left axis: (blue) measured voltage across shunt resistors linearly proportional to the current in one coil driven by the Delta Elektronika power supply for 7 hours after powering up the PSU. Right axis: (red) sliding relative stability (ratio of standard deviation to average) over the past 30 minutes.

- The presence of sharp disruptive events with an occurring frequency decreasing over time.
- A 30 minutes relative stability defined as the ratio of the standard deviation by the mean below 2.10^{-5} 4 hours after powering the PSU.

2.5 Microscope

2.5.1 Overview

The core of our experiment is centred around a high NA objective with which we gather the fluorescence for the single site resolved imaging. Before installation, we tested the objective to confirm its diffraction limited properties. The objective itself is produced by Leica, and has an effective focal length of 5.2 mm at 780 nm and a numerical aperture of 0.68. At our imaging wavelength of 770 nm, this gives us a diffraction limit of 632 nm, approximately 18% larger than the lattice spacing. This small difference allows for relatively straightforward image deconvolution.

2.5.2 Optical setup

The optics surrounding the microscope objective can be subdivided in one output ending at the iXon camera called the *fluorescence* path shown in blue in Figure 2.33 and three input named *molasses* (optics presents on Figure 2.33 but beam path not

coloured as this is not currently in use), *addressing* and *dimple* paths respectively displayed in yellow and dark orange on Figure 2.33.

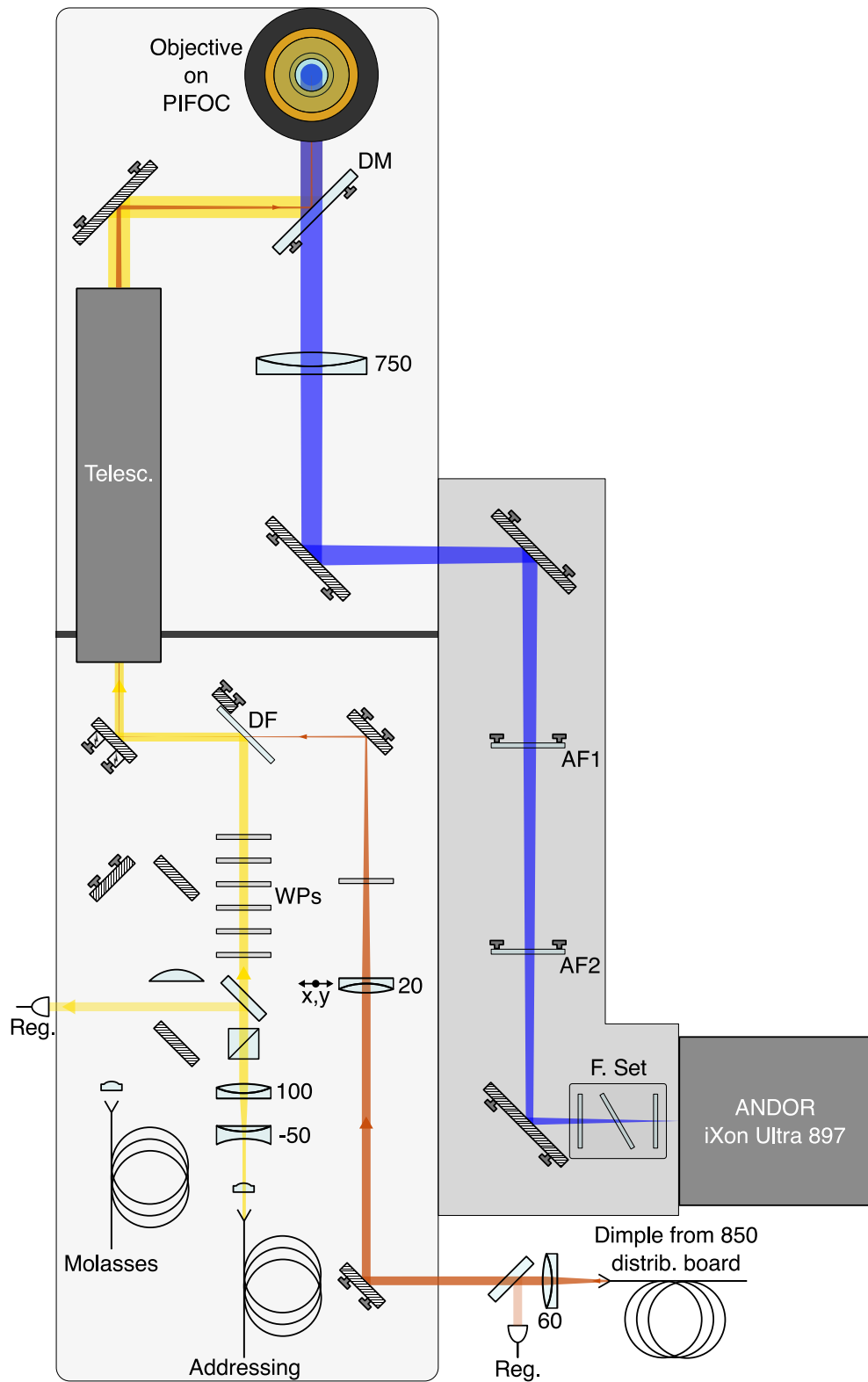


Figure 2.33: Top view of the microscope objective board (light grey rounded rectangle) with the optically shielded neighbouring imaging path (sharp dark grey polygon) on its east side.

2.5.2.1 Fluorescence

The conical fluorescence radiation comes out of the microscope objective as a 12 mm wide collimated beam which goes through a 2" dichroic mirror whose coating is highly reflective between 825 to 1100 nm ($> 99.25\%$ P-pol, $>99.6\%$ S-pol) and has a 4% reflectivity between 760 and 785 nm. Therefore, 96% of the 770 nm fluorescence light is transmitted and using an 750 mm EFL achromat an image is created on the EMCCD camera located outside the board.

On its way to the camera, a series of filters are set up to prevent any 767 nm Raman light (shone directly toward the objective from the top breadboard, see Figure 2.16), to progress further to the camera whose signal would completely dominate over the fluorescence and could even destroy the camera is set on high amplification mode.

The main tools for filtering out radiations only nm away are two ultra-narrow band filters custom-made by Alluxa Corp. These were tested using the "real condition" radiation (D_1/D_2 light from the ECDL/Ti:Sapph). The results presented in Figure 2.34 show a narrow 10° wide angular span where the filter are transparent for 770 nm radiation while exhibiting an optical density of 6 for the D_2 light. The test also shows that by increasing the tilting of the filter, the optical density for the D_1 light only equals 3, showing a worse spectral quality of the radiation coming from the ECDL than from the Ti:sapph laser as specified.

The fluorescence light not being collimated and the intensity of the Raman light fluctuating, two filters are mounted on 2-axis gimbal mounts⁴⁵ to fine tune their respective AOI in order to completely annihilate any Raman radiation hitting the EMCCD camera. After this precise extraction of the 767 nm light, three filters⁴⁶ set in a small aluminium box eliminate all the remaining unwanted background optical pollution (residual 1064 nm or ambient light). All those optics are of course enclosed into black anodised aluminium sheets from the board to the camera shutter (dark grey L-shaped polygon on Figure 2.33).

2.5.2.2 Addressing beam

To fulfill the addressing beam requirements, i.e. a diffraction limited beam focused at a lattice site, the beam shape shape needs to be matched with that of the fluorescence output of the microscope objective. The beam is first collimated by a diffraction limited 8 mm triplet⁴⁷ and expanded by a $\times 2$ magnification short telescope composed by two achromats⁴⁸. Then the beam goes through a set of six waveplates ('WPs' on Figure

⁴⁵GM200, *Thorlabs Inc.*

⁴⁶FF01-950/SP-25, Di01-R450-25x36 & FF01-780/12-25, *Semrock*

⁴⁷GLC-8.0-8.0-830, *CVI*

⁴⁸ACN254-050-B & AC254-100-B, *Thorlabs, Inc.*

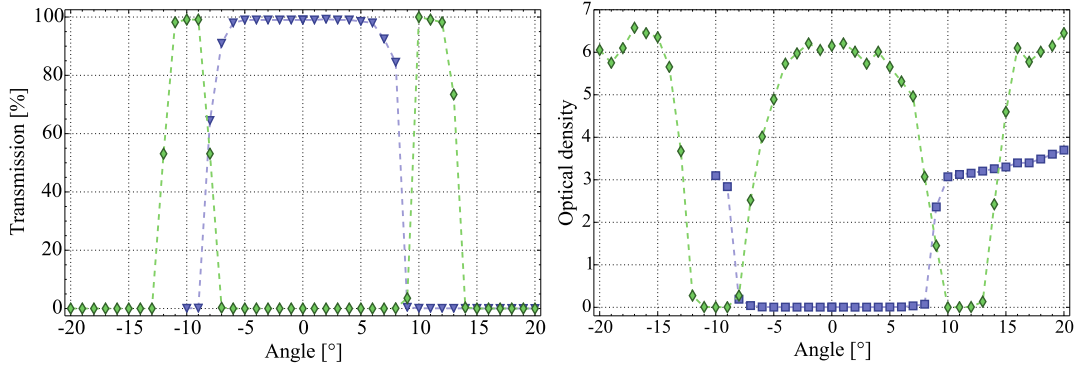


Figure 2.34: Left/right: Transmission/Optical density as a function of angle of incidence through an Ultra-Narrow Alluxa filter for the D_1 line radiation (blue triangles) from an ECDL and for the D_2 light (green diamonds) issued by the Titanium Sapphire cavity.

2.33) whose role is to make the beam polarisation as circular as possible for the D_2 lines of both ^{87}Rb and ^{40}K .

The beam is combined with the 852 nm dimple light on a dichroic filter⁴⁹ used as a mirror before being expanded by a 4 times magnifying high quality telescope to match it to the maximum usable bottom aperture of the microscope objective. The last mirror prior to the telescope is placed in a piezoelectric mount⁵⁰ allowing a tilt of 50 mrad. Slight changes of the AOI at the bottom of the objective of the addressing collimated beam are directly translated into position changes of its focus in the imaging plane of the objective. This piezoelectric mount is therefore the tool used for changing the location of our addressing beam focus. Finally the addressing beam (along with the dimple and molasses beams) is sent to the microscope objective by a large dichroic mirror reflecting 4% of the incident power.

2.5.2.3 Dimple trap

A change in the angle of inclination with the optical axis of a collimated beam propagated through the microscope to the atoms result in changes of location of beam focus. This property is used to create a dimple in the horizontal plane at the atoms location. Indeed, sending a converging beam which can be pictured as a continuous array of collimated beam with various AOI back through the objective will create an array of foci locations and therefore illuminated area larger than the point spread function.

The fibre feed from the 850 distribution board is collimated as a large beam by a 60 mm EFL achromat before being focused by a 20 mm efl achromat approximately

⁴⁹FF801-Di02-25x36, *Semrock*

⁵⁰S-334, *PIFOC*

10 mm prior to the piezoelectric mirror. The addressing telescope outputs this beam converging toward the objective microscope. The fibre z-translator serves as the main tool for changing the position of the focus created before the telescope and consequently the convergence of the beam entering the back of the objective. The dimple was set to a 23 μm waist at the atoms location.

2.5.3 Objective Mounting

The requirements of the objective positioning, i.e. 12 mm from the atom layer, 2 mm from the lower surface of the vacuum window and at an angle of inclination from the optical axis of less than 1 arc minute, place considerable constraints on both the vacuum chamber design itself, and the mounting position of the objective. In order to match the distance constraints, the objective is recessed deep into the vacuum chamber as shown in Figure 2.28.

The angular tilt control is more challenging. Due to the long imaging exposure (> 1 s), the objective mount must be extremely stable on the medium to long term, but with the requirement that the objective itself is angularly controllable. One obvious solution is to increase the mass of the objective mount, lowering the vibrational frequency and making it less susceptible to vibration induced random walks. The way we implemented this was to mount the objective, in its piezo translator⁵¹, onto a metal mounting plate, 600 x 200 x 82.7 mm (L x W x H). This itself is made of 3 components, a lower aluminium plate 50 mm thick, a middle brass plate 20 mm thick and a top aluminium Thorlabs breadboard 1/2" thick. The top two components are bolted together as one and supported above the lower plate. This support is provided by four load-bearing micrometer screws⁵², these allow angular control of the upper boards relative to the table surface, and as such relative to the chamber window. A series of high tension springs keep the boards together, holding the micrometer screws in their locating sockets. With the lower board firmly clamped down to the table surface, no significant change in alignment has been observed over 18 months.

2.5.4 Installation and Alignment

The installation of the objective itself was quite involved, due to the limited space available under the vacuum chamber. Given the height of the atoms in the lattice chamber, the working height of the objective from the table was determined to be 250 mm. The installation process will not be covered in this thesis, excepting to say it involved balancing a half kilogram coil complete with attached water cooling over the

⁵¹P726.1CD, *PIFOC*[®]

⁵²BM30.10, *Newport Corp.*

partially deconstructed, 20 kilograms objective mounting board as it was moved into position and raised up 6 cm.

2.5.5 Initial Lateral and Angular Positioning

The initial angular positioning was performed without feedback of any kind. During the testing phase, the objective was well aligned to a dummy vacuum window which was used to produce a reference for aligning the objective onto the real objective window. A single glass slide, 8 mm square, was placed on the shoulder of the piezo translator, then a laser beam with a 68 m beam path was passed through the vacuum window and onto the glass slide. By tilting this slide we were able to produce an interference pattern at the start of the beam path, resulting in a very high precision angular match between the glass slide and the dummy vacuum window. This was then glued in place, taking into account the contraction of the setting glue, to form a permanent reference perpendicular to the axis of the objective. Once the objective was mounted under and within the vacuum chamber, the interference path was recreated using the reference plate and the actual lower vacuum window. By tilting the objective board to maximise the interference fringe size we aligned the objective to what was later measured, using ^{87}Rb fluorescence imaging to be around 10 arcminutes from perpendicular. This was small enough to provide recognisable single atom imaging of ^{87}Rb .

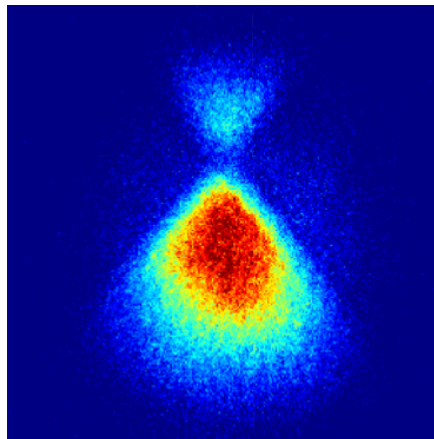


Figure 2.35: Absorption image of ^{87}Rb cloud, initially optically pumped into the $F=1$ groundstate, then spatially selectively repumped into the $F=2$ groundstate through the imaging objective and imaged on the $F=2 \rightarrow F'=3$ transition.

The lateral positioning of the objective required feedback from the atom cloud position. While the objective breadboard has a lateral position range of around 3 mm, set by the diameter of the vacuum chamber recess, both the imaging area of the objective and the atomic cloud are of the order of 50 μm in diameter. We therefore

needed some way of getting the rough positioning correct to within 25 μm in order to see any fluorescence of even a bulk cloud. We did this through a spatially selective absorption image technique, again using ^{87}Rb . The common imaging transition for ^{87}Rb is the $F=2 \rightarrow F'=3$ transition on the D_2 line. By initially exclusively populating the $F=1$ ground state, there is no absorption by the imaging light and so no atoms are imaged. By releasing a large cloud of hot atoms and illuminating them with a pulse which pumps atoms into the $F=2$ ground state just before imaging, we were able to image the size and position of the repumping beam. When this beam is inserted through the single site addressing path (see Section 2.5.2.2) the repumping beam forms a focus in roughly the middle of the imaging region and plane, Figure 2.35. By then shifting the entire objective board across the table, and changing its height by the micrometer screws, we were able to position this focus on the centre of the 3D lattice to within the tolerance of the imaging area.

2.5.6 ^{87}Rb Fluorescence Summary

The ^{87}Rb fluorescence imaging methods were based on those previously used by the Munich single site imaging group [79]. A single layer of ^{87}Rb atoms were left in the imaging plane of the objective, in a 3000 recoils deep 3D optical lattice. The atoms were then illuminated by retro-reflected beams, red detuned from the ^{87}Rb D_2 transition, as well as a single weak beam vertically inserted through the imaging objective, which together provide 3D sub-Doppler molasses cooling. The spontaneous decay during this process providing the fluorescence for imaging, allowing us to test the physical properties of our imaging setup without working ^{40}K fluorescence imaging.

2.5.7 Fine angular tilt Correction

Our first images of single site resolved ^{87}Rb showed a significant tilt, see Figure 2.36. By comparing these images with a series of test images provided by Leica, the microscope manufacturer, and to our original test setup, we were able to estimate the angular error to approximately 10 arcminutes along with the direction of the tilt needed to correct it.

One downside of the objective mounting system is the length of the objective pivot due to a change in angle. The point of rotation is approximately directly below the objective, however the imaging plane is around 180 mm away, so a small angle change results in a large imaging position change. Since our imaging region is 50 μm across, a movement of 25 μm almost completely loses our imaging reference. This corresponds to a change of approximately 0.5 arcminutes. The tilt correction process was therefore a case of alternately tilting the imaging objective board by 0.5 arcmin steps, and

shifting the entire 35 kg objective board by 25 μm , using fluorescence images of the bulk cloud as a reference for position, and checking the single site image distortion in each position. By this method we were able to reduce the tilt error to less than 1 arc minute. Image quality of the site resolved ^{87}Rb limited us at this point, the fluorescence imaging was never fully optimised as it was not a primary goal of the experiment.

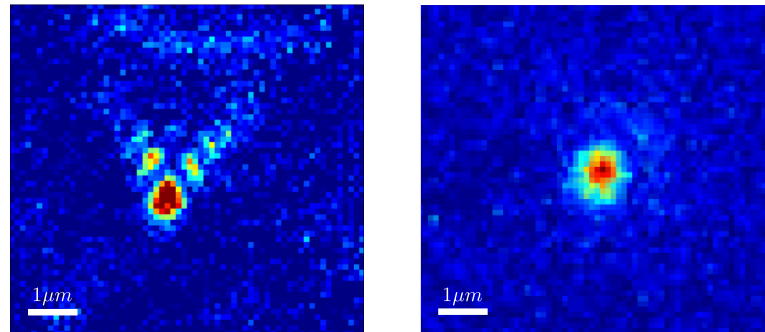


Figure 2.36: Single Rubidium atom fluorescence images, before (left) and after (right) tilt correction.

Chapter 3

Detection of single fermions

Once the single-site detection of ^{87}Rb bosons was accomplished, doing as well for fermions remained. This chapter shall present the main difficulty that arose from the impossibility of using molasses for ^{40}K due to its excited state strongly inverted trapping potential, and how EIT cooling conjointly with motion coupling via Raman transitions and layer selection were implemented to perform single-site imaging of fermions in a 2D lattice with similar characteristics to the one of bosons.

3.1 From a MOT to the microscope

1. 2D and 3D-MOT Loading

We use a flux of ^{40}K atoms generated in the 2D-MOT chamber to load a 3D-MOT. The 2D-MOT is formed from a pair of retro-reflected elliptical beams approximately 1" by 2" diameter containing both cooling and repumper light at intensities of 24 mW.cm^{-2} and 13 mW.cm^{-2} respectively. The cooling transition is defined as the $4S_{1/2} |F = 9/2\rangle \Rightarrow 4P_{3/2} |F' = 11/2\rangle$ transition and the repumper transition is on the $4S_{1/2} |F = 7/2\rangle \Rightarrow 4P_{3/2} |F' = 9/2\rangle$ transition. The 2D cooling beams are 9 MHz red detuned, while the repumping beams are 7 MHz red detuned.

The magnetic gradient is generated by a set of four magnetic coils in 'race track' configuration, producing a radial gradient of 13.5 G.cm^{-1} . Additional axial cooling is provided by 2 counter-propagating cooling beams, 5 mm waist and 60 mW.cm^{-2} intensity. Atoms are pushed from the 2D-MOT to the 3D-MOT by a 'push beam' resonant to the cooling transition, 600 μm waist and 250 mW.cm^{-2} intensity.

The 3D MOT itself is formed from a set of six counter-propagating beams of 11 mm waist and a pair of anti-Helmholtz coils, their axis is horizontal and perpendicular to the chamber axis. The beams each contain both cooler and repumper light, with intensities of 23 mW/cm^2 and 0.43 mW/cm^2 , and red detuning of 21 MHz and 34 MHz respectively. The magnetic gradient from the coils is 14 G/cm on the strong axis.

This configuration allows us to load the 3D-MOT with 1.2×10^8 ^{40}K atoms in 8 seconds.

2. Loading Angled Crossed Dipole Trap

We next transfer atoms from the MOT into a crossed optical dipole trap (CODT) formed by a pair of 100 W beams crossed at 17° , each with a $300 \mu\text{m}$ waist. We first turn on the CODT at full power, then release the MOT and perform a freespace grey molasses cooling pulse. The six beams used for the grey molasses are the MOT beams, with both the cooler and repumper 71 MHz detuned and with intensities of 23 mW/cm^2 and 0.26 mW/cm^2 respectively. This pulse cools the cloud from $200 \mu\text{K}$ to $48 \mu\text{K}$ as shown in Appendix A.2, in 16 ms, leaving 3×10^6 atoms in the CODT. We then superimpose the transport single beam optical dipole trap of 19 W with a $50 \mu\text{m}$ waist, along the chamber axis before using a 1 s forced evaporation of the angled CODT to load 1.5×10^6 atoms into it at a temperature of $90 \mu\text{K}$.

3. Optical Transport

We use the motorised translation stage to move the focus of the trap, and hence the atomic cloud, smoothly between the 3D-MOT chamber and the science chamber separated by 146 mm. The motion of the stage is defined by providing parameters such as a maximum velocity of $8 \times 10^2 \text{ mm.s}^{-1}$, a maximum acceleration of 10^4 mm.s^{-2} and a jerk of $2 \times 10^5 \text{ mm.s}^{-3}$, resulting in a total travel time of around 600 ms. The transport has an efficiency of approximately 40%, leaving us with 6×10^5 atoms in the transport trap in the science chamber.

4. Optical Lattice Loading

We transfer the atoms directly from the transport dipole into a CODT in the lattice chamber, where the beams are horizontal and aligned at 45° to the chamber axis with 20 W per beam and, before performing forced evaporation by ramping the power down to 1.5 W per beam over 2 seconds. We then ramp on a 2 W vertical lattice and ramp off the CODT linearly in 100 ms. The retro-reflection mirrors on the horizontal CODT beams are then flipped to allow the use of horizontal lattices using the same paths as the CODT. Both horizontal lattice beams are ramped on at the same time up to 2 W in 300 ms, freezing the thermal distribution in the vertical lattice.

5. Single Layer Preparation

A single layer of atoms is prepared using a spatially dependant microwave transition and an optical removal pulse (see Section 3.5).

6. Fluorescence Imaging

We ramp each lattice to matching trap frequencies of 330 kHz, a depth of 245 μK , and apply electromagnetically induced transparency cooling on the D_1 transition in the horizontal plane and Raman coupling of vibrational quanta between the vertical lattice and horizontal lattices, detuned from the D_2 line (Section 3.4.2). Filtering out the D_2 beam (Section 2.5.2.1), we gather the D_1 fluorescence photons over 1500 ms. A second image with identical parameters is then taken without the atoms present to allow background noise subtraction.

3.2 Microwave spectroscopy

Microwave spectroscopy is an essential tool to determine the occupation of the m_F hyperfine sub-levels of the $4S_{1/2}$ ground state manifold. As mentioned previously it serves various purposes from calibrating the various magnetic coils of our machine (Section 2.4.3) to the measure and reduction of non-scalar AC Stark shifts (Section 1.1.2.3) and most importantly isolating a single vertical lattice layer to be imaged by the microscope by driving position-dependent microwave transitions in a magnetic gradient and fine magnetic field direction tuning (Section 3.3).

The existence of magnetic field lifts the degeneracy of the hyperfine m_F sub-levels of the ground state in the ways and magnitudes expressed in Section 1.1.1.2. Figure 3.1 illustrates how, in the Zeeman regime, this lift results in the appearance of 16 microwave σ -transitions ($\Delta m_F \pm 1$) - 14 of them being doubly degenerate into 7 different frequencies and 8 π -transitions ($\Delta m_F = 0$).

We usually perform microwave spectroscopy in a way that provides us with the best signal-to-noise ratio and, as much as possible, minimize total atom number fluctuations: first the population of the $F = 7/2$ state is emptied (either because it already was or by applying a repumper pulse on the $F=7/2 \rightarrow F'=9/2$ transition), then a 100 ms microwave sweep at various frequencies is applied so it may (if the frequency matches) transfer atoms from the $F = 9/2$ to the $F = 7/2$ ground state, those are then imaged using repumper light only on the non-cycling D_2 $F=7/2 \rightarrow F=5/2$ transition to maximise the observed signal.

The two extremal transitions, $|9/2, 9/2\rangle \leftrightarrow |7/2, 7/2\rangle$ and $|9/2, -9/2\rangle \leftrightarrow |7/2, -7/2\rangle$, are non-degenerate and therefore provide an unambiguous signal revealing the population of the $|9/2, 9/2\rangle$ and $|9/2, -9/2\rangle$ respectively. For all other imaged populations in the $F=7/2$ manifold, one can not immediately infer the initial population of the $F=9/2$ sub-levels (as the population transferred to the $F=7/2$ hyperfine manifold results from two adjacent sub-levels from the double degeneracy of the seven other transition frequencies).

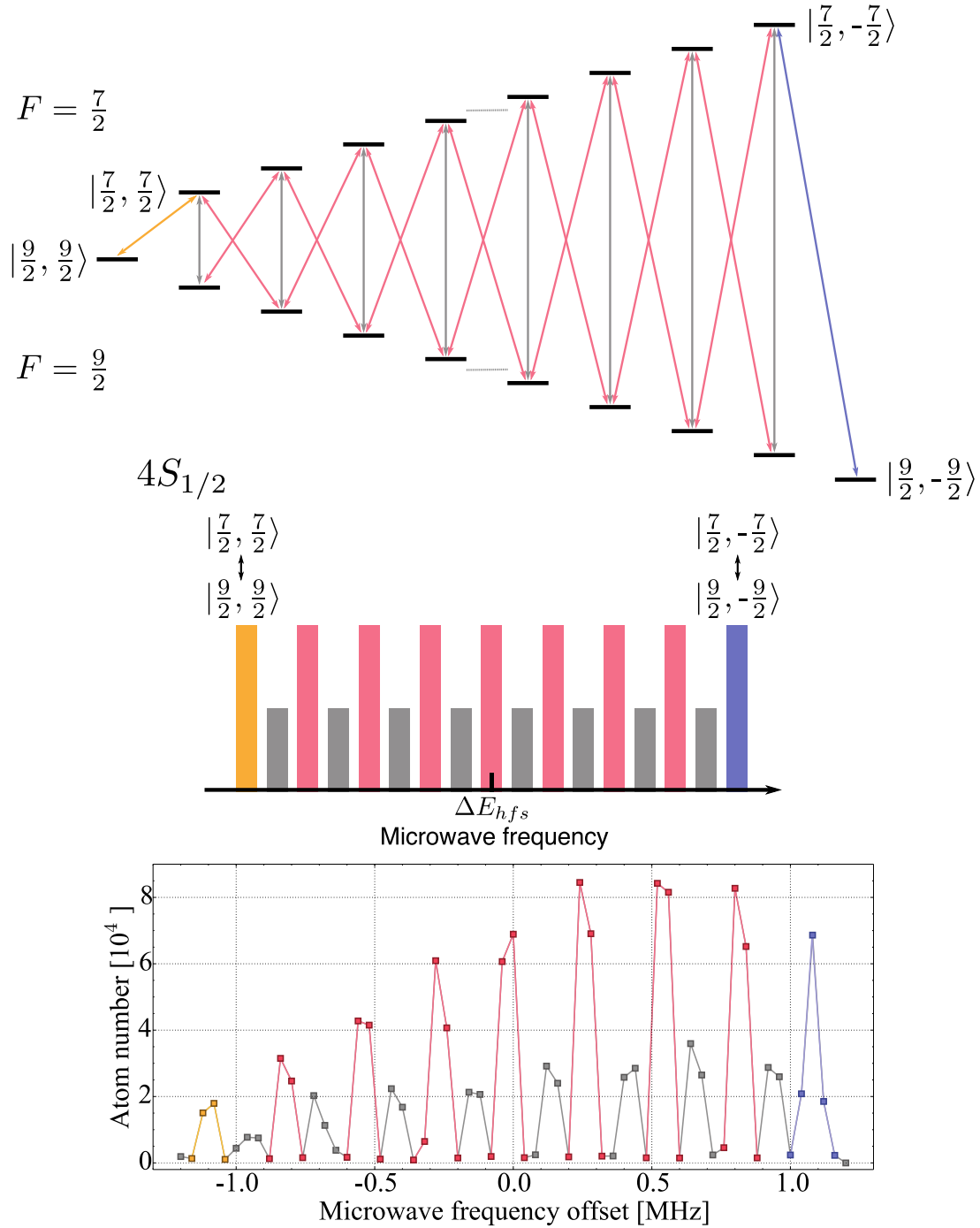


Figure 3.1: Top: Zeeman effect with the seven doubly degenerate σ (red), two outer most non-degenerate σ (orange and blue) and the eight π (gray) microwave transitions. Middle: Microwave transitions with matching color as they would appear on a spectrum. The π transitions are represented at half height for schematic purpose as our microwave antenna and orientation cause the Rabi frequencies of the σ transitions to be much higher than for the π ones. Bottom: Microwave spectrum of an unpumped sample in the Science chamber horizontal CODT right after transport. The microwave transfer has a 100 ms duration, 80 kHz wide sweep done prior to imaging the atoms in the initially empty $F=7/2$ manifold using repumping light only. The distribution slightly favours the negative m_F side of the spectrum.

3.3 EIT cooling

The necessity of performing EIT cooling arose from the impossibility of sub-Doppler molasses cooling in a deep lattice for ^{40}K as it has been successfully used in the ^{87}Rb Bloch and Greiner groups bosonic quantum gas microscopes [78, 79] for many years and more recently by the Takahashi group using ^{174}Yb [88].

3.3.1 Tensorial D_2 AC Stark shifts

Sub-Doppler cooling on the D_2 line is prohibited for ^{40}K by the strong tensorial AC Stark shift that, in deep optical lattices, mixes all the m_F sub-levels of each excited hyperfine states across the whole excited state manifold. Figure 3.2 illustrates such phenomenon which on the left shows the scalar and tensorial AC Stark shifts (purely π -polarised radiation as explained earlier in Section 1.1.2.3) effect when the radiation power/detuning is small/high enough not to cause the mixing of at least two sublevels from different hyperfine states. The graph on the right of Figure 3.2 shows the calculation of the resulting A.C. Stark shifts for all m_F sublevels as a function of the power in our West lattice beam parameters. Two striking features merit commenting and are sufficient to explain the failure of usual sub-Doppler cooling.

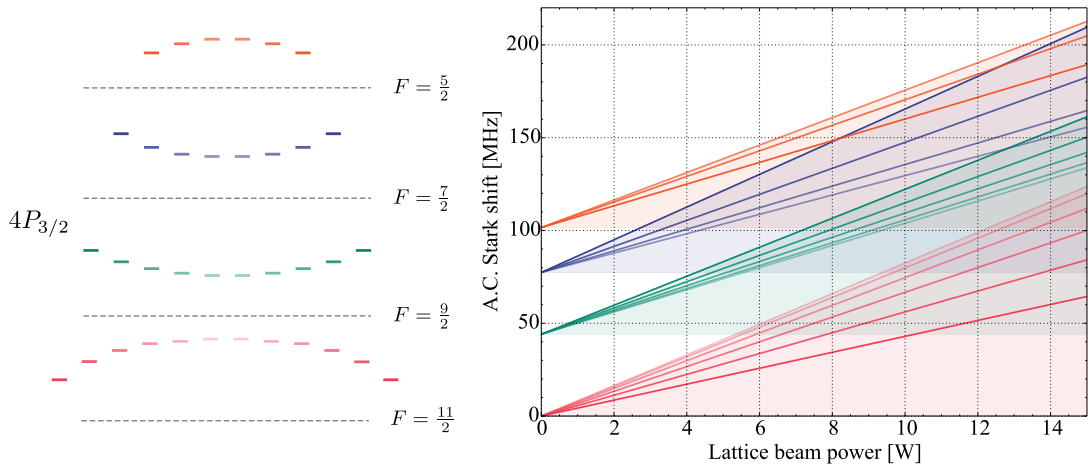


Figure 3.2: Left: Scalar and tensorial A.C. Stark shifts of the $4P_{3/2}$ hyperfine levels caused by a red detuned π -polarised radiation with the hyperfine sublevels depicted darker for increasing m_F absolute values, for an optical power sufficiently low not to exhibit mixing of states belonging to distinct F numbers. Right: A.C. Stark shifts of all the m_F hyperfine sublevels of the $4P_{3/2}$ state (in the West lattice) as a function of lattice beam power. The light shaded areas are a visual guide representing all the light shifts that an atom can take depending of its position in the lattice potential at a given power.

The first is that at a fixed laser beam power, the energies of the m_F sub-levels of different hyperfine states overlap, the first occurrence at 8 Watts involving the $|7/2, \pm 7/2\rangle$ and $|5/2, \pm 5/2\rangle$ states and later at 12.8 W between the $|7/2, \pm 1/2\rangle$ and $|9/2, \pm 9/2\rangle$ states for a beam waist of 70 μm .

The second feature is that by taking into consideration the spatial modulation of the radiation strength inherent to the lattice periodic structure, the energy of an atom at the bottom of a lattice well can be brought at the same level of one which would be less shifted being located closer to one of the nodes of the lattice potential. Even if this situation might sound extreme, the slight difference of polarisability between some pairs of states, e.g. $|11/2, \pm 1/2\rangle, |11/2, \pm 3/2\rangle$ and $|9/2, \pm 1/2\rangle, |9/2, \pm 3/2\rangle$, would bring them back into degeneracy for small displacements from the bottom of the lattice potential.

Those two effects render the whole $4P_{3/2}$ inadequate to use any kind of cooling process that would rely on cycling transitions between m_F sub-levels which are no longer "good" quantum numbers. The $4P_{1/2}$ hyperfine manifold, on the contrary, is not subject to tensorial A.C. Stark shifts and EIT cooling on the D₁ line proved to be an efficient way to cool and gather fluorescence in a deep 3D lattice.

3.3.2 Nulling vectorial light shifts

Even if the $4P_{1/2}$ manifold does not exhibit any tensorial light shift, the vectorial one could still prevent us from either performing a cooling scheme that would rely on a fully controlled lift of the degeneracy between the m_F sublevels such as Raman sideband cooling or on keeping said degeneracy as it is required by EIT cooling.

Our lattice beams' linear polarisation orientation is set by a half waveplate before being combined with the resonant EIT/molasses beams on a dichroic mirror. Those mirrors do not exhibit the same reflectivity for S and P polarisation orientation and the incident linear polarisation can acquire some circularity upon reflection (or transmission). This triggers the need to fine tune the angle of the half waveplate to obtain minimal vectorial light shifts. The detection of such light shifts is done using microwave spectroscopy. Vectorial light shift has a linear dependence with regard to the m_F quantum number and causes the degeneracy to be lifted exactly as a static magnetic field would as explained in Section 1.1.2.3.

Figure 3.3 shows how our lattice beams' polarisation circularity was detected by microwave spectroscopy of ^{87}Rb ground state manifold $5S_{1/2}$ on which 3 π and 4 σ -transitions can be driven, two of latest kind being doubly degenerate. The left part of Figure 3.3 shows the power dependence of the vectorial light shift. The power of the vertical lattice beam is changed from 0.9 to 5 Watts which causes the half microwave

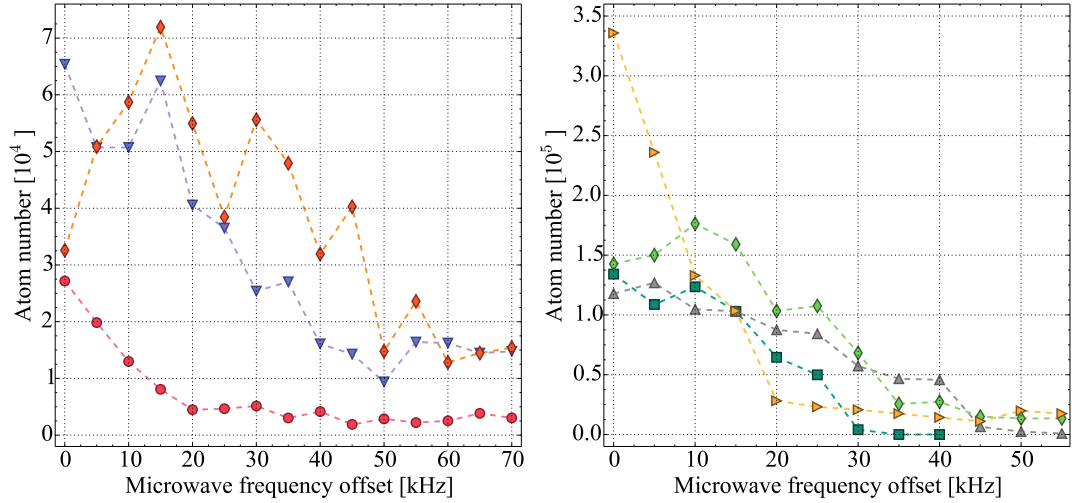


Figure 3.3: Left: Microwave spectra of ^{87}Rb for Vertical lattice powers of 0.9 W (red circles), 2 W (blue triangles) and 5 W (orange diamonds) for a single waveplate position showing that an increase of power does trigger a lift of the m_F degeneracy as expected for a partially σ polarised beam. Right: Microwave spectra taken in the West lattice at 11.5 W (dark green squares) and at 16.5 W for three different waveplate positions, initial (gray triangles), waveplate rotated slightly ccw (light green diamonds) and optimised waveplate position (orange triangles) showing that at a constant beam power the polarisation can be finely tuned to minimise the vectorial light shifts. The microwave spectra are all performed with linear sweeps whose width is twice the frequency increment between data points, here 10 kHz.

spectrum span to extend from 20 to roughly 60 kHz. On the right is an example of our optimization of polarisation linearity where the West lattice beam is raised at a quite high power to increase as much as possible the vectorial light shifts and then the half waveplate rotated by no more than a couple of degrees in each direction to narrow as much as possible the microwave spectrum span (light orange triangles).

3.3.3 Theory of EIT cooling

Generally, electromagnetically induced transparency renders a medium transparent to a certain radiation by simultaneously coherently driving another one, it thus requires at least a three-level system. This property that multi-level systems can exhibit is part of a whole class of quantum effects arising from the quantum destructive interference between the excitation amplitudes.

As demonstrated in the seminal paper of Cohen-Tannoudji team [141], in a Λ -system, as in the level scheme of Figure 3.4, coupling the excited state to one of the ground states with a radiation detuned by a frequency Δ will dress it into two virtual states $|+\rangle$ and $|-\rangle$ whose energies are respectively located ΔE_C and $-\hbar\Delta - \Delta E_C$

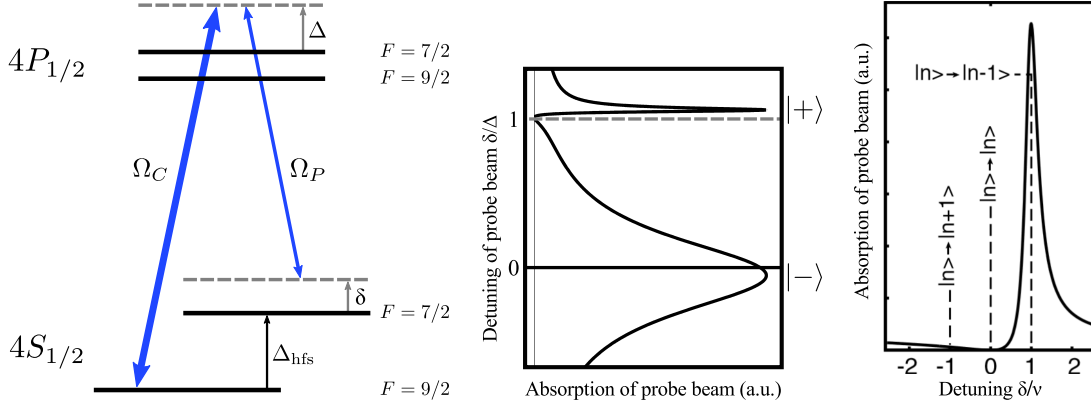


Figure 3.4: Left: Level scheme of the relevant states of ^{40}K , with near-resonant (global detuning Δ) EIT coupling and probe beams (Rabi frequencies Ω_C and Ω_P , blue) with relative detuning $\Delta_{\text{hfs}} + \delta$, δ being the EIT two-photon detuning. Middle: Absorption profile of probe beam as a function of normalised probe beam detuning. The two $|\pm\rangle$ dressed state locations coincide with the absorption curve maxima shifted by $\Delta + \Delta E_C$ and $-\Delta E_C$ from the upper level ($4P_{1/2}$ $F=7/2$) of the Λ configuration. Right: Fano-like part of the absorption profile located near the $|+\rangle$ virtual state as a function of EIT two-photon detuning δ in units of trapping potential frequency ν . In ideal EIT cooling conditions, $\delta = 0$, the carrier transition ($|g, n\rangle \rightarrow |e, n\rangle$) is nulled while the ratio of first red to blue sideband transitions is greatly enhanced. Middle and right figures taken from [140].

away from the probe beam upper energy (top dashed gray level) thus making $|-\rangle$ energetically offset from the excited state by $-\Delta E_C$ where ΔE_C designated the A.C. Stark shift caused by the coupling laser of Rabi frequency Ω_C and is given [140] by

$$\Delta E_C = \hbar \frac{\sqrt{\Delta^2 + \Omega_C^2} - |\Delta|}{2} \quad (3.3.1)$$

The absorption profile of the two dressed states presented in the middle graph of Figure 3.4 presents a broad resonance for dressed state $|-\rangle$ which linewidth Γ_- is close to the undressed excited state, i.e. $\Gamma_- \simeq \Gamma$ and a sensibly more narrow Fano-like profile which linewidth Γ_+ is significantly smaller, $\Gamma_+ \ll \Gamma$ [142]. For a broad introduction to Fano resonances from their discovery to their most example in ultracold physics, one can consult [Vittorini2009].

In a trapping potential of characteristic frequency $\nu = \omega/2\pi$, EIT cooling corresponds to the situation where a weaker probe beam simultaneously coherently drives the transition from the other ground state to the excited one with a two-photon detuning $\delta = 0$. Then the EIT condition is verified for the carrier transition $|g_{1/2}, n\rangle \rightarrow |e, n\rangle$ while, due to the asymmetry of the Fano profile, the red-sideband transition $|g_{1/2}, n\rangle \rightarrow$

$|e, n - 1\rangle$ is favoured while the blue-sideband $|g_{1/2}, n\rangle \rightarrow |e, n + 1\rangle$ is suppressed. EIT cooling is optimal when the peak of the Fano profile matches the red-sideband location, i.e. $\Delta E_C = \nu$, condition met by varying the coupling radiation Rabi frequency Ω_C for a fixed EIT detuning Δ . Here $g_{1/2}$ (e) designates the ground (excited) states coupled by the coupling radiation and n the vibrational level in the harmonic approximated lattice trapping potential.

Figure 3.4 illustrates the case for a positive detuning Δ . If the coupling laser were to be red-detuned from it, $\Delta < 0$, the whole probe absorption spectrum would be symmetric with respect to the excited state. Hence, the Fano profile would then enhance the blue-sideband transition over the red one therefore EIT cooling can only be performed blue-detuned from the excited state.

3.3.4 3D EIT Cooling

With a true coherent two-photon process, the fluorescence signal immediately gained orders of magnitude in amplitude and EIT cooling of our whole 3D lattice could be optimised not only on fluorescence acquired through the microscope restricting ourselves to only 2D horizontal EIT cooling but rather on the survival of the bulk cloud after a couple of seconds of 3D EIT exposure. Which process leads to a 3D lattice of vibrational spacing $\nu = 300$ kHz in all direction, an EIT radiation detuned by $\Delta = 6\Gamma$ and a two-photon detuning $\delta = 0$. An important requirement for EIT cooling to work for our multi-level atom consisting of many distinct m_F sublevels in each of the three hyperfine states at play is to be degenerate. EIT cooling quickly losses efficiency when the degeneracy is lifted by small static magnetic fields with our bias coil currents also being optimised on long term cloud survival at first.

Figure 3.5 displays the normalised evolution of the horizontal and vertical cloud width after 1 ms of ballistic expansion upon fast release of the 3D lattice during the first milliseconds of EIT cooling. Those widths are directly correlated to the initial temperature of the atoms in their trapping potential, the smaller the width, the colder the atoms. The atoms are rapidly cooled within 3 ms on both axes. A similar horizontal expansion width measurement was taken on the other imaging axis and shows an identical decrease. On this short time scale characteristic of EIT cooling, the expansion widths seem to stabilise at a constant value but for the long durations of 2 seconds used for bulk survival, those widths slowly diminish as some atoms are lost from anisotropic EIT cooling performance as we shall explain soon.

Another clear evidence of EIT cooling is obtained by comparing the band population in the 3D lattice using band mapping, see Section 1.10, before and after 5 ms of EIT radiation exposure as shown in Figure 3.6. The population of the excited bands is

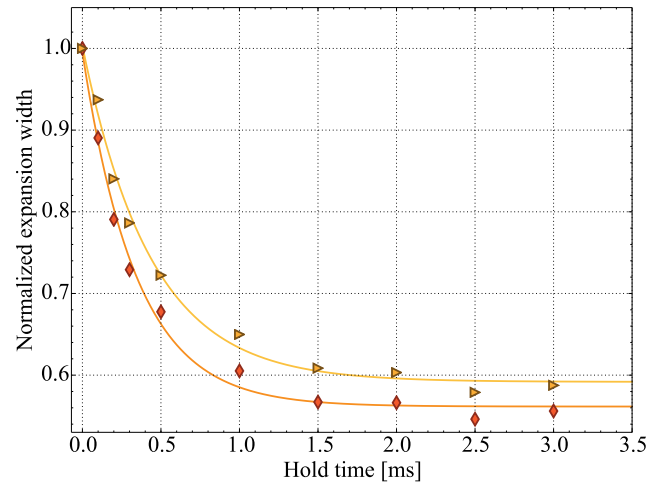


Figure 3.5: Normalised East-horizontal (light orange triangles) and vertical (dark orange diamonds) expansion width of the atomic cloud upon sudden release from the 3D lattice as a function of EIT cooling hold time. Both curves are fitted with exponential decays yielding horizontal/vertical decay time constants of 0.34(2)/0.44(3) ms.

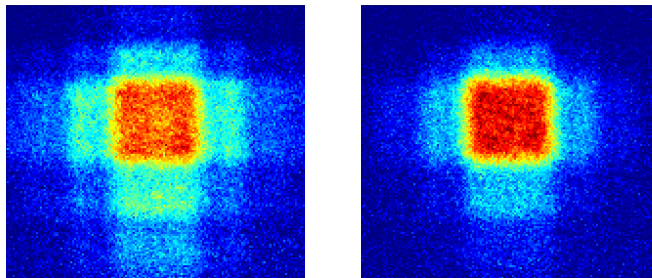


Figure 3.6: 3D band mapping expansion of the atomic cloud held for 5 ms in the 3D lattice without (left) and with (right) EIT beams present.

obviously reduced in favour of the lowest first two proving that the atoms were brought to lower vibrational states in their respective lattice sites.

3.3.5 Fluorescence with 2D EIT Cooling

The laser beams of our 3D lattice having a rather small waist - 69, 81 and 105 μm - and our field of view being roughly on the order of 100 μm , the effect of the harmonic confinement revealed itself through the anisotropy of the EIT cooling. A fixed EIT cooling condition $\Delta E_C = \nu$, see Eq. (3.3.1), is met for a given couple of detuning Δ and coupling radiation Rabi frequency Ω_C . If that condition is fulfilled for the deepest part of our 3D lattice, it shouldn't stay matched away from the 3D lattice centre as the harmonic confinement of each lattice beam will reduce the depth of lattice sites and therefore their vibrational frequency ν . Decreasing ν would require the EIT detuning Δ to be also reduced, Ω_C remaining identical, to match the EIT condition again.

This anisotropy is beautifully illustrated in the top set of microscope pictures of Figure 3.7 showing rings of normalised fluorescence appearing outward from the lattice centre for decreasing value of EIT detuning Δ . The bottom graph displays the total acquired fluorescence as a function of EIT detuning Δ with the zero corresponding to the location of the resonance of the coupling laser with the $F=7/2$ $4P_{1/2}$ state at the bottom of the 300 kHz 3D lattice. As the first picture corresponds to a detuning of $\Delta = -10$ MHz, one could be puzzled to observe EIT cooling red-detuned but at the spatial location of the ring, the A.C. Stark shift of the lattice is far less than at the centre of the lattice and the value of $\Delta = -10$ MHz, which is relative to the A.C Stark shift of the lattice deepest parts still constitute a blue-detuned radiation necessary for EIT cooling. The calculation of the total A.C. Stark shift created by the three lattice beams for a 300 kHz 3D lattice yields 107 MHz.

The bottom graph of Figure 3.7 also indicates that EIT cooling occurs blue-detuned of the $F=9/2$ $4P_{1/2}$ however its efficiency is seriously reduced from being red-detuned of the $F=7/2$ state.

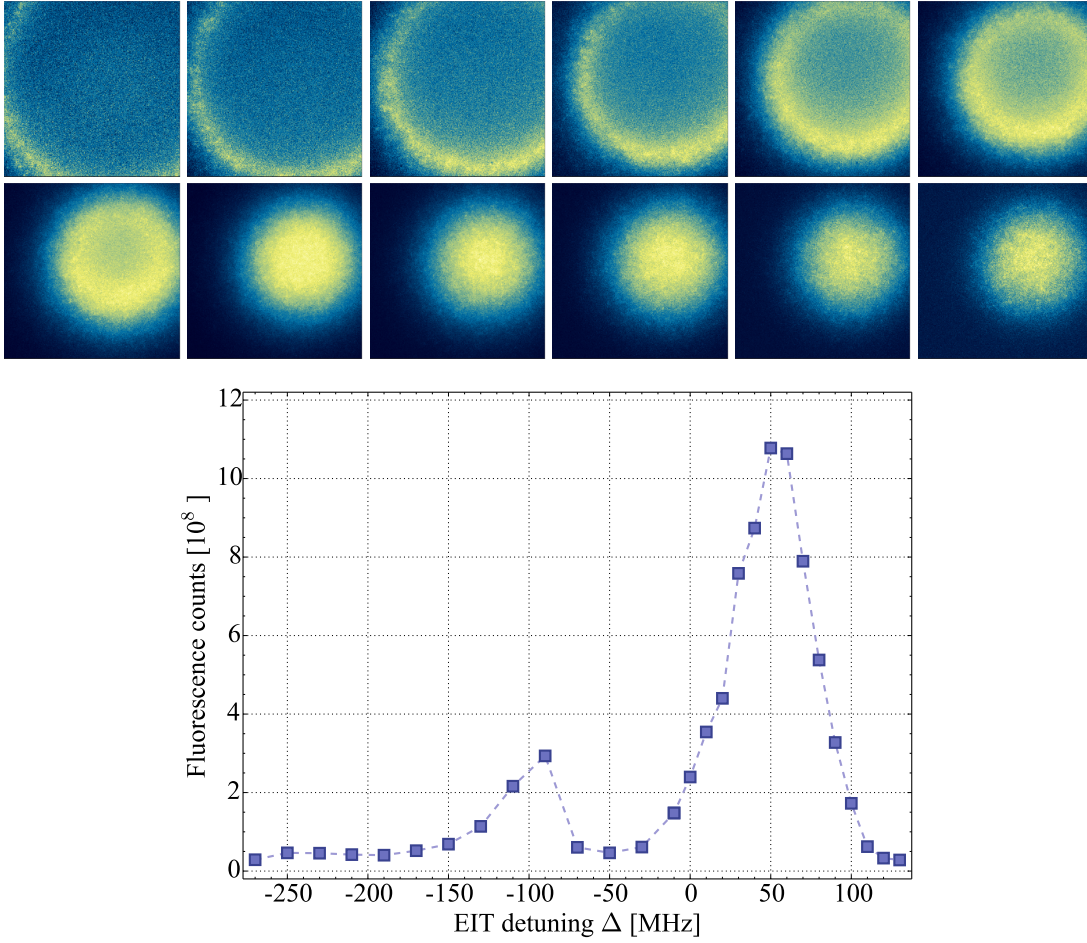


Figure 3.7: Top: Set of peak-normalised fluorescence pictures obtained varying the global EIT detuning Δ from -10 to 100 MHz. Bottom: Whole picture fluorescence counts as a function of EIT detuning Δ . Both EIT cooling resonances are located about 40-80 MHz blue detuned of the $4P_{1/2}$ $F=9/2$ ($\Delta = -155$ MHz) and $F=7/2$ ($\Delta = 0$) levels.

3.4 Motion coupling via Raman transitions

Achieving single-site resolution imaging requires cooling in the vertical direction to prevent atoms from hopping and therefore travelling along the microscope imaging direction which would result in very faint fluorescence of a single atom as the microscope depth of focus is only a couple of lattice layers. To circumvent the use of EIT radiation on the vertical axis, Raman transitions with momentum transfer between the horizontal and vertical planes were used to perform such task.

3.4.1 Far-detuned Raman transitions

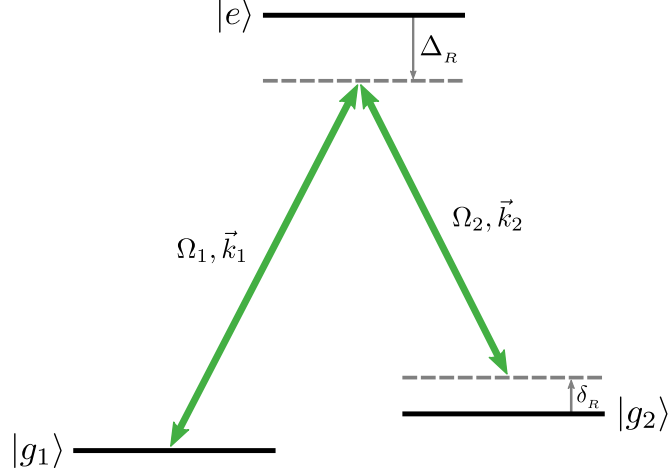


Figure 3.8: Raman transitions scheme in a Λ configuration with global detuning Δ_R from the excited state $|e\rangle$ and two-photon detuning δ_R between the two ground states $|g_i\rangle$ driven by light fields of Rabi frequency Ω_i and wavevector \vec{k}_i , $i \in \{1,2\}$.

Adiabatic elimination method

Taking the energy of level $|g_1\rangle$ as the energy reference and the frequency of the radiation coupling level $|g_1\rangle$ to $|e\rangle$ as the new rotating frame, the Hamiltonian of the Λ system depicted in Figure 3.8 can be written as [143]

$$\hat{H}/\hbar = -\Delta_R |e\rangle \langle e| - \delta_R |g_2\rangle \langle g_2| - \left(\frac{\Omega_1}{2} |e\rangle \langle g_1| + \frac{\Omega_2}{2} |e\rangle \langle g_2| + h.c. \right). \quad (3.4.1)$$

Using the general form of the wavefunction taken to be

$$|\psi\rangle = c_{g_1} |g_1\rangle + c_{g_2} |g_2\rangle + c_e |e\rangle \quad (3.4.2)$$

in the Schrödinger equation yields the following system of equation for the dynamics of the three complex amplitudes

$$\begin{cases} \dot{c}_{g_1} = i \frac{\Omega_1^*}{2} c_e \\ \dot{c}_{g_2} = i \delta_R c_{g_2} + i \frac{\Omega_2^*}{2} c_e \\ \dot{c}_e = i \Delta_R c_e + i \frac{\Omega_1}{2} c_{g_1} + i \frac{\Omega_2}{2} c_{g_2} \end{cases} \quad (3.4.3)$$

If the general detuning Δ_R is greater than any other characteristic angular frequency of the system, $\Delta_R \gg \Omega_1, \Omega_2, \delta_R, \Gamma$, the population of the excited state can be approximated to be constant, to the first order in $\Omega_{1,2}/\Delta_R$ and equals

$$c_e = -\frac{\Omega_1 c_{g_1} + \Omega_2 c_{g_2}}{2\Delta_R} \quad (3.4.4)$$

The system of equations of motion for the two ground state populations becomes

$$\begin{cases} \dot{c}_{g_1} = -i \frac{|\Omega_1|^2}{4\Delta_R} c_{g_1} - i \frac{\Omega_1^* \Omega_2}{4\Delta_R} c_{g_2} \\ \dot{c}_{g_2} = i \left(\delta_R - \frac{|\Omega_2|^2}{4\Delta_R} \right) c_{g_2} - i \frac{\Omega_1 \Omega_2^*}{4\Delta_R} c_{g_1} \end{cases} \quad (3.4.5)$$

The three level system is now seen to behave as an effective two level one where the two photon detuning δ_{eff} - two photon detuning shifted by the coupling A.C. Stark shifts - and the effective Raman Rabi frequency Ω_{eff} are identified as

$$\delta_{\text{eff}} = \delta_R - \frac{|\Omega_1|^2 + |\Omega_2|^2}{4\Delta_R} \quad \Omega_{\text{eff}} = \frac{\Omega_1 \Omega_2^*}{2\Delta_R} \quad (3.4.6)$$

So far we have neglected the motional degree of freedom of particles trapped in lattice sites which we will approximate as quantum harmonic oscillator. This notion is crucial for the understanding of motional coupling via coherent Raman transitions.

Motional degree of freedom - 1D

To take into account the motion of a particle, one needs to come back on the dipolar approximation, $e^{i\vec{k}\cdot\vec{r}} \ll 1$. For a two level atom trapped in a quantum harmonic oscillator, the total Hamiltonian to be considered is the sum of the two-level RWA Hamiltonian in an appropriate rotating frame \hat{H}_{RWA} and the quantum harmonic oscillator Hamiltonian \hat{H}_{QHO} , Eq. (1.2.6). The atomic eigenstates can be written as tensorial products of eigenstates of each Hamiltonian in the form $|g, n\rangle \equiv |g\rangle \otimes |n\rangle$.

The matrix element for a transition between states $|g, n\rangle$ and $|e, n'\rangle$ is equal to [144]

$$\langle \tilde{e}, n' | \hat{H}_{\text{tot}} | g, n \rangle = \frac{\hbar\Omega}{2} \langle n' | e^{i\vec{k}\cdot\vec{x}} | n \rangle \quad (3.4.7)$$

with $\vec{x} = \vec{x}_0(\hat{a} + \hat{a}^\dagger)$, where $\vec{x}_0 = x_0 \vec{e}_x$ and $x_0 = \sqrt{\hbar/2m\omega_x}$ is the spatial extent of the ground state wavefunction of the quantum harmonic oscillator trap on the x axis and Ω is the Rabi frequency of the driving radiation. The *Lamb-Dicke parameter* is introduced as $\eta_x = \vec{k} \cdot \vec{x}_0$ and correspond to the projection of the radiation wavevector

on the particle motion along one direction - here x . It is dimensionless and its square can be expressed as the ratio of a radiation photon recoil energy by the energy level splitting of the QHO trap

$$\eta_x^2 = \frac{\hbar^2(\vec{k} \cdot \vec{e}_x)^2}{2m} \cdot \frac{1}{\hbar\omega_x} = \frac{\omega_r}{\omega_x} \quad (3.4.8)$$

In the Lamb-Dicke regime, the expansion of $e^{i\vec{k} \cdot \vec{x}}$ leads to an approximation of the Rabi frequency corresponding to the transition $|g, n\rangle \rightarrow |e, n'\rangle$ which can be written as a cumbersome function [145] of the Lamb-Dicke parameter η :

$$\Omega_{n',n} = \Omega e^{-\eta/2} \sqrt{\frac{n_{<}!}{n_{>}!}} \eta^{|n'-n|} L_{n_{<}}^{|n'-n|}(\eta^2) \quad (3.4.9)$$

where $n_{< / >} = \min / \max(n, n')$, L_n^α are the generalised Laguerre polynomials and we have dropped the notation of the axis of motional quantisation for simplification, $\eta_x \equiv \eta$.

In the Lamb-Dicke regime where $\sqrt{n+1}\eta \ll 1$, the Rabi frequency $\Omega_{n',n}$ can be approximated to Ω for $\Delta n = n' - n = 0$; this transition which does not change the vibrational level of the particle in the trap is called *carrier transition*. The ones associated with a reduction/increase of vibrational level, $\Delta n \leq 0$ are called *red/blue sideband transitions*, the first sidebands having Rabi frequencies respectively of $\Omega_{n-1,n} = \sqrt{n}\Omega$ and $\Omega_{n+1,n} = \sqrt{n+1}\Omega$. From the definition of the *Lamb-Dicke parameter*, the *Lamb-Dicke regime* can be picture as the situation in which a photon recoil energy is so small compared to the trap energetic vibrational splitting that spontaneous emission is unlikely to change the vibrational level of the particle. So if one sets the detuning Δ of the radiation to only drive red sideband transitions, one would retrieve - upon spontaneous emission from the excited state - a particle in the ground state with a lower vibrational level, hence having performed cooling.

This method was first used for ions [146] for which vibrational trap frequencies exceed the linewidth of the spontaneous emission and single photon driving laser, a regime thus called *resolved sideband cooling*. For neutral atoms, this is rarely the case, as the laser linewidths are on the order of the spontaneous emission linewidth, in our case 6 MHz, and the achievable trap frequencies are 100-400 kHz. This is the reason why two-photon transitions are required for which the linewidth can be tuned rather small (< 10 kHz) to enter the *resolved sideband* regime.

3.4.2 2D EIT Cooling + Raman exchange

3.4.2.1 Implementation of Raman exchange

The principle of coupling the vibrational motion between two axis arises from using a two-photon Raman transition set with laser beams of different wavevector directions. The one-photon wavevector \vec{k} must now be replaced with the resulting wavevector of the two-photon Raman transition $\delta\vec{k} = \vec{k}_1 - \vec{k}_2$. If $\delta\vec{k}$ has non-null projections on at least two quantised motional axis, transitions where one quanta of motion is taken from an axis and added onto another one will occur [147].

We implement this by setting our two Raman beams with global detuning $\Delta_R = 8$ GHz, null two-photon detuning $\delta_R = 0$, $\vec{k}_1/|\vec{k}_1| = -((\vec{e}_x + \vec{e}_y)/\sqrt{2})$ (S \rightarrow N direction) and $\vec{k}_2/|\vec{k}_2| = -\vec{e}_z$ (colinear with \vec{g}) represented by the green beams on Figure 3.9. In this situation, a vibrational quantum can be exchanged between the vertical axis (z axis) and equiprobabilistically with either the West axis (x axis) or the East axis (y axis). To simplify the theoretical treatment, we assume that only the exchange occur between the x and z axes, great care having being taken on making the EIT cooling on the x and y axes as similar as possible. The Raman exchange Rabi frequency can be expressed as

$$\Omega_{n_x+1, n_z} = \Omega^0 \langle n_x + 1, n_z | e^{i\delta\vec{k}\cdot\vec{r}} | n_x, n_z + 1 \rangle \approx \Omega^0 \eta_x \eta_z \sqrt{(n_x + 1)(n_z + 1)} \quad (3.4.10)$$

where $\Omega^0 \equiv \Omega_{\text{eff}}$ is the effective two-photon Raman Rabi frequency from Eq. (3.4.6).

3.4.2.2 Final configuration

While the Raman beam couples the motion between the horizontal planes and the vertical axis, EIT cooling operates on the two horizontal x and y -axis according to Figure 3.9. The results of the cooling via Raman exchange is presented on the left graph of Figure 3.10 which depicts the expansion widths of the cloud normalised to the initial one after 1 ms time-of-flight imaging following the sudden release from the lattice. The vertical axis and the y -axis widths are respectively presented in light orange triangles and dark orange diamonds and without the Raman exchange in light green diamonds and dark green squares.

The presence of the Raman coupling changes little how EIT cooling reduces the observed cloud width - and therefore the temperature - of the horizontal axis. However the vertical axis goes from being heated by spontaneous emitted photons from the horizontal EIT cooling to being cooled when the Raman radiation couples both axes (light orange versus light green curves). The expansion widths decay curves are fitted as exponential decays and yield time constants of 0.42(2) ms and 1.7(2) ms for the

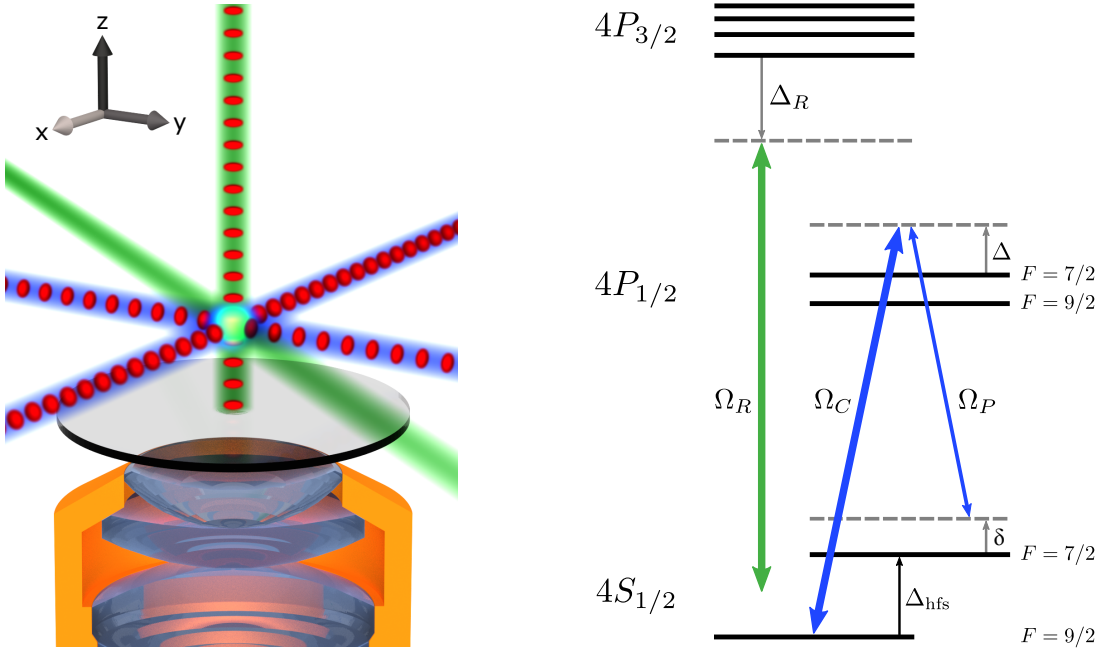


Figure 3.9: Scheme of the fermionic ^{40}K atoms in a 3D optical lattice were observed using fluorescence detection with a high-resolution optical microscope. The optical lattice (red ellipsoids) is composed of two retroreflected beams in the x- and y-axes, and a vertical beam retroreflected from the coated bottom vacuum window. Retroreflected EIT cooling beams (blue) were overlapped with the horizontal optical lattice and the Raman beams (green) were used to couple the motional states in the z-axis to the horizontal plane ones. Right: Final level scheme of the relevant states of ^{40}K , with off-resonant Raman beams (green) of global Rabi frequency Ω_R and Raman detuning Δ_R and near-resonant (detuning Δ) EIT coupling and probe beams (Rabi frequencies Ω_C and Ω_P , blue) with EIT two-photon detuning δ . From Fig. 1 of [92].

horizontal plane and vertical axis. Those correspond to cooling rates of $6(1) \hbar\omega.\text{ms}^{-1}$ and $0.8(3) \hbar\omega.\text{ms}^{-1}$ respectively, with $\omega = 2\pi \times 300(12)$ kHz being the vibrational frequency of all three lattice axes.

The narrowness of the two-photon nature of EIT cooling is verified by measuring the cloud width on the y-axis after 1.5 ms of time-of-flight ballistic expansion. As predicted theoretically, EIT cooling is optimal for a null EIT two-photon detuning $\delta = 0$ whereas blue sidebands can be favoured for negative detuning $\delta < 0$ displaying a maximal heating for $\delta = -1$ MHz. The width of the cooling feature is approximated to about 500 kHz.

With no EIT cooling beam on the vertical axis, fluorescence can be gathered through the objective with none or negligible parasitic background light, see Section 2.5.2.1. Figure 3.11 depicts our measurement of the evolutions of the whole cloud atom number and the integrated fluorescence counts versus two-photon EIT detuning δ after

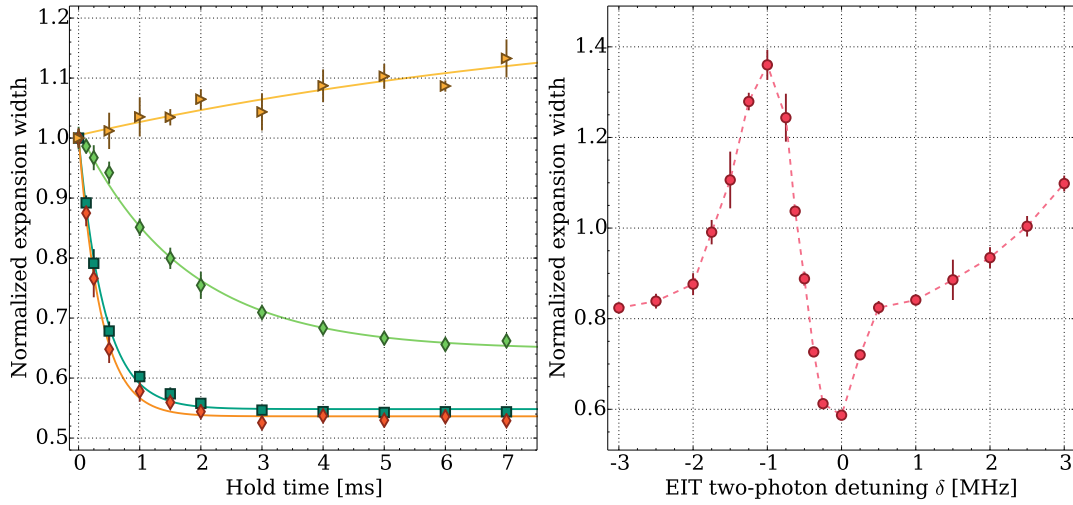


Figure 3.10: Left: expansion width of the atomic cloud after 1 ms time-of-flight, normalized to the initial width, for varying durations of EIT cooling. Cooling was observed in the y-axis (green squares). In the z-axis, we observed cooling with Raman beams present (green diamonds) and heating without (yellow triangles). Right: expansion width in y-axis as a function of two-photon detuning δ , after 1.5 ms of EIT cooling. Each datapoint is the average of five independent measurements, and the error bars represent the standard deviation as in the next figure. From Fig. 3 of [92].

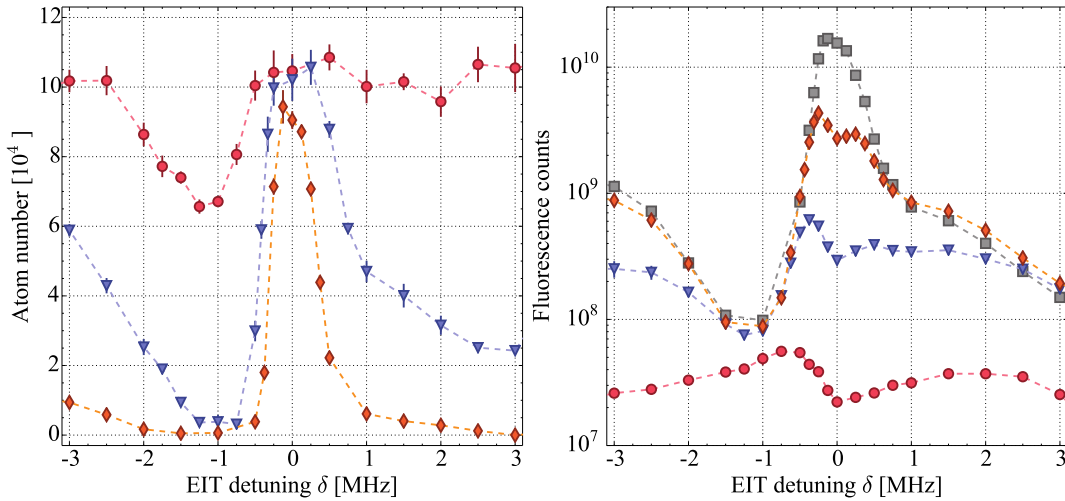


Figure 3.11: Left: atom numbers versus two photon detuning δ , after 1.5 ms (red circles), 30 ms (blue triangles) and 300 ms (orange diamonds) of EIT cooling, measured with absorption imaging. Right: integrated fluorescence counts versus δ during exposure times of 1.5 ms (red circles), 30 ms (blue triangles), 300 ms (orange diamonds) and 2,000 ms (grey squares) during EIT cooling. From Fig. 3 of [92].

EIT cooling with Raman exchange of 1.5 ms (red circles), 30 ms (blue triangles), 300 ms (orange diamonds) and 2 s (grey squares) durations.

As expected the total atom number decreases very quickly over time outside the 500 kHz wide region of efficient cooling centred at a null two-photon EIT detuning $\delta = 0$. The study of integrated fluorescence shows that the value of δ for which maximum overall fluorescence is obtained shifts as the integration time is extended, about $\delta = -750$ kHz for 1.5 ms (red circles) to $\delta = -[100, 0]$ kHz for 2 s integration duration (grey squares). When the atoms are heated out of the lattice, a much higher fluorescence rate is obtained than if they were coherently driven into a dark state by EIT cooling. On a short time scale, the high fluorescence rate primes over the short lifetime of the atoms whereas compromising for less fluorescence but longer lived atoms yields overall higher fluorescence per atoms over the time necessary to gather single site resolved fluorescence pictures.

Optimizing all the EIT cooling parameters on the complete 3D lattice population survival has been sufficient to enter the regime of single-site resolved fluorescence pictures, the next finer parameter optimisation phase being accessible after layer preparation, and with the occupation analysis software running to quantitatively study the image fidelity as shall be dealt with in Section 3.6.

3.4.2.3 Rabi frequencies

EIT beams Rabi frequencies

The determination of our EIT beams Rabi frequencies relies on the measurement of "depumping" rates. We define "depumping" as the opposite of repumping, i.e. using radiation set on transitions from the $4S_{1/2}$ $F = 9/2$ ground state to either the $4P_{1/2}$ or $4P_{3/2}$ excited states manifold, having the effect of putting the atoms into the $4S_{1/2}$ $F = 7/2$ ground state after subsequent spontaneous emission. We proceed as follow:

- First we select one of the EIT beams and reduce its power using a neutral density filter after the regulation photodiode. This ensures that depumping rate measurements are possible even close to resonance with a slow enough decay and that we can also reasonably infer the Rabi frequency at beam powers used during EIT cooling from those depumping rates using a lower power beam (operating with identical PID behaviour). With a ND 2 filter, the beam power was lowered from 660(1) μ W down to 6.8(1) μ W.
- We measure the decay of the $F = 9/2$ population using absorption imaging with cooling light only at different EIT beam offset frequencies, see Figure 3.12.

- The decay rates are extracted from fitting with exponential decays which in turn get fitted with a Lorentzian function to yield the location of resonance, the linewidth Γ and the saturation parameter s_0 as shown in the caption of Figure 3.12
- Using the value found for the saturation parameter s_0 and Γ , we use equation D.0.17 to deduce the Rabi frequency and we then bootstrap it to the power and number of beams used during horizontal EIT cooling.

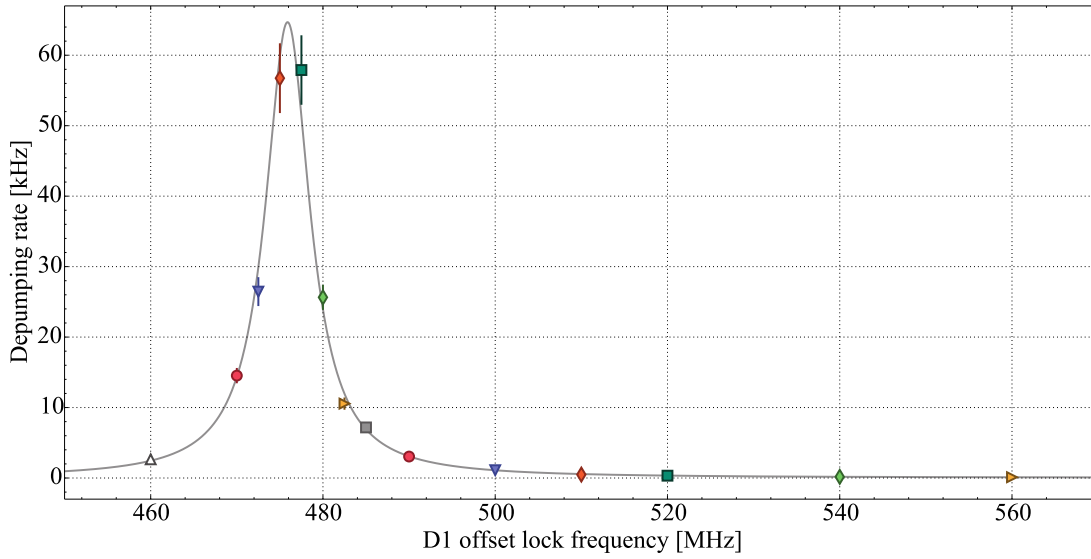


Figure 3.12: Depumping rates as a function of the radiation offset lock frequency. A Lorentzian fit yields the resonance to be located at an offset lock of 475.9(1) MHz and a saturation parameter to equal $s_0 = 3.8(1) \times 10^{-3}$.

Using the measured value of $\Gamma_{D_1} = 2\pi \times 5.956(11)$ MHz, the Lorentzian fit yields a saturation parameter $s_0 = 3.8(1) \times 10^{-3}$ leading to a Rabi frequency of one reduced power beam of $\Omega_{LP-1D} = 2\pi \times 0.65(1)$ MHz. The total EIT Rabi frequency during our procedure is then $\Omega_{HP-2D} = \Omega_{LP-1D} \sqrt{PR \times BR \times CR}$ where PR, BR and CR designates the Power, number of Beams and Cycles ratios which equal $660/6.8 = 97(1.5)$, 2 and 2 respectively. The cycle ratio CR is taken to be equal to 2 as the probability of decaying to the $F = 7/2$ ground state upon spontaneous emission from the $4P_{1/2}$ $F = 7/2$ state is roughly one half. We obtain $\Omega_{HP-2D} = \sqrt{97 \times 2 \times 2} \Omega_{LP-1D} = 2\pi \times 5.10(4)$ MHz. With the EOM setting a quarter of the optical power equally in the two sidebands, we deduce the coupling and probe EIT Rabi frequencies to be $\Omega_C = 2\pi \times 4.4(1)$ MHz and $\Omega_p = 2\pi \times 1.8(1)$ MHz respectively.

Raman Rabi frequency

Our measurement of the Raman Rabi frequency is much simpler as it involves measuring the vertical expansion width of the cloud after 5 ms of time-of-flight depending on the Raman two-photon detuning δ_R as seen on Figure 3.13. Contrary to transitions involving a state with a finite lifetime, the Raman two-photon transition couples two fundamental states of infinite lifetime making its measured linewidth differ from its bare Rabi frequency only by power broadening which is neglected as our measurement requires beam powers way below intensity saturation. The obtained set of points is fitted with a Lorentzian function to yield a half width at half maximum (HWHM) of 28(1) kHz taken to be our overall effective Raman Rabi frequency $\Omega_R/2\pi$.

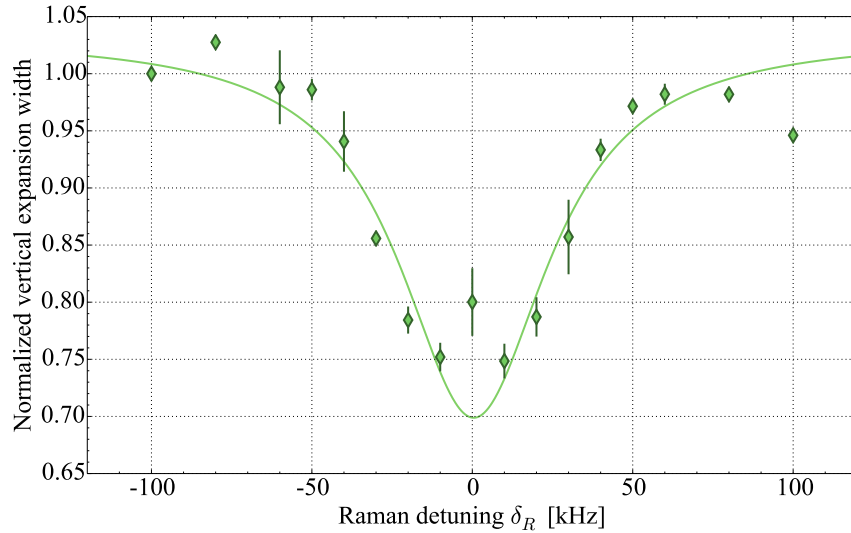


Figure 3.13: Vertical expansion width of the atomic cloud after 5 ms of EIT cooling with Raman exchange normalised to the $\delta_R = -100$ kHz point. The Lorentzian fit yields a half width at half maximum of 28(1) kHz taken to be the overall Raman Rabi frequency $\Omega_R/2\pi$.

3.4.3 Raman spectroscopy

With the Raman beams set, a convenient alternative to modulation spectroscopy could be used to measure the lattice vibrational frequency. Detuning one of the Raman laser beams from the other by δ_R , one can address the blue sideband and heat the atoms. Figure 3.14 plots the vertical normalised expansion width of the atomic cloud after sudden release of the vertical lattice from 8.4 and 10.2 Watts as a function of Raman two-photon detuning δ_R tuned by changing the driving frequency of one of the laser beam AOMs. The gaussian fits reveals that the vibrational frequencies of the

vertical lattice at those powers are respectively 301.3(8) and 331.2(4) kHz, the ratio of frequencies of $\simeq 1.10$ matches the expected value of $\sqrt{10.2/8.4} = 1.10$ knowing that the square of the vibrational frequency has a linear dependence with respect to the lattice beam power as in Eq. (1.2.33).

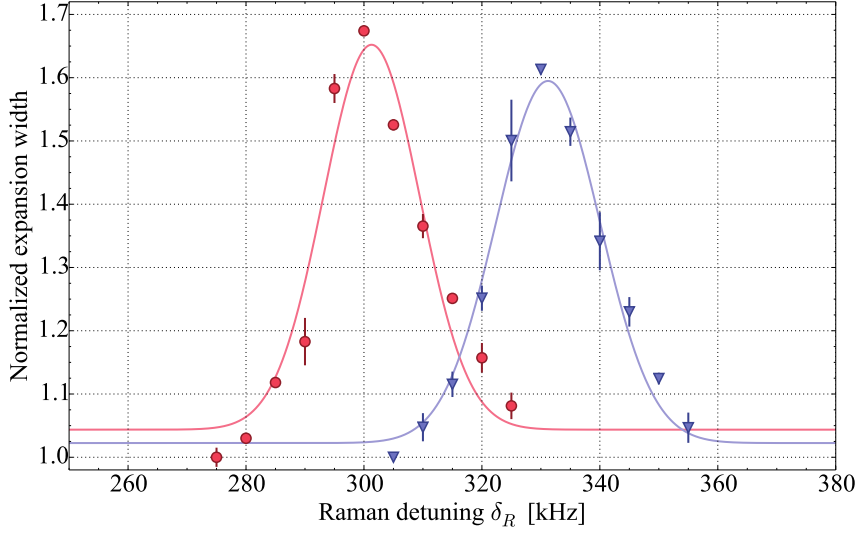


Figure 3.14: Raman spectroscopy of the vertical lattice obtained by plotting the vertical expansion width after sudden release from the 3D lattice in which the atoms were exposed to the Raman beams against two photon Raman detuning δ_R for two vertical lattice powers of 8.4 (red circles) and 10.2 W (blue triangles). Fits result in centres located at 301.3(8) and 331.2(4) kHz and widths of 8(1) and 8.9(7) kHz. As expected the temperature of the atoms in the lattice increases when the two photon Raman detuning matches the lattice vibrational frequency, driving more carrier and blue sidebands than red ones due to our initial occupation of low vibrational quantum levels.

3.5 Layer selection

With the horizontal plane being actively EIT cooled and the vertical one passively by Raman exchange making it clear of parasitic D_1 background light, the only remaining obstacle to single-layer single-site resolution fluorescence images is the layer selection process.

3.5.1 Optical pumping

The layer selection process relies on discriminating layers of atoms in the vertical lattice by means of a position dependent microwave transition, realised by a magnetic field gradient. The first step of the procedure is to put all the atoms in the same state by optical pumping.

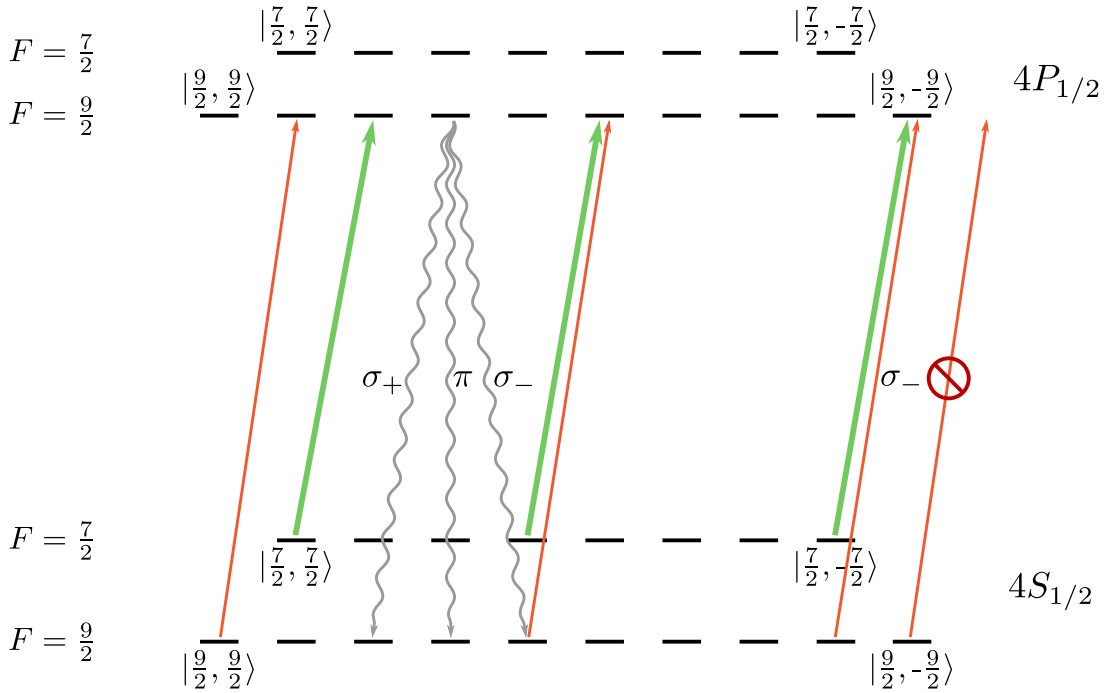


Figure 3.15: Level scheme of optical pumping on the D_1 line. The stronger repumper light (green) ensures that the atoms stay predominantly in the $4S_{1/2}$ $F=9/2$ state while the σ_- polarisation of cooler and repumper light (orange) drives them toward the $m_F = -9/2$ sublevel, a dark state to all radiations.

Figure 3.15 represents the optical pumping performed on the D_1 -line which consists in applying σ_- strong repumper and weak cooler radiations while lifting the degeneracy between the m_F sublevels with a weak static magnetic field to drive the atomic population of the $4S_{1/2}$ $F = 9/2$ exclusively in the most negative m_F sublevel, i.e. $|F = 9/2, m_F = -9/2\rangle$ in which they shall remain, this level being a "dark state" to

all the light fields of this scheme due to the lack of $m_F = -11/2$ state in the $4P_{1/2}$ manifold.

The key component of optical pumping is the quality of the circular polarisation of the cooler and repumper radiations. The purer the circular polarisation, the fewest cycles are necessary to bring the atoms to the $|9/2, -9/2\rangle$ state therefore minimising the heating caused by momentum recoil kicks.

Figure 3.16 presents two spectra, one prior to optical pumping of the atoms loaded in the vertical optical lattice only right after transport (grey squares) and the one obtained after optical pumping (blue triangles) performed with both σ_- cooler/repumper radiations propagating along the vertical axis and 50 MHz blue-detuned from $4P_{1/2}$ $F=9/2$ level. This orientation proved to be the best of all usable ones for optical pumping firstly because the polarisation circularity can be fully optimised for the D_1 line on the vertical axis - on the long axis, the path would be shared with the D_2 MOT light and has therefore slightly not pure σ polarisation and the auxiliary long axis runs at a slight angle from the direction of the long axis coils making it difficult to align the magnetic field direction with its propagating direction. As the frequency either 50 MHz blue or red detuned probably reduces the stochastic heating caused by the $4P_{1/2}$ $F=9/2$ strong inverted potential, detuning this way with identical powers in the beams increased the optical pumping process duration due to the reduced scattering rate but delivered slightly more atoms at a lower temperature than if it were performed on resonance.

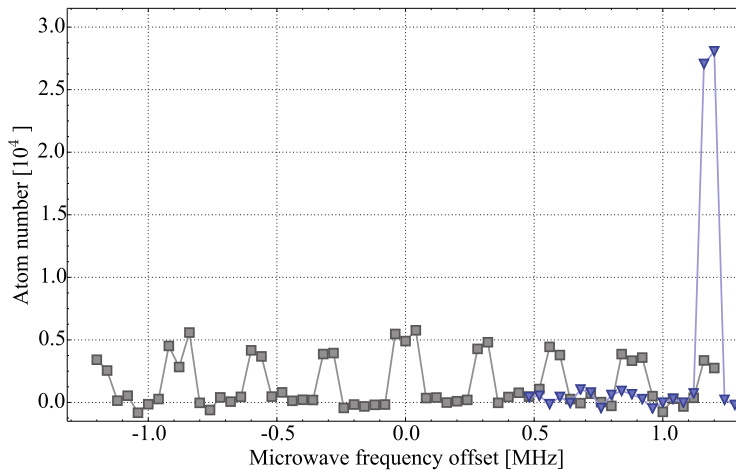


Figure 3.16: Full microwave spectra of ^{40}K trapped only in the vertical lattice for an unpumped sample (gray) and after 50 MHz blue-detuned optical pumping (blue). Whereas the atoms were roughly equally populating all the m_F sublevels of the ground state, they no longer do after optical pumping and mostly occupy the $F = 9/2, m_F = -9/2$, only contributing to the outer most right microwave transition.

Qualitatively analysing the height of the spectra of Figure 3.16, if we were to assume that each of the seven inner doubly-degenerate σ transitions contribute with half weight to the total atom number, one would calculate a $0.5 \times (7 \times \frac{1}{2} + 2 \times 1) \times 10^4 = 2.75 \times 10^4$ atom number which is exactly the height of the outer most non-degenerate peak representing the population of the $|9/2, -9/2\rangle$ state. This method gives a rough indication if optical pumping was performed well - without atom losses and with only atoms in the $|9/2, -9/2\rangle$ state. Only monitoring the increase of the $|9/2, -9/2\rangle$ population as a function of optical pumping duration (performed with repumper imaging after a MW transfer) and the evolution of the total atom number (using standard absorption imaging) is a trustworthy method, preferably accompanied by a temperature measurement of the unpumped and optically pumped sample.

Now that all the atoms have been optically pumped to the best of our capabilities into the $|9/2, -9/2\rangle$ stretch state, they are ready to undergo a height dependent microwave transfer to the other stretched $|7/2, -7/2\rangle$ state.

3.5.2 Blowout process

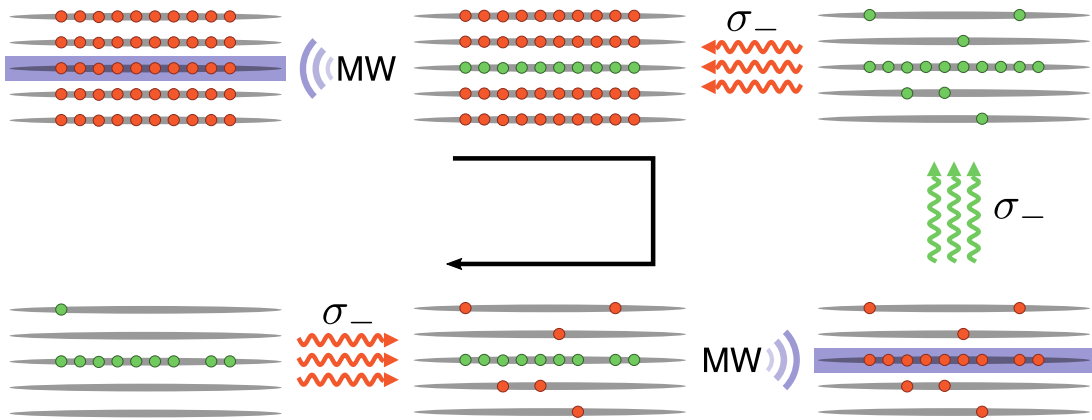


Figure 3.17: Layer selection procedure with double blowout. The atoms in the $4S_{1/2}$ $F=9/2$ and $F=7/2$ are represented in orange and green respectively. The cooling and repumper radiations are respectively coloured in orange and green. The microwave transfer is here presented as acting on a single layer of the vertical lattice as a dark blue area.

The layer selection process starts by using our Feshbach coils in anti-Helmholtz configuration to generate a strong magnetic field vertical gradient. As mentioned earlier in section 2.31, a current of 20 A causes a vertical dependence of the $4S_{1/2}$ stretched states microwave transition frequency of 20.45(5) kHz/ μm or about 10 kHz per lattice layer. The direction of the gradient is aligned with the gravity acceleration \vec{g} , the

centre of the Feshbach coils being located about 4 mm above the atomic cloud.

As illustrated on Figure 3.17, we proceed as follow:

- Using this induced feature, we perform a first order hyperbolic sequent microwave pulse (HS1 pulse) to selectively transfer one or several layers (depending on the pulse frequency width) from the optically pumped prepared $|9/2, -9/2\rangle$ state to the $|7/2, -7/2\rangle$ state.
- The vertical lattice depth is lowered to allow the atoms to escape easily upon excitations by a σ_- light pulse set on resonance with the $4S_{1/2} |9/2, -9/2\rangle \leftrightarrow 4P_{3/2} |11/2, -11/2\rangle$ cycling transition. This leaves the selected atoms previously MW transferred to the $4S_{1/2} |7/2, -7/2\rangle$ unaffected and removes most of the untransferred ones from the trapping potential.
- Unfortunately, the hyperfine splitting between the $4P_{3/2}$ $F=11/2$ and $F=9/2$ manifolds only equals 7.35Γ (44.1 MHz), see Figure 1.1, which causes a non negligible number of unselected atoms initially in the $4S_{1/2} |9/2, -9/2\rangle$ state to remain in the lattice in the $4S_{1/2} |7/2, -7/2\rangle$ state having spontaneously decayed after off-resonant excitation to the $4P_{3/2} |9/2, -9/2\rangle$ state. We therefore repump all the $4S_{1/2} |7/2, -7/2\rangle$ atoms to the $4S_{1/2} |9/2, -9/2\rangle$ state and repeat the process.

The quality of our selection procedure is nicely illustrated on Figure 3.18 which is constituted of two fluorescence pictures, the one on the left with microwave transfer of three layers and on the right with exactly the same experimental sequence but shutting down the microwave signal generator. In the later situation, all the atoms are to be blown out of the trap. As it can be guessed from the sequence missing the microwave transfer, the atoms are not all blown away even after two resonant light pulses as about two atoms per layer remain. Two in focus and some others (about 4-6) out of focus in the adjacent first to second layer in each direction, deduced from our depth of focus only being about three layers wide, making fluorescing atoms outside of said region a unrecognisable blur.

3.5.3 Layer selection optimisation

The best layer selection was achieved after optimisation of the optical pumping parameters, ensuring that the magnetic field direction during the microwave transfer was orthogonal to the vertical lattice layers (reducing all the static orthogonal magnetic fields) and correcting for small horizontal magnetic gradients.

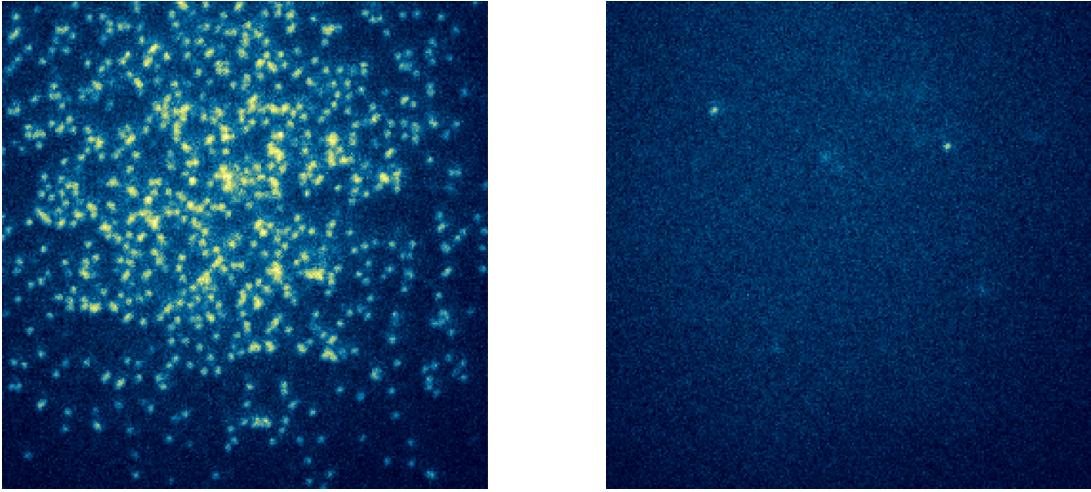


Figure 3.18: Comparison of two fluorescence pictures of a couple of selected layers with (left) and without (right) microwave signal showing us that not more than a couple of atoms are left in layers outside of the selected regions.

Optimising the optical pumping can be performed as explained earlier in Section 3.5.1 but the parameters should be readjusted not to the best microwave spectroscopy results but to the background total fluorescence after blow out. The polarisation of the optical pumping beam but more importantly its duration and offset frequency should be retuned to minimise the total fluorescence obtained after the layer selection procedure without the two microwave transfers. The resonant blow away and repumping pulses (durations and frequencies) are also finely optimised on that quantity.

3.5.3.1 Minimising horizontal bias field

Our method to minimise the horizontal static magnetic fields uses the magnetic field dependence in the following way: the centre of the Feshbach coils lying above the atoms, the gradient is accompanied by a static magnetic field of identical direction. Any added horizontal static field would enhance the norm of the total magnetic field which can be measured by microwave transfer. The conjunction of a static magnetic field with a strong vertical gradient makes it possible to obtain a spatial signature of any stray static field. Indeed if we set the microwave transfer width to be smaller than the atomic cloud but wide enough to select a large portion of the atoms, said portion would be imaged either directly with repumper-only imaging (see Section 2.31 explaining how the gradient was measured) or using normal absorption imaging after blow way.

Let's assume that a slab of selected atoms is a height z for a microwave transfer centred at a frequency f_0 . Any stray horizontal static field would add to the local total

magnetic field norm, such that to transfer an identical slab - i.e. at the same height z - the microwave frequency would have to be increased to a value f' greater than the original one $f' > f_0$. Conversely, the measurement of the best current to be run in the horizontal bias coils is easily made by taking a fixed microwave frequency f_0 and observing the height of the slab moving up in the presence of a stray static field. The direction of the move depends on the location of the coils centre relative to the atomic cloud, if it were located under the atoms, the slab would move downward instead of upward.

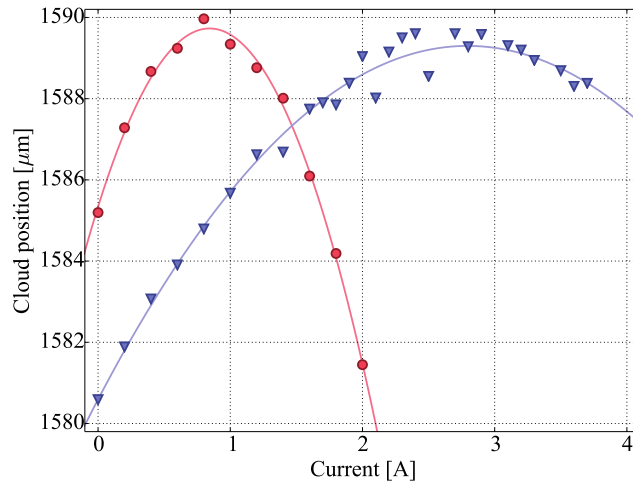


Figure 3.19: Cloud position as a function of the horizontal pairs of coils (red circles) and Longitudinal middle coil (blue squares). Both curves are fitted with second order polynomials to yield the currents of 0.84(1) and 2.8(1) A, respectively for the horizontal and longitudinal coils, corresponding to the minimal height of the cloud and hence a magnetic field most aligned with the vertical lattice axis.

Figure 3.19 displays the height of the transferred slab of atoms depending on the Long 2 axis (blue triangles) and Horizontal axis (red squares) coils current. Only because of imaging convention the lower the position of the cloud, the higher its measured position value. The slab height data are fitted with quadratic polynomial functions to yield the optimal values 0.84(1) and 2.8(1) A for the Long 2 coil and Horizontal coils current.

3.5.3.2 Compensating residual gradient

Ensuring the absence of horizontal static fields did not exclude a non negligible horizontal gradient to remain and was observed in our attempt at resolving the vertical lattice layers with layer selection procedures whose microwave transfers had a frequency width inferior to the corresponding size of one layer (< 10 kHz). The pictures

obtained looked quite promising but were exhibiting a pair a wide stripes (similarly to the left lower picture of Figure 3.22) which would shift diagonally with a change in microwave frequency.

Those stripes could only be caused by a weak horizontal gradient tilting the iso-magnetic field plane with respect to the horizontal plane. Thus making the microwave transfer addressing more than a single layer as drawn in Figure 3.21. Its top row shows a side view of the vertical lattice layers and one iso-magnetic field plane being inclined with respect to the horizontal plane as the horizontal gradient increases from right to left. The bottom row represents the horizontal view after projection along the vertical axis of the transferred atomic population at the intersections of the iso-magnetic field plane and the lattice layers.

The horizontal gradient had a direction roughly aligned diagonally on our images along the East axis direction. Due to lack of space on the NE port of said axis, we installed a single coil on the SW lattice chamber viewport to generate a magnetic gradient which could compensate the pre-existing one. Figure 3.20 illustrates how this coil was calibrated. Selecting a rather thick slab of atoms (100 kHz wide), the full cloud is not kept and the gathered fluorescence decreases when the centre of the microwave frequency sweep is scanned away from the frequency corresponding to the height of the cloud centre (left). The measurement is repeated for multiple values of the coil current (right) and the centre frequencies are fitted with a quadratic function.

Even if the minimum of horizontal static magnetic field generated at the cloud by this coil corresponds to a current of 1.5 A, our interest lies in removing the pre-existing horizontal gradient which only available signature is obtained by averaging multiple fluorescence pictures of single layer wide microwave selected atoms as in Figure 3.22. The optimal value for such cancellation is reached for a current of -250 mA. Such value was selected from the obvious lack of visible stripe structure on averaged fluorescence pictures. From the lack of an identical coil on the opposite side, this current generates a static magnetic field which raises the height of the selected layer as pictured on Figure 3.21 to which we can easily adapt to by either increasing the microwave transfer centre to select lower layers or by adjusting the PIFOC voltage to lift the focus of the microscope objective to match the raised selected layer.

3.5.3.3 Single layer resolution

With the horizontal gradient cancellation, we enter the regime where resolving single vertical lattice is possible. So far we have not mentioned the magnetic field stability at all as it should not have been issue, the second of the two microwave transfers of the layer selection process following the first one by only the duration required by the resonant blow away and repumping pulse, at most 20 ms.

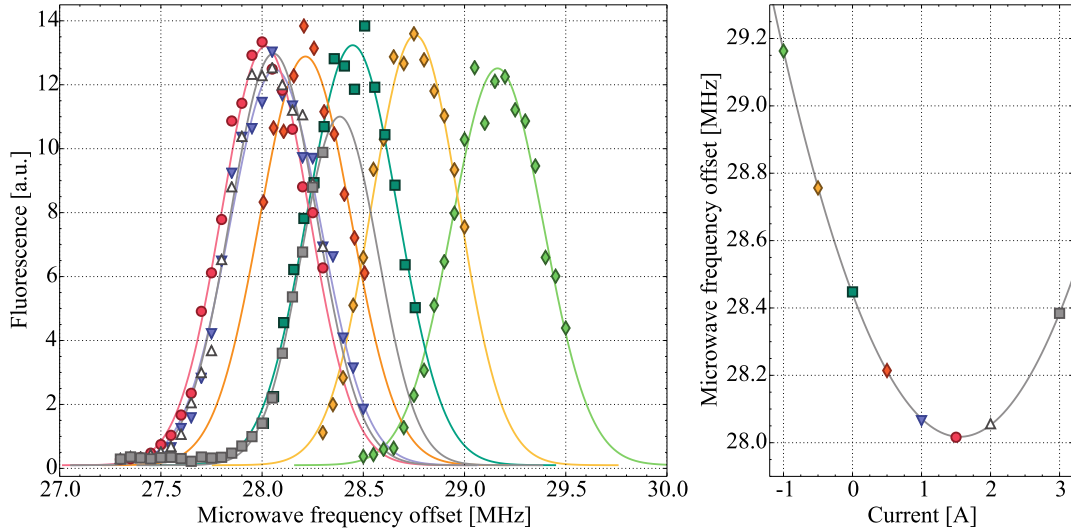


Figure 3.20: Calibration of the gradient compensating coil. Left: curves show the whole picture fluorescence counts as a function of microwave transfer frequency offset for eight different coil currents, -1, 0.5, 0, 1, 1.5, 2 and 3 A depicted as green diamonds, light orange diamonds, green squares, dark orange diamonds, blue triangles, red circles, white triangles and gray squares, respectively. The data is fitted with Gaussian functions to yield the microwave frequency offset corresponding to the height in focus of the microscope objective. Right: Those values are then plotted against the coil current and fitted with a second order polynomial to yield the current corresponding to the minimal horizontal magnetic field.

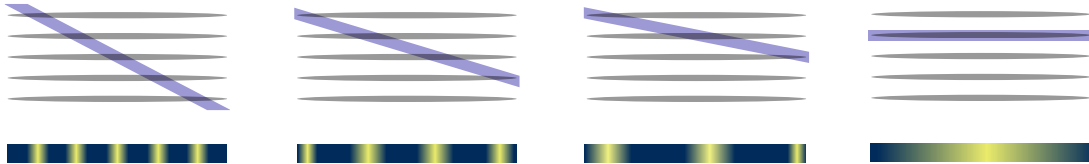


Figure 3.21: Top: set of side views of five layers of the vertical lattice for four different angular tilts of a magnetic field slab (blue) of about 5 kHz width our usual conditions. Bottom: set of strips representing the vertical projection of the kept atomic population after the layer selection process which would only conserve the atoms located at the intersection of the slab and the vertical lattice layers.

On such short time scales, thermal effects do not reveal themselves. However they do when it comes to trying to resolve the vertical lattice layers by varying the frequency of the microwave transfer to run over it vertically for different experimental sequences, each of them lasting about 30 s.

Since our bottom Feshbach coil cooling circuit leakage, its water flow had to be reduced to prevent further leakage. High currents can still be run through the Feshbach coils but the cooling being less efficient, temperature increases occur regularly when the

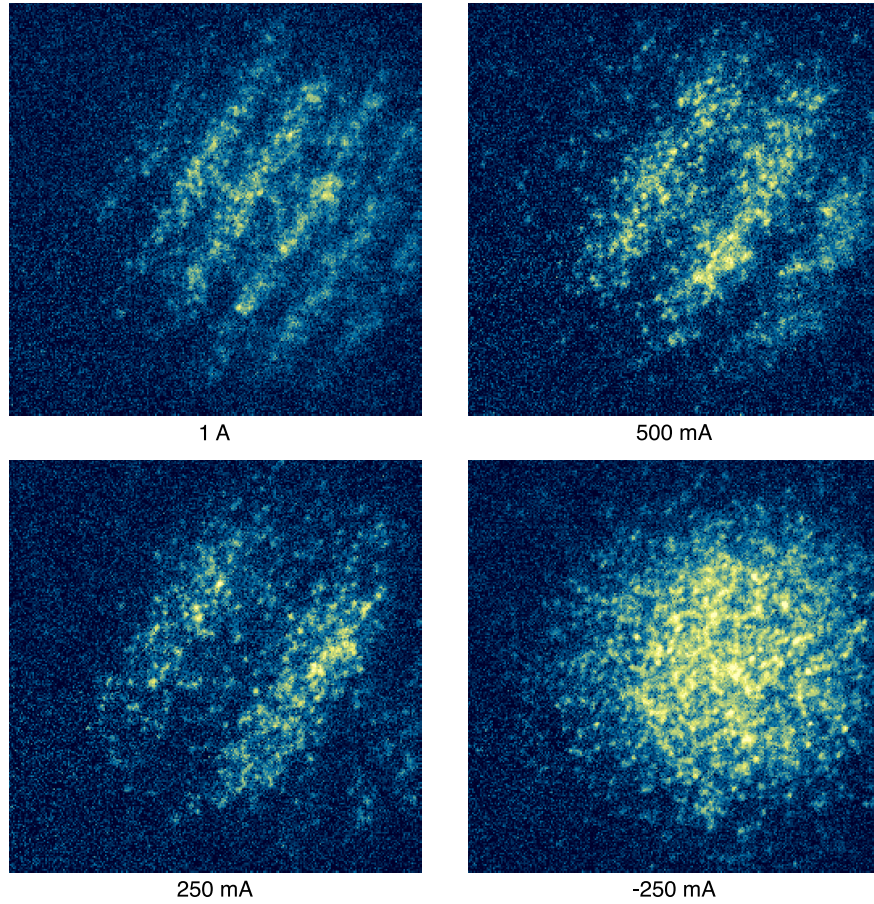


Figure 3.22: Fluorescence pictures average 30 (top left), 20 (bottom right) and 15 times (else) after microwave transfer width corresponding to one layer for four compensating gradient coil currents of 1, 0.5, 0.25 and -0.25 A (top to bottom, left to right). The magnetic gradient is progressively tilted by the gradient coil to become horizontal so the microwave transfer no longer addresses narrow regions of multiples layers, i.e. rendering stripes, but rather one entire single layer of the vertical lattice.

coils are left idle for too long. Temperature fluctuations of a few degrees change the coil characteristics and surely the microscope objective length through thermal dilatation. For instance, the linear thermal expansion coefficient of brass is $\alpha_{\text{brass}} = 20 \times 10^{-6} \text{ K}^{-1}$. Applied to our microscope objective length ($\simeq 10 \text{ cm}$), a temperature raise of one Kelvin would change its height by $2 \mu\text{m}$, a little less than four vertical lattice layers.

To stabilize the temperature of the lattice chamber close surroundings, the following requirements had to be met:

- As mentioned earlier in Section 2.4.3.3, the Feshbach magnetic field versus current response stabilises after 2-3 hours (thermalisation of the power supply internal electronics).

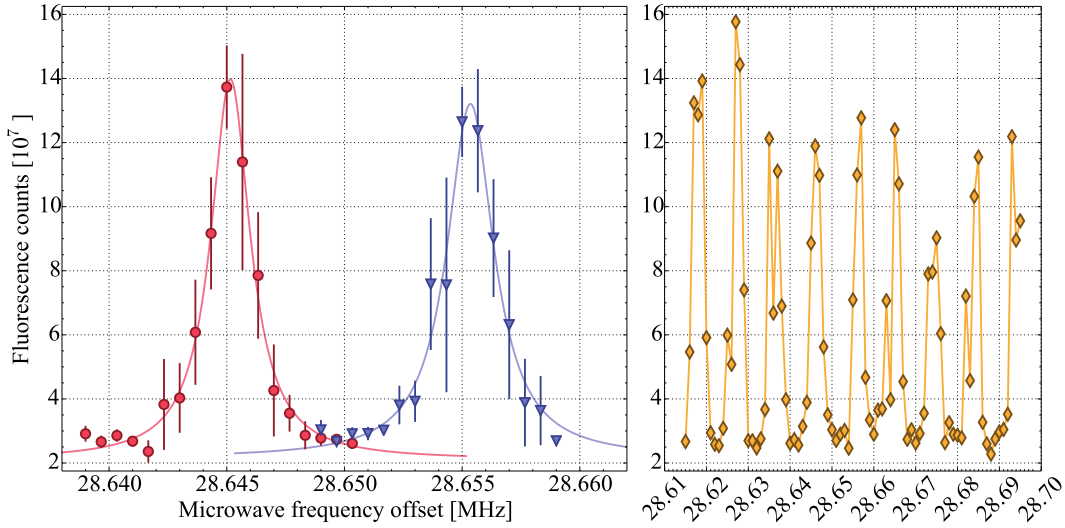


Figure 3.23: Left: Fluorescence counts of whole picture averaged 5 times as a function of microwave frequency offset. Data points are taken every 0.66 kHz for 4 kHz wide HS1 transfers. The two datasets (red and blue) are taken under the same conditions but simply colour two adjacent vertical lattice layers. Both sets are fitted with Lorentzian functions to yield a difference in microwave frequency of 10.2(1) kHz leading to an inferred layer spacing of 499(6) nm. Right: Single shot measurement of the same quantity across nine successive vertical layers. The first and last layers are separated by 76(2) kHz which leads to an averaged layer spacing of 465(16) nm. Both lattice spacing values are below the known result of 532 nm. This is certainly caused by rather slow heating of the apparatus during approximately 40 minutes, a rather long duration of data acquisition.

- Implementation of an idle sequence which consists in running an experimental sequence with all the thermal critical components active exactly as a useful sequence but with all the laser pulses disabled. The experimental software can be set to run such idle sequence each time a data taking sequence is not being operated on the machine.

The apparatus usually reached a thermal stability enabling the resolution of the vertical lattice spatial structure after one or two hours of a normal and idle sequences running. Figure 3.23 illustrates such resolution with on its left two adjacent vertical lattice layers being clearly identified by selecting vertical extents of atoms with 4 kHz width microwave transfers - $\simeq 200 \mu\text{m}$ thick - and varying their frequency centre in steps of 0.66 kHz. With five shots averaging, we obtain a very good signal to background ratio of about 7 with Lorentzian fits whose centres are separated by a little more than 10 kHz therefore spaced close to a lattice spacing away. The right data gathered without averaging describes nine consecutive vertical lattice layers with

microwave transfers of identical width but in steps of 1 kHz. Exploitation of the peaks yields in average 9.5 kHz per layer, around 464 μm . The deviation from the known value a 532 μm is caused by remaining thermal drifts but which are sufficiently small not to reduce the signal to background ratio over the total duration of the measurement ($\simeq 40$ min).

3.6 Imaging performances

3.6.1 Single-site resolution

Cooling scheme and layer selection combined lead to typical fluorescence pictures (with 2×2 binning) shown on Figure 3.24 taken after loading the lattice from a rather dilute cloud, $T = 3.0T_F$, and performing EIT cooling and Raman exchange for 1.5 s in a 3D lattice $k_B \times 245(20)\mu\text{K}$, $\omega_{lat} = 2\pi \times 300(12)$ kHz deep on all three axes. The signal-to-noise ratio exceeds one thousand and a single atom fluoresces on average 1,000(400) photons into the camera. Both properties enable the identification of atoms and therefore of lattice site positions by a deconvolution algorithm.

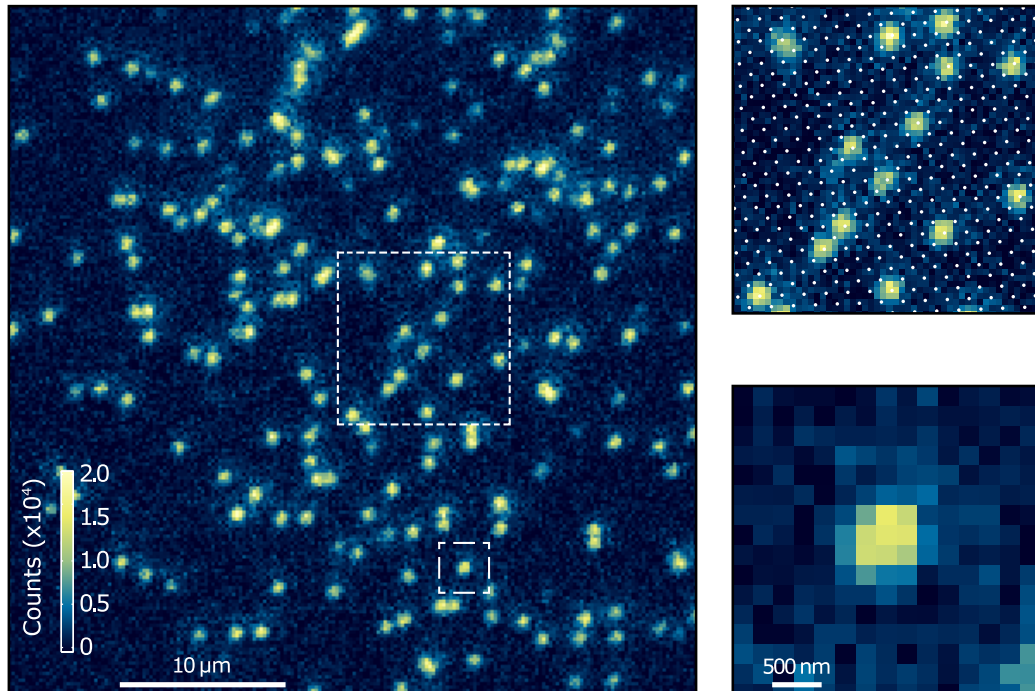


Figure 3.24: Left: fluorescence image of a dilute cloud of ^{40}K atoms in the optical lattice (1.5 s exposure time with EIT cooling). Top right: $10 \times 10 \mu\text{m}$ subsection of the left picture represented as the largest dotted square; white dots mark the lattice sites. Bottom right: magnified subsection of the left picture showing the individual atom surrounded by the smallest square box on the left picture. From Fig. 2 of [92].

Algorithms previously used by the Bloch group (MPQ, Garching) were employed to yield the precise orientation of the lattice angles, $47.599(3)^\circ$ and $-42.833(3)^\circ$ with respect to the horizontal direction of the obtained fluorescence pictures and the magnification of whole imaging system to be 5.133 pixels per lattice spacing ($532 \mu\text{m}$) from the evaluation of mutual distances between 600 isolated atoms.

Those imaging properties are then used as inputs of a deconvolution algorithm in conjunction with the averaged point-spread function, left of Figure 3.25, to infer the occupation of each lattice sites. From there, the amount of fluorescence in a 3×3 pixels area centred on the lattice location were converted to photon counts to yield a Gaussian distribution of an average of 1,000(400) photons for an occupied site and less than 200 photons for an empty one, allowing the unambiguous determination of the existence or lack of an atom at a site.

Our photon capture efficiency is estimated to be 8.6%, deducted from the objective solid angle of $\Omega/(4\pi) = 13\%$, the 80% transmission through the objective, lenses and interference filters, see Section 2.5.2.1 and the 83% quantum efficiency of the EMCCD camera¹. With $1.0(4) \times 10^3$ fluoresced photons per atom acquired, the total fluorescence rate per atom is calculated to be $8(3) \times 10^3 \text{ s}^{-1}$. The combined scattering rates on the red sideband for both horizontal axes is limited by the upper band $\gamma_+/2$ where $\gamma_+ = \omega\Gamma/(4\sqrt{\Delta^2 + \Omega_C^2 + \Omega_P^2})$ is the width of the narrow line of the Fano profile [140, 142] (right of Figure 3.4). From our measurement of the EIT Rabi frequencies, we estimate $\gamma_+ \simeq 2\pi \times 7 \text{ kHz}$.

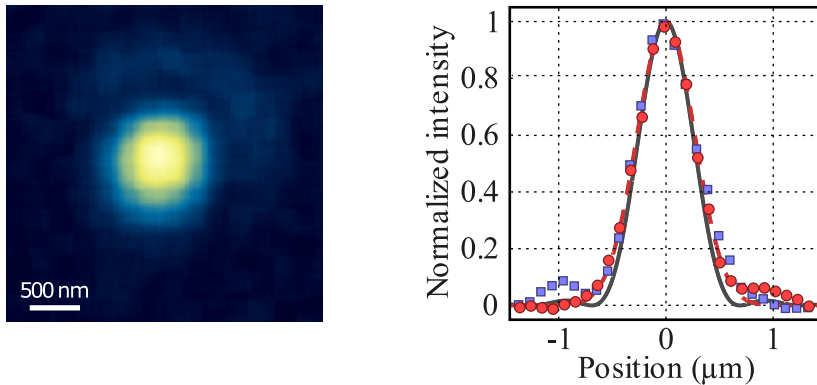


Figure 3.25: Left: measured point-spread function using 640 single-atom images similar to the bottom right magnification of the previous figure, averaged using subpixel shifting. Right: horizontal (red circles) and vertical (blue squares) profiles through the centre of the averaged single-atom images (left), fitted (horizontal only) with a Gaussian profile (red dashed line). The grey line shows the diffraction-limited point-spread function (PSF) of the microscope objective. Extracted from Fig. 2 of [92].

¹Andor iXon 897

The average using subpixel shifting of 640 distinct occupied sites similar to the unaveraged one featured on the bottom right of Figure 3.24 yields the point-spread function (PSF) of our imaging system which is compared, right of Figure 3.25 to the theoretical one (grey curve) through its two axes profiles (horizontal/vertical as red circles/blue squares). Our microscopy setup has a PSF of 630(10) nm, close to the diffraction-limited one.

3.7 Image fidelity

3.7.1 Inhomogeneity of EIT cooling - Lifetimes

The inhomogeneity of EIT cooling can be studied by comparing the accumulated fluorescence of an unprepared cloud in a 70×70 sites central region with the whole atomic cloud lifetime. The size of the square central region was chosen to be 70 lattice sites because the light shift difference in a region of this size would not exceed 20 MHz which is about the span of EIT global detuning in which the lifetimes of the complete cloud can be considered similar.

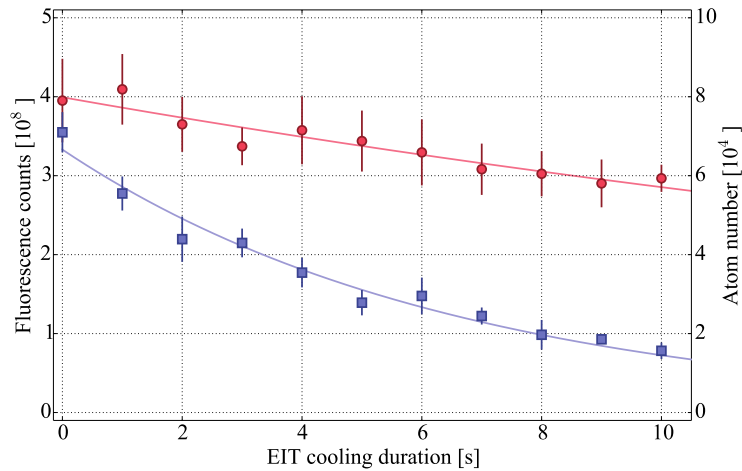


Figure 3.26: The curves show fluorescence counts within a region of 70×70 lattice sites integrated over a period of 250ms (red circles) and atom number of the complete cloud measured by absorption imaging (blue squares) for varying EIT cooling duration. Fits to exponential decays yield time constants of 30(3) and 6.6(4) s for the fluorescence counts and whole atom number respectively. In supplementary material of [92].

Figure 3.26 shows the accumulated fluorescence counts of said central region during 250 ms (red circles) and the complete cloud atom number (blue squares) measured from absorption imaging after a variable EIT cooling duration. The difference in lifetime, given by exponential fits, is quite striking with the 30(3) s lifetime of the selected

region fluorescence exceeding the 6.6(4) s one of the whole atomic cloud by almost a factor of 5 and justifies our choice to limit ourselves to studying the imaging fidelity in this square central region.

3.7.2 Hopping and losses

To characterise the imaging fidelity, two distinct fluorescences pictures of 500 ms duration were taken during the first and last 500 ms of the 1.5 s EIT cooling scheme. Even with a third of the accumulation time, the SNR of single-atom fluorescence is good enough to allow the deconvolution algorithm to output a binary map of the lattice sites occupation.

The two figures of merit introduced for image fidelity are the *fractional hopping* quantify by the fraction of atoms h defined as normalised number of appearing atoms in previously empty sites and the *fractional losses* l representing the normalised number of empty sites which were previously occupied.

The bottom graph of Figure 3.27 displays both quantities h and l respectively in blue squares and red circles versus the two-photon EIT detuning δ calculated on the central square region of 70×70 lattice sites. On the top of Figure 3.27, are two pairs of 20×20 sites binary maps which illustrate the calculation of h and l with the red circles and blue hollow squares representing the occupation map of the first and last of the two 500 ms duration fluorescence picture taken respectively. The left one corresponds to a picture taken for $\delta = -150$ kHz and the right one for $\delta = 50$ kHz.

Some improvements were performed from the previous experimental conditions to obtain such results and were:

- The global EIT detuning was increased to be more blue detuned to $\Delta = 12 - 13\Gamma$.
- The global Raman detuning was also increased to be more red detuned to $\Delta_R = 10$ GHz.
- The retro-reflection of the horizontal EIT beams was removed and the power was a little more than double to keep the same scattering rate as initially.

We report hopping and losses to be as low as $h = 3.5(1.5)\%$ and $l = 4.2(1.9)\%$ and remain close to those values in the $\delta = [-100, 100]$ kHz. The losses more than the hopping increases quickly outside of this region which echoes with the data points of the atomic counts of the whole cloud after 2 s (orange diamonds), left part of Figure 3.11.

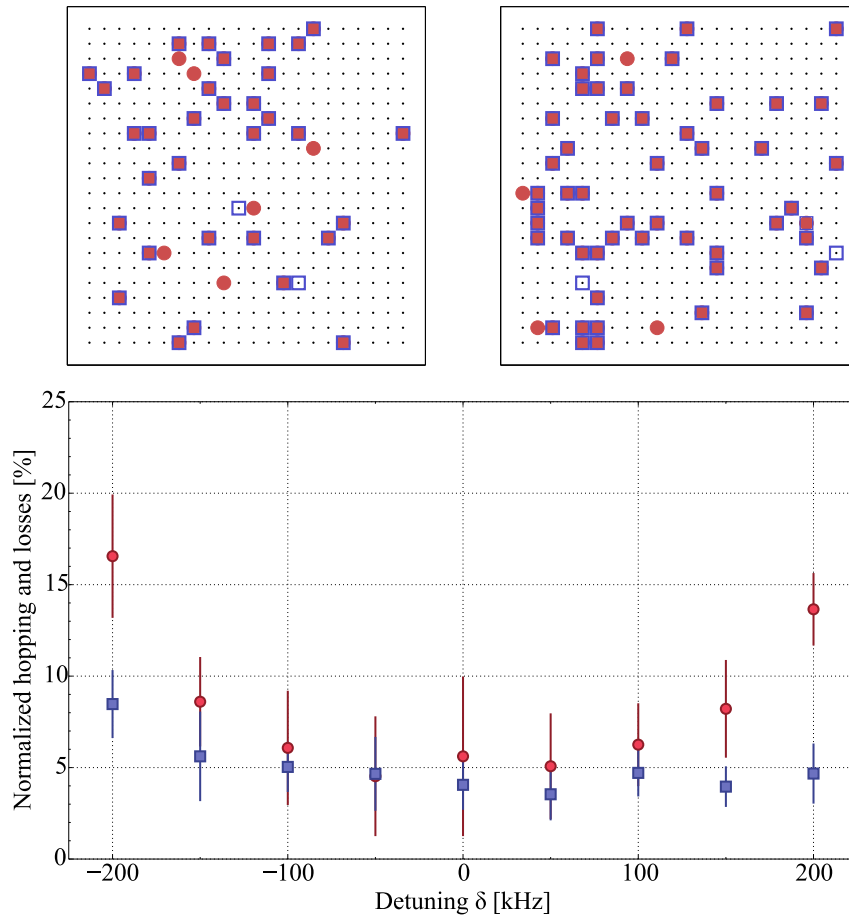


Figure 3.27: Fraction of atoms appearing (blue squares) on a previously empty site in the second of two successive fluorescence images (500 ms exposure time, 500 ms delay between the two images), normalized to the number of atoms in the first image. Also shown is the fraction of atoms lost that has disappeared between the two images (red dots). The panels show binary maps of the lattice site occupations of the first (red circles) and second image (blue squares). They show regions of 20×20 lattice sites; however, the data is analysed in a wider region of 70×70 sites. Each data point results from the average of ten fluorescence images; the error bars represent the standard deviation. Inspired from Fig. 4 of [92].

3.7.3 Stochastic heating

Even if the blue detuned EIT cooling scheme ensures that the effective upper state, of which the atom preferentially scatter, is trapped; the predominant heating process is probably caused by off-resonant excitations to the $4P$ excited states which are 5 times more anti-trapped than the $4S$ ground state is trapped due to the existence of the $1,170 \text{ nm } 4P_{1/2} \rightarrow 3D_{3/2}$ transition making the lattice trapping radiation relatively close blue detuned from this transition.

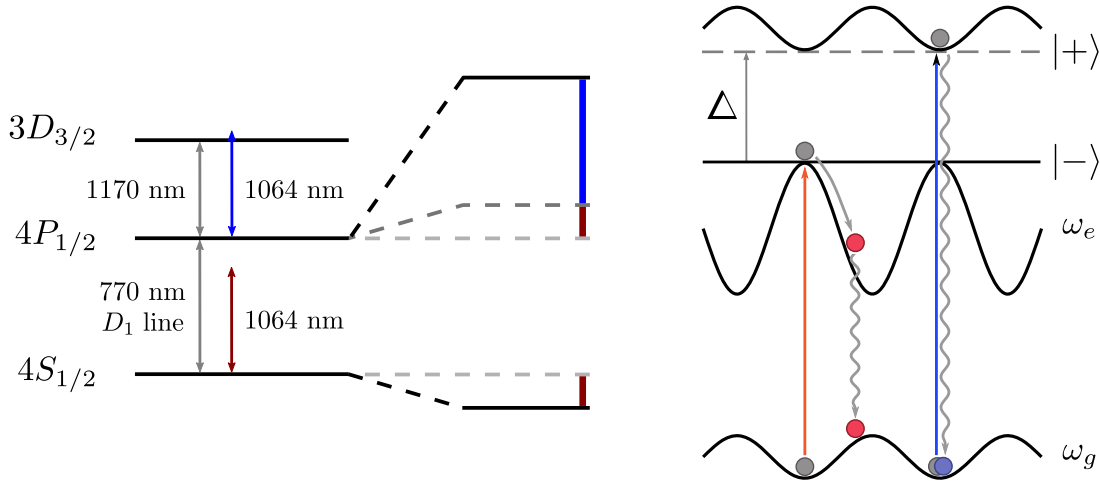


Figure 3.28: Left: level scheme of the states of ^{40}K involved in the strong inverted potential of the $4P_{1/2}$ state. With the dipolar matrix element of the $4S_{1/2} \rightarrow 4P_{1/2}$ and $4P_{1/2} \rightarrow 3D_{3/2}$ in the same order of magnitude, the trapping 1064 nm radiation being more closely blue detuned from $4P_{1/2} \rightarrow 3D_{3/2}$ transition than being red detuned from the D_1 line causes the A.C. Stark shift of the $4P_{1/2}$ to be 5.38 stronger than what it would be in the absence of the $3D_{3/2}$ state. Right: relevant level scheme of the dressed $4P_{1/2}$ state in the presence of the EIT cooling radiations. The virtual levels $|+\rangle$ and $|-\rangle$ contain predominant admixture of the $4S_{1/2}$ and $4P_{1/2}$ levels respectively making the $|+\rangle$ level, off which the atoms predominantly scatter during EIT cooling (blue), trapped with angular frequency quite close to the ground state potential one, ω_g . However close resonant radiation (orange), $\Delta = 10 - 13\Gamma$, would cause the atom to evolve in a strongly anti-trapped potential, ω_e , which will result in heating after subsequent spontaneous emission (wavy arrows) back to the trapping ground state potential.

Excitation to a strong repulsive trapping potential will result in a wavepacket quickly expanding in space. The atom can subsequently spontaneously decay into a higher vibrational state or higher band. Such heated atoms might move across the lattice before being lost or cooled down to a different lattice site.

The classical heating process of a particle evolving back and forth between potentials of distinct trapping frequencies is called *stochastic heating*. The relative gain in

energy from cycling through the excited state repulsive potential of frequency ω_e back to the ground state trapping one of frequency ω_g is given by

$$\frac{E_f}{E_i} = \frac{(\omega_g^2 + \omega_e^2)^2}{4\omega_g^2\omega_e^2} = \frac{(1 + \eta)^2}{4\eta} \quad (3.7.1)$$

where $\eta = |U_r/U_t| = (\omega_e/\omega_g)^2$ is the absolute value of the ratio between the repulsive and trapping potential, the derivation of the previous formula can be found in W. Setiawan's PhD thesis [148]. Considering the $4S_{1/2}$ and $4P_{1/2}$ levels of ^{40}K , the ratio of potential strength is $\eta = 5.38$ which leads to a tremendous energy gain of 95% per cycle.

Chapter 4

Outlook

Achieving single-site resolution imaging was the first step toward the study of strongly correlated fermions. Our sample was loaded into the 3D lattice from a temperature of $3.0 T_F$ which is well above the quantum regime. In this short chapter, the preliminary work on reaching the degeneracy regime but making the sample denser and colder shall be presented starting with the dimple optical traps followed by locating Feshbach resonances, RF mixing and high-field imaging.

4.1 Optical dimple traps

4.1.1 Squeezing beam

The vertical squeezing beam described in Section 2.3.5 aims at deepening the crossed optical dipole trap in a narrow vertical region. The waist of the squeezing beam was limited by the pre-existing optical components of our setup to a waist at focus of about $15 \mu\text{m}$. With both horizontal optical dipole trap beams constituting the CODT having waists at the atoms location of $80.6(7)$ and $69.9(4) \mu\text{m}$, we obtain an average theoretical squeezing factor of about 5.

To measure the effect of the squeezing beam, we first loaded the atoms into the CODT and superimposed the squeezing beam. The vertical lattice is then ramped up to freeze the vertical atomic distribution. The CODT and the squeezing beam are then ramped down and we proceed to slicing with a variable height thick slice ($200 \text{ kHz}/10 \mu\text{m}/20$ layers) so the total atomic population can be determined with absorption imaging as displayed in Figure 4.1.

The effect of the squeezing beam is quite evident from the three-fold increase of atomic population in the central layers. Gaussian fitting the vertical distribution yields an experimental squeezing factor close to 5 coinciding with the theoretical prediction.

4.1.2 Horizontal dimple - 850 nm

As mentioned in Section 2.5.2.3, the horizontal dimple is shone onto the atoms through the microscope objective and was set to have a waist of $23 \mu\text{m}$ at the typical height

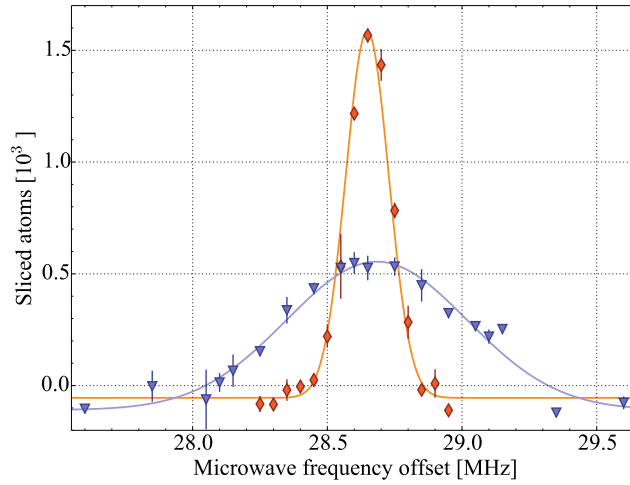


Figure 4.1: Number of atoms remaining in a 200 kHz/10 μm wide slice with/without squeezing beam (orange/blue) as a function of the slice vertical position given here as the centre frequency of the MW HS1 sweep. Gaussian fits give atomic distribution "waists" of 160(9) and 670(50) kHz corresponding to 8 and 33 μm .

of the single layer we isolate and perform fluorescence imaging onto. We directly used fluorescence imaging to align this beam precisely to the centre of the vertical lattice layers and observed its effect on the atomic distribution in it. Figure 4.2 displays two fluorescence pictures, one (left) of the typical atomic distribution in a single layer of the vertical lattice layer and the second when the dimple is brought

Both picture share the common experimental sequence which consists in loading the vertical lattice from the CODT and isolating a single layer. The difference lies in the presence of the tight dimple which is shone after the layer selection while we perform forced evaporation of the vertical lattice to half of its initial depth. Horizontal lattices are then added, and the depths of all lattices are later increased to perform fluorescence imaging.

This sequence doesn't constitute a real proof of the effect of the dimple during the vertical lattice evaporation as the atoms are not completely released from the dimple into the vertical lattice but constitute a good start in the forced evaporation of the horizontal confinement in its presence. The expected dimple effect combined with the ability to tune the atomic collision rate with Feshbach resonance should allow sufficient evaporative efficiency and bring us into the degenerate regime.

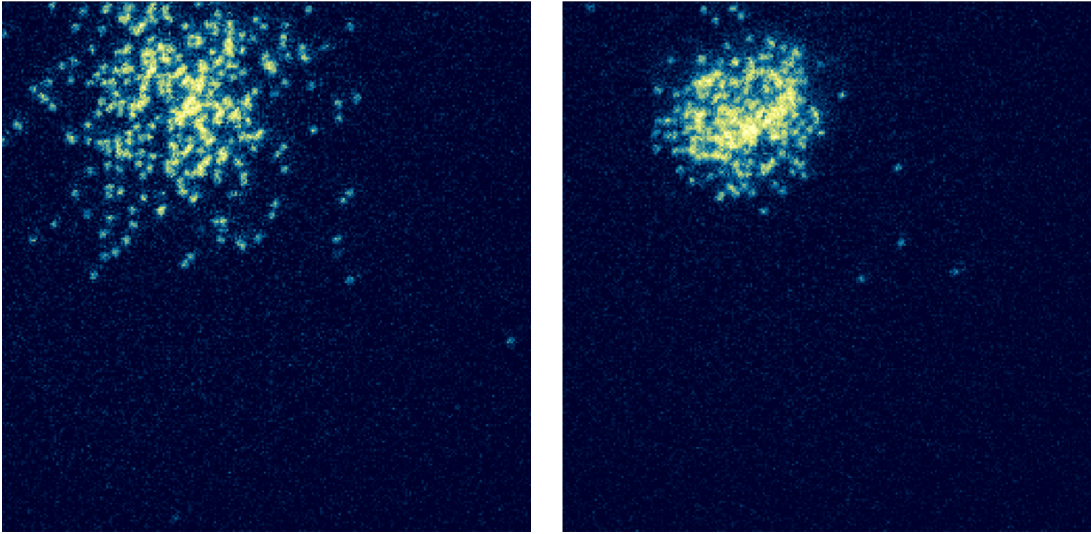


Figure 4.2: Fluorescence pictures after a typical sequence (left) and one with the horizontal dimple present with a forced evaporation in the vertical lattice to half its initial depth prior to freezing the atomic distribution in the presence of both.

4.2 Evaporation tools

Evaporating further will probably require the use of Feshbach resonances in order to increase the scattering rate to compensate for a drop in collision rate due to the low oscillation frequencies of shallow traps. This technique is routinely used in the group of Tillman Esslinger to obtain a degenerate Fermi gas mixture of ^{40}K in the $4S_{1/2}$ $|9/2, -9/2\rangle$ and $|9/2, -5/2\rangle$ states (see Niels Strohmaier PhD thesis [149] for further details).

4.2.1 Spin mixture

The first crucial step for evaporation of fermions in general and for the detection of Feshbach resonances is the ability to create a spin mixture, in our case of $|9/2, -9/2\rangle$ and $|9/2, -7/2\rangle$. Our apparatus lacks a good interaction strength between radio frequencies and the atoms in the Science chamber and we haven't been able to drive Rabi oscillations between hyperfine sublevels so far. However a slow sweep across the resonance still leads to transferring enough of the $|9/2, -9/2\rangle$ atoms in the $|9/2, -7/2\rangle$ state to obtain a spin mixture as it can be witnessed on the microwave spectrum in Figure 4.3.

To obtain such a spin mixture, the magnetic field is increased to about 90 G to lift degeneracy between the $|9/2, -9/2\rangle \leftrightarrow |9/2, -7/2\rangle$ and $|9/2, -7/2\rangle \leftrightarrow |9/2, -5/2\rangle$ hyperfine transitions as it can be seen on the right part of Figure 4.4 respectively

represented in gray and orange curves calculated using the Breit-Rabi formulae 1.1.13. Then, a linear sweep across the resonance is performed and the magnetic field ramped back down to a value appropriate for microwave spectroscopy.

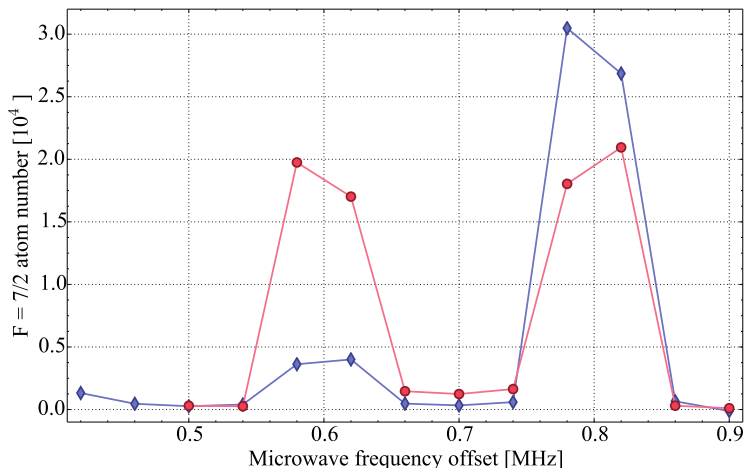


Figure 4.3: Two outermost right peaks of MW spectra, red(blue), with(without) RF transfer on the $|9/2, -9/2\rangle \leftrightarrow |9/2, -7/2\rangle$ transition.

The red and blue spectra of Figure 4.3 correspond to such a sequence with only the RF signal generator turned off for the latest one. In this case we simply obtain a MW spectrum of our hyperfine populations of an optically pumped sample: mainly atoms in the $|9/2, -9/2\rangle$ state. If the RF transfer occurs only on $|9/2, -9/2\rangle \leftrightarrow |9/2, -7/2\rangle$, the second to last MW peak height corresponding to the $|9/2, -7/2\rangle \leftrightarrow |7/2, -5/2\rangle$ and $|9/2, -5/2\rangle \leftrightarrow |7/2, -7/2\rangle$ transitions greatly increases while the next one does not; proof that only the $|9/2, -7/2\rangle$ state and not the $|9/2, -5/2\rangle$ has been populated by the RF transfer.

We then bootstrapped the RF frequency at magnetic fields encompassing the s-wave Feshbach resonance between the $|9/2, -9/2\rangle$ and $|9/2, -7/2\rangle$ states. Those results are presented in Figure 4.4. Fitting the RF frequency as a function of the magnetic field using the Breit-Rabi formula yields a magnetic field strength to coil current conversion factor of 14.93(2) G/A in good accordance with the one obtained using MW spectroscopy of 14.97(2) G/A, see Section 2.4.3.1.

4.2.2 Feshbach resonances

Feshbach resonances arise from the coupling between an energetically closed molecular bound state and a pair of scattering atoms. While the process enables molecular formation under certain circumstances, they are more broadly used as a tool to tune

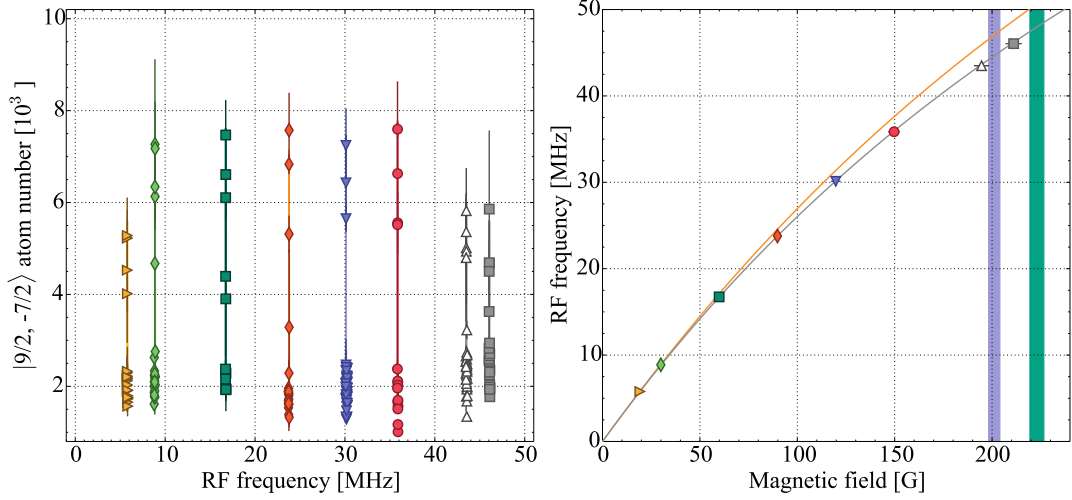


Figure 4.4: Left: Atom number of the $|9/2, -7/2\rangle$ hyperfine level after 20 kHz wide, 100 ms long RF linear sweeps for various magnetic field strength. Right: Fitting the RF transfer centre frequency with the theoretical one of the $|9/2, -9/2\rangle \leftrightarrow |9/2, -7/2\rangle$ transition (grey) yields a factor of 14.93(2) G/A for the magnetic field to Feshbach coils current conversion factor. Additionally, the yellow curve represents the $|9/2, -7/2\rangle \leftrightarrow |9/2, -5/2\rangle$ transition expected frequency and the blue/green filled areas depict the magnetic field regions in which the scattering length are 3 times their background values for the s-wave Feshbach resonances between $|9/2, -9/2\rangle \leftrightarrow |9/2, -7/2\rangle$ ($|9/2, -5/2\rangle$) respectively located at 202.10(7) and 224.21(5) G [72, 150].

the inter-atomic scattering length, noted a , which behaves as

$$a(B) = a_{\text{bg}} \left(1 - \frac{\Delta B}{B - B_0} \right) \quad (4.2.1)$$

where a_{bg} is the background scattering length, B_0 the Feshbach resonance location and ΔB its width. Figure 4.5 plots the scattering length for the two last mentioned s-wave Feshbach resonances.

In the last stages of forced evaporation, when trap potentials become shallow, the trapping oscillation frequency is reduced and so is the collision rate. This tends to slow the evaporation procedure, and enhancing the scattering length can compensate shallow trap geometries and restore a collision rate high enough so evaporation can be performed in less than a minute.

To locate the Feshbach resonances, a spin mixture of $|9/2, -9/2\rangle$ and $|9/2, -7/2\rangle$ was created from an optical pumped sample in the CODT and the magnetic field was then increased to values near the measured value of 202.1 G [151]. We let the sample settle at this magnetic field magnitude before ramping it down and performing absorption imaging to measure the atom number. Two Feshbach resonances were

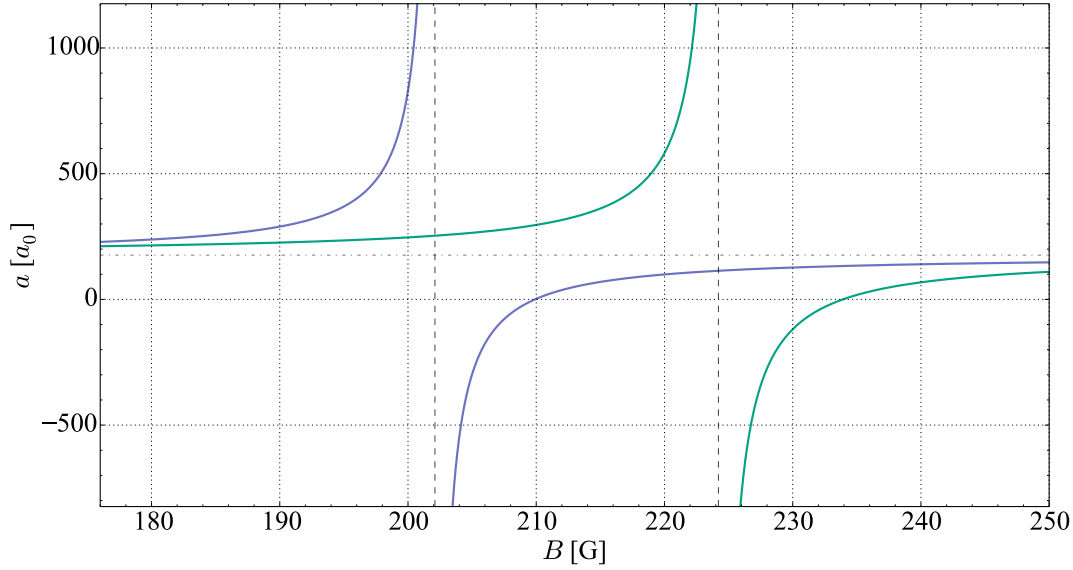


Figure 4.5: Scattering length in units of Bohr radii as a function of magnetic field in the vicinity of the Feshbach resonances involving the scattering pairs of hyperfine levels $|9/2, -9/2\rangle, |9/2, -7/2\rangle$ (blue) and $|9/2, -9/2\rangle, |9/2, -5/2\rangle$ (green) respectively centred at 202.1 and 224.21 G (pair of vertical dotted lines). The horizontal dash-dotted line coincides with the background scattering length of $176 a_0$ [72, 150].

detected as losses in atom number caused by the enhancement of the scattering rate at 119.9(5) and 202.3(1) G as displayed in Figure 4.6.

The precise calibration of the Feshbach coils enables us to almost certainly identify at 200 G, the p-wave resonance between two $|9/2, -7/2\rangle$ atoms a couple of Gauss before the s-wave $|9/2, -9/2\rangle \leftrightarrow |9/2, -7/2\rangle$ resonance itself located at 202.1 G. The p-wave resonance is predominant probably because our sample is too hot and favours it over the s-wave one. The temperature of the sample also shifts it toward higher magnetic field [152]. Unfortunately our RF Rabi frequency is not high enough to allow us to fully transfer all the $|9/2, -9/2\rangle$ atoms into the $|9/2, -7/2\rangle$ state (only obtain a 50/50 spin mixture of the two could be achieved) to unambiguously identify the strongest observed one as the p-wave resonance. It also would have been ideal to create a spin mixture of the $|9/2, -9/2\rangle$ and $|9/2, -5/2\rangle$ states and search for their s-wave resonance located around 224.21(5) G [153].

4.2.3 High Field Imaging

When working at the high magnetic fields required for the use of Feshbach resonances, high (magnetic) field imaging could be useful tool if not necessary to diagnose what happens to the hyperfine populations when the scattering length is enhanced or if some

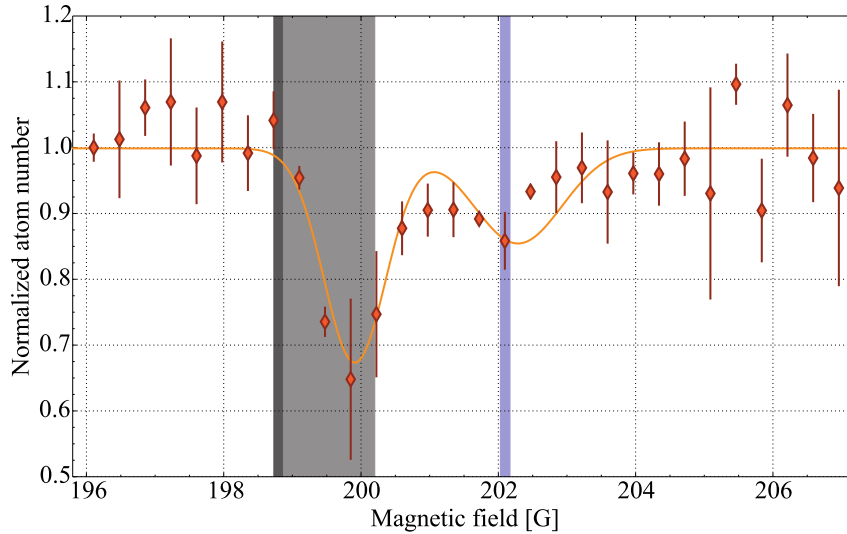


Figure 4.6: Normalized atomic number losses due to the increase of scattering length as magnetic field strength. A double Gaussian fit yields centres at 199.9(5) and 202.28(8) G. Dark gray area shows tabulated 198.8 G centre for the $|9/2, -7/2 \parallel -7/2\rangle$ p-wave resonance broadened by a temperature increase in light gray [154] and blue area representing the $|9/2, -9/2 \parallel -7/2\rangle$ s-wave resonance location at 202.1(2) G with its measured uncertainty as width.

dramatic atomic losses or molecular formation occur when crossing or near the Feshbach resonances. The Esslinger group found out the best scattering length to be $-1700 a_0$ for the latest stages of their evaporation [155]. Negative scattering length occur for magnetic field magnitudes greater than the Feshbach resonance location and studying the behaviour of our system in such regime would require to cross the resonance in the molecular formation direction before absorption imaging.

To establish our high field imaging frequency, we raised the magnetic field to values close to the Feshbach resonances and shifted the imaging frequency according to the predictions of the Breit-Rabi formula for the $4S_{1/2} |9/2, -9/2\rangle \leftrightarrow 4P_{3/2} |11/2, -11/2\rangle$ transition. Figure 4.7 shows the experimental results of high field imaging frequencies for five values surrounding the two s-wave Feshbach resonances.

A non trivial feature of high field imaging is its ability to perform m_F dependent detection. Indeed, at those high magnetic fields the degeneracy of the imaging resonances between adjacent m_F hyperfine level are well lifted and it becomes possible to probe each m_F level population independently by an appropriate shifting of the imaging frequency. An important factor when using this technique is to reduce the absorption imaging duration so as to reduce the unwanted transfer of atoms to a different

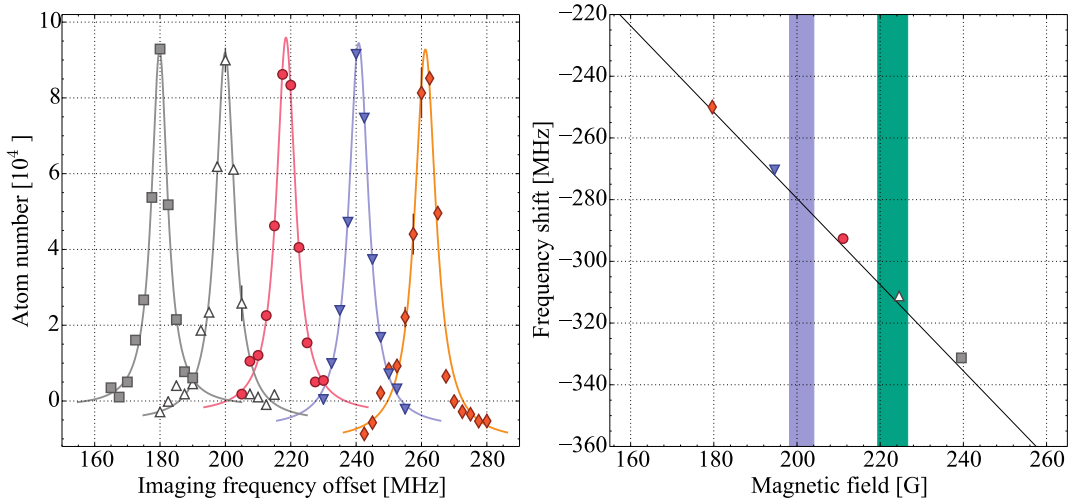


Figure 4.7: Left: Set of imaging frequency resonances for Feshbach coil currents of 12, 13, 14.1, 15 and 16 A. The resonance at null-field is centred at an offset of 511 MHz. Right: Black line represents the theoretical frequency shift of the $4S_{1/2} |9/2, -9/2\rangle \leftrightarrow 4P_{3/2} |11/2, -11/2\rangle$ imaging transition. Coloured bars have the same characteristics as in Figure 4.4.

m_F state by spontaneous emission after absorption of an imaging photon. This is illustrated on Figure 4.8 where we have performed absorption imaging on the $|9/2, -7/2\rangle$ and $|9/2, -9/2\rangle$ levels with a rather short 20 μs (orange) and standard 100 μs (blue) imaging pulse on a spin mixture.

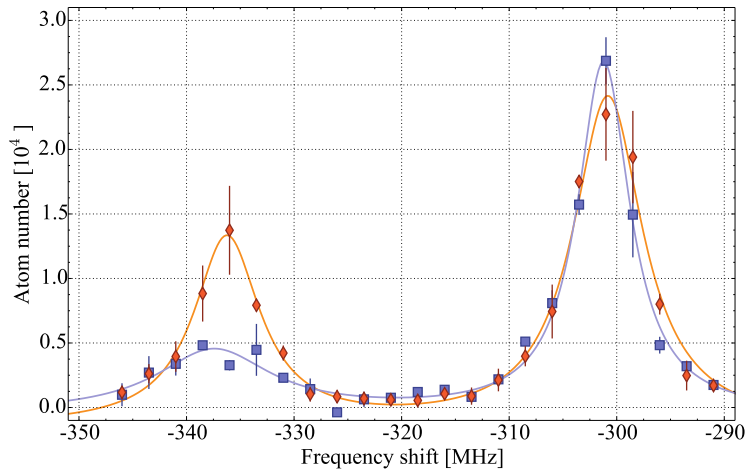


Figure 4.8: Imaging transitions spectra of the $4S_{1/2} |9/2, -7/2\rangle \leftrightarrow 4P_{3/2} |11/2, -11/2\rangle$ and $4S_{1/2} |9/2, -9/2\rangle \leftrightarrow 4P_{3/2} |11/2, -11/2\rangle$ respectively centred about -300 and 335 MHz at 217 G for an imaging pulse duration of 20 μs (orange) and 100 μs (blue).

Conclusion

At the beginning of my doctorate work, achieving single-site resolution of fermions in optical lattices was a rather elusive objective quested by an handful of research teams around the globe. This dissertation has put into light all the technical and physical aspect of how we accomplish it with EIT cooling.

With two other groups proving that for different atoms the same result could be obtained using Raman sideband cooling, we took the first steps toward the, classically computationally limited, understanding of the physics ruling the quantum world of strongly-correlated many-body fermionic systems. This breakthrough was quickly followed by a series of long awaited experimental studies and realisations that eluded the field from the lack of single-site capability as the site-resolved measurement of the spin-correlation function [156] and the observation of spatial charge and spin correlations in the 2D Fermi-Hubbard model [157], the spin- and density-resolved microscopy of antiferromagnetic correlations in Fermi-Hubbard chains [158] and even more remarkably and recently the experimental realization of a long-range antiferromagnet in the Hubbard model with ultracold atoms [159]. Those prove with no doubt that such quantum simulators will in a relatively close future be able to play a major role if not determinant in the humankind mastering of the quantum world.

So far, the lack of atom number and efficient evaporative processes in the last stage of the experimental sequence has made the ultracold temperatures out of our grasp but recent machine upgrades should enable us to reach degeneracy and enter the strongly correlated regime by reaching the fermionic Mott insulator state.

Appendix A : Publications

A.1 Single-atom imaging of fermions in a quantum-gas microscope

Elmar Haller, James Hudson, Andrew Kelly, Dylan A. Cotta, Bruno Peaudecerf, Graham D. Bruce and Stefan Kuhr

Nature Physics **11**, 738-742 (2015)

A.2 Sub-Doppler laser cooling of ^{40}K with Raman gray molasses on the D_2 line

Bruce, Graham D.; Haller, Elmar; Peaudecerf, Bruno; Cotta, Dylan A.; Andia, Manuel; Wu, Saijun; Johnson, Matthew Y. H.; Lovett, Brendon W.; Kuhr, Stefan

J. Phys. B: At. Mol. Opt. Phys. **50**, 095002 (2017)

Single-atom imaging of fermions in a quantum-gas microscope

Elmar Haller, James Hudson, Andrew Kelly, Dylan A. Cotta, Bruno Peaudecerf, Graham D. Bruce[†] and Stefan Kuhr^{*}

Single-atom-resolved detection in optical lattices using quantum-gas microscopes^{1,2} has enabled a new generation of experiments in the field of quantum simulation. Although such devices have been realized with bosonic species, a fermionic quantum-gas microscope has remained elusive. Here we demonstrate single-site- and single-atom-resolved fluorescence imaging of fermionic potassium-40 atoms in a quantum-gas microscope set-up, using electromagnetically-induced-transparency cooling^{3,4}. We detected on average 1,000 fluorescence photons from a single atom within 1.5 s, while keeping it close to the vibrational ground state of the optical lattice. A quantum simulator for fermions with single-particle access will be an excellent test bed to investigate phenomena and properties of strongly correlated fermionic quantum systems, allowing direct measurement of ordered quantum phases⁵⁻⁹ and out-of-equilibrium dynamics^{10,11}, with access to quantities ranging from spin-spin correlation functions to many-particle entanglement¹².

The ability to observe and control quantum systems at the single-particle level has revolutionized the field of quantum optics over recent decades. At the same time, the possibility to trap atoms in well-controlled engineered environments in optical lattices has proved to be a powerful tool for the investigation of strongly correlated quantum systems¹³. It was only recently that the great challenge to have full single-site resolution and single-atom control in optical lattices was overcome by the development of quantum-gas microscopes^{1,2}. These have been realized with bosonic ⁸⁷Rb (refs 1,2) and ¹⁷⁴Yb atoms¹⁴. However, until this work and that presented in refs 15,16, single-site resolution for fermions has remained elusive.

Some of the most interesting effects in many-body quantum systems are due to the properties of strongly interacting Fermi gases. Within solid-state physics, the fermionic nature of the electron is vital to understand a range of phenomena, such as electron pairing in superconductivity, and quantum magnetism (including colossal magnetoresistance). However, some of the properties of many-body fermionic quantum systems are very challenging to compute, even with the most advanced numerical methods, due to the antisymmetric nature of the wavefunction, and the resulting sign problem for quantum Monte Carlo methods¹⁷. A quantum simulator for fermions with single-particle resolution would be an excellent test bed to investigate many of the phenomena and properties of strongly correlated fermionic quantum systems. Such a fermionic quantum-gas microscope will provide the possibility to probe quantities that are difficult to access directly, such as spin-spin correlation functions or string order¹⁸. It would allow the study of out-of-equilibrium dynamics, the spreading of correlations¹⁰ and the build-up of entanglement in many-particle fermionic

quantum systems¹². It could perform quantum simulation of the Fermi-Hubbard model, which is conjectured to capture the key mechanism behind high- T_c superconductors, allowing researchers to gain insight into electronic properties that could potentially be applied in future materials engineering.

To achieve single-site-resolved detection of individual atoms on the lattice, it is desirable to maximize the fluorescence yield while at the same time maintaining a negligible particle loss rate and preventing the atoms from hopping between lattice sites. These conditions can be efficiently achieved by simultaneously laser cooling the atoms to sub-Doppler temperatures while detecting the fluorescence photons emitted during this process. However, cooling of fermionic alkaline atoms in optical lattices is challenging, as their low mass and small excited-state hyperfine splitting make it more difficult to obtain low temperatures using the standard technique of polarization-gradient cooling.

In this work, we achieved single-atom-resolved fluorescence imaging of ⁴⁰K using electromagnetically-induced-transparency (EIT) cooling^{3,4}. This technique has been used to efficiently cool trapped ions¹⁹ and to manipulate individual neutral atoms in an optical cavity^{20,21}. EIT cooling is similar to grey molasses, recently used to cool atoms and enhance density in free-space atomic samples^{22,23}. Both methods rely on the existence of a spectrally narrow, Fano-like line profile and dark resonances arising from quantum interference in a Λ -like level scheme. In confining potentials with quantized vibrational levels, as is the case in our optical lattice, the narrow absorption line can selectively excite red-sideband transitions that cool the atomic motion by removing one vibrational quantum, while carrier and blue-sideband excitations are suppressed. We present EIT cooling as an alternative to Raman sideband cooling techniques²⁴, which have been applied to image atomic clouds²⁵ and individual atoms²⁶, and which have been used recently by other research groups to achieve single-site imaging of fermionic potassium¹⁵ or lithium¹⁶, independently of the work presented here.

The key component of our experimental set-up is a high-resolution optical microscope² (Fig. 1a) with numerical aperture (NA) = 0.68, providing a diffraction-limited resolution of 580 nm (full-width at half-maximum, FWHM) at the wavelength of the $4S_{1/2} \rightarrow 4P_{1/2}$ transition, $\lambda_{D1} = 770.1$ nm (D_1 -line). We prepared a sample of cold fermionic ⁴⁰K atoms within the focal plane of the microscope (Methods) in a three-dimensional (3D) optical lattice (wavelength $\lambda = 1,064$ nm). To implement the EIT cooling scheme, we tuned both coupling and probe beams (Rabi frequencies Ω_C and Ω_p) close to the D_1 -line (see atomic level scheme in Fig. 1b). The coupling light was blue-detuned by $\Delta = 10\Gamma$ ($\Gamma = 2\pi \times 6.0$ MHz is the linewidth of the $4P$ excited states) from the $F = 9/2 \rightarrow F' = 7/2$

University of Strathclyde, Department of Physics, Scottish Universities Physics Alliance, Glasgow G4 0NG, UK. [†]Present address: School of Physics and Astronomy, University of St Andrews, St Andrews, Fife KY16 9AJ, UK. *e-mail: stefan.kuhr@strath.ac.uk

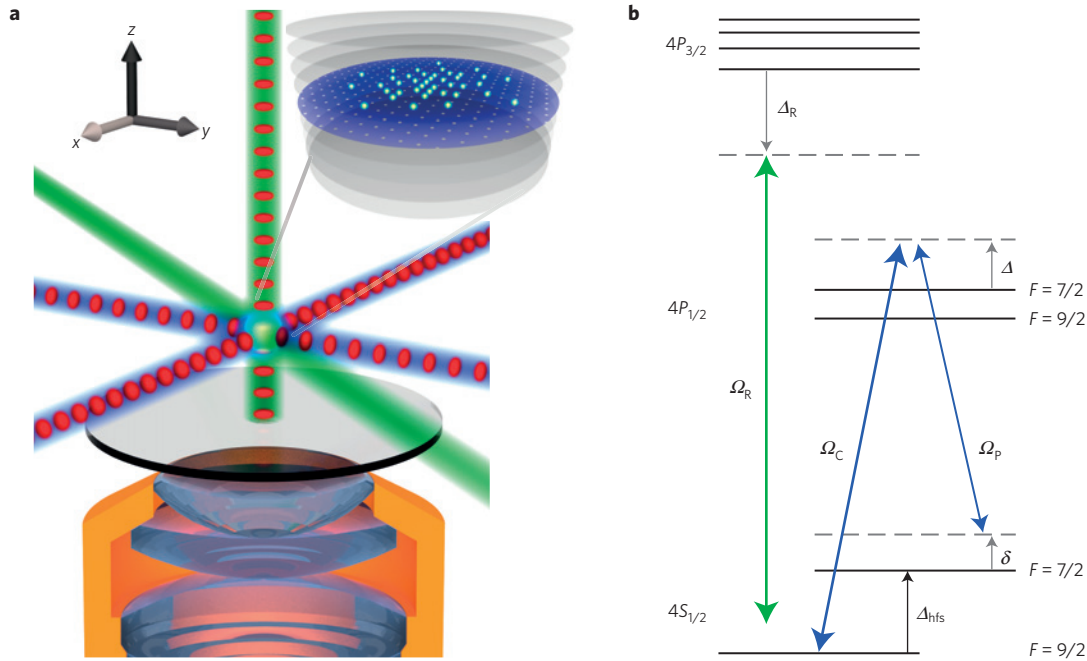


Figure 1 | Experimental set-up, laser beam configuration and level scheme. **a**, Fermionic ^{40}K atoms in an optical lattice were observed using fluorescence detection with a high-resolution optical microscope (NA = 0.68, working distance = 12.8 mm; see ref. 2). The optical lattice (red dots) is composed of two retroreflected beams in the x - and y -axes, and a vertical beam retroreflected from the coated vacuum window. Retroreflected EIT cooling beams (blue) were overlapped with the horizontal optical lattice. Raman beams (green) were used to couple the motional states in the z -axis to the horizontal plane. Atoms were prepared in the focal plane of the microscope objective (inset). **b**, Level scheme of the relevant states of ^{40}K , with off-resonant Raman beams (green) and near-resonant (detuning Δ) EIT coupling and probe beams (Rabi frequencies Ω_C and Ω_P , blue) with relative detuning $\Delta_{\text{hfs}} + \delta$.

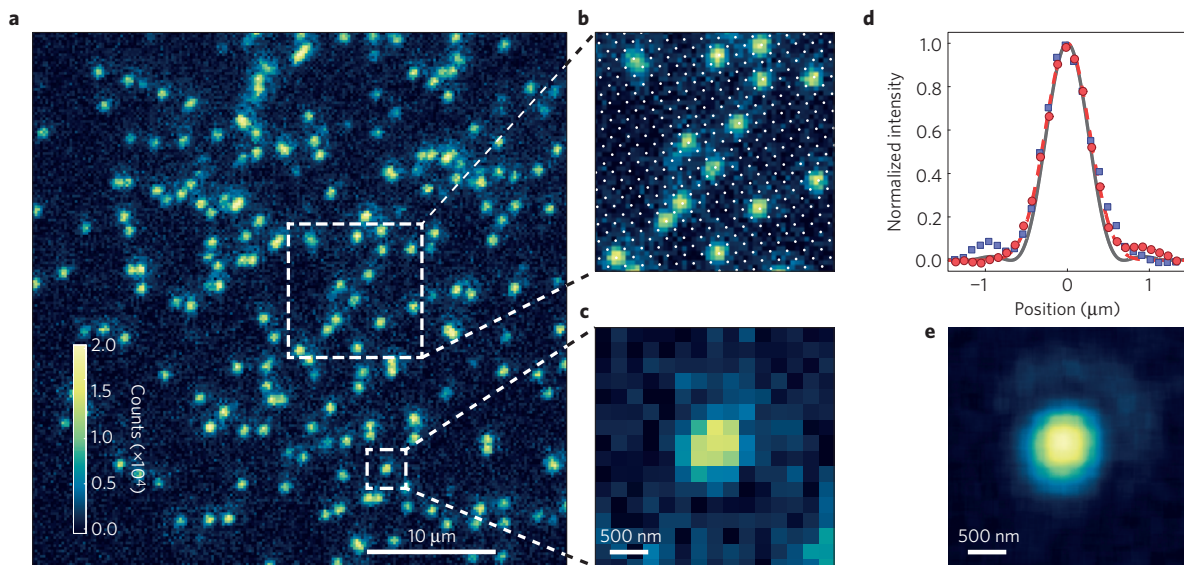


Figure 2 | Single-atom-resolved fluorescence images of fermions. **a**, Fluorescence image of a dilute cloud of ^{40}K atoms in the optical lattice (1.5 s exposure time with EIT cooling). **b**, $10\ \mu\text{m} \times 10\ \mu\text{m}$ subsection of **a**; white dots mark the lattice sites. **c**, Magnified subsection of **a** showing an individual atom. **d**, Horizontal (red circles) and vertical (blue squares) profiles through the centre of the averaged single-atom images shown in **e**, fitted (horizontal only) with a Gaussian profile (red dashed line). The grey line shows the diffraction-limited point-spread function (PSF) of the microscope objective. **e**, Measured point-spread function using 640 single-atom images as presented in **c**, averaged using subpixel shifting¹.

transition in the lattice; similarly, the probe beam was detuned by $\Delta = 10\Gamma$ from the $F = 7/2 \rightarrow F' = 7/2$ transition. Both pump and probe beams were derived from the same laser by passing the light through an electro-optical modulator (EOM), which generates sidebands at the frequency of the ground-state hyperfine splitting, $\Delta_{\text{hfs}} = 2\pi \times 1.2858\ \text{GHz}$. A retroreflected EIT beam in $\sigma^+ - \sigma^-$ configuration is overlapped with each of the optical lattice beams in

the x - and y -directions (Fig. 1a) to provide cooling in the horizontal plane. We avoided the use of vertical EIT beams to prevent stray light along the imaging axis. Instead, we used an off-resonant two-photon Raman transition red-detuned by $\Delta_R = 2\pi \times 8\ \text{GHz}$ from the $4S_{1/2} \rightarrow 4P_{3/2}$ transition (D_2 -line at 767.7 nm) to couple the motional states between the vertical and horizontal lattice axes (Methods). One Raman beam was aligned vertically and the other

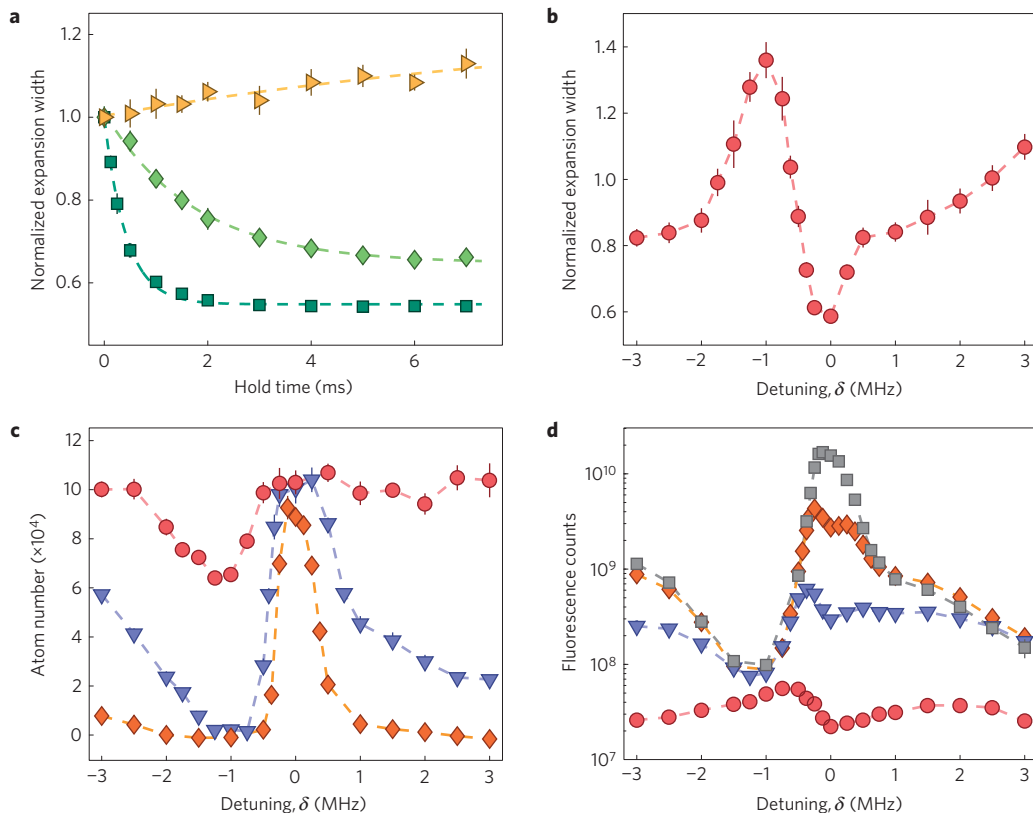


Figure 3 | Demonstration of EIT cooling. **a**, Expansion width of the atomic cloud after 1 ms time-of-flight, normalized to the initial width, for varying durations of EIT cooling. Cooling was observed in the y-axis (green squares). In the z-axis, we observed cooling with Raman beams present (green diamonds) and heating without (yellow triangles). **b**, Expansion width in y-axis as a function of two-photon detuning δ , after 1.5 ms of EIT cooling. **c**, Atom numbers versus δ , after 1.5 ms (red circles), 30 ms (blue triangles) and 300 ms (orange diamonds) of EIT cooling, measured with absorption imaging. **d**, Integrated fluorescence counts versus δ during exposure times of 1.5 ms (red circles), 30 ms (blue triangles), 300 ms (orange diamonds) and 2,000 ms (grey squares) during EIT cooling. Each datapoint in **a–d** is the average of five independent measurements, and the error bars represent the standard deviation.

beam horizontally at a 45° angle between the x - and y -axes (Fig. 1a). We blocked the stray light of the vertical Raman beam with narrow-band interference filters (Alluxa) placed in front of the electron multiplying charge-coupled device (EMCCD) camera, which detects fluorescence photons scattered from the EIT beams on the D_1 line.

Our cooling scheme allowed us to image individual ^{40}K atoms in a sparsely populated thermal cloud (Fig. 2a) with an excellent signal-to-noise ratio. We detected on average 1,000(400) (where the number in parentheses denotes the 1σ uncertainty of the last digits) fluorescence photons per atom within an illumination time of 1.5 s using a lattice depth of $k_B \times 245(20) \mu\text{K}$ (k_B is Boltzmann's constant) on all axes (Methods). Taking into account the collection efficiency of 8.6% of our imaging system (Methods), we calculated a corresponding atomic fluorescence rate of $8(3) \times 10^3$ photons s^{-1} . This is large enough to unambiguously identify the presence or absence of an atom for each lattice site (Fig. 2b and Methods); however, it is more than a factor of ten smaller than those obtained in the quantum-gas-microscope set-ups with ^{87}Rb (refs 1,2). Our measured point-spread function, obtained by averaging 640 fluorescence images of individual atoms (Fig. 2e), has a FWHM of 630(10) nm, close to the diffraction-limited resolution of the microscope objective (Fig. 2d).

To characterize the cooling process, we determined the cloud width (measured using absorption images after rapid release from the lattice potential, Methods) for increasing durations of exposure to the EIT and Raman beams. The cooling results in a decrease of the cloud width to a stationary value, with a time constant of 0.42(2) ms in the horizontal plane and 1.7(2) ms in

the vertical direction (Fig. 3a). These time constants correspond to cooling rates of $6(1) \hbar\omega \text{ ms}^{-1}$ and $0.8(3) \hbar\omega \text{ ms}^{-1}$ respectively, where $\omega = 2\pi \times 300(12) \text{ kHz}$ is the spacing of vibrational levels in all three lattice axes. From our measured Rabi frequencies, $\Omega_C = 2\pi \times 4.8(1) \text{ MHz}$, $\Omega_P = 2\pi \times 1.6(1) \text{ MHz}$ (Methods), we estimated the width of the narrow line in the Fano profile, $\gamma_+ = \omega\Gamma / (4\sqrt{\Delta^2 + \Omega_C^2 + \Omega_P^2}) \approx 2\pi \times 6 \text{ kHz}$ (ref. 4). This value gives an upper limit for the combined scattering rate, $\gamma_+/2$, on the red sideband for both horizontal axes; our observed cooling (and fluorescence) rates are about a factor of three less. The cooling rate in the vertical direction is different, as there are no vertical EIT beams; instead, cooling is achieved by transferring vibrational excitation quanta via Raman transitions from the vertical axis to the cooled horizontal axes (Methods). Without the Raman beams we observed no cooling in the vertical axis, but instead an increase of the vertical cloud width with time (Fig. 3a), caused by heating due to spontaneously emitted photons from the EIT beams. We estimated a mean number of vibrational quanta of 0.9(1) in each horizontal axis, after 5 ms of cooling, by measuring the steady-state expansion energy with time-of-flight imaging (Methods).

We studied the characteristics of EIT cooling in our experiment by measuring the cloud width, after 1.5 ms of cooling, as a function of the two-photon detuning δ . On resonance, $\delta = 0$, cooling works most efficiently (Fig. 3b), as the atoms are pumped into the dark state and their lifetime is significantly enhanced (Fig. 3c). However, at negative detuning, $\delta < 0$, we predominantly drive carrier and blue-sideband transitions which heat the atoms (Fig. 3b). For $\delta \neq 0$, heating resulted in atom loss over timescales of milliseconds.

Maximizing the number of fluorescence photons for the single-atom imaging necessitates a compromise between a long lifetime (atoms in the dark state) and a large scattering rate. This can be seen in a shift of the maximum of fluorescence counts with increasing accumulation time (Fig. 3d), from the position of strong heating ($\delta < 0$) towards resonance ($\delta = 0$), where most efficient cooling is achieved. Note that Fig. 3c and d compare the atom number and the fluorescence counts of the complete cloud without layer preparation, to match the conditions of Fig. 3a and b. However, the spatially varying light shift due to the Gaussian intensity profile of the lattice beams causes a position-dependent detuning Δ . As a consequence, optimum conditions for EIT cooling are met only in the central 70×70 lattice sites, where Δ changes by less than 20 MHz. This fact causes loss of atoms outside the area of most efficient cooling, resulting in a reduced lifetime for the full cloud of 6.6(5) s. The lifetime of the atoms inferred by measuring fluorescence from the central 70×70 lattice sites is 30(4) s (see Supplementary Fig. 1).

We investigated in more detail to what extent the atoms are lost and move in the lattice during the imaging process. For this purpose, we recorded two successive fluorescence images of the same atoms with 500 ms exposure time each, and a 500 ms separation between the two images. From each of the images we determined the atom distribution on the lattice using a deconvolution algorithm (Methods), providing us with a binary map of the lattice site occupation. To estimate hopping, we calculated the fraction of atoms, h , that appeared on previously empty lattice sites as well as the fraction of atoms lost, l , from the first to the second image (Fig. 4). Varying δ , we measured hopping fractions as low as $h = 3.5(1.5)\%$ and observed that l increased from 4.2(1.9)% at $\delta = 0$ to larger values for $\delta \neq 0$. We attribute this increased loss to the less efficient cooling due to the absence of a dark state, as discussed above (Fig. 3c). Even at $\delta = 0$, both loss and hopping could result from off-resonant excitation by the EIT and Raman beams to the $4P_{1/2}$ and $4P_{3/2}$ excited states. Both $4P$ states experience a light shift more than five times greater and opposite to the ground-state light shift, due to the proximity of the lattice wavelength to the $4P \rightarrow 3D$ resonance at 1,180 nm. In our case, the use of blue-detuned EIT beams ensures that the atoms preferentially scatter off a trapped dressed state. However, an atom resonantly excited to the $4P$ state experiences a repulsive potential which causes the excited-state wavepacket to expand rapidly in space. During the subsequent spontaneous emission the atoms can decay into a high vibrational state or a high band in which the atoms are no longer bound to the lattice sites. These hot atoms can now move across the lattice, and then potentially be recooled and bound to a different lattice site. We are currently investigating this heating process in more detail using numerical simulations of the full quantum evolution of an atom on a few lattice sites.

The single-site-resolved detection of ^{40}K in an optical lattice will open the path to the study of strongly correlated fermionic quantum systems with unprecedented insight into their properties. In particular, our new technique will allow the study of strongly correlated phases in the Fermi–Hubbard model, for example, counting thermal excitations in fermionic Mott insulators^{27,28} and directly probing local entropy distributions², or detecting the propagation of correlations after quenches¹⁰. The quantum-gas microscope will also enable manipulation of the system on a local scale with single-site addressing resolution²⁹, allowing deterministic preparation of non-thermal initial states³⁰ and probing the ensuing dynamics. This would allow, for example, further investigation of intriguing phenomena in Luttinger liquid theory, such as spin–charge separation³¹ and the growth of many-body spatial entanglement¹². The high-resolution microscope could also be used to implement proposals for removing high-entropy regions by locally modifying the confining potential³² to attain low-entropy states. The fermionic quantum-gas microscope is an ideal tool to detect the onset of antiferromagnetic ordering^{5–9} with single-site

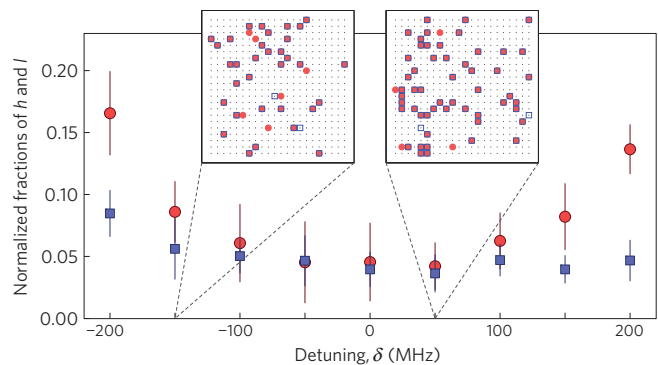


Figure 4 | Hopping and atom losses. Fraction of atoms, h , appearing (blue squares) on a previously empty site in the second of two successive fluorescence images (500 ms exposure time, 500 ms delay between the two images), normalized to the number of atoms in the first image. Also shown is the fraction of atoms, l , that has disappeared between the two images (red dots). The panels show binary maps of the lattice site occupations of the first (red circles) and second image (blue squares). They show regions of 20×20 lattice sites; however, the data is analysed in a region of 70×70 sites. Each data point results from the average of ten fluorescence images; the error bars represent the standard deviation.

resolution, by directly measuring the spin–spin correlations. In different lattice geometries these measurements would allow the study of, for example, both equilibrium properties and out-of-equilibrium dynamics in frustrated spin systems¹¹.

Methods

Methods and any associated references are available in the [online version of the paper](#).

Received 2 April 2015; accepted 15 June 2015;
published online 13 July 2015

References

- Bakr, W. S., Gillen, J. I., Peng, A., Fölling, S. & Greiner, M. A quantum gas microscope for detecting single atoms in a Hubbard-regime optical lattice. *Nature* **462**, 74–77 (2009).
- Sherson, J. F. *et al.* Single-atom-resolved fluorescence imaging of an atomic Mott insulator. *Nature* **467**, 68–72 (2010).
- Morigi, G., Eschner, J. & Keitel, C. H. Ground state laser cooling using electromagnetically induced transparency. *Phys. Rev. Lett.* **85**, 4458–4461 (2000).
- Morigi, G. Cooling atomic motion with quantum interference. *Phys. Rev. A* **67**, 033402 (2003).
- Snoek, M., Titvinidze, I., Töke, C., Byczuk, K. & Hofstetter, W. Antiferromagnetic order of strongly interacting fermions in a trap: Real-space dynamical mean-field analysis. *New J. Phys.* **10**, 093008 (2008).
- Paiva, T., Scalettar, R., Randeria, M. & Trivedi, N. Fermions in 2D optical lattices: Temperature and entropy scales for observing antiferromagnetism and superfluidity. *Phys. Rev. Lett.* **104**, 066406 (2010).
- Simon, J. *et al.* Quantum simulation of antiferromagnetic spin chains in an optical lattice. *Nature* **472**, 307–312 (2011).
- Greif, D., Uehlinger, T., Jotzu, G., Tarruell, L. & Esslinger, T. Short-range quantum magnetism of ultracold fermions in an optical lattice. *Science* **340**, 1307–1310 (2013).
- Hart, R. A. *et al.* Observation of antiferromagnetic correlations in the Hubbard model with ultracold atoms. *Nature* **519**, 211–214 (2015).
- Cheneau, M. *et al.* Light-cone-like spreading of correlations in a quantum many-body system. *Nature* **481**, 484–487 (2012).
- Eisert, J., Friesdorf, M. & Gogolin, C. Quantum many-body systems out of equilibrium. *Nature Phys.* **11**, 124–130 (2015).
- Pichler, H., Bonnes, L., Daley, A. J., Läuchli, A. M. & Zoller, P. Thermal versus entanglement entropy: A measurement protocol for fermionic atoms with a quantum gas microscope. *New J. Phys.* **15**, 063003 (2013).
- Bloch, I., Dalibard, J. & Zwerger, W. Many-body physics with ultracold gases. *Rev. Mod. Phys.* **80**, 885–964 (2008).

14. Miranda, M., Inoue, R., Okuyama, Y., Nakamoto, A. & Kozuma, M. Site-resolved imaging of ytterbium atoms in a two-dimensional optical lattice. *Phys. Rev. A* **91**, 063414 (2015).
15. Cheuk, L. W. *et al.* A quantum gas microscope for fermionic atoms. *Phys. Rev. Lett.* **114**, 193001 (2015).
16. Parsons, M. F. *et al.* Site-resolved imaging of fermionic ^6Li in an optical lattice. *Phys. Rev. Lett.* **114**, 213002 (2015).
17. Troyer, M. & Wiese, U.-J. Computational complexity and fundamental limitations to fermionic quantum Monte Carlo simulations. *Phys. Rev. Lett.* **94**, 170201 (2005).
18. Endres, M. *et al.* Observation of correlated particle-hole pairs and string order in low-dimensional Mott insulators. *Science* **334**, 200–203 (2011).
19. Roos, C. F. *et al.* Experimental demonstration of ground state laser cooling with electromagnetically induced transparency. *Phys. Rev. Lett.* **85**, 5547–5550 (2000).
20. Mücke, M. *et al.* Electromagnetically induced transparency with single atoms in a cavity. *Nature* **465**, 755–758 (2010).
21. Kampschulte, T. *et al.* Electromagnetically-induced-transparency control of single-atom motion in an optical cavity. *Phys. Rev. A* **89**, 033404 (2014).
22. Fernandes, D. R. *et al.* Sub-Doppler laser cooling of fermionic 40 K atoms in three-dimensional gray optical molasses. *Europhys. Lett.* **100**, 63001 (2012).
23. Grier, A. T. *et al.* Λ -enhanced sub-Doppler cooling of lithium atoms in D1 gray molasses. *Phys. Rev. A* **87**, 063411 (2013).
24. Hamann, S. E. *et al.* Resolved-sideband Raman cooling to the ground state of an optical lattice. *Phys. Rev. Lett.* **80**, 4149–4152 (1998).
25. Patil, Y. S., Chakram, S., Aycock, L. M. & Vengalattore, M. Nondestructive imaging of an ultracold lattice gas. *Phys. Rev. A* **90**, 033422 (2014).
26. Lester, B. J., Kaufman, A. M. & Regal, C. A. Raman cooling imaging: Detecting single atoms near their ground state of motion. *Phys. Rev. A* **90**, 011804 (2014).
27. Jördens, R., Strohmaier, N., Günter, K., Moritz, H. & Esslinger, T. A Mott insulator of fermionic atoms in an optical lattice. *Nature* **455**, 204–207 (2008).
28. Schneider, U. *et al.* Metallic and insulating phases of repulsively interacting fermions in a 3D optical lattice. *Science* **322**, 1520–1525 (2008).
29. Weitenberg, C. *et al.* Single-spin addressing in an atomic Mott insulator. *Nature* **471**, 319–324 (2011).
30. Fukuhara, T. *et al.* Quantum dynamics of a mobile spin impurity. *Nature Phys.* **9**, 235–241 (2013).
31. Kollath, C., Schollwöck, U. & Zwirger, W. Spin-charge separation in cold Fermi gases: A real time analysis. *Phys. Rev. Lett.* **95**, 176401 (2005).
32. Bernier, J.-S. *et al.* Cooling fermionic atoms in optical lattices by shaping the confinement. *Phys. Rev. A* **79**, 061601(R) (2009).

Acknowledgements

We thank G. Morigi, A. Daley and A. Buyskikh for fruitful discussions. We acknowledge the contribution of A. Schindewolf, N. Sangouard and J. Hinney during the construction of the experiment. We acknowledge support by EU (ERC-StG FERMILATT, SIQS, Marie Curie Fellowship to E.H.), EPSRC, Scottish Universities Physics Alliance (SUPA).

Author contributions

E.H., J.H., D.A.C., B.P. and S.K. performed the experiments and data analysis. All authors contributed to the design and set-up of the experiment and to the writing of the manuscript.

Additional information

Supplementary information is available in the online version of the paper. Reprints and permissions information is available online at www.nature.com/reprints. Correspondence and requests for materials should be addressed to S.K.

Competing financial interests

The authors declare no competing financial interests.

Methods

Loading of ^{40}K atoms into the optical lattice. Our experimental sequence started with an atomic beam of ^{40}K produced by a 2D magneto-optical trap (MOT) loaded from 10^{-7} mbar of potassium vapour (our atomic source is enriched to 3% ^{40}K). This atomic beam passes through a differential pumping section to a standard 3D MOT, which captures 2×10^8 atoms in 4 s. The atoms were further cooled in an optical molasses and loaded into an optical dipole trap formed by two beams of 100 W each (beam radius $w_0 = 150 \mu\text{m}$, wavelength 1,070 nm) crossing at an angle of 15° . The atoms were then loaded into a translatable optical tweezer (beam radius $w_0 = 50 \mu\text{m}$, 18 W power) and moved 13 cm within 1.5 s to within the field-of-view of the high-resolution microscope². We initially transferred 1×10^6 ^{40}K atoms from the single-beam trap into a crossed optical dipole trap, which is formed by the optical lattice beams with their retroreflectors blocked by mechanical shutters, and evaporatively cooled the atoms to $T = 4.0(1) \mu\text{K}$. We then transferred the sample into the vertical optical lattice (beam radius $w_0 = 60 \mu\text{m}$) and subsequently switched on both horizontal optical lattices ($w_0 = 75 \mu\text{m}$) with the retroreflectors unblocked. The lattice depth was determined by measuring the frequency of the blue-sideband transitions in the lattice using Raman transitions. Driving this sideband results in an increase of the cloud width after time-of-flight. The error of the lattice depth cited in the main text is the $1/e$ -width of the excitation peak of the spectrum.

Preparation of 2D atomic samples. To prepare a thin sample within the focal plane of the microscope, we used a position-dependent microwave transition in a vertical magnetic field gradient² of $\partial B/\partial z = 80 \text{ G cm}^{-1}$. This gradient results in a shift of the ground-state hyperfine transition $|F=9/2, m_F = -9/2\rangle \rightarrow |F=7/2, m_F = -7/2\rangle$ of $20 \text{ kHz } \mu\text{m}^{-1}$. We initially optically pumped the atoms into the $|F=9/2, m_F = -9/2\rangle$ state while holding them in a shallow 3D optical lattice, before applying a microwave sweep (HS1-pulse²⁹ of 5 kHz width) to transfer atoms out of one selected layer into the $|F=7/2, m_F = -7/2\rangle$ state. All atoms remaining in $F=9/2$ were then removed using a circularly polarized resonant laser beam on the $F=9/2 \rightarrow F'=11/2$ cycling transition of the D_2 line. The microwave transfer and removal processes have an overall efficiency of $>90\%$, resulting in residual atoms in the $F=7/2$ manifold across all layers. To remove these atoms, we optically pumped the atoms back to the initial $|F=9/2, m_F = -9/2\rangle$ state and again performed a microwave transfer followed by a removal pulse. Using this technique, we were able to prepare about 100 atoms in a single layer of the 3D optical lattice, with a negligible population in other layers. Note that for the images in Fig. 2, we prepared two adjacent layers within the depth of focus of the imaging system, to increase the number of atoms visible. For the data sets presented in Fig. 3, we used absorption images of the full atomic cloud, without single-layer preparation. The atoms are initially in $F=9/2$, but once the EIT cooling beams are switched on, the population is predominantly in state $F=7/2$.

Analysis of fluorescence images. To analyse our fluorescence images, we used procedures and computer algorithms based on earlier work². The precise orientation of the lattice angles, $47.599(3)^\circ$ and $-42.833(3)^\circ$ with respect to the horizontal baseline of the Fig. 2a,b, and the magnification (5.133 pixels on the CCD camera correspond to $\lambda/2$ at the atoms; $\lambda = 1,064 \text{ nm}$ is the lattice wavelength) were determined by evaluating the mutual distances between 600 isolated atoms from several fluorescence images (see Supplementary Information of ref. 2).

Lattice angles and spacings were taken as the input for our deconvolution algorithm², which uses the averaged point-spread function from Fig. 2e to determine the occupation of the lattice sites. To estimate the average fluorescence rate, we summed the number of counts from a 3×3 pixel area centred on each occupied lattice site, and converted this value to a photon number. The resulting histogram of the detected photon number follows a Gaussian distribution of mean 1,000 and standard deviation of 400. The same analysis performed on the empty lattice sites yielded a photon number of less than 200.

Our imaging system has a total fluorescence collection efficiency of 8.6%, given by the objective's solid angle of $\Omega/(4\pi) = 13\%$, the 80% transmission through the objective, lenses and interference filters, and the 83% quantum efficiency of the EMCCD camera (Andor iXon 897).

Characterization of EIT cooling. We determined the kinetic energy of a cloud of atoms in time-of-flight measurements after a rapid release from the lattice potential. The initial change in kinetic energy due to the EIT and Raman beams was different for the horizontal and vertical axes, with a horizontal cooling rate of $83(14) \mu\text{K ms}^{-1}$ during the first 150 μs and a vertical cooling rate of $12(4) \mu\text{K ms}^{-1}$ during the first 400 μs . After a hold time of 5 ms with EIT cooling, the atoms maintained constant horizontal and vertical expansion energies of $10.0(2) \mu\text{K}$ and $14.8(2) \mu\text{K}$. These kinetic energies correspond to mean excitation numbers of 0.9(1) and 1.6(1), respectively, for a harmonic oscillator potential with a trap frequency $\omega = 2\pi \times 300(12) \text{ kHz}$.

We determined the combined Rabi frequencies of all EIT beams by measuring the off-resonant scattering rate of one beam, with the EOM switched off. The coupling and probe beam Rabi frequencies, $\Omega_C = 2\pi \times 4.8(1) \text{ MHz}$ and $\Omega_P = 2\pi \times 1.6(1) \text{ MHz}$, are determined by the modulation depth of the EOM (25% of the power in the first sideband) and by taking into account the transition strengths. The values of the Rabi frequencies do not take into account the fact that there could be different distributions of the magnetic sublevels during this measurement compared with EIT cooling in the lattice.

Raman coupling of motional axes. In our set-up, we achieved cooling of the vertical axis by transferring its vibrational excitation quanta, via Raman transitions, to the cooled horizontal axes³³. We used two Raman beams of identical frequency, such that the exchange of vibrational quanta between two axes is a resonant two-photon process. The Rabi frequency for the transition $|n_x, n_z + 1\rangle \rightarrow |n_x + 1, n_z\rangle$ can be calculated as $\Omega_R = \Omega^0 \langle n_x + 1, n_z | e^{i\mathbf{k}\cdot\mathbf{r}} | n_x, n_z + 1 \rangle$, where n_x and n_z are the vibrational quantum numbers, $\delta\mathbf{k} = \mathbf{k}_1 - \mathbf{k}_2$ is the momentum transfer from the Raman beams, and Ω^0 is the two-photon Rabi frequency of the carrier transition. Expanding the exponential yields $\Omega_R = \Omega^0 \eta_x \eta_z \sqrt{(n_x + 1)(n_z + 1)}$, where we have used the Lamb-Dicke factors $\eta_j = \delta\mathbf{k} \cdot \mathbf{e}_j \Delta x_0^j$. For our parameters, $\eta_x = 0.118(2)$, $\eta_z = 0.168(3)$, with $\Delta x_0^j = \sqrt{\hbar/(2m\omega)} = 20.5(4) \text{ nm}$ the width of the ground-state wavepacket of the harmonic oscillator in directions $j=x, z$; m is the mass of a ^{40}K atom. We estimate a Rabi frequency of $\Omega_R = 2\pi \times 27(2) \text{ kHz}$ by measuring how the vertical expansion width after 0.5 ms of cooling changes as a function of the detuning between the two Raman beams.

References

- Steinbach, J., Twamley, J. & Knight, P. L. Engineering two-mode interactions in ion traps. *Phys. Rev. A* **56**, 4815–4825 (1997).

Single-atom imaging of fermions in a quantum-gas microscope

Elmar Haller¹, James Hudson¹, Andrew Kelly¹, Dylan Cotta¹, Bruno Peaudecerf¹,
Graham D. Bruce^{1,*} & Stefan Kuhr¹

¹University of Strathclyde, Department of Physics, Scottish Universities Physics Alliance,
Glasgow G4 0NG, United Kingdom

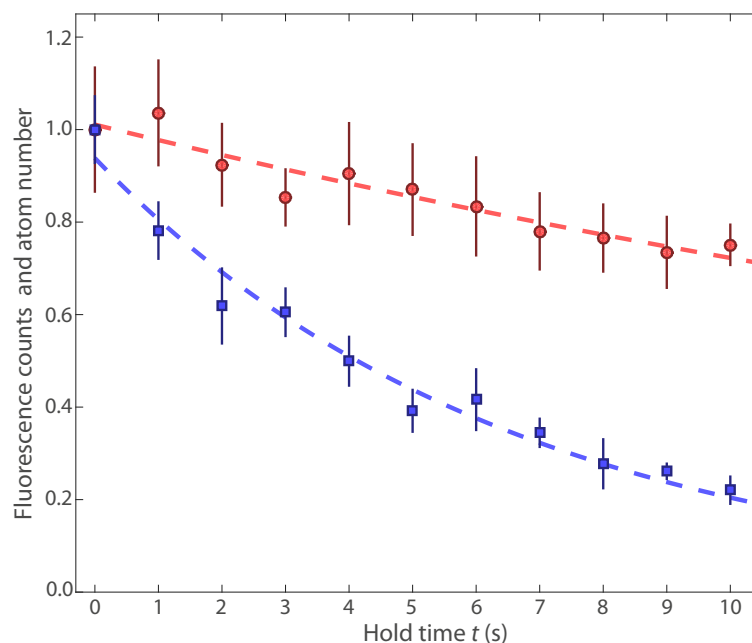


Figure S1 Lifetime measurement. The curves show fluorescence counts within a region of 70×70 lattice sites integrated over a period of 250 ms (red circles) and atom number of the complete cloud measured by absorption imaging (blue squares) for varying duration, t , of EIT cooling. Both curves were normalised to the respective initial values at $t = 0$. We determine the time constants of 30(4) s and 6.6(5) s from exponential fits (dashed lines).

*Present address: University of St. Andrews, School of Physics and Astronomy, United Kingdom

Sub-Doppler laser cooling of ^{40}K with Raman gray molasses on the D_2 line

G D Bruce^{1,2}, E Haller¹, B Peaudecerf¹, D A Cotta¹, M Andia¹, S Wu³,
M Y H Johnson^{1,2}, B W Lovett² and S Kuhr^{1,4}

¹University of Strathclyde, Department of Physics, SUPA, Glasgow G4 0NG, United Kingdom

²SUPA School of Physics and Astronomy, University of St Andrews, North Haugh, St Andrews KY16 9SS, United Kingdom

³Department of Physics, State Key Laboratory of Surface Physics and Key Laboratory of Micro and Nano Photonic Structures (Ministry of Education), Fudan University, Shanghai 200433, People's Republic of China

E-mail: stefan.kuhr@strath.ac.uk

Received 14 December 2016, revised 20 February 2017

Accepted for publication 10 March 2017

Published 12 April 2017



CrossMark

Abstract

Gray molasses is a powerful tool for sub-Doppler laser cooling of atoms to low temperatures. For alkaline atoms, this technique is commonly implemented with cooling lasers which are blue-detuned from either the D_1 or D_2 line. Here we show that efficient gray molasses can be implemented on the D_2 line of ^{40}K with red-detuned lasers. We obtained temperatures of $48(2) \mu\text{K}$, which enables direct loading of $9.2(3) \times 10^6$ atoms from a magneto-optical trap into an optical dipole trap. We support our findings by a one-dimensional model and three-dimensional numerical simulations of the optical Bloch equations which qualitatively reproduce the experimentally observed cooling effects.

Keywords: atomic physics, gray molasses, laser cooling, ultracold atoms, sub-Doppler cooling

(Some figures may appear in colour only in the online journal)

1. Introduction

Ultracold quantum gases have attracted much interest in recent years, and have become a versatile tool to investigate strongly interacting and strongly correlated quantum systems [1]. Cooling of an atomic gas to ultralow temperatures requires a multi-stage cooling process, which starts with a laser cooling phase in a magneto-optical trap (MOT), followed by evaporative cooling in magnetic or optical traps. Directly after collecting atoms in a MOT, lower temperatures and a higher phase space density can be achieved by sub-Doppler laser cooling techniques [2]. A ‘standard’ red-detuned optical molasses allows the heavier alkaline atoms Rb and Cs to be cooled well below the Doppler limit. It relies

on a Sisyphus-like cooling effect in which atoms climb potential hills created by polarization or intensity gradients, thereby losing kinetic energy before being optically pumped to a lower energy level. In the case of Li and K, the only alkalines with stable *fermionic* isotopes, polarization gradient cooling in a standard optical molasses is less efficient because the smaller excited state hyperfine splitting leads to a higher excitation probability of transitions other than the ones used for cooling. Nonetheless, sub-Doppler temperatures were achieved for K [3–6] and Li [7] at low atom densities using a red-detuned optical molasses. In most experimental setups, the MOT uses light near-red detuned to the $F \rightarrow F' = F + 1$ cycling transition of the D_2 ($nS_{1/2} \rightarrow nP_{3/2}$) line (n is principal quantum number). It was also shown that Doppler cooling on the narrower linewidth $nS_{1/2} \rightarrow (n + 1)P_{3/2}$ transition can achieve low temperature at high density in ^6Li [8, 9] and ^{40}K [10], but this technique requires lasers in the ultraviolet or blue wavelength range.

Gray molasses is another powerful method for sub-Doppler laser cooling to high densities and low temperatures [11, 12], and it relies on the presence of bright and dark states.

⁴ Author to whom any correspondence should be addressed.



Original content from this work may be used under the terms of the [Creative Commons Attribution 3.0 licence](https://creativecommons.org/licenses/by/3.0/). Any further distribution of this work must maintain attribution to the author(s) and the title of the work, journal citation and DOI.

A spatially varying light shift of the bright states allows moving atoms to undergo a Sisyphus-like cooling effect [2], in a way that hot atoms are transferred from a dark to a bright state at a potential minimum of the bright state and back again into a dark state at a potential maximum. The coupling between the dark and bright states is velocity-selective, such that the coldest atoms are trapped in the dark states with substantially reduced interaction with the light field. Most early experiments using gray molasses created *Zeeman* dark states by using circularly polarized light on $F \rightarrow F' = F$ [13, 14] or $F \rightarrow F' = F - 1$ transitions [15–17] within the D_2 line, and blue-detuned lasers so that the energy of bright states lay above those of the dark states. In those experiments with Rb and Cs, the large hyperfine splitting in the $P_{3/2}$ states allows a large detuning of the gray molasses laser from the other transitions (in particular from the MOT $F \rightarrow F' + 1$ cycling transition) such that the gray molasses provides the dominant light-scattering process. In contrast, the poorly-resolved $P_{3/2}$ states in Li and K increase the probability of undergoing transitions on the MOT cycling transition, which was thought to limit the effectiveness of the gray molasses. Efficient implementations of gray molasses with ^{39}K [18–20], ^{40}K [21, 22], ^6Li [22, 23] and ^7Li [24] have therefore used transitions of the D_1 line ($nS_{1/2} \rightarrow nP_{1/2}$ transitions), requiring the use of additional lasers. In some of these experiments, cooling was found to be enhanced at a Raman resonance between the cooling and repumping light fields [18, 22, 24]. This Λ configuration creates additional, coherent dark states, as in velocity-selective coherent population trapping schemes [25, 26].

In this work, we demonstrate that such Raman dark states can be utilized for cooling of ^{40}K to high atom densities in a *red*-detuned gray molasses using only light at a frequency close to the $F \rightarrow F' = F + 1$ transition on the D_2 line. In contrast to the D_1 -line or narrow-line cooling schemes, our scheme requires minimal experimental overhead, because the lasers are the same as the ones used for the MOT. Our paper is structured as follows. Firstly, we model the gray molasses by computing the energy levels and photon scattering rates of bright and dark states by numerical solution of the optical Bloch equations. We present experimental evidence that our method reaches sub-Doppler temperatures and efficiently loads atoms into an optical dipole trap (ODT). We analyze our results using a semi-classical Monte Carlo simulation and find qualitative agreement with our experimental data.

2. 1D model of red-detuned gray molasses

In our one-dimensional model of the gray molasses, we considered ^{40}K atoms moving in a light field consisting of counter-propagating beams in $\text{lin}\perp\text{lin}$ configuration [2]. This results in constant light intensity and a polarization gradient (figure 1(a)), which periodically varies from pure circular to pure linear polarization over a spatial period of half a wavelength. Each molasses beam consists of a strong cooling beam ($s = I/I_s = 3$) and a weaker ($s = 0.17$) repumper beam. Here, I is the light intensity, $I_s = 1.75 \text{ mW cm}^{-2}$ is the saturation intensity of the transition and $\Gamma = 2\pi \times 6.035 \text{ MHz}$ is the natural linewidth of

the D_2 line. The cooling light is red-detuned by $\Delta = -12.3 \Gamma$ from the $F = 9/2 \rightarrow F' = 9/2$ transition and the repumper light is detuned by $\Delta - \delta$ from the $F = 7/2 \rightarrow F' = 9/2$ transition (see level scheme in figure 1(d)).

Using the method outlined in [22], we calculated eigenstates and light shifts, ϵ , of the dressed states (see appendix), and the photon scattering rate γ for each of the states. The eigenstates correspond to the bare m_F states at positions of pure $\sigma^{+/-}$ polarization (figure 1(b)) and for arbitrary polarization, they are predominantly superpositions of the m_F states within a specific F manifold. The eigenstates can be grouped into dark states ($\gamma \sim 0$ at all positions) and bright states ($\gamma > 0$ at all positions). The dark states are predominantly superpositions of the m_F states from the $F = 7/2$ manifold, and the bright states are superpositions of m_F states predominantly from the $F = 9/2$ manifolds with small admixtures of states from the $F' = 11/2$ manifold. The energy of the bright states is spatially varying (blue curves in figure 1(b)) with the dominant light-shift contribution from the $F = 9/2 \rightarrow F' = 11/2$ transition, while the light shifts of the dark eigenstates have negligible spatial variation (green curves in figure 1(b)). For negative two-photon detuning ($\delta < 0$), the energy of the dark states is below the bright states (figure 1(b)), and above for positive detunings.

We calculated the optical pumping rate, γ_D , which is the rate at which an atom scatters a photon and returns to a different state (see appendix), at each point in space by numerical solution of the optical Bloch equations [22]. Atoms are preferentially depumped from the bright states at positions of pure linear polarization (figure 1(c)), which occurs at the potential maxima of the lowest-lying bright state. The probability of motional coupling is largest when the energy difference between bright and dark states is smallest [27]. By choosing δ such that the dark states have lower energy than all the bright states (in our case $\delta = -0.17\Gamma$), we ensure that motional coupling is strongest between the dark state and lowest-energy bright state at the potential minima.

It is critical for our scheme that the bright states belong mostly to the $F = 9/2$ manifold and the dark states to the $F = 7/2$ manifold, with smaller F . Only in this case it is possible that the energetically lowest bright state experiences the strongest light shift (at $z = \lambda/8$) while its depumping rate to the dark states is actually lowest. The main component of this bright state at $z = \lambda/8$ is from the stretched $F = 9/2$, $m_F = 9/2$ state whose scattering rate is highest. At this position the light polarization is circular, and the state is coupled predominantly to the $F' = 11/2$, $m_F = 11/2$ excited state, from which the atom can decay only into the bright state manifold and not into a dark state.

3. Experiment

The experimental setup relevant for this study is a part of our fermionic quantum-gas microscope [28] and the cooling technique presented here is used to load atoms from a MOT into a crossed ODT, see figure 2. Our MOT consists of three pairs of counter-propagating circularly polarized beams containing both

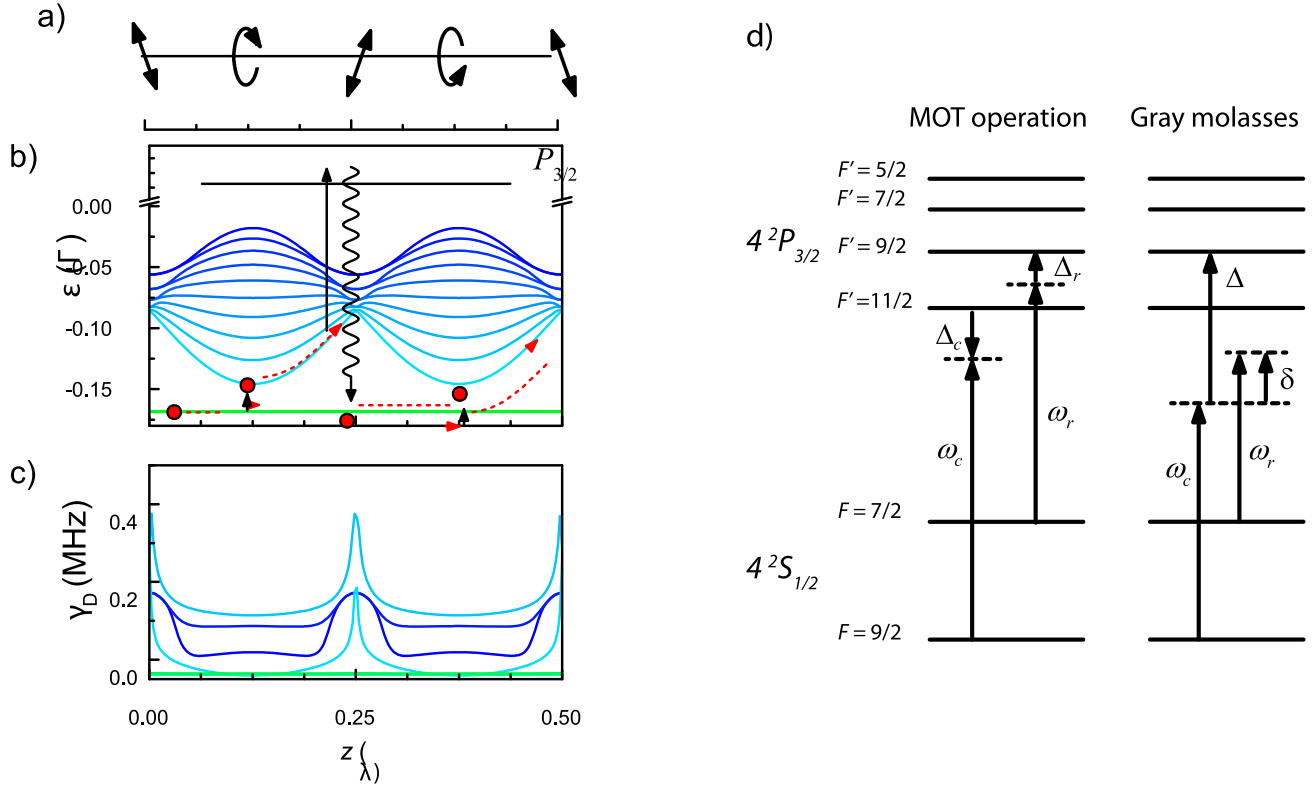


Figure 1. Cooling mechanism in 1D lin⊥lin red-detuned gray molasses ($\delta = -0.17 \Gamma$). (a) Variation of polarization with position z over the period of the standing wave. (b) Energies, ϵ , of the dressed states which group in families of bright (blue) and dark states (green). An atom (red circle) in a dark state moving along $+z$ most efficiently couples to a bright state at $z = \lambda/8$. The atom undergoes Sisyphus-like cooling by traveling to an increased potential energy before an absorption followed by a spontaneous emission event returns it to a dark state at $z = \lambda/4$. (c) Optical pumping rate γ_D , showing the dark states and the bright states corresponding to $m_F = -9/2, -7/2, 3/2,$ and $1/2$ at positions of σ^+ polarization (others omitted for clarity). The most likely pumping to dark states occurs at $z = \lambda/4$. (d) Atomic level scheme of then $^{40}\text{K } D_2$ line together with the relevant laser fields and detunings for MOT operation (left) and gray molasses cooling (right). Cooling light and repumping light are at frequencies ω_c and ω_r , respectively.

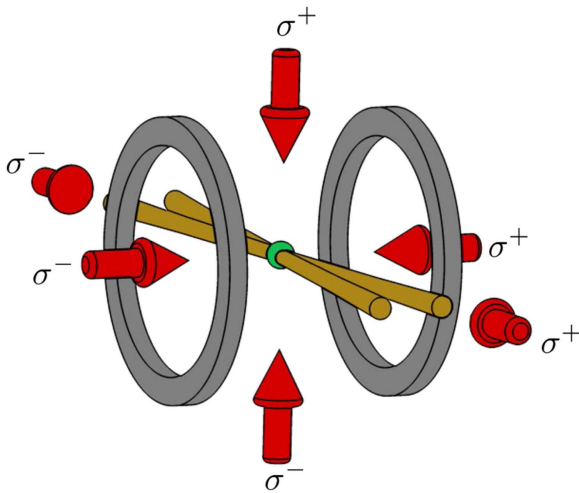


Figure 2. Beam configuration in our experimental setup. Three pairs of counterpropagating beams (red arrows) in $\sigma^+ - \sigma^-$ configuration provide light to laser cool atoms in the MOT region (green ball). The same lasers are also used for gray molasses cooling. Atoms are loaded into an ODT, which is formed by two laser beams (yellow) intersecting at a 17° angle. Coils which provide the magnetic field for the MOT are shown in gray.

cooling and repumping frequencies with the same polarization. The laser light at a wavelength of 767.7 nm for the cooling and repumper transitions is generated using two diode lasers with tapered amplifiers. Both lasers are offset-locked relative to a common master laser which is stabilized using saturated absorption spectroscopy in a vapor cell containing ^{39}K . The six MOT beams each have 30 mm diameter and powers of up to 18 mW (cooling laser) and 0.7 mW (repumper). Cooling and repumper laser detunings are $\Delta_c = -4.6\Gamma$ and $\Delta_r = -4.2 \Gamma$, where Δ_c is the detuning from the $F = 9/2 \rightarrow F' = 11/2$ transition and Δ_r is the detuning from the $F = 7/2 \rightarrow F' = 9/2$ transition (see level scheme in figure 1(d)). We loaded ^{40}K emanating from a 2D-MOT into the MOT for 4 s and collected up to 1.3×10^8 atoms. The atom cloud was then compressed for 10 ms by changing the detunings to $\Delta_c = -1.8 \Gamma$ and $\Delta_r = -10.6 \Gamma$. All lasers and the magnetic-field gradient were then switched off and we waited for 1.5 ms to allow for eddy currents in the system to decay.

For the subsequent gray molasses phase, cooling and repumper light were switched back on with powers of 17.7 mW and 0.1 mW, respectively, for a duration of 9 ms. The detunings of cooling and repumper beams were set such that they are now

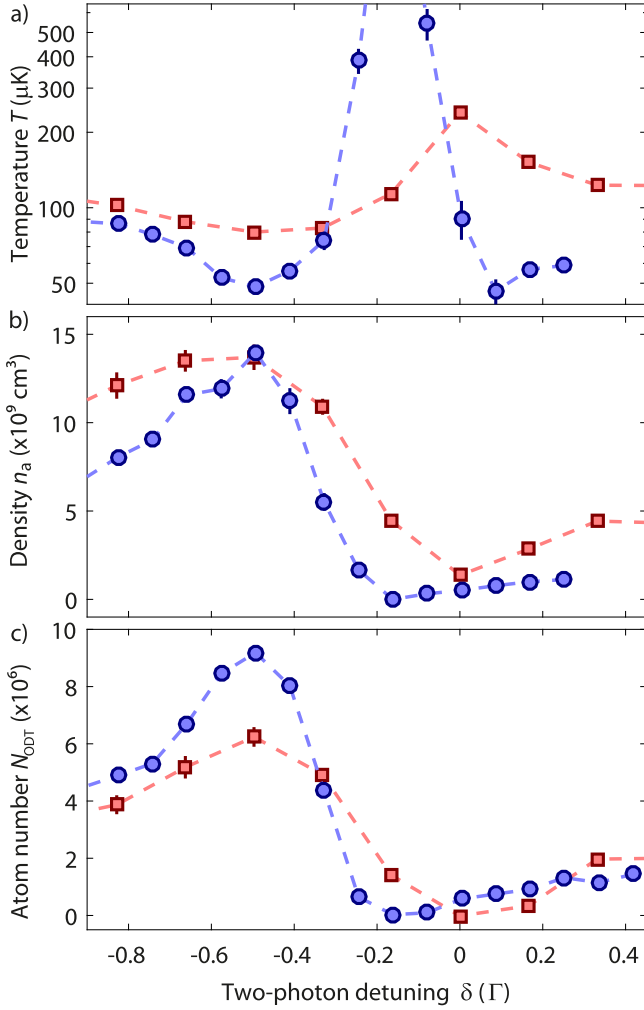


Figure 3. Experimental demonstration of D_2 -line gray molasses cooling. Dependence of (a) temperature, T , (b) free space atomic density, n_a , and (c) number of atoms, N_{ODT} , loaded into the optical dipole trap as a function of two-photon detuning, δ , for fixed detuning Δ , (red squares) and for the optimized loading sequence using a time-varying Δ (blue circles). The error bars are fit errors, and the dotted lines are to guide the eye.

close to the Raman resonance with single-photon Raman detuning $\Delta \simeq -13 \Gamma$. We varied the two-photon detuning δ and measured the temperature, T , of the atoms by time-of-flight absorption imaging (red squares in figure 3(a)). We found a Fano-like profile with a minimum of $T = 80(1) \mu\text{K}$ at $\delta = -0.5 \Gamma$ (where the number in parentheses denotes the 1σ uncertainty of the last digits). The maximum density of the free atom cloud, n_a , after gray molasses cooling was $n_a = 1.4(1) \times 10^{10} \text{ cm}^{-3}$ at the same detuning that yielded the lowest temperature (red datapoints in figure 3(b)). At this optimal two-photon detuning, atom losses during the molasses phase are negligible, whereas for higher temperatures a significant number of atoms was lost from the molasses.

We then loaded the atoms into an ODT, which is created by two 100 W laser beams from a multimode fiber laser at 1070 nm wavelength. The Gaussian beams have orthogonal linear polarization, are focused to a $300 \mu\text{m}$ $1/e^2$ beam waist

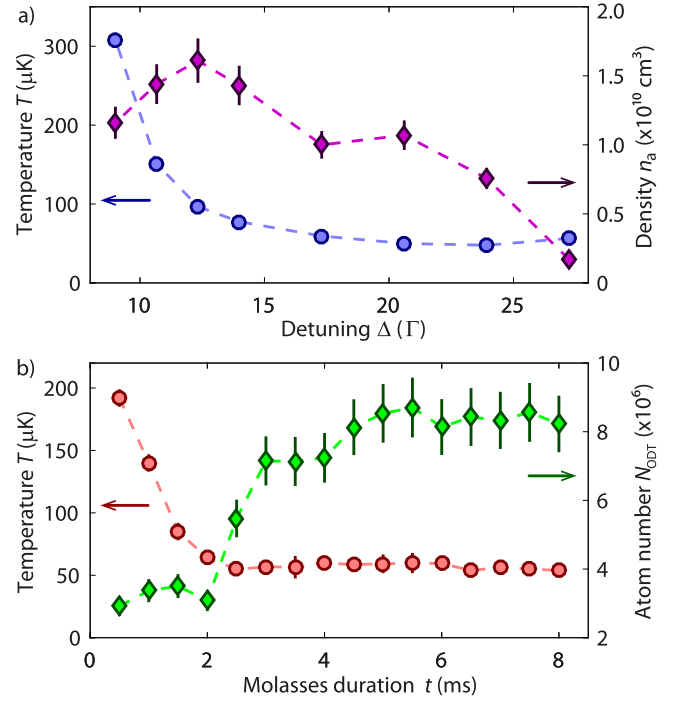


Figure 4. Optimization of gray-molasses cooling. (a) Temperature T (blue circles) and free space atomic density, n_a (purple diamonds), as a function of the one-photon Raman detuning Δ after 6 ms of gray molasses cooling. (b) Temperature T (red circles) and atom number loaded into the ODT N_{ODT} (green diamonds) a function of the molasses duration.

and intersect at an angle of 17° at the center of the MOT, creating a trap of $180 \mu\text{K}$ depth. The ODT is switched on at full power just after the compression phase. Using the experimental procedure as described above, we loaded up to $N_{\text{ODT}} = 6.2(3) \times 10^6$ atoms into the ODT (figure 3(c)). The atom number was measured using absorption imaging after time-of-flight. The maximum atom number was found at the two-photon detuning which yielded the lowest temperatures and highest densities in free space.

In a second step, we investigated how the density changed as a function of the detuning from the excited state, Δ (figure 4(a)). For each value of Δ , we optimized the temperature and density by varying δ to account for changes in light shifts and small uncertainties in the offset lock calibration. We found that by moving farther away from resonance, both the temperature and density are reduced. While the reduction in temperature is desirable, the reduction in density reduces the loading efficiency into the ODT. In order to achieve both lower temperatures and higher densities, we ramped both Δ and δ during the molasses phase. We found that optimal loading was achieved by ramping Δ from -10.8Γ to -20.3Γ and δ from -0.81Γ to -0.56Γ over a duration of 6 ms followed by an additional hold time of 3 ms, leading to temperatures of $48(2) \mu\text{K}$ (blue circles in figure 3(a)). The temperatures reported here are clearly in the sub-Doppler regime, and lower than the temperatures of $63 \mu\text{K}$ achieved with the UV MOT [10], but larger than the

lowest temperatures of $11 \mu\text{K}$ obtained with D1-line gray molasses cooling [22].

When varying the duration of the gray molasses phase (figure 4(b)), we found the decrease in temperature occurred during the first 2 ms before a steady state was reached, whereas the number of atoms in the dipole trap kept increasing and saturated after about 5 ms of cooling. We could load up to $N_{\text{ODT}} = 9.2(3) \times 10^6$ atoms into the ODT, which corresponds to 7% of the initial atom number in the molasses. This value is limited by the volume overlap of the ODT and the molasses and it could in principle be increased by using more laser power for the ODT, which would allow us either increase the trap depth or use larger beam diameters for the same trap depth.

Our one-dimensional model can also explain the heating seen for $\delta = 0$. At this detuning, the energy of the dark states is higher than the energy of the bright states, and motional coupling occurs preferentially to the most energetic bright state at the potential maxima. The atom will proceed to a lower potential before absorption and spontaneous emission pumps it to the dark state, at which point it will have *gained* kinetic energy. This process is the inverse of Sisyphus cooling.

4. 3D numerical simulation

To quantitatively model the cooling effect in our experimental setup, we have performed a three-dimensional numerical simulation using the same semi-classical Monte-Carlo wavefunction method detailed in [22]. As in the experiment, the light field in the simulation consists of three orthogonal pairs of counter-propagating laser beams in $\sigma^+ - \sigma^-$ configuration, which results in both polarization and intensity gradients. Our simulation computes the coherent evolution of all of an atom's classical external states and its internal quantum states in timesteps of $1 \mu\text{s}$ as it travels through the light field for a total simulation time of 10 ms. The internal states coherently evolve as governed by the optical Bloch equations until a randomly generated photon absorption and subsequent emission event, at which point the state is projected onto one of the ground state eigenstates. The classical external states are updated at instances of photon absorption and emission, which cause a momentum kick, but also continuously via a force proportional to the expectation value of the Hamiltonian. Each atom originates at the center of intersection of the three pairs of laser beams. If it travels more than 15 mm ($1/e^2$ radius of our beams) from this point, in any direction, the atom is considered to have been lost.

We ran these simulations for 10 ms duration at $\Delta = -12.3 \Gamma$ and varied the values of the two-photon detuning, δ , for a fixed initial velocity of $v = 0.7 \text{ m s}^{-1}$ corresponding to a temperature of $T = 800 \mu\text{K}$ using the equipartition theorem $\frac{3}{2}k_B T = \frac{1}{2}m \langle v^2 \rangle$. The temperature extracted using the final velocity distribution and the equipartition theorem (figure 5(a)) as a function of δ shows a dependence very similar to the experimental data presented in

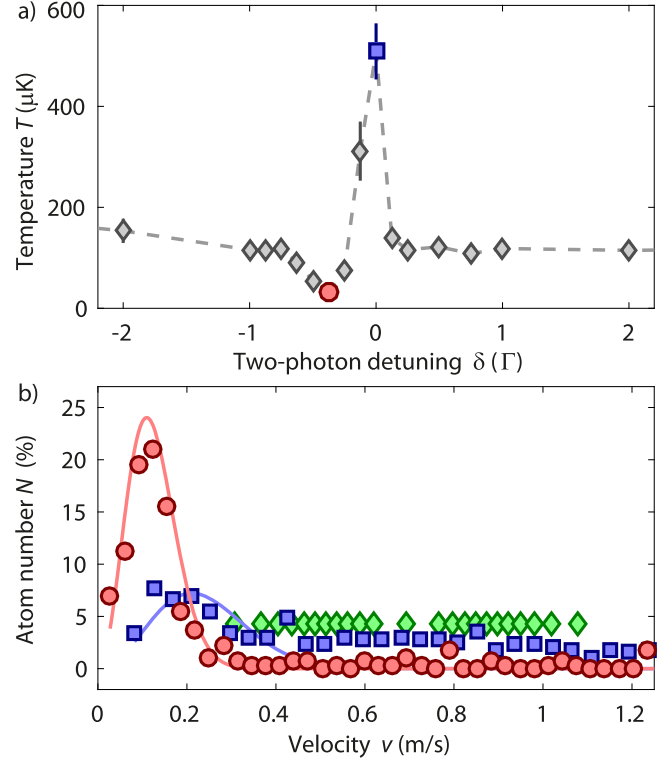


Figure 5. Semi-classical Monte-Carlo simulations of cooling in a 3D optical molasses. (a) Dependence of temperature T versus two-photon detuning δ resulting from the numerical simulations. The highlighted red and blue data points are calculated from the velocity distributions shown in (b). (b) An initial non-thermal velocity distribution (green diamonds) is narrowed by Raman gray molasses cooling at $\delta = -0.4 \Gamma$ (red circles). The red line is a fit with a Maxwell-Boltzmann distribution yielding $T = 29(1) \mu\text{K}$. For $\delta = 0$ (blue squares), the velocity distribution broadens, and is not well described by a Maxwell-Boltzmann distribution (blue line).

figure 3. Far away from the two-photon resonance, the temperature of the atoms reached $180(67) \mu\text{K}$, close to the Doppler temperature of $145 \mu\text{K}$. For $\delta = -0.4 \Gamma$ and $\delta = 0$, we simulated the time-evolution of an ensemble of atoms with an initial non-thermal distribution of velocities between 0.3 and 1.1 m s^{-1} . At $\delta = -0.4 \Gamma$ the final velocity distribution is fit with a Maxwell-Boltzmann distribution (with temperature as the only free parameter) which yields $T = 29(1) \mu\text{K}$, which indicates cooling and thermalization (figure 5(b)). On two-photon resonance, ($\delta = 0$), poor cooling and no thermalization was observed and the corresponding temperature was $460(60) \mu\text{K}$. The simulation results are in accordance with both the experimental data and one-dimensional model, and we observe efficient cooling when the dark states are tuned below the bright states (now $\delta = -0.4 \Gamma$ due to the increased light-shift from the additional beams).

5. Summary and Conclusions

In summary we have presented a method to realize efficient gray molasses cooling using red-detuned lasers on the D_2 line

of fermionic ^{40}K . A key advantage of our technique that it uses the same lasers as for the MOT and it does not require additional lasers near the D_1 line. Starting from a MOT, we could reduce the temperature of the atom cloud and increase the phase-space density, such that we loaded $9.2(3) \times 10^6$ atoms into an ODT. Our technique can be used for an efficient production of degenerate Fermi gases of ^{40}K , or larger number of cold atoms in multi-species experiments.

The data and code used in this work may be found in [29].

Acknowledgments

We acknowledge support by EU (ERC-StG FERMILATT, SIQS, Marie Curie Fellowships to EH and BP), Scottish Universities Physics Alliance (SUPA), and the Leverhulme Trust (GB, grant no. RPG-2013-074). Numerical simulations were performed using the high-performance computer ARCHIE-WeSt (www.archie-west.ac.uk) at the University of Strathclyde, funded by EPSRC grants EP/K000586/1 and EP/K000195/1.

Appendix. 1D gray molasses modeling

In our one-dimensional model of the gray molasses cooling (which follows the methods of [22]), we consider a stationary atom at position z within a 1D lin \perp lin bichromatic optical molasses, consisting of both cooling and repumper frequencies. The cooling and repumper light field is decomposed into σ^+ and σ^- polarizations for each beam, with quantization axis along z .

We find the energy eigenvalues of the dressed states (eigenstates) of the atom in the light-field by diagonalizing the Hamiltonian

$$H = H_0 + H_C. \quad (\text{A.1})$$

Here

$$\begin{aligned} \frac{H_0}{\hbar} = & \sum_m |F = 7/2, m\rangle \delta \langle F = 7/2, m| \\ & + \sum_{F'm'} |F', m'\rangle (\delta_{\text{hfs},F'} + \Delta) \langle F', m'|, \end{aligned} \quad (\text{A.2})$$

is the Hamiltonian of the free atom, and $\delta_{\text{hfs},F'}$ the hyperfine splitting of the excited state ($\delta_{\text{hfs},F'} = 0$ for $F' = 11/2$).

The light-atom coupling Hamiltonian is

$$\begin{aligned} H_C = & \hbar \sum_{F,m,\sigma,F',m'} [c_{F,m,\sigma,F',m'} \Omega_{F,\sigma}(z) \\ & \times |F, m\rangle \langle F', m'| + h.c.], \end{aligned} \quad (\text{A.3})$$

where $\Omega_{F,\sigma}(z)$ are the position-dependent Rabi frequencies and $c_{F,m,\sigma,F',m'}$ the relevant Clebsch-Gordan coefficients for the transitions. The off-resonant coupling between the cooling (repumper) laser and atoms in the $F = 7/2$ ($F = 9/2$) ground state was neglected due to the large hyperfine splitting of the ground states.

The total scattering rate, γ , of each eigenstate at each position is the natural linewidth multiplied by the excited-state fraction of that eigenstate. The optical pumping rate γ_D is the total scattering rate minus the rate at which the atom undergoes an absorption and emission cycle and returns to the same eigenstate (elastic scattering).

References

- [1] Bloch I, Dalibard J and Zwerger W 2008 *Rev. Mod. Phys.* **80** 885
- [2] Dalibard J and Cohen-Tannoudji C 1989 *J. Opt. Soc. Am. B* **6** 2023
- [3] Modugno G, Benkó C, Hannaford P, Roati G and Inguscio M 1999 *Phys. Rev. A* **60** R3373
- [4] Taglieber M, Voigt A C, Henkel F, Fray S, Hänsch T W and Dieckmann K 2006 *Phys. Rev. A* **73** 011402
- [5] Gokhroo V, Rajalakshmi G, Easwaran R K and Unnikrishnan C S 2011 *J. Phys. B: At. Mol. Opt. Phys.* **44** 115307
- [6] Landini M, Roy S, Carcagní L, Trypogeorgos D, Fattori M, Inguscio M and Modugno G 2011 *Phys. Rev. A* **84** 043432
- [7] Hamilton P, Kim G, Joshi T, Mukherjee B, Tiarks D and Müller H 2014 *Phys. Rev. A* **89** 023409
- [8] Duarte P M, Hart R A, Hitchcock J M, Corcovilos T A, Yang T L, Reed A and Hulet R G 2011 *Phys. Rev. A* **84** 061406
- [9] Sebastian J, Gross C, Li K, Gan H C J, Li W and Dieckmann K 2014 *Phys. Rev. A* **90** 033417
- [10] McKay D C, Jervis D, Fine D J, Simpson-Porco J W, Edge G J A and Thywissen J H 2011 *Phys. Rev. A* **84** 063420
- [11] Grynberg G and Courtois J Y 1994 *Europhys. Lett.* **27** 41–6
- [12] Weidemüller M, Esslinger T, Ol'shanii M A, Hemmerich A and Hänsch T W 1994 *Europhys. Lett.* **27** 109–14
- [13] Hemmerich A, Weidemüller M, Esslinger T, Zimmermann C and Hänsch T 1995 *Phys. Rev. Lett.* **75** 37–40
- [14] Esslinger T, Sander F, Hemmerich A, Hänsch T W, Ritsch H and Weidemüller M 1996 *Opt. Lett.* **21** 991–3
- [15] Boiron D, Triché C, Meacher D R, Verkerk P and Grynberg G 1995 *Phys. Rev. A* **52** 3425–8
- [16] Boiron D, Michaud A, Lemonde P, Castin Y, Salomon C, Weyers S, Szymaniec K, Cognet L and Clairon A 1996 *Phys. Rev. A* **53** R3734
- [17] Boiron B, Michaud A, Fournier J, Simard L, Sprenger M, Grynberg G and Salomon C 1998 *Phys. Rev. A* **57** R4106
- [18] Nath D, Easwaran R K, Rajalakshmi G and Unnikrishnan C S 2013 *Phys. Rev. A* **88** 053407
- [19] Salomon G, Fouché L, Wang P, Aspect A, Bouyer P and Bourdel T 2013 *Europhys. Lett.* **104** 63002
- [20] Salomon G, Fouché L, Lepoutre S, Aspect A and Bourdel T 2014 *Phys. Rev. A* **90** 033405
- [21] Rio F D, Sievers F, Kretzschmar N, Wu S, Salomon C and Chevy F 2012 *Europhys. Lett.* **100** 63001
- [22] Sievers F, Kretzschmar N, Fernandes D R, Suchet D, Rabinovic M, Wu S, Parker C V, Khaykovich L, Salomon C and Chevy F 2015 *Phys. Rev. A* **91** 023426
- [23] Burchianti A, Valtolina G, Seman J A, Pace E, De Pas M, Inguscio M, Zaccanti M and Roati G 2014 *Phys. Rev. A* **90** 043408

- [24] Grier A T, Ferrier-Barbut I, Rem B S, Delehay M, Khaykovich L, Chevy F and Salomon C 2013 *Phys. Rev. A* **87** 063411
- [25] Aspect A, Arimondo E, Kaiser R, Vansteenkiste N and Cohen-Tannoudji C 1988 *Phys. Rev. Lett.* **61** 826
- [26] Aspect A, Arimondo E, Kaiser R, Vansteenkiste N and Cohen-Tannoudji C 1989 *J. Opt. Soc. Am. B* **6** 2112
- [27] Rio Fernandes D 2014 Trapping and cooling of fermionic alkali atoms to quantum degeneracy: sub-Doppler cooling of Potassium-40 and Lithium-6 in gray molasses *PhD Thesis* Université Pierre et Marie Curie
- [28] Haller E, Hudson J, Kelly A, Cotta D A, Peaudecerf B, Bruce G D and Kuhr S 2015 *Nat. Phys.* **11** 738
- [29] Bruce G D, Haller E, Peaudecerf B, Cotta D A, Andia M, Wu S, Johnson M Y H, Lovett B W and Kuhr S 2017 Sub-Doppler laser cooling of 40K with Raman gray molasses on the D2 line: dataset (<https://doi.org/10.15129/d638461d-9d68-43ff-b6e7-151d66fc7f2b>)

Appendix B : m_F dependent A.C. Stark shift "experimentalist" form

The aim of this appendix is to demonstrate how to obtain the practical formula, Eq. (1.1.40), [117] from the one, Eq. (1.1.39), obtained directly from second order perturbation theory:

$$\Delta E_{F,m_F} = \frac{1}{4} \sum_{F',m'_F} \frac{1}{\hbar} \left(\frac{1}{\omega - \omega_{FF'}} + \frac{1}{-\omega - \omega_{FF'}} \right) |\langle F,m_F | \hat{d}\vec{E} | F',m'_F \rangle|^2 \quad (\text{B.0.1})$$

First, the intensity of the radiation is brought into the formula replacing the square of the electric field amplitude $|E_0|^2 = 2I/c\epsilon_0$ and we also expand the dipole matrix element $|\langle F,m_F | \hat{d}\vec{E} | F',m'_F \rangle|$ as function of quantum numbers, 3j and 6j symbols and of the reduced dipole matrix element $\langle J \| e\vec{r} \| J' \rangle = d$ using expressions (1.1.33) and (1.1.37).

$$|\langle F,m_F | \hat{d}\vec{E} | F',m'_F \rangle|^2 = (2F+1)(2F'+1)(2J+1) \begin{Bmatrix} J & J' & 1 \\ F' & F & I \end{Bmatrix}^2 \begin{pmatrix} F' & 1 & F \\ m'_F & q & -m_F \end{pmatrix}^2 d^2 \quad (\text{B.0.2})$$

From now on, the following shortened notations of the non rotating wave approximated detuning Δ , 6j and 3j-symbols shall be used to prevent multiple lines equations:

$$\frac{1}{\Delta_{FF'}} = \left(\frac{1}{\omega - \omega_{FF'}} + \frac{1}{-\omega - \omega_{FF'}} \right) \quad 6j = \begin{Bmatrix} J & J' & 1 \\ F' & F & I \end{Bmatrix} \quad 3j = \begin{pmatrix} F' & 1 & F \\ m'_F & q & -m_F \end{pmatrix} \quad (\text{B.0.3})$$

Equation B.0.1 becomes

$$\Delta E_{F,m_F} = \frac{I}{2\hbar c\epsilon_0} \sum_{F',m'_F} \frac{1}{\Delta_{FF'}} (2F+1)(2F'+1)(2J+1) 6j^2 3j^2 d^2 \quad (\text{B.0.4})$$

The next step consists in multiplying the expression by $3\pi c^2/3\pi c^2$, $2J'+1/2J'+1$ and $\omega_{FF'}^3/\omega_{FF'}^3$ to make the general pre-factor of the final formula and its shape appear,

leading to :

$$\Delta E_{F,m_F} = \frac{3\pi I c^2}{2} \sum_{F',m'_F} \frac{\omega_{FF'}^3}{3\pi\hbar c^3 \epsilon_0} \frac{2J+1}{2J'+1} d_{SI}^2 \frac{1}{\Delta_{FF'} \omega_{FF'}^3} (2F+1)(2F'+1)(2J'+1) 6j^2 3j^2 \quad (\text{B.0.5})$$

In this form, the expression looks almost identical to the one provided in the paper. We can identify the component that should identify to $A_{FF'}$ from the first three terms after the sum sign which will be denoted $B_{FF'}$ for now

$$B_{FF'} \equiv \frac{\omega_{FF'}^3}{3\pi\hbar c^3 \epsilon_0} \frac{2J+1}{2J'+1} d_{SI}^2 \quad (\text{B.0.6})$$

The transition angular frequency $\omega_{FF'}$ is replaced with its expression in terms of the transition wavelength $\lambda_{FF'}$ i.e. $\omega_{FF'} = (2\pi c)^3 / \lambda_{FF'}^3$ to give

$$B_{FF'} = \frac{8\pi^2}{3\hbar\epsilon_0} \frac{1}{\lambda_{FF',SI}^3} \frac{2J+1}{2J'+1} d_{SI}^2 \quad (\text{B.0.7})$$

Finally the dipole matrix elements and transition wavelength so far in SI are expressed in Angstroms and atomic units of ea_0 , respectively to yield

$$B_{FF'} = \frac{8\pi^2}{3\hbar\epsilon_0} \frac{(ea_0)^2}{\text{\AA}^3} \frac{1}{\lambda_{FF',\text{\AA}}^3} \frac{2J+1}{2J'+1} d_{ea_0}^2 \quad (\text{B.0.8})$$

A numerical application reveals that the pre-factor in the expression of B equals

$$\frac{8\pi^2}{3\hbar\epsilon_0} \frac{(ea_0)^2}{\text{\AA}^3} = 2.02613 \times 10^{18} \text{ s}^{-1} \quad (\text{B.0.9})$$

uniquely identifying $B_{FF'}$ with $A_{FF'}$ and therefore concluding this derivation.

Appendix C : Squeezing beam

Measurements of beam waists

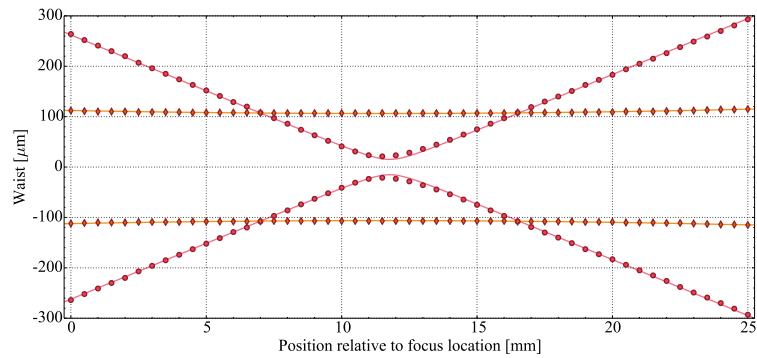


Figure C.0.1: Squeezing beam vertical (red circles) and horizontal (orange diamonds) beam waist in μm as a function of longitudinal position in mm prior to being moved onto the experimental apparatus. Fits give a waist at focus w_0 and its location z_0 for the vertical/horizontal axis of $15.23(3)/106.24(8)$ μm and $11.77(1)/11.4(1)$ mm.

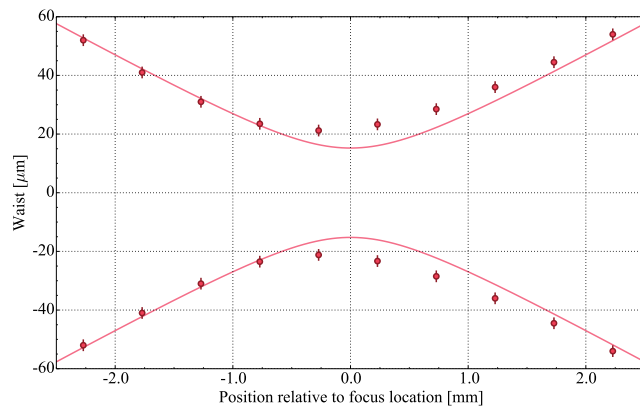


Figure C.0.2: Vertical waist of the squeezing beam in a 5 mm range, approximately 4 Rayleigh ranges, centred on its focus location. The fit using all the data points shown on the previous Figure predicts a smaller waist than the smallest measured one of $21(2)$ μm .

Effect of clipping

Obtaining a smaller vertical waist and therefore a higher squeezing factor was attempted by building a triplet composed of a -100, -50 and a 300 mm EFL cylindrical lenses spaced in that order by 50 and 262 mm resulting in a two fold increase of magnification compared to the duet cylindrical telescope and of a waist at focus in the vacuum chamber halved to about $8.5 \mu\text{m}$.

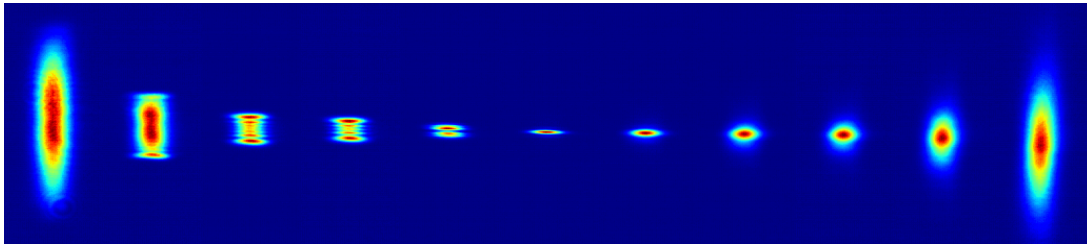


Figure C.0.3: Normalised transverse beam profiles taken at the following relative longitudinal positions from the focus (centre) from left to right: -1000, -450, -250, 200, -100, 0, 100, 200, 250, 450, 1100 μm . Only on one side of the focus, horizontal stripes due to vertical clipping of the beam appear. The measured waist at the focus is $14(2) \mu\text{m}$ with a theoretically predicted value of about $8.5 \mu\text{m}$.

While measuring the beam profile at the focus, horizontal stripes were discovered on one side of the focus. This effect is characteristic of clipping in the far field which causes interference-like stripes close to the Fourier plane (focus location) by "removing" amplitude and phase "information" in regions located one waist away which can't be obviously seen in the far field as presented on Figure C.0.3. For our setup, the most limiting clear aperture is the transport/squeezing combining PBS mount which is 12.7 mm in radius. For a beam waist of about 12 mm, the clipping occurs just above a waist away which is evidently too close. A common rule of thumb is to limit the clipping at a three waists distance. The duet telescope was diagnosed the same way and for a clipping slightly above two waist away, no defect was spotted close to the focus even when setting the camera to be overexposed in order to see if some faint stripes outside the centre region are present signalling the onset of clipping too closely.

Appendix D : Atomic physics derivations

Rabi oscillations

We can obtain a system of coupled equations for the complex eigenstate coefficients $c_g(t)$ and $c_e(t)$ by inserting equations (1.1.24) and (1.1.23) into the Schrödinger equation (1.1.15).

$$\begin{cases} i\hbar\dot{c}_g = -\frac{1}{2}\mu^*(E_0e^{-i\omega t} + E_0^*e^{i\omega t})c_e \\ i\hbar\dot{c}_e = \hbar\omega_0c_e - \frac{1}{2}\mu(E_0e^{-i\omega t} + E_0^*e^{i\omega t})c_g \end{cases} \quad (\text{D.0.1})$$

where $\mu = \mu_{e,g} = \mu_{g,e}^*$, $c_{g,e}(t) \equiv c_{g,e}$ and $\dot{c}_{g,e}$ is the time derivative of $c_{g,e}$.

The system of equation can be further simplified by introducing the slowly varying coefficient $\tilde{c}_e \equiv c_e e^{i\omega t}$ commonly denominated the *rotation frame transformation*. The system of equations becomes

$$\begin{cases} i\hbar\dot{c}_g = -\frac{1}{2}\mu^*(E_0e^{-i2\omega t} + E_0^*)\tilde{c}_e \\ i\hbar\dot{\tilde{c}}_e = \hbar(\omega_0 - \omega)\tilde{c}_e - \frac{1}{2}\mu(E_0 + E_0^*e^{i2\omega t})c_g \end{cases} \quad (\text{D.0.2})$$

What the rotating frame transformation does is simply to create a virtual state $|\tilde{e}\rangle$ which does not contain the quickly rotating phase factor $e^{i\omega t}$. On an energy diagram $|\tilde{e}\rangle$ lies $\hbar\omega$ below the excited state $|e\rangle$ and therefore $-\hbar\Delta$ away from the ground state $|g\rangle$ and is coupled to $|g\rangle$ with an interaction strength $\hbar\Omega$.

Defining the *Rabi frequency* Ω and detuning Δ

$$\Omega \equiv \frac{\mu E_0}{\hbar} \quad ; \quad \Delta \equiv \omega - \omega_0 \quad (\text{D.0.3})$$

Eq. (D.0.2) can be rewritten as

$$\begin{cases} i\dot{c}_g = -\frac{1}{2}\Omega^*\left(\frac{E_0}{E_0^*}e^{-i2\omega t} + 1\right)\tilde{c}_e \\ i\dot{\tilde{c}}_e = -\Delta\tilde{c}_e - \frac{1}{2}\Omega\left(1 + \frac{E_0^*}{E_0}e^{i2\omega t}\right)c_g \end{cases} \quad (\text{D.0.4})$$

N.B: In all this dissertation, the frequencies will have the usual unit of Hz and the angular frequencies will be expressed in rad/s. The detuning Δ and the *Rabi frequency* Ω are angular frequencies even if the use of *Rabi frequency* to designate an angular frequency is quite misleading. It is very useful to adopt the convention of expressing

an angular frequency as the product of a frequency and 2π . In this convention, if one reads $\delta = 2\pi \cdot 1$ Hz, it would mean that δ is an angular frequency of 2π rad/s.

The last approximation to be made is called the *Rotating Wave Approximation* (RWA) and allows an analytical resolution of the system. In the situation where the induced coupling is weak compared to the energy of the driving field and the field is close from resonance i.e. $\Omega' \ll \omega$ and $\omega \ll \omega_0$, the quickly oscillating terms $e^{\pm i2\omega t}$ can be neglected out as oscillating too fast and therefore averaging to zero over a reasonable interaction time ($\frac{2\pi}{\Omega'}$). The system of equation takes the solvable form

$$\begin{cases} i\dot{c}_g = -\frac{1}{2}\Omega^* \tilde{c}_e \\ i\dot{\tilde{c}}_e = -\Delta \tilde{c}_e - \frac{1}{2}\Omega c_g \end{cases} \quad (\text{D.0.5})$$

The exact analytical solution of the system is straightforward by taking the time derivative of the second equation of the system and substituting \dot{c}_g using the first one. One gets

$$\ddot{\tilde{c}}_e - i\Delta \dot{\tilde{c}}_e + \frac{|\Omega|^2}{4} \tilde{c}_e = 0 \quad (\text{D.0.6})$$

Taking the initial parameters $c_g(0) = 1$ and $c_e(0) = 0$ (i.e. the atom was purely in his ground state before applying the electric field), we obtain the following solution

$$\tilde{c}_e = -i \frac{\Omega}{\Omega'} \sin\left(\frac{\Omega' t}{2}\right) e^{i\frac{\Delta}{2} t} \quad ; \quad c_e = -i \frac{\Omega}{\Omega'} \sin\left(\frac{\Omega' t}{2}\right) e^{i(\frac{\Delta}{2} - \omega) t} \quad (\text{D.0.7})$$

where the *generalized Rabi frequency* is introduced as

$$\Omega' \equiv \sqrt{|\Omega|^2 + \Delta^2} \quad (\text{D.0.8})$$

Spontaneous emission - Density operator

The density matrix operator is formally defined as $\hat{\rho} = |\varphi\rangle \langle \varphi|$. Decomposing the wavefunction onto a complete set of orthogonal *pure* states $\{\varphi_i\}$ with $i = \{1, 2, \dots, n\}$, one can write the wavefunction as

$$|\varphi\rangle = \sum_{i=1}^n c_i |\varphi_i\rangle \quad (\text{D.0.9})$$

the density matrix operator as

$$\hat{\rho} = \sum_{i=1}^n p_i |\varphi_i\rangle \langle \varphi_i| \quad (\text{D.0.10})$$

with p_i , the probability of founding the wavefunction in the pure state φ_i , and the density matrix coefficients are given by

$$\rho_{ij} = \langle \varphi_i | \hat{\rho} | \varphi_j \rangle = \langle \varphi_i | \varphi \rangle \langle \varphi | \varphi_j \rangle = c_i c_j^* \quad (\text{D.0.11})$$

The dynamics of the density operator can be derivated by taking the time derivative of the density operator, Eq. (D.0.10), and identifying the Schrödinger equation (1.1.15).

$$\begin{aligned} i\hbar \frac{\partial \rho}{\partial t} &= i\hbar \sum_{i=1}^n p_i \left[\left(\frac{\partial}{\partial t} |\varphi_i(t)\rangle \right) \langle \varphi_i(t)| + |\varphi_i(t)\rangle \left(\frac{\partial}{\partial t} \langle \varphi_i(t)| \right) \right] \\ &= \sum_{i=1}^n p_i \left[\left(\hat{H} |\varphi_i(t)\rangle \right) \langle \varphi_i(t)| - |\varphi_i(t)\rangle \left(\langle \varphi_i(t)| \hat{H} \right) \right] \\ &= \hat{H} \hat{\rho} - \hat{\rho} \hat{H} \\ &= [\hat{H}, \hat{\rho}] \end{aligned} \quad (\text{D.0.12})$$

For a two-level system, the density matrix operator simplifies to

$$\hat{\rho} = \begin{pmatrix} c_e c_e^* & c_e c_g^* \\ c_g c_e^* & c_g c_g^* \end{pmatrix} = \begin{pmatrix} \rho_{ee} & \rho_{eg} \\ \rho_{ge} & \rho_{gg} \end{pmatrix} \quad (\text{D.0.13})$$

In the rotation frame, $\tilde{c}_e \equiv c_e e^{i\omega t}$ from which follows $\tilde{\rho}_{ge} \equiv c_g \tilde{c}_e = c_g c_e e^{i\omega t} = \rho_{ge} e^{i\omega t}$. Substituting equations (D.0.13) and (1.1.26) into (D.0.12), we obtain the following set of coupled equations of motion called the *Optical Bloch Equations*

$$\begin{aligned} \dot{\rho}_{gg} &= \frac{i}{2} (\Omega^* \tilde{\rho}_{eg} - \Omega \tilde{\rho}_{ge}) \\ \dot{\rho}_{ee} &= \frac{i}{2} (\Omega \tilde{\rho}_{ge} - \Omega^* \tilde{\rho}_{eg}) \\ \dot{\rho}_{ge} &= -i\Delta \tilde{\rho}_{ge} + \frac{i}{2} \Omega^* (\rho_{ee} - \rho_{gg}) \end{aligned} \quad (\text{D.0.14})$$

So far we have neglected spontaneous emission, it can be taken into account by simply adding its contribution to the time derivatives of the states population ρ_{ee} , ρ_{gg} and coherence terms $\tilde{\rho}_{eg}$, $\tilde{\rho}_{ge}$.

The spontaneous emission rate describes an exponential decrease/increase of the excited/ground state population ρ_{ee}/ρ_{gg} proportional to the excited state population ρ_{ee} . Therefore one simply needs to add $\mp \Gamma \rho_{ee}$ to $\dot{\rho}_{ee}/\dot{\rho}_{gg}$.

As for the coherence terms, they exponentially decrease at half the rate of the population terms, ie. $\partial \tilde{\rho}_{eg} = -\Gamma/2 \tilde{\rho}_{eg}$. The proof rely on the quantum theory of damping and is beyond the scope of this thesis, the reader should consult Daniel Steck quantum optics

notes [114] for a thorough derivation. We finally obtain the Optical Bloch Equations with spontaneous emission.

$$\begin{aligned}
\dot{\rho}_{gg} &= \Gamma\rho_{ee} + \frac{i}{2}(\Omega^*\tilde{\rho}_{eg} - \Omega\tilde{\rho}_{ge}) \\
\dot{\rho}_{ee} &= -\Gamma\rho_{ee} + \frac{i}{2}(\Omega\tilde{\rho}_{ge} - \Omega^*\tilde{\rho}_{eg}) \\
\dot{\tilde{\rho}}_{ge} &= -\left(\frac{\Gamma}{2} + i\Delta\right)\tilde{\rho}_{ge} + \frac{i}{2}\Omega^*(\rho_{ee} - \rho_{gg})
\end{aligned} \tag{D.0.15}$$

Saturation - Power-broadening

In the steady state regime, all time derivatives can be taken as null and the population in the excited state is found to be

$$\rho_{ee} = \frac{s_0/2}{1 + s_0 + (2\Delta/\Gamma)^2} \tag{D.0.16}$$

where s_0 is the *on-resonance saturation parameter* and the *saturation intensity* I_{sat} are given by

$$s_0 \equiv \frac{2|\Omega|^2}{\Gamma^2} = \frac{I}{I_{\text{sat}}} \quad I_{\text{sat}} \equiv \frac{\pi}{3} \frac{hc}{\lambda_0^3 \tau} \tag{D.0.17}$$

with λ and τ are respectively the wavelength associated with the resonance radiation, $\lambda_0 = 2\pi c/\omega_0$, and the characteristic time of the spontaneous emission process, $\tau = 1/\Gamma$ and I is the intensity of the driving radiation field. For the D_2 line of ^{40}K , $I_{\text{sat}} = 1.75 \text{ mW/cm}^2$, those units are typically the ones that an experimentalist manipulate on a daily basis and it becomes much easier to know in what saturation regime one can be using the intensity of the laser beam instead of dealing with the cumbersome calculation of $|\Omega|^2$.

By taking the asymptotic limit of the excited state population when going into high saturation regimes, we can immediately recover the know result that the population in the excited state cannot exceed one half, i.e. there cannot be a population inversion in a two-level system. The total scattering rate Γ_{tot} results from the spontaneous emission of the excited state population

$$\Gamma_{\text{tot}} = \Gamma\rho_{ee} = \frac{s_0}{1 + s_0} \frac{\Gamma/2}{1 + (2\Delta/\Gamma')^2} \quad \Gamma' = \Gamma\sqrt{1 + s_0} \tag{D.0.18}$$

which is a Lorentzian function of the detuning Δ and where we have introduced the *power-broadened linewidth* of the transition, Γ' .

Appendix E : Optical components legend

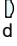
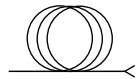
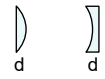
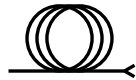
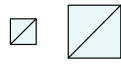
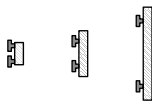








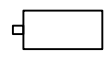
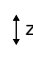

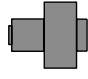


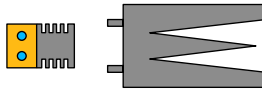


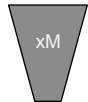
	Aspheric lens EFL: d mm		Optical fibre
	Plano-convex/concave lens EFL: d mm		High power optical fibre
	Polarising Beam Splitter (PBS) cubes		0.5"/1"/2" dielectric mirrors in kinematic mounts
	Polarising Plate Beam Splitter (PPBS) / Pick Off Plate (POP) / Dichroic Mirror (DM)		1" and 0.5" D-shaped fixed mirrors
	Waveplate		Piezoelectric mirror mount
	Optical density		Photodiode
	Optical Isolator (OI)		Fast photodiode
	Acousto-Optical Modulator (AOM)		Longitudinal translation stage
	Iris		Rotation stage
	Air cooled beam dump		Optical shutter
	Water cooled beam dump		External Cavity Diode Laser
	Gas glass cell		Beam expander Magnification xM

Figure E.0.1: Optical components legend.

Appendix F : ^{39}K hyperfine level structure

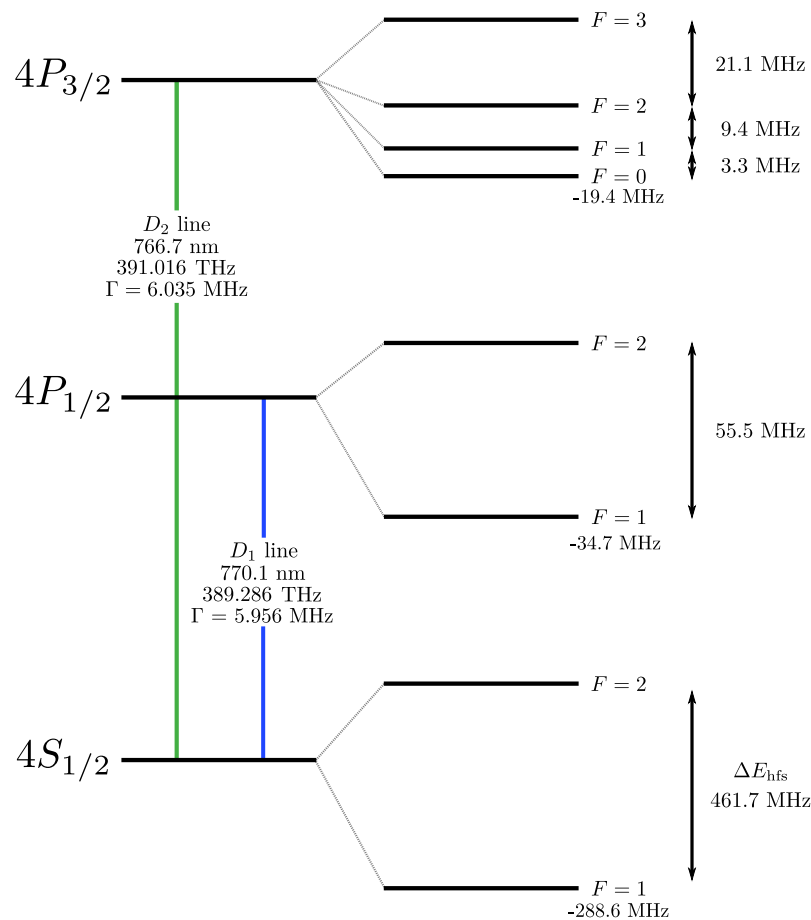


Figure F.0.1: Hyperfine level structure of ^{39}K . The values for the energy splitting not to scale and are taken from [160]. Their measured uncertainties are much smaller than the last significant number displayed and have been removed for clarity. The frequency appearing under one F level of each hyperfine splitting corresponds to its energetic offset from its parent J level.

Appendix G : Waist measurements

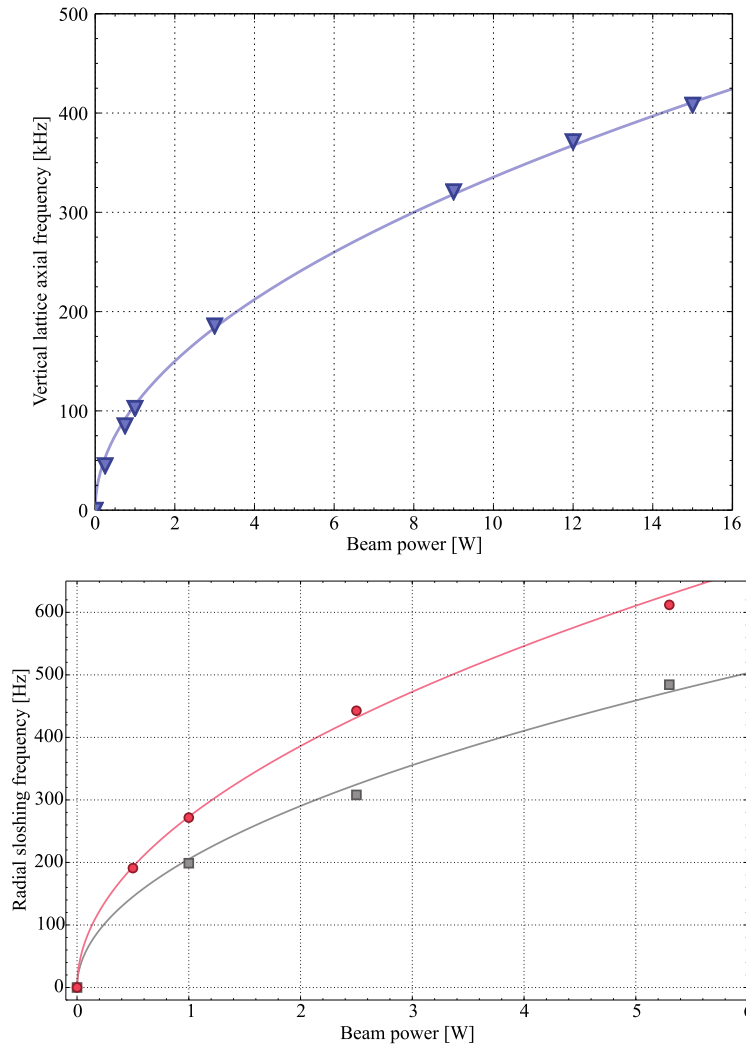


Figure G.0.1: Top: Twice the vertical lattice radial frequencies versus vertical lattice beam power and corresponding fit using Eq. (1.2.34) yielding a waist of $104.9(7) \mu\text{m}$. Bottom: Horizontal/vertical sloshing frequencies of the East/West ODTs versus beam powers in grey squares/red circles extracted from Figure 2.23 and fits according to Eq. (1.2.20) yielding waists of $80.6(7)$ and $69.9(4) \mu\text{m}$.

Bibliography

- [1] Heike Kamerlingh Onnes. “” *Commun. Phys. Lab. Univ. Leiden.* 108 (1908).
- [2] Heike Kamerlingh Onnes. “” *Commun. Phys. Lab. Univ. Leiden. Suppl.* 29 (Nov. 1911).
- [3] Heike Kamerlingh Onnes. “” *Commun. Phys. Lab. Univ. Leiden.* (May 1913).
- [4] Walther Meissner and Robert Ochsenfeld. “Ein neuer Effekt bei Eintritt der Supraleitfähigkeit”. *Naturwissenschaften* 21 (1933), pp. 787–788. DOI: 10.1007/BF01504252.
- [5] John Bardeen, Leon Neil Cooper, and John Robert Schrieffer. “Microscopic Theory of Superconductivity”. *Physical Review* 106.5 (1957), pp. 1175–1204. ISSN: 0031899X. DOI: 10.1103/PhysRev.106.162. arXiv: arXiv:1011.1669v3. URL: <http://link.aps.org/doi/10.1103/PhysRev.106.162>.
- [6] J. Bardeen, L. N. Cooper, and J. R. Schrieffer. “Theory of superconductivity”. *Physical Review* 108.5 (1957), pp. 1175–1204. ISSN: 0031899X. DOI: 10.1103/PhysRev.108.1175.
- [7] J. R. Gavaler. “Superconductivity in Nb-Ge films above 22 K”. *Applied Physics Letters* 23.8 (1973), pp. 480–482. ISSN: 00036951. DOI: 10.1063/1.1654966.
- [8] J. R. Gavaler, M. A. Janocko, and C. K. Jones. “Preparation and properties of high- T_c Nb-Ge films”. *Journal of Applied Physics* 45.7 (1974), pp. 3009–3013. ISSN: 0021-8979. DOI: 10.1063/1.1663717. URL: <http://aip.scitation.org/doi/10.1063/1.1663717>.
- [9] Pia Jensen Ray. “Structural investigation of $\text{La}_{2-x}\text{Sr}_x\text{CuO}_{4+y}$ - Following staging as a function of temperature”. Niels Bohr Institute, Faculty of Science, University of Copenhagen, Nov. 2015. DOI: 10.6084/m9.figshare.2075680.v2.
- [10] J. G. Bednorz and K. A. Muller. “Possible High T_c Superconductivity in the Ba-La-Cu-O System”. *Zeitschrift für Physik B: Condensed Matter* 64 (1986), pp. 189–193. ISSN: 0722-3277. DOI: 10.1007/BF01303701.
- [11] M. K. Wu, J. R. Ashburn, C. J. Torng, P. H. Hor, R. L. Meng, L. Gao, Z. J. Huang, Y. Q. Wang, and C. W. Chu. “Superconductivity at 93 K in a new mixed-phase Yb-Ba-Cu-O compound system at ambient pressure”. *Physical Review Letters* 58.9 (1987), pp. 908–910. ISSN: 00319007. DOI: 10.1103/PhysRevLett.58.908.

- [12] Rolf Heid, Klaus Peter Bohnen, Roland Zeyher, and Dirk Manske. “Momentum dependence of the electron-phonon coupling and self-energy effects in superconducting $\text{YBa}_2\text{Cu}_3\text{O}_7$ within the local density approximation”. *Physical Review Letters* 100.13 (2008), pp. 2–5. ISSN: 00319007. DOI: 10.1103/PhysRevLett.100.137001. arXiv: 0707.4429.
- [13] Feliciano Giustino, Marvin L. Cohen, and Steven G. Louie. “Small phonon contribution to the photoemission kink in the copper oxide superconductors.” *Nature* 452.7190 (2008), pp. 975–978. ISSN: 0028-0836. DOI: 10.1038/nature06874.
- [14] A. Schilling, M. Cantoni, J. D. Guo, and H. R. Ott. “Superconductivity above 130 K in the Hg-Ba-Ca-Cu-O system”. *Nature* 363 (1993), pp. 56–58.
- [15] C. W. Chu, L. Gao, F. Chen, Z. J. Huang, R. L. Meng, and Y. Y. Xue. “Superconductivity above 150 K in $\text{HgBa}_2\text{Ca}_2\text{Cu}_3\text{O}_{8+\delta}$ at high pressures”. *Nature* 365 (1993), pp. 323–325. ISSN: 0028-0836. DOI: 10.1038/365323a0.
- [16] Y. Kamihara, H. Hiramatsu, M. Hirano, R. Kawamura, H. Yanagi, T. Kamiya, and H. Hosono. “Iron-based layered superconductor: LaOFeP ”. *Journal of the American Chemical Society* 128.31 (2006), pp. 10012–10013. ISSN: 0002-7863. DOI: 10.1021/ja063355c.
- [17] Yoichi Kamihara, Takumi Watanabe, Masahiro Hirano, and Hideo Hosono. “Iron-Based Layered Superconductor $\text{La}[\text{O}_{1-x}\text{F}_x]\text{FeAs}$ ($x = 0.050.12$) with $T_c = 26$ K”. *Journal of the American Chemical Society* 130.11 (2008). PMID: 18293989, pp. 3296–3297. DOI: 10.1021/ja800073m. eprint: <https://doi.org/10.1021/ja800073m>. URL: <https://doi.org/10.1021/ja800073m>.
- [18] Ren Zhi-An, Che Guang-Can, Dong Xiao-Li, Yang Jie, Lu Wei, Yi Wei, Shen Xiao-Li, Li Zheng-Cai, Sun Li-Ling, Zhou Fang, and Zhao Zhong-Xian. “Superconductivity and phase diagram in iron-based arsenic-oxides $\text{ReFeAsO}_{1\delta}$ (Re = rare-earth metal) without fluorine doping”. *EPL (Europhysics Letters)* 83 (2008), p. 17002. ISSN: 0295-5075. DOI: 10.1209/0295-5075/83/17002. arXiv: 0804.2582. URL: <http://stacks.iop.org/0295-5075/83/i=1/a=17002>.
- [19] Jan Zaanen. “Towards a complete theory of high T_c ”. *Nature Physics* 2.March (2006), pp. 138–143. ISSN: 1745-2473. DOI: 10.1038/nphys253. URL: <http://dx.doi.org/10.1038/nphys253%7B%5C%7D5Cnhttp://www.nature.com/doifinder/10.1038/nphys253>.
- [20] Leon Balents. “Spin liquids in frustrated magnets.” *Nature* 464.7286 (2010), pp. 199–208. ISSN: 1476-4687. DOI: 10.1038/nature08917. arXiv: 9904169 [cond-mat]. URL: <http://www.ncbi.nlm.nih.gov/pubmed/20220838>.

- [21] Andrew J Schofield. “Non-Fermi liquids”. *Contemporary Physics* 40.2 (1999), pp. 95–115. ISSN: 0010-7514. DOI: 10.1080/001075199181602. URL: <http://dx.doi.org/10.1080/001075199181602>.
- [22] E Schrödinger. “Discussion of Probability Relations between Separated Systems”. *Math. Proc. Cambridge Phil. Soc.* 31.04 (1935), pp. 555–563. ISSN: 0305-0041. DOI: 10.1017/S0305004100013554. URL: http://journals.cambridge.org/article%7B%5C_%7DS0305004100013554.
- [23] Nicholas Metropolis and S Ulam. *The Monte Carlo Method*. 1949. DOI: 10.1080/01621459.1949.10483310. arXiv: 44:335–341. URL: <http://www.tandfonline.com/doi/abs/10.1080/01621459.1949.10483310>.
- [24] J. E. Hirsch, R. L. Sugar, D. J. Scalapino, and R. Blankenbecler. “Monte Carlo simulations of one-dimensional fermion systems”. *Physical Review B* 26.9 (1982), pp. 5033–5055. ISSN: 01631829. DOI: 10.1103/PhysRevB.26.5033.
- [25] E. Y. Loh, J. E. Gubernatis, R. T. Scalettar, S. R. White, D. J. Scalapino, and R. L. Sugar. “Sign problem in the numerical simulation of many-electron systems”. *Physical Review B* 41.13 (1990), pp. 9301–9307. ISSN: 01631829. DOI: 10.1103/PhysRevB.41.9301.
- [26] Matthias Troyer and Uwe-Jens Wiese. “Computational complexity and fundamental limitations to fermionic quantum Monte Carlo simulations.” *Phys. Rev. Lett.* 94.17 (2005), p. 170201. ISSN: 0031-9007. DOI: 10.1103/PhysRevLett.94.170201. arXiv: 0408370 [cond-mat].
- [27] Richard P. Feynman. “Simulating physics with computers”. *International Journal of Theoretical Physics* 21.6-7 (1982), pp. 467–488. ISSN: 00207748. DOI: 10.1007/BF02650179. arXiv: 9508027 [quant-ph].
- [28] D. Deutsch. “Quantum theory, the Church-Turing principle and the universal quantum computer”. *Proceedings of the Royal Society of London* 400.1818 (1985), pp. 97–117. ISSN: 1364-5021. DOI: 10.1098/rspa.1974.0120.
- [29] A. Church. “A Note on the Entscheidungsproblem”. *The Journal of Symbolic Logic* 1.1 (1936), pp. 40–41.
- [30] Alan Mathison Turing. *Intelligent Machinery*. Tech. rep. National Physical Laboratory, July 1948.
- [31] P. W. Shor. *Algorithms for quantum computation: discrete logarithms and factoring*. 1994. DOI: 10.1109/SFCS.1994.365700. arXiv: 9605043 [quant-ph].

- [32] Ch. H. Bennett. “Logical Reversibility of Computation”. *IBM Journal of Research and Development* 17 (Dec. 1973), pp. 525–532. DOI: 10.1147/rd.176.0525.
- [33] M.A. Nielsen and I.L. Chuang. *Quantum Computation and Quantum Information: 10th Anniversary Edition*. Cambridge University Press, 2010. ISBN: 9781139495486. URL: <https://books.google.co.uk/books?id=-s4DEy7o-a0C>.
- [34] T. Toffoli. *Reversible Computing*. Tech. rep. MIT/LCS/TM-151. MIT Lab. for Comp. Sci., 1980.
- [35] LMK Vandersypen, M Steffen, and Gregory Breyta. “Experimental realization of Shor’s quantum factoring algorithm using nuclear magnetic resonance”. *Nature* 120.1976 (2001), pp. 883–887. URL: <http://www.nature.com/nature/journal/v414/n6866/abs/414883a.html>.
- [36] Wolfgang Paul. “Electromagnetic Traps for Charged and Neutral Particles (Nobel Lecture)”. *Angewandte Chemie International Edition in English* 29.7 (1990), pp. 739–748. ISSN: 15213773. DOI: 10.1002/anie.199007391.
- [37] F. Schmidt-Kaler, Mark Riebe, and Stephan Gulde. “Realization of the Cirac – Zoller controlled-NOT quantum gate”. *Nature* 422.March (2003), p. 408. URL: <http://www.nature.com/nature/journal/v422/n6930/abs/nature01494.html>.
- [38] J. I. Cirac and P. Zoller. “Quantum computations with cold trapped ions”. *Physical Review Letters* 74.20 (1995), pp. 4091–4094. ISSN: 00319007. DOI: 10.1103/PhysRevLett.74.4091. arXiv: 0305129 [quant-ph].
- [39] T. Monz, K. Kim, W. Hänsel, M. Riebe, A. S. Villar, P. Schindler, M. Chwalla, M. Hennrich, and R. Blatt. “Realization of the quantum Toffoli gate with trapped ions”. *Physical Review Letters* 102.4 (2009), pp. 1–4. ISSN: 00319007. DOI: 10.1103/PhysRevLett.102.040501. arXiv: 0804.0082.
- [40] C. J. Ballance, T. P. Harty, N. M. Linke, M. A. Sepiol, and D. M. Lucas. “High-Fidelity Quantum Logic Gates Using Trapped-Ion Hyperfine Qubits”. *Physical Review Letters* 117.6 (2016), pp. 1–6. ISSN: 10797114. DOI: 10.1103/PhysRevLett.117.060504. arXiv: 1512.04600.
- [41] Emanuel Knill, Raymond Laflamme, and Wojciech Hubert Zurek. “Resilient Quantum Computation”. *Science* 279.5349 (1998), pp. 342–345. ISSN: 00368075. DOI: 10.1126/science.279.5349.342. arXiv: 9702058 [quant-ph]. URL: <http://science.sciencemag.org/content/279/5349/342>.

- [42] J. M. Amini, H. Uys, J. H. Wesenberg, S. Seidelin, J. Britton, J. J. Bollinger, D. Leibfried, C. Ospelkaus, A. P. Vandevender, and D. J. Wineland. “Toward scalable ion traps for quantum information processing”. *New Journal of Physics* 12 (2010), p. 033031. ISSN: 13672630. DOI: 10.1088/1367-2630/12/3/033031.
- [43] J. Kelly, R. Barends, A. G. Fowler, A. Megrant, E. Jeffrey, T. C. White, D. Sank, J. Y. Mutus, B. Campbell, Yu Chen, Z. Chen, B. Chiaro, A. Dunsworth, I.-C. Hoi, C. Neill, P. J. J. O’Malley, C. Quintana, P. Roushan, A. Vainsencher, J. Wenner, A. N. Cleland, and John M. Martinis. “State preservation by repetitive error detection in a superconducting quantum circuit”. *Nature* 519.7541 (2015), p. 66. ISSN: 0028-0836. DOI: 10.1038/nature14270. arXiv: 1411.7403. URL: <http://dx.doi.org/10.1038/nature14270>.
- [44] D. Kielpinski, C. Monroe, and D. J. Wineland. “Architecture for a large-scale ion-trap quantum computer”. *Nature* 417.6890 (2002), pp. 709–711. ISSN: 0028-0836. DOI: 10.1038/nature00784. URL: <http://www.nature.com/nature/journal/v417/n6890/abs/nature00784.html%7B%5C%7D5Cnhttp://www.nature.com/nature/journal/v417/n6890/pdf/nature00784.pdf>.
- [45] R. B. Blakestad, C. Ospelkaus, A. P. Vandevender, J. M. Amini, J. Britton, D. Leibfried, and D. J. Wineland. “High-fidelity transport of trapped-ion qubits through an X-junction trap array”. *Physical Review Letters* 102.15 (2009), pp. 1–4. ISSN: 00319007. DOI: 10.1103/PhysRevLett.102.153002. arXiv: 0901.0533.
- [46] Kenneth R Brown, Jungsang Kim, and Christopher Monroe. “Co-designing a scalable quantum computer with trapped atomic ions”. *npj Quantum Information* 2.August (2016), p. 16034. ISSN: 2056-6387. DOI: 10.1038/npjqi.2016.34. URL: <http://www.nature.com/articles/npjqi201634>.
- [47] J. Clarke and F. K. Wilhelm. “Superconducting quantum bits”. *Nature* 453.6 (2008), pp. 1031–1042. ISSN: 09538585. DOI: 10.1038/nature07128.
- [48] R. Barends, J. Kelly, A. Megrant, A. Veitia, D. Sank, E. Jeffrey, T. C. White, J. Mutus, Austin G. Fowler, B. Campbell, Y. Chen, Z. Chen, B. Chiaro, A. Dunsworth, C. Neill, P. O’Malley, P. Roushan, A. Vainsencher, J. Wenner, A. N. Korotkov, A. N. Cleland, and John M. Martinis. “Logic gates at the surface code threshold: Superconducting qubits poised for fault-tolerant quantum computing”. *Nature* 508.7497 (2014), pp. 501–503. ISSN: 1476-4687. DOI: 10.1038/nature13171. arXiv: 1402.4848. URL: <http://arxiv.org/abs/1402.4848>.

- [49] D. Jaksch, J. I. Cirac, P. Zoller, S. L. Rolston, R. Côté, and M. D. Lukin. “Fast quantum gates for neutral atoms”. *Physical Review Letters* 85.10 (2000), pp. 2208–2211. ISSN: 00319007. DOI: 10.1103/PhysRevLett.85.2208. arXiv: 0004038 [quant-ph].
- [50] Mark Saffman. “Quantum computing with atomic qubits and Rydberg interactions: Progress and challenges”. *J. Phys. B: At. Mol. Opt. Phys.* 49.202001 (2016), pp. 1–24. ISSN: 0953-4075. DOI: 10.1088/0953-4075/49/20/202001. arXiv: 1605.05207. URL: <http://iopscience.iop.org/article/10.1088/0953-4075/49/20/202001>.
- [51] Marco Anderlini, Patricia J. Lee, Benjamin L. Brown, Jennifer Sebby-Strabley, William D. Phillips, and J. V. Porto. “Controlled exchange interaction between pairs of neutral atoms in an optical lattice”. *Nature* 448.7152 (2007), pp. 452–456. ISSN: 0028-0836. DOI: 10.1038/nature06011. arXiv: 0708.2073. URL: <http://www.nature.com/nature/journal/v448/n7152/full/nature06011.html%7B%5C%7D5Cnhttp://www.nature.com/nature/journal/v448/n7152/pdf/nature06011.pdf>.
- [52] C. Weitenberg, S. Kuhr, K. Mølmer, and J. F. Sherson. “Quantum computation architecture using optical tweezers”. *Phys. Rev. A* 84.3 (2011), p. 32322. ISSN: 1050-2947. DOI: 10.1103/PhysRevA.84.032322. URL: <http://link.aps.org/doi/10.1103/PhysRevA.84.032322>.
- [53] A. Ashkin. “Trapping of atoms by resonance radiation pressure”. *Physical Review Letters* 40.12 (1978), pp. 729–732. ISSN: 00319007. DOI: 10.1103/PhysRevLett.40.729.
- [54] Steven Chu, L. Hoolberg, J. E. Bjorkholm, Alex Cable, and A. Ashkin. “Three-Dimensional Viscous Confinement and Cooling of Atoms by Resonance Radiation Pressure Steven”. 55.1 (1985), pp. 48–51. DOI: <https://doi.org/10.1103/PhysRevLett.55.48>.
- [55] A. Aspect, J. Dalibard, A. Heidmann, C. Salomon, and C. Cohen-Tannoudji. “Cooling atoms with stimulated emission”. *Physical Review Letters* 57.14 (1986), pp. 1688–1691. ISSN: 00319007. DOI: 10.1103/PhysRevLett.57.1688.
- [56] Paul D. Lett, Richard N. Watts, Christoph I. Westbrook, William D. Phillips, Phillip L. Gould, and Harold J. Metcalf. “Observation of atoms laser cooled below the doppler limit”. *Physical Review Letters* 61.2 (1988), pp. 169–172. ISSN: 00319007. DOI: 10.1103/PhysRevLett.61.169.

- [57] A. Aspect, E. Arimondo, R. Kaiser, N. Vansteenkiste, and C. Cohen-Tannoudji. “Laser Cooling below the One-Photon Recoil Energy by Velocity-Selective Coherent Population Trapping”. *Phys. Rev. Lett* 61 (1988), pp. 826–829. DOI: <http://dx.doi.org/10.1103/PhysRevLett.61.826>.
- [58] Albert Einstein. “Quantentheorie des einatomigen idealen Gases”. *Königliche Preußische Akademie der Wissenschaften. Sitzungsberichte* (1924), pp. 261–267.
- [59] M. H. Anderson, J. R. Ensher, M. R. Matthews, C. E. Wieman, and E. A. Cornell. “Observation of Bose-Einstein Condensation in a Dilute Atomic Vapor”. *Science* 269.5221 (1995), pp. 198–201. ISSN: 0036-8075. DOI: 10.1126/science.269.5221.198. arXiv: arXiv:1011.1669v3.
- [60] C. C. Bradley, C. A. Sackett, J. J. Tollett, and R. G. Hulet. “Evidence of Bose-Einstein condensation in an atomic gas with attractive interactions”. *Physical Review Letters* 75.9 (1995), pp. 1687–1690. ISSN: 00319007. DOI: 10.1103/PhysRevLett.75.1687.
- [61] K. B. Davis, M. O. Mewes, M. R. Andrews, N. J. Van Druten, D. S. Durfee, D. M. Kurn, and W. Ketterle. “Bose-Einstein condensation in a gas of sodium atoms”. *Physical Review Letters* 75.22 (1995), pp. 3969–3973. ISSN: 00319007. DOI: 10.1103/PhysRevLett.75.3969. arXiv: 9604005 [quant-ph].
- [62] Louis De Broglie. “Recherche sur la théorie des quanta”. *Annales de Physique* 3 (Jan. 1925), pp. 22–128.
- [63] *Ultracold quantum matter / University of Oxford Department of Physics*. 2017. URL: <https://www2.physics.ox.ac.uk/research/ultracold-quantum-matter>.
- [64] D. Jaksch, C. Bruder, J. I. Cirac, C. W. Gardiner, and P. Zoller. “Cold bosonic atoms in optical lattices”. *Physical Review Letters* 81.15 (1998), pp. 3108–3111. ISSN: 0031-9007. DOI: 10.1103/PhysRevLett.81.3108. arXiv: 9805329 [cond-mat].
- [65] Markus Greiner, Olaf Mandel, Tilman Esslinger, Theodor W. Hänsch, and Immanuel Bloch. “Quantum phase transition from a superfluid to a Mott insulator in a gas of ultracold atoms”. *Nature* 415.6867 (2002), pp. 39–44. ISSN: 00280836. DOI: 10.1038/415039a. URL: <http://dx.doi.org/10.1038/415039a>.
- [66] Herman Feshbach. “Unified theory of nuclear reactions”. *Annals of Physics* 5 (4 Dec. 1958), pp. 357–390. DOI: 10.1016/0003-4916(58)90007-1.
- [67] Cheng Chin, Rudolf Grimm, Paul Julienne, and Eite Tiesinga. “Feshbach resonances in ultracold gases”. *Reviews of Modern Physics* 82.2 (2010), pp. 1225–1286. ISSN: 00346861. DOI: 10.1103/RevModPhys.82.1225. arXiv: 0812.1496.

- [68] J. Struck, C. Ölschläger, R. Le Targat, P. Soltan-Panahi, A. Eckart, M. Lewestein, P. Windpassinger, and K. Sengstock. “Quantum Simulation of Frustrated Classical Magnetism in Triangular Optical Lattices”. *Science* 333.6045 (2011), pp. 996–999. DOI: 10.1126/science.1207239.
- [69] Gyu-Boong Jo, Jennie Guzman, Claire K. Thomas, Pavan Hosur, Ashvin Vishwanath, and Dan M. Stamper-Kurn. “Ultracold Atoms in a Tunable Optical Kagome Lattice”. *Phys. Rev. Lett.* 108.4 (2012), p. 045305. ISSN: 0031-9007. DOI: 10.1103/PhysRevLett.108.045305. arXiv: 1109.1591. URL: <http://arxiv.org/abs/1109.1591>.
- [70] Thomas Uehlinger, Gregor Jotzu, Michael Messer, Daniel Greif, Walter Hofstetter, Ulf Bissbort, and Tilman Esslinger. “Artificial graphene with tunable interactions”. *Physical Review Letters* 111.18 (2013), p. 185307. ISSN: 00319007. DOI: 10.1103/PhysRevLett.111.185307. arXiv: 1308.4401.
- [71] Widagdo Setiawan. “Fermi Gas Microscope”. Physics Department, Harvard University, 2012.
- [72] B. DeMarco and D. S. Jin. “Onset of Fermi Degeneracy in a Trapped Atomic Gas”. *Science* 285.5434 (1999), pp. 1703–1706. ISSN: 00368075. DOI: 10.1126/science.285.5434.1703.
- [73] F. Schreck, L. Khaykovich, K. L. Corwin, G. Ferrari, T. Bourdel, J. Cubizolles, and C. Salomon. “Quasipure Bose-Einstein condensate immersed in a Fermi sea”. *Physical Review Letters* 87.8 (2001), pp. 804031–804034. ISSN: 00319007. DOI: 10.1103/PhysRevLett.87.080403. arXiv: 0107442 [cond-mat].
- [74] Andrew G Truscott. “Observation of Fermi Pressure in a Gas of Trapped Atoms”. *Science* 291.5513 (2001), pp. 2570–2572. ISSN: 00368075. DOI: 10.1126/science.1059318. URL: <http://www.sciencemag.org/cgi/doi/10.1126/science.1059318>.
- [75] Robert Jördens, Niels Strohmaier, Kenneth Günter, Henning Moritz, and Tilman Esslinger. “A Mott insulator of fermionic atoms in an optical lattice”. *Nature* 455.7210 (2008), pp. 204–207. ISSN: 0028-0836. DOI: 10.1038/nature07244. arXiv: arXiv:0804.4009v2. URL: <http://www.nature.com/doi/10.1038/nature07244>.
- [76] U. Schneider, L. Hackermüller, S. Will, Th. Best, I. Bloch, T. A. Costi, R. W. Helmes, D. Rasch, and A. Rosch. “Research articles”. *Science* 322.5907 (2008), pp. 1520–1525. ISSN: 0006-8055. DOI: 10.1126/science.1165449.

- [77] M. Lewenstein, A. Sanpera, and V. Ahufinger. *Ultracold Atoms in Optical Lattices: Simulating quantum many-body systems*. OUP Oxford, 2012. ISBN: 9780191627439. URL: <https://books.google.es/books?id=Wpl91RDxV5IC>.
- [78] Waseem S. Bakr, Jonathon I. Gillen, Amy Peng, Simon Fölling, and Markus Greiner. “A quantum gas microscope for detecting single atoms in a Hubbard-regime optical lattice.” *Nature* 462.7269 (Nov. 2009), pp. 74–77. ISSN: 1476-4687. DOI: 10.1038/nature08482. URL: <http://www.ncbi.nlm.nih.gov/pubmed/19890326>.
- [79] Jacob F Sherson, Christof Weitenberg, Manuel Endres, Marc Cheneau, Immanuel Bloch, and Stefan Kuhr. “Single-atom-resolved fluorescence imaging of an atomic Mott insulator.” *Nature* 467 (2010), pp. 68–72. ISSN: 1476-4687. DOI: 10.1038/nature09378. URL: <http://www.ncbi.nlm.nih.gov/pubmed/20720540>.
- [80] W. S. Bakr, A. Peng, M. E. Tai, R. Ma, J. Simon, J. I. Gillen, S. Fölling, L. Pollet, and M. Greiner. “Probing the Superfluid-to-Mott Insulator Transition at the Single-Atom Level”. *Science* 329.5991 (2010), p. 547. DOI: 10.1126/science.1192368.
- [81] M. Endres, M. Cheneau, T. Fukuhara, C. Weitenberg, P. Schauß C. Gross, L. Mazza, M. C. Bañuls, L. Pollet, I. Bloch, and S. Kuhr. “Observation of Correlated Particle-Hole and String Order in Low-Dimensional Mott Insulators”. *Science* 334 (2011), p. 200. ISSN: 1095-9203. DOI: 10.1126/science.1209284. URL: <http://www.sciencemag.org/content/334/6053/200.abstract>.
- [82] Marc Cheneau, Peter Barmettler, Dario Poletti, Manuel Endres, Peter Schauß, Takeshi Fukuhara, Christian Gross, Immanuel Bloch, Corinna Kollath, and Stefan Kuhr. “Light-cone-like spreading of correlations in a quantum many-body system”. *Nature* 481.7382 (2012), pp. 484–487. ISSN: 0028-0836. DOI: 10.1038/nature10748. arXiv: 1111.0776. URL: <http://www.ncbi.nlm.nih.gov/pubmed/22281597%7B%5C%7D5Cnhttp://www.nature.com/doifinder/10.1038/nature10748>.
- [83] Takeshi Fukuhara, Peter Schaus, Manuel Endres, Sebastian Hild, Marc Cheneau, Immanuel Bloch, and Christian Gross. “Microscopic observation of magnon bound states and their dynamics”. *Nature* 502.7469 (2013), pp. 76–79. ISSN: 0028-0836. DOI: 10.1038/nature12541. arXiv: 1305.6598. URL: <http://www.nature.com/nature/journal/v502/n7469/full/nature12541.html%7B%5C%7D5Cnhttp://www.nature.com/nature/journal/v502/n7469/pdf/nature12541.pdf>.

- [84] Philipp M Preiss, R. Ma, M Eric Tai, Alexander Lukin, Matthew Rispoli, Philip Zupancic, Yoav Lahini, Rajibul Islam, and Markus Greiner. “Strongly correlated quantum walks in optical lattices”. *Science (New York, N. Y.)* 347.6227 (2015), pp. 1229–1233. ISSN: 0036-8075. DOI: 10.1126/science.1260364. arXiv: 1409.3100. URL: <http://www.sciencemag.org/cgi/doi/10.1126/science.1260364>.
- [85] Jonathan Simon, Waseem S. Bakr, Ruichao Ma, M. Eric Tai, Philipp M. Preiss, and Markus Greiner. “Quantum simulation of antiferromagnetic spin chains in an optical lattice.” *Nature* 472.7343 (2011), pp. 307–312. ISSN: 0028-0836. DOI: 10.1038/nature09994. URL: <http://dx.doi.org/10.1038/nature09994>.
- [86] Waseem S. Bakr, Philipp M. Preiss, M. Eric Tai, Ruichao Ma, Jonathan Simon, and Markus Greiner. “Orbital excitation blockade and algorithmic cooling in quantum gases”. *Nature* 480.7378 (2011), pp. 500–503. ISSN: 0028-0836. DOI: 10.1038/nature10668. arXiv: arXiv:1105.5834v1. URL: <http://dx.doi.org/10.1038/nature10668>.
- [87] Christof Weitenberg, Manuel Endres, Jacob F. Sherson, Marc Cheneau, Peter Schauß, Takeshi Fukuhara, Immanuel Bloch, and Stefan Kuhr. “Single-spin addressing in an atomic Mott insulator”. *Nature* 471.7338 (Mar. 2011), pp. 319–324. ISSN: 0028-0836. DOI: 10.1038/nature09827. URL: <http://www.nature.com/doi/10.1038/nature09827>.
- [88] K. Shibata, R. Yamamoto, and Y. Takahashi. “High-Sensitivity In situ Fluorescence Imaging of Ytterbium Atoms in a Two-Dimensional Optical Lattice with Dual Optical Molasses”. *J. Phys. Soc. Jpn.* 83 (2014), p. 014301. DOI: 10.7566/JPSJ.83.014301.
- [89] Ryuta Yamamoto, Jun Kobayashi, Kohei Kato, Takuma Kuno, Yuto Sakura, and Yoshiro Takahashi. “Site-resolved imaging of single atoms with a Faraday quantum gas microscope”. *arXiv* 1607.07045 (2016), pp. 1–8. arXiv: arXiv:1607.07045v1.
- [90] W. Hofstetter, J. I. Cirac, P. Zoller, E. Demler, and M. D. Lukin. “High-temperature superfluidity of fermionic atoms in optical lattices.” *Physical review letters* 89.22 (2002), p. 220407. ISSN: 0031-9007. DOI: 10.1103/PhysRevLett.89.220407. arXiv: 0204237 [cond-mat]. URL: <http://link.aps.org/doi/10.1103/PhysRevLett.89.220407>.
- [91] Simon Trebst, Ulrich Schollwöck, Matthias Troyer, and Peter Zoller. “d-Wave resonating valence bond states of fermionic atoms in optical lattices”. *Phys-*

- ical Review Letters* 96.25 (2006), p. 250402. ISSN: 00319007. DOI: 10.1103/PhysRevLett.96.250402. arXiv: 0506809 [cond-mat].
- [92] Elmar Haller, James Hudson, Andrew Kelly, Dylan A. Cotta, Bruno Peaudecerf, Graham D. Bruce, and Stefan Kuhr. “Single-atom imaging of fermions in a quantum-gas microscope”. *Nature Physics* 11 (July 2015), p. 738. ISSN: 1745-2481. URL: <http://dx.doi.org/10.1038/nphys3403%2010.1038/nphys3403%20http://www.nature.com/nphys/journal/vaop/ncurrent/abs/nphys3403.html%7B%5C%7Dsupplementary-information>.
- [93] Lawrence W. Cheuk, Matthew A. Nichols, Melih Okan, Thomas Gersdorf, Vinay V. Ramasesh, Waseem S. Bakr, Thomas Lompe, and Martin W. Zwierlein. “Quantum-gas microscope for fermionic atoms”. *Physical Review Letters* 114.19 (2015), p. 193001. ISSN: 10797114. DOI: 10.1103/PhysRevLett.114.193001. arXiv: 1503.02648.
- [94] Maxwell F Parsons, Florian Huber, Anton Mazurenko, Christie S. Chiu, Widagdo Setiawan, Katherine Wooley-Brown, Sebastian Blatt, and Markus Greiner. “Site-Resolved Imaging of Fermionic ${}^6\text{Li}$ in an Optical Lattice”. *Physical Review Letters* 114.213002 (2015), pp. 1–5. ISSN: 0031-9007. DOI: 10.1103/PhysRevLett.114.213002. arXiv: 1504.04397. URL: <http://link.aps.org/doi/10.1103/PhysRevLett.114.213002>.
- [95] G. J. A. Edge, R. Anderson, D. Jervis, D. C. McKay, R. Day, S. Trotzky, and J. H. Thywissen. “Imaging and addressing of individual fermionic atoms in an optical lattice”. *Physical Review A - Atomic, Molecular, and Optical Physics* 92.6 (2015), p. 063406. ISSN: 10941622. DOI: 10.1103/PhysRevA.92.063406. arXiv: 1510.04744.
- [96] Ahmed Omran, Martin Boll, Timon A. Hilker, Katharina Kleinlein, Guillaume Salomon, Immanuel Bloch, and Christian Gross. “Microscopic Observation of Pauli Blocking in Degenerate Fermionic Lattice Gases”. *Physical Review Letters* 115.26 (2015), p. 263001. ISSN: 10797114. DOI: 10.1103/PhysRevLett.115.263001. arXiv: 1510.04599.
- [97] Daniel Greif, Maxwell F Parsons, Anton Mazurenko, Christie S Chiu, Sebastian Blatt, Florian Huber, Geoffrey Ji, and Markus Greiner. “Site-resolved imaging of a fermionic Mott insulator”. *Science* 351.6276 (2016), pp. 953–957. ISSN: 0036-8075. DOI: 10.1126/science.aad9041. arXiv: 1511.06366. URL: <http://arxiv.org/abs/1511.06366%7B%5C%7D5Cnhttp://www.sciencemag.org/cgi/doi/10.1126/science.aad9041>.

- [98] Maxwell F. Parsons, Anton Mazurenko, Christie S. Chiu, Geoffrey Ji, Daniel Greif, and Markus Greiner. “Site-resolved measurement of the spin-correlation function in the Fermi-Hubbard model”. *Science* 353.6305 (2016), pp. 1253–1256. ISSN: 0036-8075. DOI: 10.1126/science.aag1430. arXiv: 1605.02704.
- [99] Stephan Falke, Eberhard Tiemann, Christian Lisdat, Harald Schnatz, and Gesine Grosche. “Transition frequencies of the D lines of ^{39}K , 40K, and 41K measured with a femtosecond laser frequency comb”. *Physical Review A* 74.3 (2006), pp. 1–9. ISSN: 1050-2947. DOI: 10.1103/PhysRevA.74.032503.
- [100] E. Arimondo, M. Inguscio, and P. Violino. “Experimental determinations of the hyperfine structure in the alkali atoms”. *Reviews of Modern Physics* 49.1 (1977), pp. 31–75. ISSN: 00346861. DOI: 10.1103/RevModPhys.49.31.
- [101] Pieter Zeeman. “The Effect of Magnetisation on the Nature of Light Emitted by a Substance”. *Nature* 55 (Feb. 1897), p. 347. DOI: 10.1038/055347a0.
- [102] Thomas Preston. “Radiation Phenomena in a Strong Magnetic Field”. *Transaction Royal Dublin Society* 6 (1898), pp. 385–391.
- [103] Friedrich Paschen and Ernst Back. “Liniengruppen magnetisch vervollständigt”. *Physica* 1 (1921), pp. 261–273.
- [104] G. Breit and I. I. Rabi. “Measurement of Nuclear Spin”. *Physical Review* 38.11 (1931), pp. 2082–2083. ISSN: 0031-899X. DOI: 10.1103/PhysRev.38.2082.2. URL: <http://link.aps.org/doi/10.1103/PhysRev.38.2082.2>.
- [105] G. D. Bruce, E. Haller, B. Peaudecerf, D. A. Cotta, M. Andia, S. Wu, M. Y. H. Johnson, B. W. Lovett, and S. Kuhr. “Sub-Doppler laser cooling of ^{40}K with Raman gray molasses on the D_2 line”. *Journal of Physics B: Atomic, Molecular and Optical Physics* 50.9 (2017), p. 095002. URL: <http://stacks.iop.org/0953-4075/50/i=9/a=095002>.
- [106] E. Schrödinger. “An undulatory theory of the mechanics of atoms and molecules”. *Physical Review* 28.6 (1926), pp. 1049–1070. ISSN: 0031899X. DOI: 10.1103/PhysRev.28.1049. arXiv: 1112.5320.
- [107] M. Born and V. Fock. “Beweis des Adiabatenatzes”. *Zeitschrift für Physik* 51 (Mar. 1928), pp. 165–180. DOI: 10.1007/BF01343193.
- [108] Lev Davidovitch Landau. “Zur Theorie der Energieübertragung. II”. *Physikalische Zeitschrift der Sowjetunion* 2 (1932), pp. 46–51. DOI: 1.

- [109] Clarence Zener. “Non-adiabatic crossing of energy levels”. *Proceedings of the Royal Society of London A: Mathematical, Physical and Engineering Sciences* 137.833 (1932), pp. 696–702. ISSN: 0950-1207. DOI: 10.1098/rspa.1932.0165. eprint: <http://rspa.royalsocietypublishing.org/content/137/833/696.full.pdf>. URL: <http://rspa.royalsocietypublishing.org/content/137/833/696>.
- [110] A. R. Edmonds. *Angular Momentum in Quantum Mechanics*. Investigations in Physics Series. Princeton University Press, 1996. ISBN: 9780691025896. URL: <https://books.google.fr/books?id=0BS0g0oHhZ0C>.
- [111] C. Eckart. “The Application of Group theory to the Quantum Dynamics of Monatomic Systems”. *Reviews of Modern Physics* 2.3 (1930), pp. 305–380. ISSN: 0034-6861. DOI: 10.1103/RevModPhys.2.305. URL: <http://link.aps.org/doi/10.1103/RevModPhys.2.305>.
- [112] E. P. Wigner and J. J. Griffin. *Group Theory and Its Application to the Quantum Mechanics of Atomic Spectra*. Pure and applied Physics. Academic Press, 1959. URL: <https://books.google.co.uk/books?id=IOJEAAAAIAAJ>.
- [113] M. Auzinsh, D. Budker, and S. Rochester. *Optically Polarized Atoms: Understanding Light-atom Interactions*. OUP Oxford, 2010. ISBN: 9780199565122. URL: <https://books.google.fr/books?id=ySwUDAAAQBAJ>.
- [114] Daniel Adam Steck. “Quantum and Atom Optics”. *Book* ().
- [115] Rodney Loudon. *The quantum theory of light*. Oxford science publications. Clarendon Press, 1983. ISBN: 9780198511526. URL: https://books.google.fr/books?id=%5C_FTwAAAAMAAJ.
- [116] J.J. Sakurai and J. Napolitano. *Modern Quantum Mechanics*. Addison-Wesley, 2011. ISBN: 9780805382914. URL: <https://books.google.fr/books?id=N4I-AQAACAAJ>.
- [117] Chung Yu Shih and Michael S. Chapman. “Nondestructive light-shift measurements of single atoms in optical dipole traps”. *Physical Review A - Atomic, Molecular, and Optical Physics* 87.6 (2013), pp. 2–6. ISSN: 10502947. DOI: 10.1103/PhysRevA.87.063408. arXiv: 1304.3346.
- [118] Albert Einstein. “On the Quantum Theory of Radiation”. *Physik. Zeit.* 18 (1917), p. 121.
- [119] Victor Weisskopf and Eugene Wigner. “Berechnung der natürlichen Linienbreite auf Grund der Diracschen Lichttheorie”. *Zeit. f. Phys.* 63 (1930), p. 54.

- [120] Wikipedia. *Hermite Polynomials*. 2017. URL: https://en.wikipedia.org/wiki/Hermite_polynomials.
- [121] A. E. Siegman. *Lasers*. University Science Books, 1986. ISBN: 9780935702118. URL: <https://books.google.fr/books?id=1BZVwUZLTkAC>.
- [122] N. W. Ashcroft and N. D. Mermin. *Solid State Physics*. HRW international editions. Holt, Rinehart and Winston, 1976. ISBN: 9780030839931. URL: <https://books.google.ca/books?id=oXIfaQAAMAAJ>.
- [123] A. Kastberg, W. D. Phillips, S. L. Rolston, R. J C Spreuw, and P. S. Jessen. “Adiabatic cooling of cesium to 700 nK in an optical lattice”. *Physical Review Letters* 74.9 (1995), pp. 1542–1545. ISSN: 00319007. DOI: 10.1103/PhysRevLett.74.1542.
- [124] M. Greiner, I. Bloch, O. Mandel, T. W. Hänsch, and T. Esslinger. “Exploring phase coherence in a 2D lattice of Bose-Einstein condensates.” *Physical review letters* 87.16 (2001), p. 160405. ISSN: 0031-9007. DOI: 10.1103/PhysRevLett.87.160405. arXiv: 0105105 [cond-mat].
- [125] Maxime Ben Dahan, Ekkehard Peik, Jakob Reichel, Yvan Castin, and Christophe Salomon. “Bloch Oscillations of Atoms in an Optical Potential”. *Physical Review Letters* 76.24 (1996), pp. 4508–4511. ISSN: 0031-9007. DOI: 10.1103/PhysRevLett.76.4508. URL: <http://dx.doi.org/10.1103/PhysRevLett.76.4508>.
- [126] Torben Müller. “Exploring excited Bloch bands in optical lattices via stimulated Raman transitions”. PhD thesis. Johannes Gutenberg-Universität Mainz, 2006.
- [127] Jean Dalibard. “Collisional dynamics of ultra-cold atomic gases”. *Proceedings of the International School of Physics- ...* (1999), pp. 1–29. DOI: 10.3254. URL: http://www.uni-ulm.de/fileadmin/website%7B%5C_%7Duni%7B%5C_%7Dulm/nawi.inst.235/Lehre/Ultrakalte%7B%5C_%7DQuantengase/Dalibard%7B%5C_%7D-%7B%5C_%7DCollisional%7B%5C_%7Ddynamics%7B%5C_%7Dof%7B%5C_%7Dultra-cold%7B%5C_%7Datomic%7B%5C_%7Dgases%7B%5C_%7D%7B%5C_%7DVarenna%7B%5C_%7D98%7B%5C_%7D.pdf.
- [128] Manfred Sigrist. “Solid State Theory”. *Institute fur Theoretische Physik Course Notes* (2013), pp. 15–21.
- [129] Tilman Esslinger. “Fermi-Hubbard Physics with Atoms in an Optical Lattice”. *Annual Reviews of Condensed Matter Physics* 1 (2010), pp. 129–152. ISSN: 1947-5454. DOI: 10.1146/annurev-conmatphys-070909-104059. arXiv: 1007.0012. URL: <http://arxiv.org/abs/1007.0012>.

- [130] R. Micnas, J. Ranninger, and S. Robaszkiewicz. “Superconductivity in narrow-band systems with local nonretarded attractive interactions”. *Reviews of Modern Physics* 62.1 (1990), pp. 113–171. ISSN: 00346861. DOI: 10.1103/RevModPhys.62.113.
- [131] P. G. J. Van Dongen. “Thermodynamics of the extended Hubbard model in high dimensions”. *Physical Review Letters* 67.6 (1991), pp. 757–760. ISSN: 00319007. DOI: 10.1103/PhysRevLett.67.757.
- [132] P. G. J. Van Dongen. “Extended Hubbard model at weak coupling”. *Physical Review B* 50.19 (1994), pp. 14016–14031. ISSN: 01631829. DOI: 10.1103/PhysRevB.50.14016.
- [133] G. S. Rushbrooke, G. A. JR. Baker, P. J. Wood, C. Domb, and M. S. Green. *Phase Transitions and Critical Phenomena*. Vol. 3. Academic Press, London, pp. 245–356.
- [134] D. O. Soares-Pinto, I. S. Oliveira, and M. S. Reis. “Phase diagram of a 2D Ising model within a nonextensive approach”. *The European Physical Journal B* 62.3 (Apr. 2008), pp. 337–340. ISSN: 1434-6036. DOI: 10.1140/epjb/e2008-00170-5. URL: <https://doi.org/10.1140/epjb/e2008-00170-5>.
- [135] Ulrich Schneider. “Interacting Fermionic Atoms in Optical Lattices—A Quantum Simulator for Condensed Matter Physics”. *PhD thesis* (2010), pp. 1–191. URL: <http://ubm.opus.hbz-nrw.de/volltexte/2011/2860/>.
- [136] Jacob Hinney, Aline Dinkelaker, and Vicky Anderson. *ECDL manual*. 2014.
- [137] Nicolas Sangouard. “D₁-line cooling of potassium 40 and magnetic field control in a cold atom experiment”. Physics Department, University of Strathclyde, 2014.
- [138] R. W. P. Drever, J. L. Hall, F. V. Kowalski, J. Hough, G. M. Ford, A. J. Munley, and H. Ward. “Laser phase and frequency stabilization using an optical resonator”. *Applied Physics B* 31 (2 1983), pp. 97–105. DOI: 10.1007/BF00702605.
- [139] Qiang Liu, Xianjin Zeng, Junhai Zhang, and Weimin Sun. “Polarization spectroscopy in cesium”. In: *2010 Academic Symposium on Optoelectronics and Microelectronics Technology and 10th Chinese-Russian Symposium on Laser Physics and Laser Technology, RCSLPLT/ASOT 2010*. 2010, pp. 200–203. ISBN: 9781424455133. DOI: 10.1109/RCSLPLT.2010.5615354.
- [140] Giovanna Morigi, Jürgen Eschner, and Christoph H. Keitel. “Ground state laser cooling using electromagnetically induced transparency”. *Phys. Rev. Lett.* 85 (2000), pp. 4458–4461. ISSN: 00319007. DOI: 10.1103/PhysRevLett.85.4458. URL: <http://www.ncbi.nlm.nih.gov/pubmed/11082570>.

- [141] B. Lounis and C. Cohen-Tannoudji. “Coherent population trapping and Fano profiles”. *Journal de Physique II* 2 (1992), pp. 579–592. ISSN: 1155-4312. DOI: 10.1051/jp2:1992153.
- [142] Giovanna Morigi. “Cooling atomic motion with quantum interference”. *Phys. Rev. A* 67 (2003), p. 033402. ISSN: 1050-2947. DOI: 10.1103/PhysRevA.67.033402.
- [143] M. Lukin. *Modern Atomic Optical Physics II*. 2006, pp. 1–285. URL: papers2://publication/uuid/A5CFC11A-4601-4704-A837-5459BB81611A.
- [144] Peter Staantum. “Quantum Optics with Trapped Calcium Ions”. PhD thesis. University of Aarhus, 2004.
- [145] D. Wineland, C. Monroe, W. Itano, D. Leibfried, B. King, and D. Meekhof. “Experimental issues in coherent quantum-state manipulation of trapped atomic ions”. 103.3 (1998), p. 259. URL: citeseer.ist.psu.edu/wineland98experimental.html.
- [146] C. F. Roos, D. Leibfried, A. Mundt, F. Schmidt-Kaler, J. Eschner, and R. Blatt. “Experimental demonstration of ground state laser cooling with electromagnetically induced transparency.” *Phys. Rev. Lett.* 85 (2000), pp. 5547–5550. ISSN: 0031-9007. DOI: 10.1103/PhysRevLett.85.5547.
- [147] J. Steinbach, J. Twamley, and P. L. Knight. “Engineering two-mode interactions in ion traps”. *Phys. Rev. A* 56.6 (1997), pp. 4815–4825. ISSN: 1050-2947. DOI: 10.1103/PhysRevA.56.4815. arXiv: 9708008 [quant-ph]. URL: <http://arxiv.org/abs/quant-ph/9708008>.
- [148] Widagdo Setiawan. “Fermi Gas Microscope”. PhD thesis. Harvard University, 2012, p. 176.
- [149] Niels Strohmaier. “Exploring the Hubbard model with ultracold fermionic atoms in an optical lattice”. PhD thesis. ETH Zurich, 2010.
- [150] John L. Bohn. “Cooper pairing in ultracold ^{40}K using Feshbach resonances”. *Phys. Rev. A* 61 (5 Apr. 2000), p. 053409. DOI: 10.1103/PhysRevA.61.053409. URL: <https://link.aps.org/doi/10.1103/PhysRevA.61.053409>.
- [151] C. A. Regal, M. Greiner, and D. S. Jin. “Observation of resonance condensation of fermionic atom pairs”. *Physical Review Letters* 92.4 (2004), p. 40403. ISSN: 0031-9007. DOI: 10.1103/PhysRevLett.92.040403. arXiv: 0401554 [cond-mat].

- [152] C. Ticknor, C. A. Regal, D. S. Jin, and J. L. Bohn. “Multiplet structure of Feshbach resonances in nonzero partial waves”. *Physical Review A - Atomic, Molecular, and Optical Physics* 69.4 (2004), pp. 1–6. ISSN: 10502947. DOI: 10.1103/PhysRevA.69.042712. arXiv: 0310121 [physics].
- [153] C. A. Regal and D. S. Jin. “Measurement of positive and negative scattering lengths in a Fermi gas of atoms”. *Physical Review Letters* 90.23 (2003), p. 230404. ISSN: 0031-9007. DOI: 230404\r10.1103/PhysRevLett.90.230404. arXiv: 0302246 [arXiv:cond-mat].
- [154] C. A. Regal, C. Ticknor, J. L. Bohn, and D. S. Jin. “Tuning p-wave interactions in an ultracold Fermi gas of atoms”. *Physical Review Letters* 90.5 (2003), p. 53201. ISSN: 0031-9007. DOI: 053201\r10.1103/PhysRevLett.90.053201. arXiv: 0209071 [cond-mat].
- [155] Robert Jördens. “Metallic and Mott-Insulating Phases in Fermionic Quantum Gases”. en. PhD thesis. EC, 2010. DOI: 10.3929/ethz-a-006278918.
- [156] Maxwell F. Parsons, Anton Mazurenko, Christie S. Chiu, Geoffrey Ji, Daniel Greif, and Markus Greiner. “Site-resolved measurement of the spin-correlation function in the Fermi-Hubbard model”. *Science* 353.6305 (2016), pp. 1253–1256. ISSN: 0036-8075. DOI: 10.1126/science.aag1430. arXiv: 1605.02704.
- [157] Lawrence W. Cheuk, Matthew A. Nichols, Katherine R. Lawrence, Melih Okan, Hao Zhang, Ehsan Khatami, Nandini Trivedi, Thereza Paiva, Marcos Rigol, and Martin W. Zwierlein. “Observation of spatial charge and spin correlations in the 2D Fermi-Hubbard model”. *Science* 353.6305 (2016), pp. 1260–1264.
- [158] Martin Boll, Timon A Hilker, Guillaume Salomon, Ahmed Omran, Jacopo Nespolo, Lode Pollet, Immanuel Bloch, and Christian Gross. “Spin- and density-resolved microscopy of antiferromagnetic correlations in Fermi-Hubbard chains”. *Science* 353.6305 (2016), pp. 1257–1260. ISSN: 0036-8075. DOI: 10.1126/science.aag1635. arXiv: 1605.05661.
- [159] A. Mazurenko, C. S. Chiu, G. Ji, M. F. Parsons, M Kanász-Nagy, R. Schmidt, F. Grusdt, E. Demler, D. Greif, and M. Greiner. “A cold-atom Fermi-Hubbard antiferromagnet”. *Nature* 545 (2016), p. 462. DOI: 10.1038/nature22362. arXiv: 1612.08436. URL: <http://dx.doi.org/10.1038/nature22362>.
- [160] Tobias Tiecke. *Potassium properties*. 2011. URL: <http://www.tobiastiecke.nl/archive/PotassiumProperties.pdf>.